Durham E-Theses

Toward Efficient Organic Photovoltaics: From Formulation and Novel Materials to Device Architectures

DAVID ALEJANDRO PALACIOS-GOMEZ

Toward Efficient Organic Photovoltaics: From Formulation and Novel Materials to Device Architectures

David A. Palacios-Gómez

Ustinov College

A Thesis presented for the Degree of

Doctor of Philosophy

Centre for Molecular and Nanoscale Electronics

Department of Engineering

Faculty of Science

Durham University

September 2021

"The important thing is to not stop questioning. Curiosity has its own reason for existing." **-Albert Einstein**

"Nature is our kindest friend and best critic in experimental science if we only allow her intimations to fall unbiased in our minds." **-Michael Faraday**

ABSTRACT

Toward Efficient Organic Photovoltaics: From Formulation and Novel Materials to Device Architectures

David A. Palacios-Gómez

Organic photovoltaic (OPV) offer unique advantages such as molecular engineering, flexibility and roll-to-roll manufacturing that can significantly reduce production costs. However, their efficiencies still lag behind inorganic PVs. It has been demonstrated that morphology control and recombination mechanisms play a key role in the efficiency. In this way, methods to enhance the performance by enabling morphology tuneability to further optimise OPVs are needed. To this end, this thesis introduces three novel approaches that can be utilised to improve the efficiency in OPVs.

In the first part of this work, a formulation approach is investigated by examining OPVs in which the morphology is optimised by ternary blends. Particularly, donor polymers P3HT, PTB7 and fullerene acceptors $PC_{71}BM$ and ICBA were systematically characterised. It is shown that different combinations of ternary blends outperformed binary controls. Results demonstrated that depending on the donor material used, the molecular intermixing of the constituents was different, yielding varied impacts on the performance and thus determining whether ternary blends offer a benefit or not.

The second approach reviewed consisted in the study of charge transport in novel materials, specifically non-fullerenes (NFA), hybrid fullerenes and fullerenes. For the first time, electron mobility was probed, which can be a limiting factor of the efficiency. It was demonstrated that NFA realised higher electron mobilities (closer to benchmark PCBM) in contrast to hybrid fullerenes, which yielded low mobilities. It was shown that the synthetic approach utilised to fabricate these compounds and its resulting morphology had a profound impact in their capability to mediate electron transport.

For the third method, device architectures were simulated in the form of multi junction OPVs termed as tandems. In such devices, a current matching between photoactive layers is generally required to maximise the performance. Through advanced modelling, it was shown that devices with unbalanced current matching are dominated by recombination losses of charges in the layer doing most of the absorption. It was demonstrated that changing the transport properties of the layer performing least of the absorption could assist alleviating these losses. It is also shown that different illumination conditions can further reduce the performance in tandem OPVs and that one can mitigate these reductions by suitable materials selection.

TABLE OF CONTENTS

LIST OF FIGURES

LIST OF TABLES

DECLARATION

I hereby declare that my research and work carried out within this thesis has not been published or submitted previously for any other degree and is not being used at present in candidature for any other degree.

<div align="right">

David A. Palacios-Gómez

September 2021

</div>

STATEMENT OF COPYRIGHT

PUBLICATIONS

- **David A. Palacios-Gómez,** Ali M. Huerta-Flores, Roderick C. I. MacKenzie, Chris Pearson, Faisal Alanazi, Budhika G. Mendis and Chris. Groves. *'Differing Impacts of Blended Fullerene Acceptors on the Performance of Ternary Organic Solar Cells'*. ACS Appl. Energy Mater. 2021, 4 (10), 10867-10876.

- **David A. Palacios-Gómez,** Roderick C. I. MacKenzie and Chris Groves. *'Insights Into the Operation of Imperfectly Matched Tandem Organic Photovoltaic Cells'*. **Submitted** (revised) to Cell Reports Physical Science.

- Philip A. Hope, **David A. Palacios-Gómez,** Krishnamurthy Munusamy, Debasis Semanta, Christopher Groves, Alyssa-Jennifer Avestro. *'A Multi-Electron Acceptor with a Fullerene Core: Evaluating Charge Transfer in Acceptor Hybrids'*. **In preparation**.

CONFERENCES

- Durham Engineering Research Day, **2018**. *Oral Presentation* "Impact of Morphology in Ternary Cascade OPVs."

- NECEM International Conference on Energy Materials and Interfaces, **2019**. *Poster Presentation* (**poster award**).

- NanoGe International Conference in Berlin. Fall Meeting: Organic Photovoltaics, Recent Breakthroughs, Advanced Characterization and Modelling, **2019**. *Oral Presentation* "Impact of Morphology in Ternary Cascade OPVs".

- MUFRAMEX International Symposium in Strasbourg (virtual), **2020**. *Oral Presentation* "Impact of Morphology in Ternary OPV Cells".

- NECEM Workshop on Thin-Film Photovoltaics, **2021**. *Poster Presentation* (**poster award**).

- Durham Postgraduate Research Day, **2021**. *Oral Presentation* "Minimising the Impact of Imperfect Current Matching in Tandem OPVs".

ACKNOWLEDGEMENTS

First and foremost, I would like to thank God and my family who have always been there for me to support me in all aspects. Working at Durham University for the past 4 years has been an extraordinary life experience for me, not only academically but socially as well. There are many people who have influenced and helped me during all this time, and I've made wonderful friends and colleagues along the way, so I apologise in advance if I've forgotten to mention some!

I would like to extend my most deep and sincere gratitude to my supervisor Professor Chris Groves for all the guidance, patience and support throughout my PhD. I truly feel privileged to have studied under his tutelage and I could not have imagined having a better supervisor for my PhD. I appreciate the feedback I've had during all this time, especially when I was pointed in the right direction and needed to work things out on my own; which ultimately helped me to become a better researcher. I won't forget the accurate assessments and advices that allowed me to make my work more solid. I cannot say enough words to thank Prof. Chris and undoubtedly, the work herein wouldn't have been possible if it wasn't for his continued support. I firmly believe everything I have learned from Prof. Chris will assist me in widening my perspective to become a better researcher.

I would like to wholeheartedly thank to Dr. Chris Pearson for being my laboratory mentor. Also, for teaching me how to fabricate my first devices, and how to use most of the equipment in the cleanroom. His continued assistance and accurate suggestions when I was having hard times in the laboratory meant a lot to me. I would also like to thank Dr. Mujeeb Chaudhry for his words of guidance and insightful comments when I was in need during my laboratory experiments or with data analysis. Special thanks to Dr. Ali Huerta with whom I did part of this work that constitutes the core of my thesis. I am grateful for all the conversations that we had, suggestions shared and the exceptional help you provided. I'd also like to thank Dr. Budhika and PhD fellow Faisal for assistance with the TEM scans and valuable insights provided.

I would like to express my special thanks to Dr. Alyssa Avestro and PhD fellow Phil Hope for the collaborative work that we had and for synthesising organic materials

DEDICATION

This work is dedicated to my beloved parents Benito Palacios and María D. Gómez, for their unconditional love, endless support, and guidance. Whose good examples have taught me to work hard for the things I want to accomplish in life. For the precious values they taught me and bountiful words of encouragement.

To my brother Benito J. Palacios and sister Fabiola A. Palacios who have always been by my side and motivate me to pursue my dreams.

CHAPTER 1

INTRODUCTION, OBJECTIVE AND THESIS STRUCTURE

1.1 Introduction

At present, one of the most vital challenges faced by humanity is the energy consumption, which is expected to grow from 17 Terawatts (TW) in 2010 to 27 TW by the year 2040, with a great participation from developing countries [1]. Today, fossil fuels such as coal, oil and gas still play a major role as the main source of energy for the world's population. Besides the issue of large CO_2 emissions derived from these non-renewable sources, as they become scarcer, their production costs are bound to be increased resulting in more expensive energy [2]. These reasons represent a pressing problem entering the 21st century, due to the fast growth of the world's population in the last decades, which has led to a significant consumption of resources and it is expected to continue to grow at a fast rate in years to come [3]. Even though improvements in current technologies and energy conservation are constantly made, investment in new energies is paramount in order to meet future energy demands [1, 3]. In addition, as observed in recent times, higher pollution levels have led to important changes in the ecosystem, such as raise in temperature with adverse effects in different locations of the earth [4]. Table 1.1 presents a rough approximation on non-renewable fossil fuels and estimated time until they are consumed.

Fuel	Consumption (TW)	Annual consumption (ZJ year^{-1})	Energy reserve (ZJ^2)	Time left (years)
Coal (solid)	3.8	0.12	290	2400
Oil (liquid)	5.6	0.18	57	316
Natural gas (gaseous)	3.5	0.11	30	272

Table 1.1. Fossil fuels compared to their reserves. The time estimated is considering no annual consumption increase. For reference, 1 TW = terawatt = 10^{12} W and 1 ZJ = zettajoule = 10^{21} J. Adapted from [5].

How can we best plan for the future and mitigate some of these problems? A way to do so is to utilise energy from renewable sources. Hydropower is currently one of the most widely used renewable source, followed by wind, biomass, geothermal, biofuel, tidal and solar power [2]. However, yet another important question arises, that is how can renewable energies compete with the already established technologies? If delivered with a competitive price, these new emerging technologies could be more attractive [2]. Among the green energies aforementioned, solar energy is especially attractive since the sun delivers a constant energy of 1360 Wm^{-2} on the atmosphere [6]. When related to the human energy consumption, all energy needs could theoretically be covered with the incoming energy from the sun as portrayed in Figure 1.1. Although in real life is not possible to capture much of this energy, it helps to put in perspective the potential of solar energy.
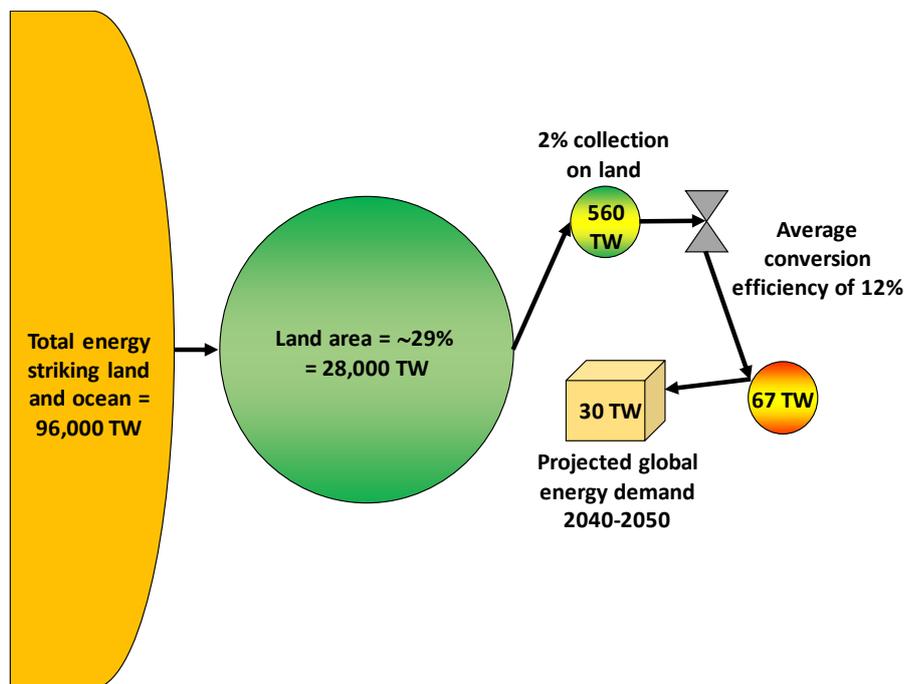
Figure 1.1. Approximation of feasible PV solar energy supply (worldwide) considering a land usage of 2% and a power conversion efficiency of 12%. Adapted from [6].

Solar energy can also be used by photocatalysis and thermal energy. For instance, plants already make use of the sun's energy during the photosynthesis process [6, 7]. In addition, the sun irradiance can be directly converted into electricity with photovoltaics (PV). Therefore, PVs have become more common in the past decades with yearly growths

of around 35% [2]. However, most of this market is dominated by inorganic crystalline silicon solar cells. Although the price for inorganic PV has decreased dramatically, it uses a large amount of energy during its fabrication in addition to the rigidness of silicon wafers [8]. In contrast, organic photovoltaics (OPV) are strong candidates that can potentially improve aspects not found on mature PV technologies, for instance: cheap fabrication, solution processing at room temperature, low thermal budget and the capacity of roll-to-roll printing with flexible substrates [5].
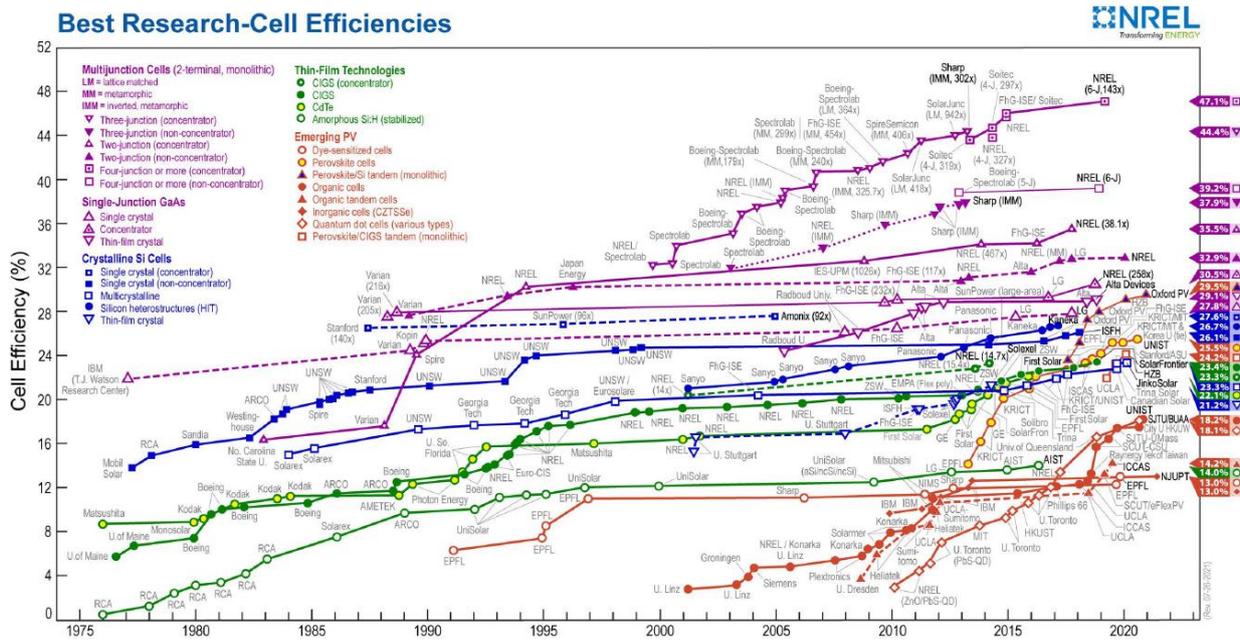
Figure 1.2. Best confirmed cell efficiency chart as reported by the National Renewable Energy Laboratory (NREL) for a range of PV technologies. From [9].

Enormous improvements have been achieved in OPV technologies in the last two decades and efficiencies of ~17-18% have been obtained very recently in controlled environments [10, 11]. Still, one of the main issues with OPV are routinely reduced performances compared to existing technologies (i.e. silicon solar cells) as observed in Figure 1.2, which hinders commercialisation. It has been proposed that efficiencies of between 10-15% with lifetimes of 5-10 years are necessary for OPVs to finally realise commercialisation [12].

What drives the efficiency enhancement in novel OPVs? How can we best optimise an OPV system? These questions and more are addressed in this study in order to provide design criteria that can be helpful to fabricate future OPVs. Lastly, the

elementary mechanisms related to performance enhancement in OPVs are varied, involving morphology control, processing conditions, suitability of materials and device engineering [6, 13].

1.2 Thesis objective

The underlying mechanisms responsible for the increase or reduction in OPV's efficiency, although reported in literature, have not been fully understood. Thus, the inspiration of this thesis stems from this pivotal issue, so that one may investigate how to best design OPVs to increase the performance. In order to elucidate what influences the efficiency increase, three different approaches were utilised in this study: formulation, novel materials and device engineering. As such, OPVs based on novel polymers and fullerenes, in addition to electron-only diodes comprised of non-fullerenes, hybrid fullerenes and fullerenes, were fabricated in the Durham Engineering cleanroom in an attempt to increase performance. The results from this work provide design insights for future OPV optimisation, whether you are a student, scientist or researcher in the field of OPVs.

1.3 Thesis structure

This thesis is organised in the following way:

Chapter 2

This Chapter contains relevant literature review regarding the current status for photovoltaics and why is it that research on OPVs is important. It also discusses the history of OPVs, important milestones, the current generation of PV technologies and a brief introduction to organic semiconductors. A detailed explanation with illustrations on the main operating principle of OPVs, types of architectures, and key elements that make up a bulk heterojunction (BHJ) is offered. In addition, the electrical parameters of OPVs and loss mechanisms in the form of charge carrier recombination are also reviewed. At the end, the different approaches utilised in this work to enhance the performance of

OPVs are introduced: 1) formulation, 2) novel materials and 3) device engineering, which serve as a predecessor to all the results Chapters.

Chapter 3

This Chapter covers the experimental methods and characterisation techniques used throughout this thesis. It begins with a description of the materials used, the fabrication process to make OPVs and provides pictures to further assist in the discussion of each section. Testing techniques with detailed illustrations are also included in this Chapter. Towards the end, numerical parameters used to run drift diffusion simulations with OPVs are also explained.

Chapter 4

Chapter 4 is the first results Chapter comprising preparatory work to maximise the performance of binary blends, to enable us to better understand the performance when a third component is added into a binary blend, resulting in a ternary OPV. In here, experimental data of two OPV blend systems based on P3HT:PCBM were investigated in which the morphology is optimised by thermal annealing or solvent vapour annealing. This Chapter presents relevant work which was a necessary base to investigate the formulation approach in Chapter 5.

Chapter 5

In this Chapter the formulation method is presented in which a third component is added into binary OPVs to make ternary blends, with the objective of better discerning the impact that these have on the efficiency. Like so, binary systems based on P3HT:$PC_{71}BM$, PTB7:$PC_{71}BM$ and ternary systems based on P3HT:ICBA:$PC_{71}BM$, PTB7:ICBA:$PC_{71}BM$ were fabricated with and without DIO additive, in an attempt to increase the performance. The utility of ICBA:$PC_{71}BM$ with either P3HT and PTB7 polymers is examined by comparing electrical parameters of these blends and relating them to the morphology.

Chapter 6

New PV devices may benefit from materials with higher mobilities, as such, in this Chapter the electron transport properties are probed for the first time in a family of novel acceptors, specifically: NDI_2, $NDI_{12}C_{60}$, $Alk_{12}C_{60}$, *bis*-NDI, and benchmark PCBM fullerene. First, relevant information regarding the choice of materials is presented

followed by electron mobility measurements based on the Space Charge Limited Current formulism. Electron-only diodes are fabricated, compared and discussed to understand the differences in mobilities which can assist when developing novel materials.

Chapter 7

In this Chapter, a tandem structure (multi junction) was investigated with advanced modelling to simulate how tandem OPVs can maximise efficiency for a range of device thicknesses, mobility and absorption spectra. It is demonstrated that unbalanced current between cells can be mitigated by changing the transport properties of the photoactive layer performing the least of the absorption. In addition, the data is also investigated under different illumination conditions (i.e. dust, pollution) to demonstrate the impact that material selection can have in alleviating the reduction in performance. Device insights are offered which can be helpful to design tandems beyond current matching.

Chapter 8

This Chapter contains the summary findings of this thesis work and provides possible directions for future work.

1.4 References

1. Mazzio, K.A. and C.K. Luscombe, *The Future of Organic Photovoltaics.* Chem. Soc. Rev., 2015. **44**(1): p. 78-90.

2. Lukas Schmidt-Mende, J.W., *Chapter 1: Introduction*, in *Organic and Hybrid Solar Cells*, W.d.G. GmbH, Editor. 2016, De Gruyter: Berlin/Boston. p. 1-5.

3. Bilgili, M., et al., *An Overview of Renewable Electric Power Capacity and Progress in New Technologies in the World.* Renew. Sustain. Energy Rev., 2015. **49**: p. 323-334.

4. Ahmad, T. and D. Zhang, *A Critical Review of Comparative Global Historical Energy Consumption and Future Demand: The Story Told so Far.* Energy Rep., 2020. **6**: p. 1973-1991.

5. Krebs, F.C., *Chapter 1: Introduction*, in *Polymer Photovoltaics A Practical Approach*, F.C. Krebs, Editor. 2008, SPIE Press: Washington. p. 1-10.

6. Darling, S.B. and F. You, *The Case for Organic Photovoltaics.* RSC Adv., 2013. **3**(39).

7. Durrant, T.M.C.a.J.R., *Charge Photogeneration in Organic Solar Cells.* Chem. Rev., 2010. **110**(11): p. 6736-6767.

8. Arno Smets, K.J., Olindo Isabella, René Van Swaaij, Miro Zeman, *Chapter 12: Crystalline Silicon Solar Cells*, in *Solar Energy, The Physics and Engineering of Photovoltaic Conversion, Technologies and Systems*. 2015, UIT Cambridge Ltd. p. 153-176.

9. Laboratory, N.R.E. *Photovoltaic Research: Best Research-Cell Efficiency Chart*. 2021 [Accessed: 12-sep-2021]; Available from: https://www.nrel.gov/pv/cell-efficiency.html.

10. Cui, Y., et al., *Over 16% Efficiency Organic Photovoltaic Cells Enabled by a Chlorinated Acceptor with Increased Open-Circuit Voltages.* Nat. Commun., 2019. **10**(1): p. 2515.

11. Salim, M.B., R. Nekovei, and R. Jeyakumar, *Organic Tandem Solar Cells with 18.6% Efficiency.* Sol. Energy, 2020. **198**: p. 160-166.

12. Espinosa, N., et al., *Solar Cells with One-Day Energy Payback for the Factories of the Future.* Energy Environ. Sci., 2012. **5**(1): p. 5117-5132.

13. Xiao, S., Q. Zhang, and W. You, *Molecular Engineering of Conjugated Polymers for Solar Cells: An Updated Report.* Adv. Mater., 2017. **29**(20): p. 1601391.

CHAPTER 2

OPV BACKGROUND, DEVICE PHYSICS AND FUNDAMENTAL CONCEPTS

2.1 Introduction

In the last decades, the increasing depletion of fossil fuels and the rise in global energy demand have sparked interest in academia and industry alike in the pursuit for renewable or alternative energy sources [1]. Solar energy represents a promising substitute to fossil fuels since the energy of the sun is vast compared to other renewable types of energy [2]. A way in which sunlight can be harvested and converted into electricity is through photovoltaic devices (PV) [2]. These devices can convert light directly into electricity via semiconductor materials, and the electricity can be consumed on site or stored in batteries [3]. At present, the most commonly used PV technologies are made from inorganic semiconductors [4]. For example, commercial silicon solar cells have achieved efficiencies >20% with lifetimes over 20 years and thus occupy approximately 95% of the global PV market, followed by roughly ~ 5% for thin film technologies and less than 1% for emergent PVs [4-6]. Although solar cells have decreased their price significantly over the last two decades, they are still offset by higher production costs [4]. Further, silicon solar panels are bulky, heavy and need more material during its fabrication [7]. Hence, much effort has been focused into developing alternative PV technologies in past years, which can provide flexibility, lower costs, use less material and that can be easily incorporated into existing infrastructure, minimising impact on land usage [5, 7].

Along these lines, organic semiconductors have risen as promising candidates that can offer low-cost electricity due to advantages such as solution-processing, molecular tuneability, and compatibility with large area fabrication [2, 8]. In order for organic photovoltaics (OPVs) to compete with established PV technologies, a deep understanding of the underlying processes is needed [2, 7, 9]. In this thesis, we work towards improving the efficiency of OPV by utilising three different methods. First, Chapter 4 presents preparatory work to maximise the performance of binary blends, to better understand the performance when a third component is added. The formulation approach is introduced

in Chapter 5 by adding a third component into binary OPVs, to discern the impact these ternary OPVs have on the efficiency. Since new PV materials may benefit from higher mobilities, on Chapter 6 the electron transport of novel materials is probed for the first time. The third approach corresponding to new architectures is investigated with advanced modelling in Chapter 7 by device engineering multi junction OPVs. Relevant background to this is included in section 2.11. But first, this Chapter offers a general overview of the fundamental concepts that pertain to OPVs and scrutinizes through the importance of solar energy, followed by a brief review of OPV history and key milestones. Then, the three generations of PV devices are introduced as well as the main operating principle in an OPV device. Concepts related to type of architectures, electrical parameters and loss mechanisms are also reviewed.

2.2 Brief history of OPVs

Back in 1839 while experimenting with two metal electrodes and an electrolytic material (electrically conducting solution), Edmund Becquerel observed that when exposed to sunlight, a small electrical current could be generated and this phenomenon was named as the "photovoltaic" effect [10]. This discovery paved the path for the photovoltaic field and the generation of electricity from sunlight [10]. Shortly afterwards, Willoughby Smith fabricated the first selenium solar cell in 1877 [11]. In 1905, Albert Einstein published a paper on the photoelectric effect describing that light consisted of "packets" of energy called photons and some years after his theory was published, the PV effect was observed for the first time in cadmium-selenide (1932) [11]. Pearson, Chapin and Fuller working at Bell laboratories reported the first practical solar cell made of silicon in 1954 [12].

Fast forward to more recent times, we now turn the attention to organic materials. Figure 2.1 presents a number of valuable milestones achieved throughout the last decades in the field of OPVs. One of the most important breakthroughs realised with organic semiconductors was the detection of conductivity in conjugated polymers in the late 70's [13]. For this pivotal discovery, Heeger, MacDiarmid and Shirakawa were awarded the chemistry Nobel prize in the year 2000. Later, in 1986 Tang and colleagues introduced the first modern donor:acceptor (D:A) bilayer solar cells by using copper phthalocyanine with perylene derivative materials, realising an efficiency of nearly 1% [14].
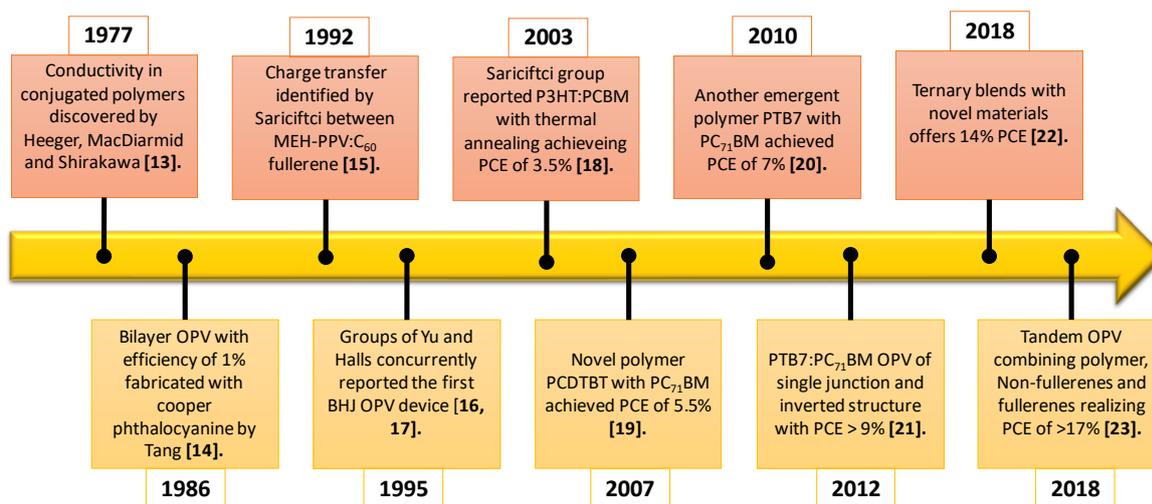
Figure 2.1. Brief history timeline of OPVs and important discoveries of recent years. References from figure: [13-23]. Adapted from: [24].

Moving on to the 1990's decade, two different groups concurrently reported the first polymer and fullerene bulk heterojunction (BHJ) blend, which still represents to this date the fundamental system of D:A organic solar cells [16, 17]. In the early 2000's, Padinger et al [18] observed that in P3HT:PCBM BHJ OPVs, the utilisation of postproduction treatment such as thermal annealing (TA) could increase the short-circuit current (J_{SC}) due to more favourable charge carrier mobilities, yielding higher efficiencies in their devices. Subsequent advances with new materials and polymers have continued to raise the bar in efficiency, establishing new records. For example, the introduction of novel polymers like PCDTBT and PTB7, which show strong absorption in the near-infrared region, allowed for higher efficiencies [19, 20]. In addition, these novel materials also permitted device engineers to reach higher efficiencies by fabricating solution-processed tandem solar cells [23, 25]. By stacking two or more active layers with complementary absorption, the sun's spectrum is more efficiently covered, since the light that is not absorbed in one layer can be absorbed in the other [26].

As briefly summarised in this section, the OPV research field is interesting and vibrant with new developments being reported very often by different groups worldwide.

2.3 Current generation of PV technologies

Besides common inorganic solar cells, other types of PV technologies are constantly being developed and improved with the objective of enhancing efficiency whilst reducing fabrication costs [5, 27]. Presently, PV technologies are generally

classified into three main categories, depending on properties, efficiency and electricity output cost. Figure 2.2 presents the different generations of PV solar cells plotted with the efficiency vs the cost per square-meter.
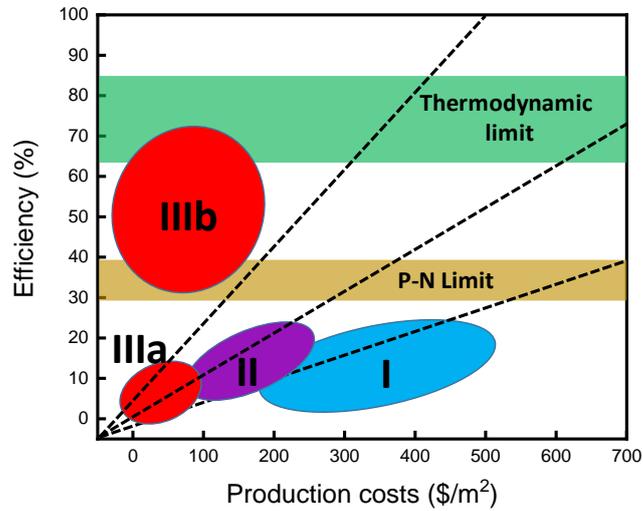
Figure 2.2. Three generations of PV technologies. Adapted from [11, 27]. Efficiency limits will be discussed in section 2.11.

2.3.1 First generation

The first generation encompasses PV solar cells made of crystalline silicon wafers (c-Si), namely monocrystalline (single continuous crystal) and polycrystalline (many small crystalline grains) [4, 28]. Commercial modules of these type of solar cells have efficiencies in the range of 15%-20% [29] and can reach efficiencies over 25% in standard test conditions [11, 30]. Presently, c-Si solar cells occupy approximately 95% of the total PV market and they can last for >20 years with a higher performance when compared to other generations [4]. This type of solar cell is made of wafers which are rigid, brittle and are fabricated with deposition methods that consume a lot of energy, for example the Siemens process for polysilicon [28]. Although recent advances have shown that thinning the back wafer can reduce some of the cell cost [31], generally the thickness of the first generation PVs is in the order of 50 μm - 500 μm which means they still use more material compared to the next generations [28]. In addition, c-Si has an indirect bandgap thus it requires a thicker active layer to absorb light [32]. This in turn, has encouraged researchers to look at cheaper materials for PV applications.

11

2.3.2 Second generation

The next alternative family of PV technologies consist of thin-film cells and is referred to as the second generation [33]. Unlike c-Si solar cells, in the second generation materials have a direct bandgap, which allows for a higher absorption coefficient [32]. As a result, these type of PV devices are much thinner than the c-Si wafers from the first generation, with thicknesses in the order of a few microns [34]. Semiconductors like cadmium telluride (CdTe), amorphous silicon (a-Si), copper indium selenide (CIS), cooper zinc tin sulphide (CZTS) and copper indium gallium diselenide (CIGs) are part of this generation [33]. Unlike the first generation of solar cells based on wafers, the thin-film cells are solution deposited (e.g. hydrazine method, nanoparticle inks) which makes them dependent on deposition parameters [33, 35, 36]. Although they were originally envisioned to be cheaper than the first generation, due to the price decline in wafer solar cells, these thin-film PVs have not become economically favourable as it was originally intended [33]. At present, commercial performances range around 10-18% and they occupy ~5% of the current PV cells installed in the market [4]. More specifically, PCEs of ~13% have been realised with CdTe and CZTS, whilst below 18% for CIS and CIGS thin films [4, 35]. On the downside, a matter that can be of concern is the long-term stability and that they are less efficient per unit area [11].

2.3.3 Third generation

The third generation is comprised of emergent and novel PV technologies, made from organic materials, dyes, nanotubes, quantum dots and organic-inorganic devices (e.g. perovskites) [11, 37]. Generally, the third generation of PV technologies includes two categories: IIIa and IIIb. To start the discussion with the IIIa generation, the main goal is to achieve a lower cost/watt balance with much moderate efficiencies (10% – 15%) [4, 11]. In order to realise this, organic semiconductors are used which are flexible, require low temperature fabrication processes, fewer materials (thicknesses of 100 nm – 500nm range) and generally a lower investment in terms of equipment [11, 37]. For instance, dye sensitized solar cells made up from organic dye molecules belong to this category, however, this type of devices is limited by low efficiencies and poor stability [38]. More recently, Perovskites have proved to be a promising type of PV device, achieving efficiencies of ~20% in laboratory settings [39, 40]. Yet, a main hurdle is the

stability, and much research is still undergoing before this technology becomes fully commercial [39].

Another promising approach is that of OPVs which are manufactured from earth abundant materials and processed as polymers or plastic [41]. Although efficiency has been improved lately as observed section 2.2, it still lags compared to first generations solar cells in addition to a limited lifetime [42]. Altogether, mainly due to its low cost and potential for continuous printing processes, it has become an important contender to compete with established PV technologies, which are generally offset by a higher price and complex manufacture [41]. For OPVs to successfully become commercial, a balance between lifetime, costs and efficiency must be met otherwise they will be limited to niche markets [43].

To finish this section, the IIIb encompasses approaches with higher theoretical efficiencies affording higher costs but still with a satisfactory cost/wattage balance [11]. For example, multijunction PV cells – or multilayer- which increase the amount of sunlight and materials that can harvest more energy from a single photon (i.e. quantum dots, organic dyes) are candidates for this generation [26, 44]. Multijunction cells represent the most efficient devices at present, and have been successfully used in satellites and in concentrator PV systems, reaching efficiencies of 46% in the latter [45]. At present, most of the work on the IIIa generation is still carried out at universities and research facilities, meaning that devices based on this type of technology are not fully commercially available [4]. In the next sections the focus will be on OPVs as these types of devices have shown to be promising to compete with mature inorganic PVs.

2.4 Why OPVs are considered important

OPVs are made from semiconducting materials such as organic polymers and organic molecules based on carbon, which will be discussed fuller in the following section [33]. Inspiration for OPVs initially came from plants and photosynthesis, in which incident solar energy is separated into electronic charges and converted to chemical energy by a series of energy transfer steps [46]. As previously stated, OPVs have attracted considerable attention due to solution-cast processing at low-temperatures, molecular tuneability and roll-to-roll printing which holds promise for low cost manufacturing, easing the constraints for large area fabrication [43]. Indeed, efficiency in OPVs has come a long way since its early development, with PCEs from 1% to ~17% in recent times [14,

47]. Although this raise in performance is promising, OPVs are still behind inorganic solar cells not only in efficiency but also in device lifetime [48]. In order to realise commercialisation, OPVs need consistent performances around 10% – 15% for at least 10 years of operating life to compete with mature technologies [49]. Table 2.1 provides a brief review of the state-of-the-art OPVs and their PV values.

Donor material	Acceptor material	V_{OC} (V)	J_{SC} (mA/cm^2)	FF (%)	PCE (%)	Ref.
P3HT	PCBM	0.63	9.5	68%	5%	50
P3HT	ICBA	0.84	9.7	67%	5.4%	51
PCDTBT	PC$_{71}$BM	0.62	16	55%	5.5%	19
PTB7	PC$_{71}$BM	0.74	15	69%	7.4%	20
PBDT-TFQ	PC$_{71}$BM	0.76	18	58%	7.8%	52
PTB7-Th	PC$_{71}$BM	0.75	15	71%	8.2%	21
PTB7-Th	COi8DFIC	0.69	24	64%	11%	22
PBDB-T-2F	IT-4Cl	0.79	23	75%	14%	53
PM6	YM6	0.86	24	73%	15%	54
PBDB-T-F	BTP-4Cl	0.86	25	75%	17%	47

Table 2.1. Survey with the PV performance of state-of-the-art OPVs. References from table: [19-22, 47, 50-54].

Thusly, because OPVs have demonstrated potential to surpass current efficiency results, novel methods and scenarios are currently being developed. Now, the materials which are used as photoactive layers in OPVs will be reviewed.

2.5 Brief introduction to organic semiconductors

Up to now, common solar cells discussed earlier are made from inorganic semiconductors like c-Si, CIGS and CdTe. In this section, we take a closer look at the materials that conform OPVs. Organic polymers and organic molecules are the semiconducting materials used as active layers in OPVs [33]. The term "organic" in these semiconductors stems from the carbon atoms from which these components are made of, meaning that "C" atoms and their bonds (i.e. C-C) are the backbone [55]. Typically, they are grouped into small systems and large systems. The former is normally referred to as oligomers, containing a few mers or repeat units per molecule, whereas the latter is known as a polymer, comprising numerous mers i.e. hundreds or thousands mers per molecule (Figure 2.3) [56].
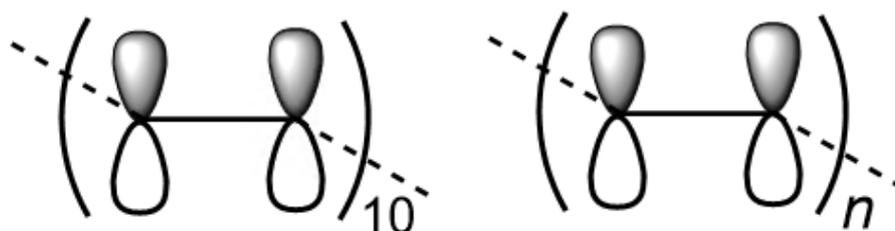
Figure 2.3. Representation of orbitals in an oligomer (left) and polymer (right). The solid line in the middle represents the σ bond between the carbon atoms and the dashed lines the end repeat units (i.e. the same structure repeating) which are different between the two, whereby a polymer has a large number of repeat units, as explained in the text. Adapted from: [25].

To fully understand how organic semiconductors conduct electricity, basic concepts are first reviewed to elucidate the origin of the energy levels and charge transport. In typical polymers, the valence electrons of the carbon atoms are fully used for bonding in a carbon chain, otherwise known as saturated polymers [56]. Polyethylene (Figure 2.4), consists of a carbon atom with 6 electrons occupying energy states of $1s^2$ $2s^2$ $2p^2$, and is a characteristic example for a saturated polymer. Now, considering the carbon atom in polyethylene, the four electrons in the $2s^2$ $2p^2$ shell achieve a low energy state (hybridised sp^3) that combines s-orbital and p-orbitals, known as σ bonds which are strongly bound because of the orbital end to end overlapping and are located in orbitals at lower energies [55, 56]. In Figure 2.4, the σ bonds are represented with the solid lines.
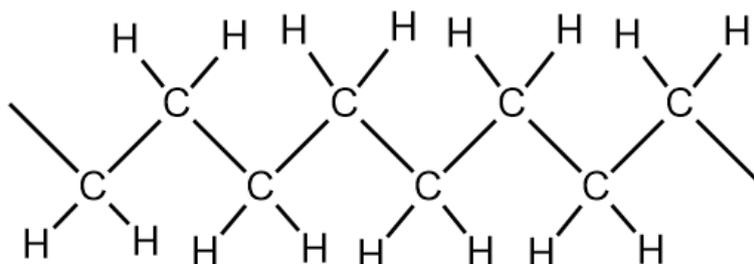
Figure 2.4. Polyethylene polymer molecular structure. In this schematic, the solid lines represent σ bonds with a total of 25 bonds. Redrawn from [56].

On the other hand, polyacetylene is a typical example of a conductive polymer (Figure 2.5). It is made of a carbon chain with one hydrogen per atom, with alternating single and double bonds between them. In polyacetylene there are three nearest neighbours leading to a hybridization of sp^2p_z, where only three of the four valence

electrons are utilised for bonding, and one π electron (i.e. electron in a π bond) is left and available for electrical conduction [56]. Polymers with this configuration are termed conjugated, where delocalized π electrons are less bound (due to lateral overlapping of orbitals) and occupy higher energy states in a molecule [55, 56]. Taking into account a chain of closely spaced carbons, many π electrons will interact with other close π electrons to form energy bands (π sub-bands). In Figure 2.5, σ bonds are represented by a solid line and the double bonds depict a σ plus a π bond.
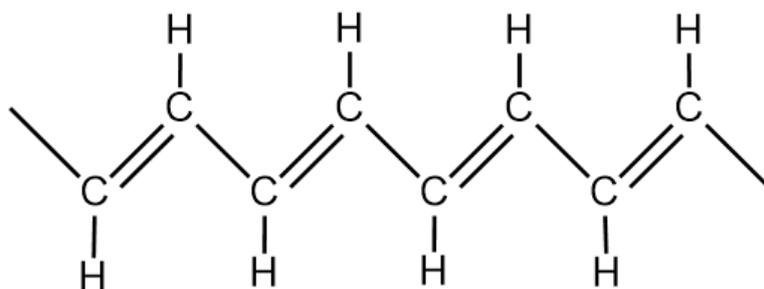
Figure 2.5. Polyacetylene polymer molecular structure. In here, the double bonds represent a σ plus a π bond. There is a total of 17 σ bonds and 4 π bonds. Redrawn from [56].

Thus, electrical conductivity arises from these π electron in sub-bands since they become delocalized [56]. Further, because of this delocalization, they can move freely (relatively) through a molecule and be excited to higher energy states by low-energy optical transitions like visible or near infra-red photons [55]. We now look at ethylene (Figure 2.6a, b) to further explain the location of bonds. In here, there is a double bond between the carbons, formed by σ bond (i.e. the overlapping of sp^2 orbitals) and π bond (i.e. overlapping of p-orbitals). Also, there are σ bonds between hydrogen and carbon atoms formed by s-sp^2 orbitals. In total there are 5 σ bonds and one π bond. In addition, the energy difference between the highest occupied π sub-band and the lowest unoccupied π sub-band determines the energy bandgap in semiconducting polymers; the former referred to as the highest molecular orbital (HOMO) whereas the latter to lowest unoccupied molecular orbital (LUMO) [55]. Alternatively, the unoccupied π bands are generally denoted as π* bands [56]. Figure 2.6c shows the HOMO and LUMO orbitals of ethylene. This bandgap determines the necessary energy to excite an electron from the HOMO to the LUMO and the maximum absorption of the polymer [57]. Depending on the polymers, typically bandgaps are found between 1.4 eV to >2 eV [57].
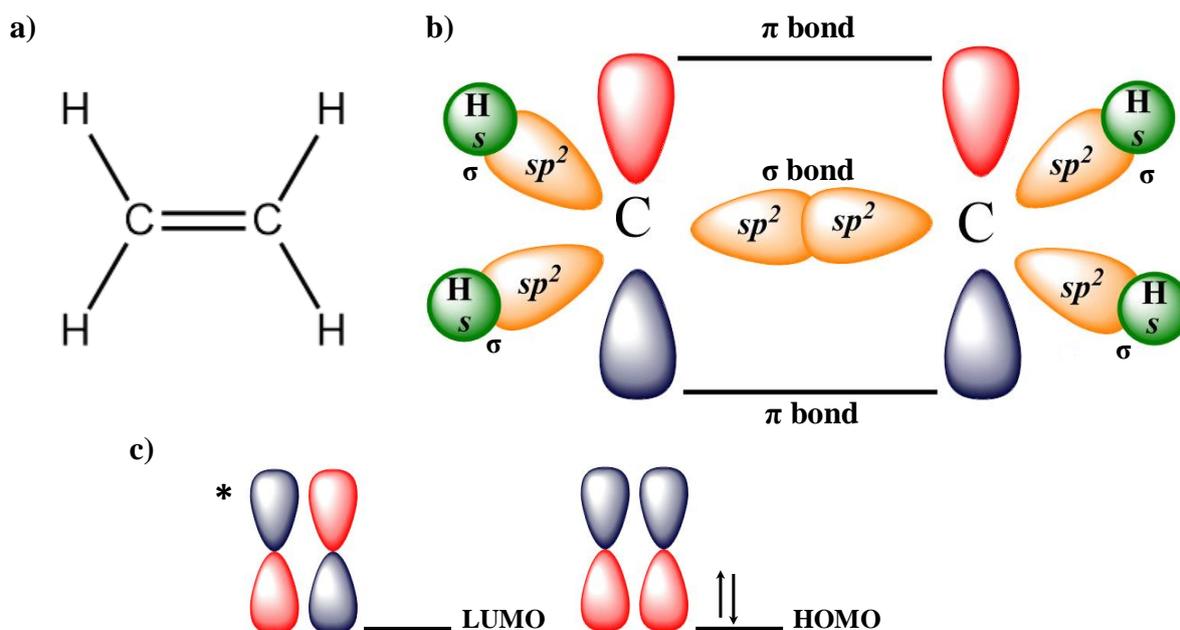
Figure 2.6. a) chemical structure of ethylene ($CH_2 = CH_2$). b) carbon atoms with orbitals depicting 5 σ bonds (formed from s-sp^2 and sp^2-sp^2 orbitals) and 1 π bond (from π-π overlap). c) HOMO-LUMO orbitals showing π electrons with black arrows. Redrawn from: [58].

Having defined what organic semiconductors are made of, we focus the attention on the basics of charge transport. Compared to the highly crystalline structures found on inorganic materials, in disordered materials like organic semiconductors charge transport is dominated by "hopping" which is the process of electron transfer between molecules when electronic coupling is weak [55, 59, 60]. Although there are different models to describe charge transport in organic semiconductors such as: the Hamiltonian model, Marcus theory, Miller-Abrahams and Bässler model, the focus will be on Miller-Abrahams (Figure 2.7) since it uses a Gaussian distribution to approximate the distribution of energy in disordered materials, which yields good predictions for charge transport [55]. As seen elsewhere, this formulism is suitable for molecular crystals, polymer materials and different types of solids [55]. In here, a compact description on the theory is covered, and interested readers are referred elsewhere for a broader discussion [61, 62]. Following photon absorption in a photoactive material, a carrier is set in a high-energy state in the Gaussian density with a standard deviation. Then, hopping takes place into lower states of energies until the charge arrives at an average energy referred to as transport energy that is temperature dependent [55].
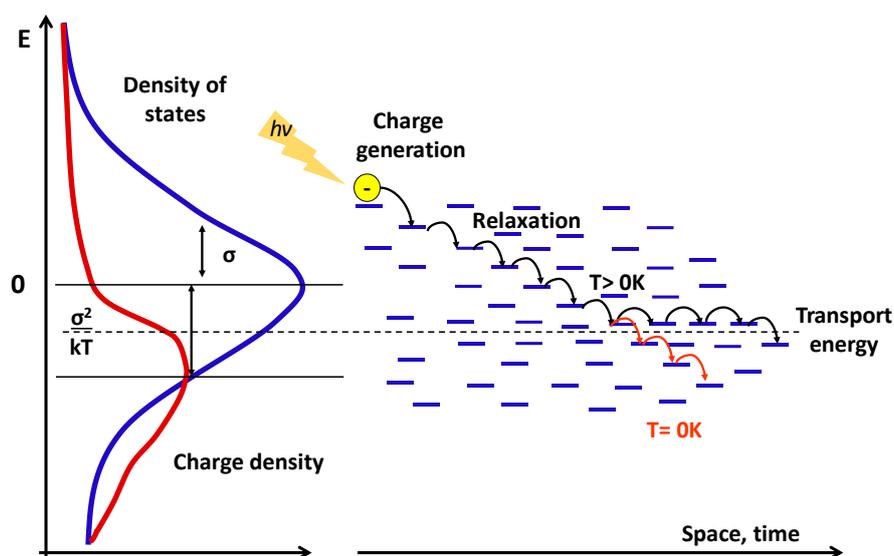
Figure 2.7. Representation of the energetic picture in a disordered organic semiconductor considering the Miller-Abrahams hopping mechanism. Once charges are separated after photoexcitation, they hop in a Gaussian density of states with standard deviation to lower sites that are energetically favourable whilst diffusing through the material. At temperature of 0K carriers are relaxed to the deepest states. Hand drawn from [55].

The first hops occur more rapidly whereas later hops are slower attributed to the temperature dependence leading to a reduced mobility. As such, the film thickness plays an important role in a device since carriers can be completely "relaxed" prior to being collected by the contacts [55]. This leads us to the difference in charge carrier mobilities between organic and inorganic semiconductors, whereby the former mobilities range from 10^{-7} cm^2 V^{-1} s^{-1} to 1 cm^2 V^{-1} s^{-1} in contrast to the higher mobilities in the latter, typically in the order of 10^3 cm^2 V^{-1} s^{-1} (e.g. for c-Si) [56]. Nevertheless, as we shall see later, OPVs made from organic semiconductors offer interesting chemical, electronic and optical opportunities that make them attractive for PV applications.

2.6 Electricity production in a P-N junction photovoltaic cell

Because PV cells can be fabricated from organic and inorganic semiconductors, a good understanding of diode based devices requires basic knowledge of P-N junctions. To start the discussion, fundamentally, a P-N junction represents a diode that can provide current flow in one direction and block current in the other direction [63]. The area of interest for photovoltaics is in the middle where the transition from one material to the other occurs. A common P-N junction diode is illustrated in Figure 2.8. In general, the PV process with organic semiconductors differs from the inorganic counterparts.
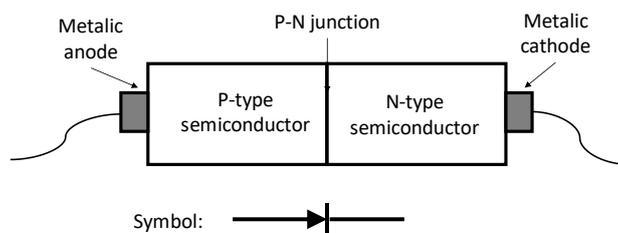
Figure 2.8. Representation of a diode device and its symbol. Adapted from [63].

On the one hand, with inorganics, following photon absorption in the semiconductor leads to the formation of highly delocalized electron-hole pairs (Wannier excitons) due to the low binding energies ~0.01 eV, and high dielectric constant of $\varepsilon = 12$ (i.e. silicon), which can separate at the P-N junction or depletion zone (Figure 2.9) [55, 64, 65]. In here, the built-in electric field drives them to the opposite directions and finally to their corresponding electrodes [64]. Further, depending on the material free charges can be realised by thermal energy (kT = ~0.025 eV) at room temperature, since its lower than the binding energy of these excitons [55]. Also, adding impurities (doping) allow one to control the concentration of electrons and holes. For the sake of explanation, by doping with group V elements from the periodic table (i.e. adding phosphorous to silicon) results in a N-type semiconductor because of the extra electron in phosphorous, referred to as donor doping [32]. Now, replacing with group III elements (i.e. adding aluminium to silicon) results in a P-type semiconductor, since aluminium has one less electron inducing an excess of holes [32].
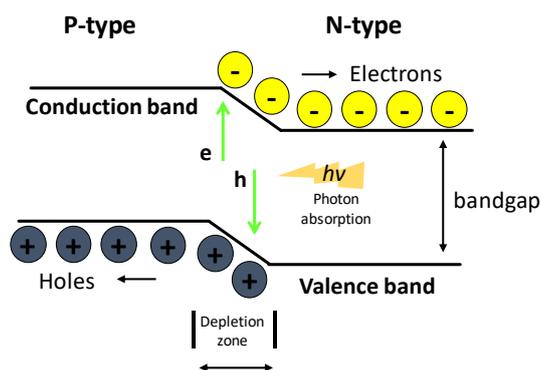
Figure 2.9. Representation of energy level diagram in a P-N junction photodiode. From [68].

On the other hand, organic semiconductors have a low dielectric constant of $\varepsilon = 2$-4 resulting in a strong Coulomb barrier between electron and holes with binding energies of 0.5 – 1.0 eV and binding radius of ~1 nm [55, 65, 66]. So, once a photon is absorbed

in an organic semiconductor, it leads to generation of strongly bound electron-hole pairs (Frenkel exciton) instead of free charge carriers [66, 67]. Now, for these excitons to be useful in generating electricity, they need to be dissociated into free carriers first. If an exciton fails to dissociate within its lifetime the absorbed energy is lost (more on the loss mechanisms in section 2.10) [67]. Thus, OPV requires different strategies to separate electron-hole pairs, for example a large applied electric field and the presence of two semiconducting materials one of which has a high affinity to accept electrons and the other a high ionization potential to donate them [66, 67]. In these organic semiconductors, the hole transport material is known as P-type whereas the electron transport material is termed as N-type [69]. Considering the latter, dissociation can occur if the offset in the HOMO or the LUMO is sufficient to overcome the binding energy of the exciton [66]. The result is that the junction of these two organic semiconducting materials is similar to a P-N junction in a common PV device [67]. In the next section, more discussion on the operating principle of OPVs will be covered.

2.7 Operating principles of OPVs

As previously explained, the dissociation process in OPVs it requires an interface between two semiconductor materials. Figure 2.10 presents a basic energy band diagram showing the energetic offsets between the D:A HOMO and LUMO to further understand charge transport in OPVs [67]. In here, the I_P denotes ionization potential which is the energy required for the material to move an electron from the HOMO to vacuum [67]. The definition of the vacuum level (vacuo) is the energy of a free stationary electron that is outside of any material, and is used as the level of alignment for energy levels between two different materials like shown in the figure [33].
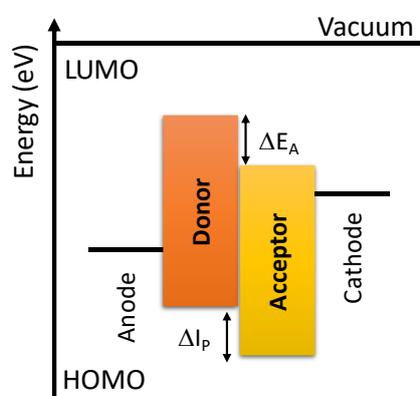
Figure 2.10. Energy band diagram and heterojunction of a D:A material. Adapted from [67].

20

The E_A stands for electron affinity, and it represents the ability of the materials to act as an electron acceptor and is normally represented by the LUMO relative to the vacuum. The HOMO-LUMO gap shown in the figure denotes the energy required as minimum to excite an electron from the HOMO to the LUMO as previously stated [67].

Moving on, a simplified overview on the PV process in an OPV device is depicted in Figure 2.11. Generally, the operation of a PV device may be visualised as taking place in four fundamental steps that happen consecutively. After light is absorbed (step 1), an electron can be excited from the donor HOMO to its LUMO resulting in an exciton which is an electron-hole pair strongly bound as formerly discussed [70]. Therefore, in order to split the exciton into free carriers, it diffuses into D:A interfaces (step 2) during its lifetime where the electron can transfer to the LUMO of the acceptor material [70]. The lifetime of the excitons is estimated to be around ~100 ps – 1 ns [46] with a diffusion length of ~10 nm [71, 72]. Further, because diffusion has no direction (more on section 3.7.4 of Chapter 3) the D:A nanostructure plays an important role, since the mixture of these components tends to form a phase segregated morphology, thus increasing the interface area between these constituents to assist in the exciton splitting [73]. In addition, when the energy difference between the donor and acceptor's LUMO (ΔE_A from Figure 2.10) is greater than the binding energy, this charge transfer is more favourable to occur. This process can take place in two ways: 1) The first is for an exciton on the donor material, which splits up resulting in the injection of electron to the LUMO of the acceptor and the hole remaining in the HOMO of the donor. 2) The second, if the acceptor material is excited, a hole is injected in the HOMO of the donor while the electron remains in the LUMO of the acceptor [64].
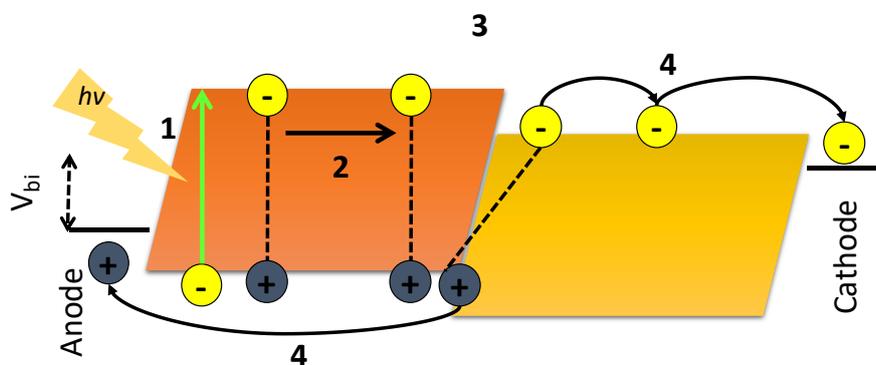
Figure 2.11. Working principle (basic schematic) in an OPV device. The orange (left) depicts the donor material and the yellow (right) depicts the acceptor material. The light is represented by the *hv* symbol and carriers are collected in the anode (holes) and cathode (electrons) respectively. The V_{bi} shows the difference of work function between contacts. From [67].

Once the exciton is located across the D:A interface, it becomes a charge transfer exciton (CT) which means that the electron is in the acceptor, the hole on the donor, but that they are still Coulombically bound, with a typical capture radius (r_c) of ~20 nm in organic semiconductors with dielectric constant of $\varepsilon = 2 - 4$ [74]. This r_c is also termed thermal capture radius, and describes the distances opposite charges would have to be apart for their attraction to decay to kT [74]. Once the distance between the electron and hole is greater than r_c, they separate to become free carriers (step 3) [67]. Nevertheless, in contrast to inorganic PV materials, charge transport in organic materials is more limited. For instance, in inorganics, crystals allow electrons to move almost freely but in view of the inherent disordered materials like organics, the lack of long-range order and weak intermolecular forces leads electrons to hop from molecule to molecule, as specified previously [75]. And lastly, once the carriers are free they can transport through the donor or acceptor channels into their respective electrodes to be used in an external circuit (step 4) [67]. In addition, due to the difference in the work function of the electrodes, an internal potential is generated (V_{bi}) as indicated in Figure 2.11. Under illumination, this potential assist free carriers to move into the contacts: electrons to the lower function metal and holes to the opposed contact thus working as a solar cell [70]. Again, there are loss mechanisms that directly compete with these four steps, which will be discussed in section 2.10. For a thorough explanation on charge generation in OPVs, interested readers are referred elsewhere [46].

2.8 Evolution of common organic photovoltaic architectures

Owing it to the energy offset that is necessary to dissociate electron-hole pairs in OPVs, different types of architectures have been used in the past to lessen this constraint.
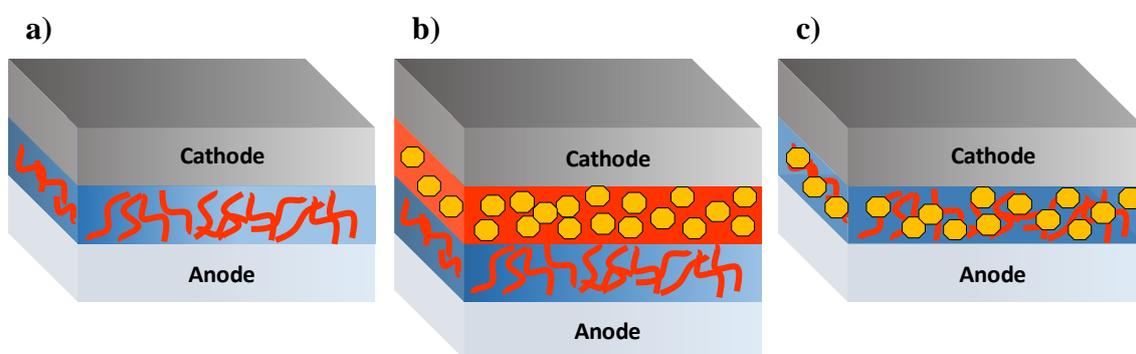
Figure 2.12. Illustration of different device architectures used for the fabrication of OPVs; a) single layer, b) bilayer and c) BHJ of a donor and acceptor. Orange lines represent the donor material and the yellow circles represent the acceptor material.

Figure 2.12 shows the typical architectures used on OPV devices, which include single layer OPV, bilayer and the BHJ. Enhancements to the BHJ cell concepts are discussed later.

2.8.1 Single layer

Originally, the first OPVs were fabricated with an active layer of a single material evaporated and sandwiched between electrodes of differing work functions [70]. These first OPVs were based in bioorganic materials such as Chlorophyll, which can absorb light (i.e. like in plants) [76]. In order for these devices to generate current, the binding energy needed to be overcome by thermal energy or by the separation of excitons at the electrodes [75]. However, under normal operating conditions, the temperature is not high enough and because of the sample thickness, most excitons could not dissociate into free carriers, thus limiting the operation of these OPVs [75]. Further, considering the small exciton diffusion length ($\sim$10 nm), only a small area within 10 nm – 20 nm from the contacts could contribute to generate current [70]. Therefore, due to the inefficient electron-hole pair separation, the efficiencies in single layer OPVs were lower to 0.1% [76].

2.8.2 Bilayer

An important innovation in OPV research was realised when a second organic semiconductor layer was added to a device. As discussed in section 2.2, the bilayer OPV was first introduced by Tang and colleagues and unlike the single layer, efficiencies of up to 1% could be attained [14]. In this device architecture, the light is normally absorbed in the donor species, a hole conducting material (i.e. copper phthalocyanine) [14, 75]. Then, the photo generated excitons move within the donor layer until they reach the interface with the second material, the acceptor, which is strongly electronegative (i.e. a buckminsterfullerene C_{60}) and thus provides enough energy to separate the excitons [75]. Therefore, the breakthrough with this device architecture compared to the previous one, was the improvement in the exciton dissociation provided by the planar interface of the donor and acceptor constituents [14]. However, a key issue with this type of devices is that the thicknesses need to be of approximately 100 nm – 200 nm to more effectively absorb light, contrasting to the small diffusion length of the excitons as discussed previously. Hence, only a small fraction of absorbed photons make it to the D:A junction

23

before recombining, resulting in an OPV design hard to exploit due to the limited performances attainable [75].

2.8.3 Bulk heterojunction (BHJ)

Another novel concept was introduced in the mid 1990's simultaneously by two research groups, with the aim of overcoming the limitations of bilayer OPVs, briefly discussed in the history of OPV section [16, 17]. The aim of this concept, termed the BHJ, was to address the small exciton diffusion lengths of organic semiconductors as well as the active layer thicknesses [75]. This BHJ strategy features a mixture of the donor and acceptor components in such way that they become interpenetrated one another, meaning that the interface between them is no longer planar, but spatially distributed and consequently leading to D:A interfaces within the distance of the exciton diffusion length [70, 75]. By mixing the donor and acceptor materials in a blend, efficiencies of 1 – 3% could be attained in early devices [16, 17]. One of the main advantages of this approach is the increased interfacial area where exciton dissociation into free carriers can take place over the whole device [70]. However, an important downside is that continuous percolation pathways are not always guaranteed in disorder materials which allow free carriers to transport into their respective electrodes [70, 75]. This means that the BHJ concept is more sensitive to the nanoscale microstructure, in contrast to the bilayer whereby the donor and acceptor phase contact the electrodes selectively [70]. Even so, the benefits of this approach compensate its negative sides, since most high performing OPVs of recent past have been achieved with this method [54, 77].

For an optimal device performance with this approach, a control of morphology is required [78]. In the past, some methods to enhance the morphology have been successfully implemented, which may lead to a more favourable inner structure in terms of exciton dissociation, transport and collection at the contacts. These device engineering topics that relate to morphology optimisation and efficiency enhancement will be discussed in section 2.11 and the results Chapters that come next.

2.9 About the solar spectrum and electrical parameters of OPVs

To better understand the ways in which OPVs have been developed since the BHJ concept, we review now some of the basic terminology related to PV performance in this section, and efficiency loss mechanisms in OPVs in section 2.10. Because research on

PV devices is carried out in different places (i.e. universities, companies) it is important to set a common ground that allows these devices to be tested and compared in a reproducible way. A communal convention is characterised by a solar irradiance of 1000 W/m^2, a device temperature of 25° C, and an air mass (AM) of 1.5 [79]. For the purpose of explanation, when light passes through the atmosphere, the spectrum is attenuated because of absorption of ozone (O_3), water molecules (H_2O) and carbon dioxide (CO_2), which also depends on the angle, position and earth season [64, 79].
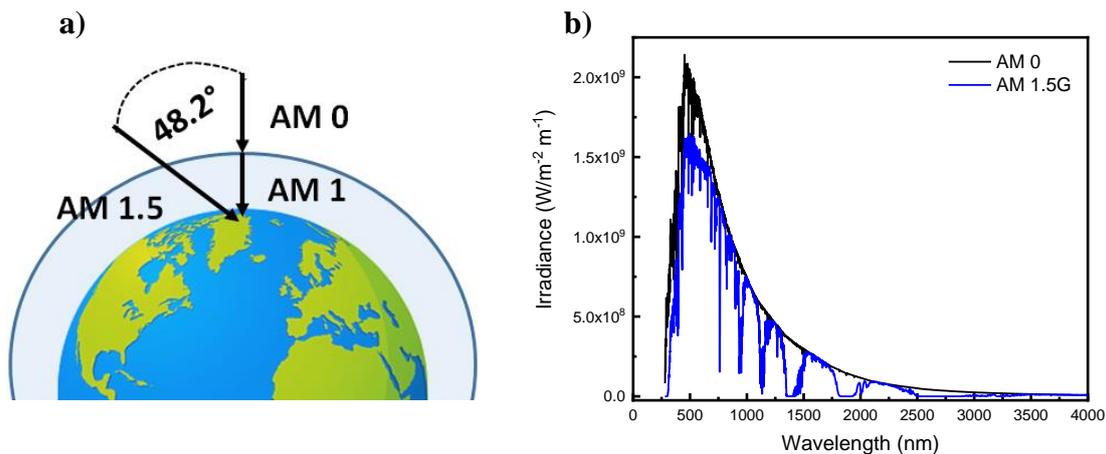
Figure 2.13. a) Schematic showing sunlight (dark arrow) passing through the atmosphere. AM 0 represents the solar spectrum outside the atmosphere. AM1 denotes sunlight traveling through 1 atmosphere and AM1.5 through 1.5 of atmosphere thickness. From [64]. b) Different solar spectrum showing the impact of AM 0 and AM 1.5G.

Therefore, to classify the amount of atmosphere the light has gone through, the concept of AM was created. Further, D and G notations can be added to this classification which represents if the spectrum is direct or global where global means the direct sunlight plus the light scattering accounted for [64]. Thusly, for solar cell testing, AM 1.5G is typically used as this denotes the amount of sunlight passing through 1.5 atmospheres (zenith angle of 48.2°) with an illumination intensity of 1000 W/m^2 representing one sun [64]. A sketch is provided in Figure 2.13 showing the different classifications of AM and a comparison of spectrums.

2.9.1 Power conversion efficiency (PCE)

We now move on onto the basic parameters of PVs. As observed previously, the power conversion efficiency (PCE) also represented by the symbol "η" is one of the most important figures to describe the performance of a PV device. The PCE is given by the

maximum power (P_M) to the total incident power from sunlight (P_L), and it is determined by the next expression [67, 75, 80]:

$$\eta = \frac{P_m}{P_L} = \frac{FF * J_{SC} * V_{OC}}{P_L} \tag{2.1}$$

In short, the PCE indicates how efficiently a PV device can convert sunlight into electricity. Further, the PCE is based on the open circuit voltage (V_{OC}), J_{SC} and fill factor (FF) all of which can be extracted from a J-V curve [81]. The J-V curve revealing these parameters is generated when the electrical response of a PV device is conducted under illumination with a solar simulator and an irradiance of AM 1.5G, typically by applying a voltage sweep, i.e. -1 V to 1 V, that depends on the open circuit voltage [81]. Figure 2.14 depicts these PV characteristics which are discussed below. During dark measurements, the J-V passes through the origin (almost no current generation) and under illumination, the J-V curve shifts downwards in an equal amount to the photocurrent (J) in the forward bias region, as demonstrated in the figure.
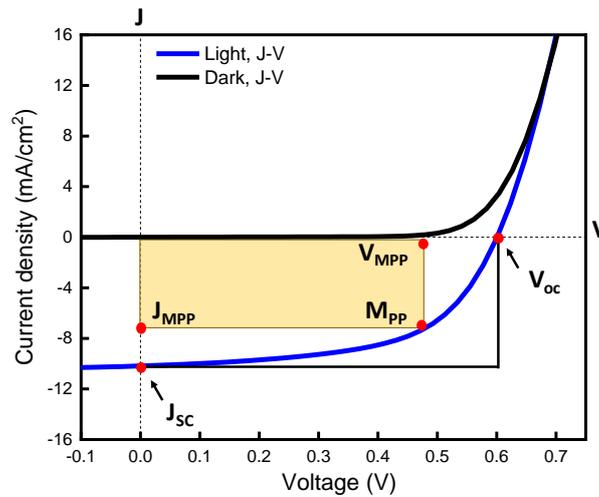
Figure 2.14. J-V light (blue) and dark (black) curves with points of interest.

The maximum power point (M_{PP}) denotes the location in the J-V curve where the current density and voltage are at its maximum [67]. The J_{MPP} and V_{MPP} stand for the current density at the maximum power point and the voltage at maximum power point respectively [67].

2.9.2 Short-circuit current density (J_{SC})

The J_{SC} is defined as the current that flows through an illuminated device when there is no applied voltage and is used as a measure of the photo-generated current in PV devices [64]. The J_{SC} is directly correlated to the amount of light absorbed by the active layer and factors related to the efficiency of each step of the PV process as previously introduced: light absorption, exciton diffusion, exciton dissociation and charge transport/collection [80, 82]. For example, the interplay between mobility of charges and percolation pathways have a direct impact in J_{SC} [80]. A way in which J_{SC} can be improved is to absorb more light in the device. One approach is to increase the thickness of the active layer although this is limited until certain extent due to the low mobility of charges which can lead to recombination [80, 82]. Another approach is to absorb more light in the 600 nm – 800 nm region where there is a maximum of solar photon flux [80, 82]. For instance, a polymer MDMO-PPV used in OPVs in the past has its absorption peak at 500 nm, which is offset from the maximum photon flux region [80]. This represents a clear example of why new materials are needed, because in this case the absorption profile of the donor polymer is strongly mismatched with the solar spectrum. Thus, there is ongoing research to develop novel polymers and small molecules with lower bandgaps that can strongly absorb in these regions [83].

2.9.3 Open circuit voltage (V_{OC})

In PVs, the V_{OC} is the applied voltage for which there is no current flow and defines the maximum voltage that a device can deliver to an external load [84]. Although the changes in V_{OC} can be attributed to a number of factors, to name a few: illumination intensity, temperature and carrier lifetime [84], it is generally agreed with supports in literature that V_{OC} is mainly related to the energy difference between the LUMO of the acceptor and the HOMO of the donor materials [80, 84]. V_{OC} can be calculated using the next equation [84, 85]:

$$V_{OC} = e^{-1} \left(|E_{HOMO}{}^{donor}| - |E_{LUMO}{}^{acceptor}| - 0.3\ eV \right) \qquad \textbf{(2.2)}$$

Where "*e*" is the elementary charge, "*E*" the energy levels of the HOMO or LUMO components and *"0.3 eV"* is an empirical value used to represent charge separation in polymer:fullerene systems [85]. For example, Figure 2.15 presents a

schematic of a P3HT:PCBM OPV with energy levels and V_{OC} of ~0.6 V, and can be used as reference for the design of other polymers [85].
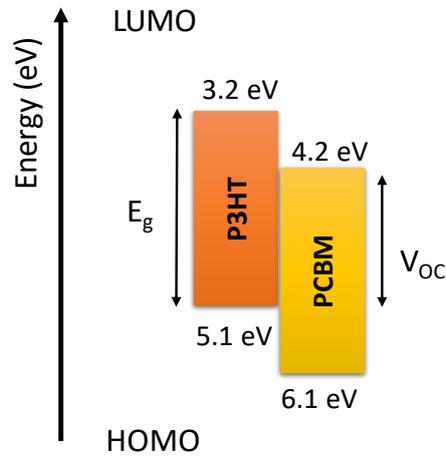
Figure 2.15. Energy band diagram of P3HT:PCBM OPV showing the bandgap (E_G) and V_{OC}. Energy levels from [86].

2.9.4 Fill Factor (FF)

In PVs, the FF is an important parameter that indicates how easily charges can be extracted from the device and is typically expressed by the squareness of the J-V curve, i.e. by the quotient of the maximum power and the product of the V_{OC} and J_{SC} (yellow and white rectangles correspondingly in Figure 2.14) [85, 87]. The FF is determined by the formulism [87]:

$$FF = \frac{J_{MPP} * V_{MPP}}{J_{SC} * V_{OC}} \qquad (2.3)$$

Where J_{MPP} and V_{MPP} are the current density and voltage at maximum power point as indicated before. The FF reveals the quality of the diode properties in PV cells under illumination and an "ideal" value would be represented by unity e.g. 100%, when the J-V curve depicts a rectangle, however, in real life is not possible to achieve this value [87]. A number of factors can adversely affect FF including series and shunt resistances, carrier mobility and morphology [80, 85]. Recent advances in device engineering have demonstrated that adding a small amount of lithium fluoride (LiF) at the interface between the active layer and the metal contact can be beneficial to increase FF [88]. For instance, an LiF evaporated layer of ~1 nm can increase FF (and V_{OC}), resulting in higher PCEs

[80]. This can be attributed to: lowering the work function of the cathode and protection of the photoactive layer from hot atoms resulting during the evaporation of the contact [80]. To finish this section, there are different ways in which PCE can be enhanced in OPV devices. At present, the study of novel materials, formulation (processing methods) and new architectures is a major force driving the performance in OPVs [65, 89, 90].

2.10 Efficiency loss mechanisms in OPVs: Recombination

Having discussed the main 4 consecutive steps occurring in an OPV to generate electricity, we now take a closer look at the processes that compete against them. The recombination of charge carriers is an important loss mechanism in semiconductors where the energy is lost for power conversion, thus limiting the performance by decreasing FF, J_{SC}, V_{OC} and PCE [75, 91]. Due to the low dielectric constant in organic semiconductors as previously specified, the separation of electron-hole pairs into free carriers and collection at the contacts can be inefficient in many cases [92]. This loss mechanism takes place when electron-hole pairs recombine back to the ground state before fully dissociating or when opposing free carriers encounter each other on their way to the electrodes [92, 93].
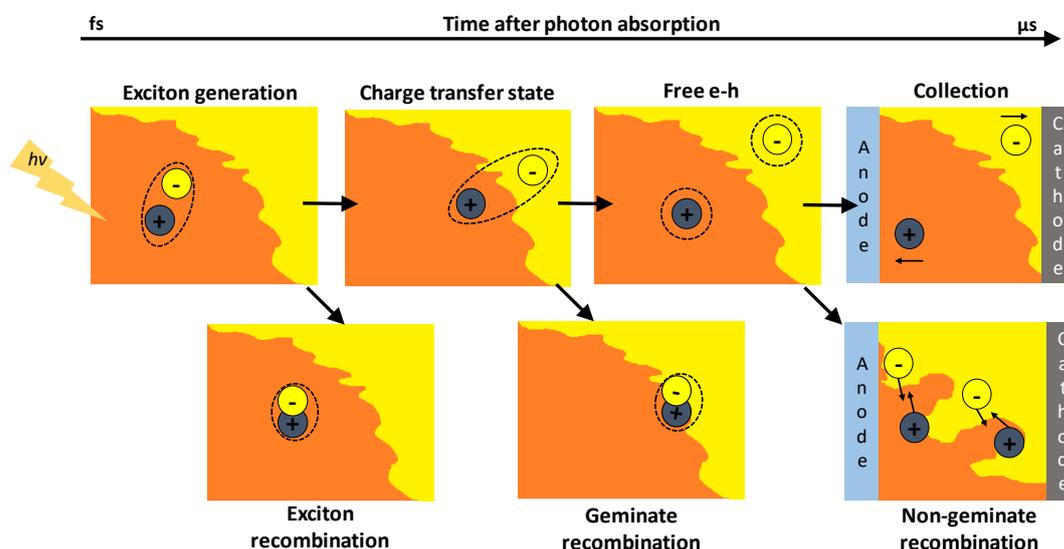
Figure 2.16. Schematic with general overview of the processes involved following photon absorption, showing geminate and non-geminate recombination mechanisms and the time scales. Redrawn from [94].

When this happens, a part of the photon energy is lost and hence fewer carriers collected which reduces the device's performance. OPVs are largely dominated by two

29

types of charge recombination, namely, geminate recombination and non-geminate recombination which will be discussed next. In addition, the exciton recombination, where the exciton decays before reaching a D:A interface, is usually not a problem in BHJ systems since both materials are blended as declared before, so it won't be further discussed. Figure 2.16 presents a sketch of the main processes involved in recombination mechanisms and charge carriers.

2.10.1 Geminate recombination

The mechanism of geminate recombination takes place before an electron-hole pair is dissociated into free carriers, as illustrated in Figure 2.17 A, B. To briefly recap, after a photon is absorbed, an electron-hole pair is formed called an exciton, which is bound by strong Coulomb forces making it complicated for these constituents to separate into free carriers, an issue unique to OPV devices [95]. Once it reaches a D:A interface, the exciton forms a CT state as formerly described, where the electron and hole are still bound by a lessened Coulomb binding energy, which in most cases is larger than kT (~0.025 eV) at room temperature [86]. In order for the electron-hole to separate, they must overcome this binding force, otherwise they recombine geminately [95]. Although there has been ample discussion in literature regarding what determines if electron-holes will separate or recombine at the D:A interface, is generally agreed upon that energy level offsets close to the heterojunction are the main cause of free charge generation [96]. Factors that can assist in overcoming geminate recombination are the electric field and energetic disorder [92]. In addition, there is compelling evidence showing that the delocalization of CT states can also assist in reducing geminate recombination [92]. Alternatively, geminate recombination of a photo generated electron-hole pair at the interface is known to be monomolecular, because these two constituents originate from the same photon [93].
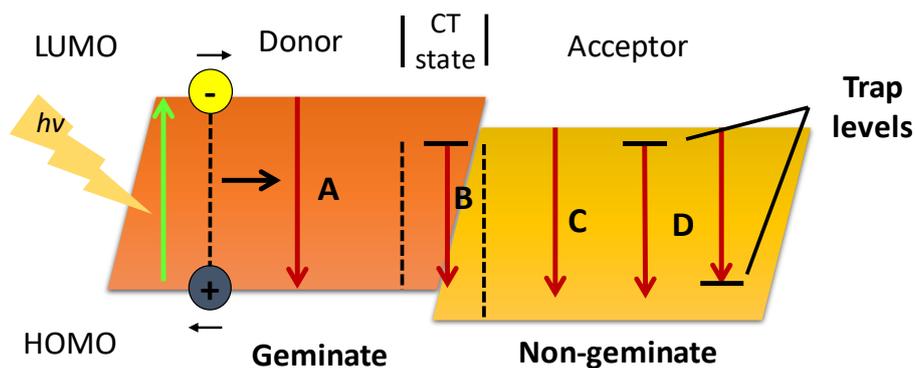
Figure 2.17. Geminate and non-geminate recombination mechanism, adapted from [92]. Following light absorption, an exciton is formed (green arrow), which is bound as indicated by the dashed line with the electron and hole figures. Then, the exciton starts to diffuse into a D:A interface (black arrow). The geminate recombination mechanisms are: 'A' exciton decay before reaching a D:A interface and 'B' recombination through the CT state before fully dissociating into free carriers. The CT is represented by the dashed lines to the left and right of 'B'. Typical non-geminate recombination mechanisms include: 'C' bimolecular (opposing free carriers) and 'D' trap assisted, which is represented by the arrows to the left and right of 'D' showing distinct energetic traps.

Reports in literature have demonstrated that in some OPV blend systems, the absorbed photons are converted to free electron-hole pairs with values over <95% or near unity [77]. However, geminate recombination can adversely impact J_{SC} in blend systems that do not reach such values [97, 98]. Thus, the need to engineer ways to overcome geminate recombination when the above-mentioned factors are absent is significant and an important area of research in the OPV field.

2.10.2 Non-geminate recombination

When electron-hole pairs are dissociated into free carriers, they drift towards their respective electrodes (hole to the anode, electrons to the cathode) assisted by the device internal electric field [92]. However, pathways to the electrodes are not always certain in blended systems as established before, and since charge transport takes place by hopping from one molecule to another, recombination of oppositely charged carriers may still occur [59]. This is termed as non-geminate recombination, whereby opposing free carriers do not originate from the same photoexcitation event [93] (Figure 2.17 C, D). Because non-geminate recombination competes with carrier extraction, once all charges are collected a higher photocurrent can be attained in the device [93]. Thus, non-geminate recombination is an important loss channel that has a profound impact in J_{SC}, V_{OC}, FF and consequently the PCE. Therefore, a comprehensive understanding on this type of recombination is necessary to realise higher performances in OPVs [99, 100].

Factors that have been shown to suppress non-geminate recombination include the spatial separation of charges via a "cascade" energy structure at a D:A interface, which can be formed by adding a third component into a BHJ blend [74]. This method can increase carrier lifetime and thus yields a higher opportunity for carriers to reach the contacts [101]. Also, adding additives into a BHJ blend can assist in optimising the morphology and reduce charge carrier recombination [102]. Lastly, there are three main physical processes in OPVs that arise from non-geminate recombination: bimolecular, trap-assisted and surface recombination (contacts) which are individually discussed in what comes next.

a) Bimolecular recombination

This type of non-geminate recombination is the most common and describes the recombination of a free hole with a free electron as demonstrated in Figure 2.16, evidencing the competing process against carrier extraction [99, 103]. Therefore, slower carriers are more likely to find each other, thusly the rate of bimolecular recombination in OPVs depends on the mobility of charge carriers [92, 99, 104]. This type of recombination is described by the Langevin formulism as:

$$R_L = \frac{q}{\varepsilon}\,(\mu_n + \mu_p)(np - n_i^2) \qquad\qquad \textbf{(2.4)}$$

Where q is the elementary charge, ε the dielectric constant, μ_n the mobility of electrons through the acceptor LUMO, μ_p the mobility of holes through donor HOMO, n and p the electron and hole charge density respectively and n_i is the intrinsic carrier concentration [92]. To simplify, this equation describes the recombination of two opposite charge carriers that are attracted to each other by their Coulomb radius [92].

b) Trap assisted recombination

This type of recombination occurs when an electron and hole recombine through a localised energetic trap; for instance, one carrier is trapped then a second (oppositely charged carrier) finds the trapped carrier [92]. In disordered materials such as BHJs, traps arise from chemical impurities, defects and unoptimised morphology, enhancing this type of recombination [105]. Additionally, defects can lead to the formation of shallow and deep traps, both of which can limit the mobility of carriers [106]. In this loss mechanisms, the recombination rate is determined by the number of trap sites that act as charge trapping and detrapping, and how quickly a free carrier can find a trapped one [99]. This type of

non-geminate recombination is also known as Shockley-Read-Hall (SRH) model and is defined by the next equation, which has been used to describe inorganic semiconductors in the past as well as OPVs [99]:

$$R_{SRH} = \frac{C_n C_p N_{tr}(np - n_i^2)}{[C_n(n + n_1)C_p(p - p_1)]} \tag{2.5}$$

Here, C_n means the probability per unit time that an electron in the conduction band will be captured when a trap is empty and able to capture an electron. Consistently, C_p means that probability per unit time that a hole will be captured when a trap is filled with an electron and able to capture the hole. N_{tr} denotes the density of electron traps, n and p are the electron and hole density in the conduction and valence band accordingly. Also, n_i stands for the intrinsic carrier concentration in the device [92]. It has been discussed in literature that in most polymer:fullerene based blends, trap recombination originates in the donor material whilst the acceptor is trap free mostly attributed to defects from the donor and because fullerenes are known to be limited by space charge [92, 107, 108]. Regardless, it has also been discussed in literature that most of high efficient OPVs are not limited by this type of non-geminate recombination [105].

c) Surface recombination

Although this type of non-geminate recombination has remained somewhat obscure in literature in contrast to recombination mechanisms occurring in the bulk, it may also affect the efficiency in OPVs [92, 100]. Surface recombination refers to the metal-semiconductor interface at the contacts, where the presence of minority carriers will dominate the recombination [100]. For example, this type of behaviour is observed when electrons diffuse to the anode and recombine with injected holes, and when holes diffuse to the cathode and recombine with injected electrons [92]. Further, low charge transfer rates and energy barriers from the active layer can lead to space charge accumulation in the contacts [100]. Not surprisingly, minority carriers near the electrodes can reduce the cell performance since those carriers will recombine and the energy is lost [92]. In any case, Street et al [109] investigated different recombination mechanisms in a polymer:fullerene based blend and it was found that surface recombination is not a dominant loss that determines the shape of the OPV characteristics which was further corroborated with modelling studies.

2.11 Efficiency enhancement

At present, the possibility of commercialisation and large area fabrication of OPVs is still limited by low efficiencies [43, 110]. As stated before, efficiencies over 10% – 15% are desired which can be accompanied by larger lifetimes, as this is another major constraint in OPVs [111]. Nevertheless, many questions remained unanswered or highly debated in literature such as the nature and morphology evolution in OPVs [112, 113], which is closely related to all the PV processes (charge generation, separation, transport and collection) [85].
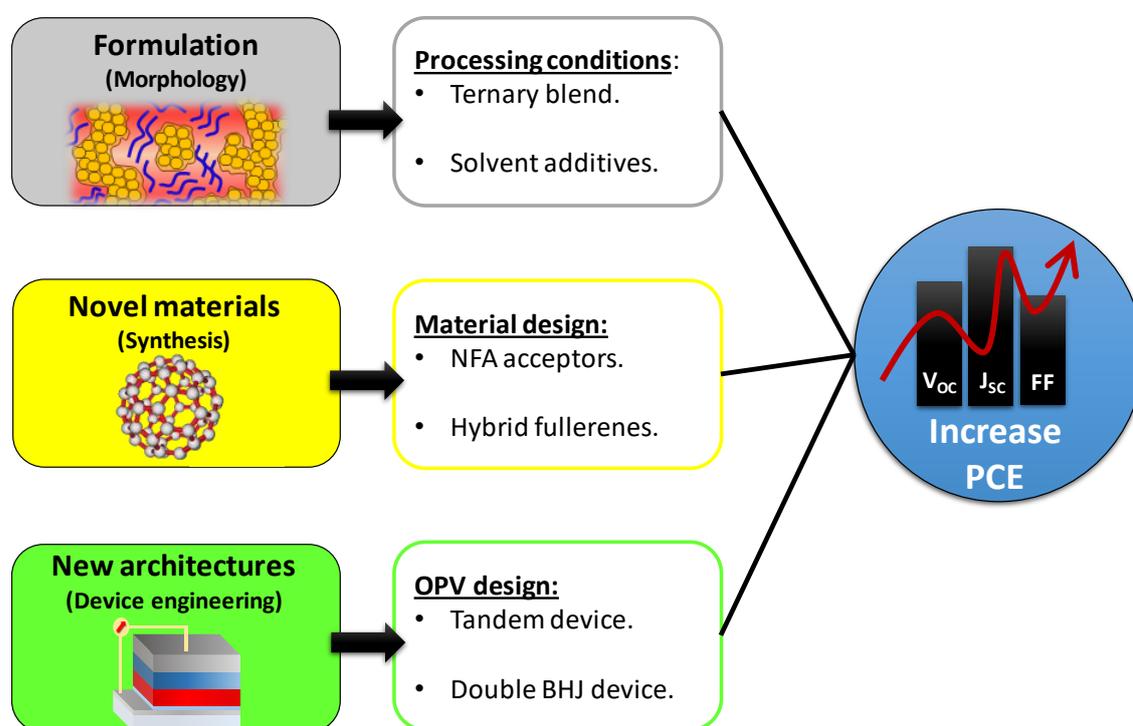
Figure 2.18. Methods to improve efficiency utilised in this thesis.

To this end, in this thesis we address perhaps one of the most important aspects related to OPV research, that is how to improve the performance (Figure 2.18). Three key points are investigated here: New formulation in blends (1), comprising ternary blends with solvent additives. Novel materials (2) that include non-fullerene (NFA), hybrid fullerenes and fullerenes probed for the first time. Lastly, new architectures (3) made up of a tandem structure with and without an intermediate layer. In the following sections, each type of methodology used in this thesis will be briefly introduced, as an antecedent

to the results Chapters from 5 to 7. But first, the preparatory work included in Chapter 4 will be discussed.

2.11.1 Preparatory work to optimise binary blends

In this section we first discuss the precursor work carried out to optimise binary blends, which was a necessary to better discern the impact of the formulation method by adding a third component to the blends.

To start, the control of the active layer morphology remains one of the key aspects to address in OPV fabrication [113, 114]. Considering the many options for materials, device design and processing conditions, it is often that the outcomes may lead to mixed results. However, as with other types of PV technology, there has been a continuous effort to overcome these limitations in order to understand how to manipulate the morphology and yield higher efficiencies in a predictive way [73, 115]. Among different methods that have been investigated, thermal annealing (TA) and solvent vapour annealing (SVA) are examined in Chapter 4, since these have demonstrated to influence the morphology and thus to realise higher performances. As the name implies, TA is when substrates are heated to temperatures below the melting point of the materials, which allows changes in the orientation of the components [116].

Hotplate   Glass petri dish
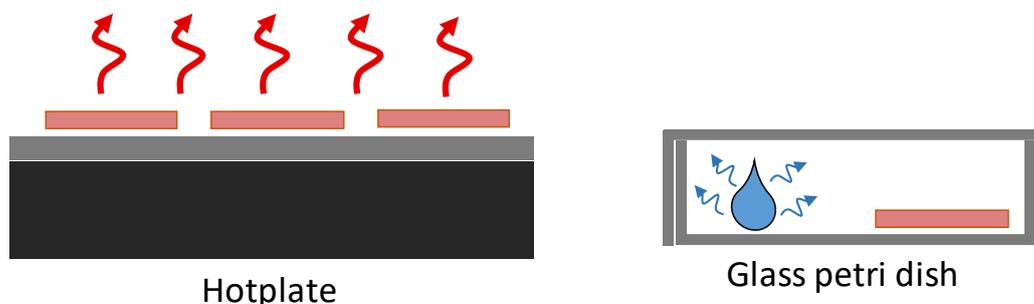
Figure 2.19. Sketch showing TA on a hotplate (left) and SVA by saturating a petri dish with solvent vapours (right). The light red rectangle represents the sample.

On the other hand, SVA introduces solvent vapour into the active layer by adding small amounts of solvent into a container (i.e. petri dish or desiccator) to make it saturated, in this way promoting reorientation in the morphology [117]. Both types of annealing have resulted in increased crystallinity of the donor (i.e. P3HT) which extends the optical absorption and improves charge transport mobilities [116, 117]. Figure 2.19

depicts a sketch of these two methods. In Chapter 4 we investigate this further, specifically to determine optimal TA and SVA conditions for devices fabricated in the Durham engineering cleanroom. The objective of this Chapter is to determine the optimal binary blend to use it as a base going forward into the formulation approach.

2.11.2 Formulation approach by ternary blends

A promising formulation method is through the addition of a third component into the active layer -the ternary blend- which can be another donor or acceptor component [118]. Ternary blends retain the fabrication conditions used in binary blends plus broadening the absorption bandwidth of the active layer, similar to a multi-junction device approach [118]. In addition, strategies that have been used to optimise binary blends can also be applied to ternary blends, like TA, SVA and co-solvents aforementioned [118]. Further, the third component can assist with the nanoscale organisation to improve charge generation, transport and collection [119, 120].
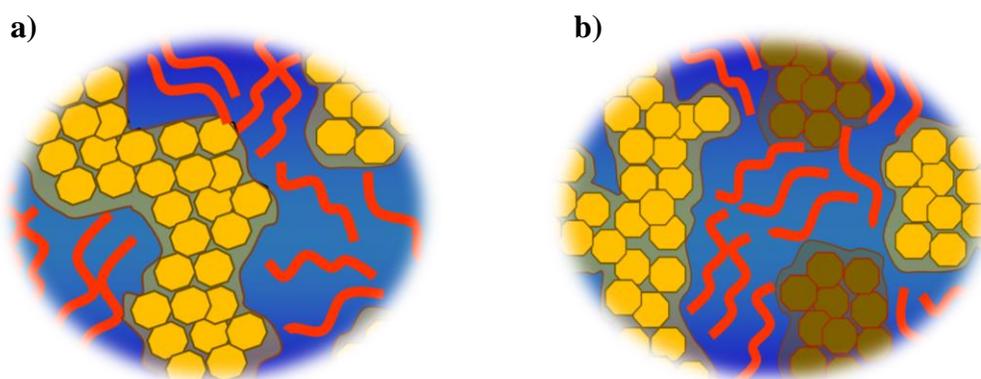
Figure 2.20. Sketch depicting a binary blend a) and ternary blend morphology b). The yellow and brown figures denote the acceptor materials (i.e. different fullerenes) whilst the orange polymer chains.

A general schematic of a ternary blend OPV compared to a regular binary BHJ is presented in Figure 2.20a, b. In ternary blends, the third component may be a supplementary: polymer, fullerene and derivatives, NFAs, dyes, and quantum dots [119]. By using a myriad of different materials, numerous authors have demonstrated that ternary blends can effectively be used to increase J_{SC}, V_{OC} and FF, providing a new strategy to boost PCE [121, 122].

Further, the utilisation of co-solvents (additives) have been demonstrated to drastically change the nanostructure of the active layer in BHJ [123]. Typically, additives are added to the mixture of D:A and have a higher boiling point than the base solvent, so that it can effectively dissolve one of the main components [124]. Not long ago, reports in literature have shown that 1,8-Diiodooctane (DIO) can assist in yielding higher results compared to other additives [125]. One of the reasons being that the co-solvent dissolves fullerene molecules and therefore promotes better domain sizes and D:A interfaces, which can increase the exciton dissociation efficiency [124].

Notwithstanding, the role of the third component is still a matter of debate, and different papers have been published to try and underpin the underlying mechanisms at work [119]. Why do some ternary blend systems work and others do not? This pressing question is addressed in Chapter 5 by systematically investigating and comparing two different ternary systems with the objective of understanding how is it that ternary blends operate and how can one best optimise them. Lastly, insights and design rules are also provided in Chapter 5 that should be taking into consideration when fabricating future ternary blends.

2.11.3 Novel materials

Since the PV outcomes on a device are highly dependent on the optical and electronic characteristics, much effort has also been focused on developing and synthesising new materials for active layers [8]. Indeed, much of this attention has been leveraged by donor polymers due to their optical properties, π-π stacking and processability, however, the development of new acceptor materials with tuneable energy levels that can improve J_{SC}, V_{OC} and carrier mobilities also represents a promising way to further drive OPV performance [69]. Typically, PCBM is a common used acceptor because of its high electron mobility and solubility with organic solvents [126]. However, it also suffers from low absorption (visible region) and deep LUMO which can limit the J_{SC} and V_{OC} [126]. Thusly, new approaches to alleviate these drawbacks involve the development of NFAs and hybrid fullerenes which present tuneable electronic properties, stability and synthetic flexibility [127]. In Chapter 6, 4 different components made of NFAs and hybrid fullerene materials were prepared by Dr. Avestro and fellow PhD Phil Hope in a collaborative work. Figure 2.21 presents an example of common PCBM and a

novel acceptor. More details on the materials used are included in Chapter 3 and a full discussion on Chapter 6.
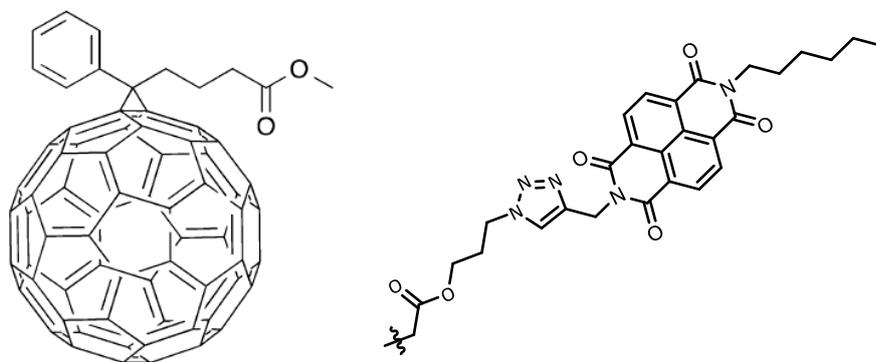
Figure 2.21. Example of benchmark PCBM (left) and NFA NDI$_2$ (right). The full molecular structure of the other materials is included in Chapter 6.

The main objective of Chapter 6 is to utilise these new materials and probe the electron transport characteristics for the first time. Such mobility studies are extremely vital to properly design the next generation of acceptor materials and to ensure their functionality before they are blended with donors to fabricate binary or ternary OPVs.

2.11.4 Device engineering, tandem and double BHJ

In typical BHJ OPVs there are two main issues that can limit the performance. First, because of the inherent low mobility carriers, thicknesses range between 100 nm-250 nm which can limit the amount of photon harvesting [26]. The second is related to the limits of P-N junctions and energy conversion published by Shockley and Queisser [128], where photons with lower bandgap than the active layer are not absorbed and transmitted through the device and thus lost. Further, the thermodynamic limit in PVs predicts and ideal efficiency of 68% for an infinite number of cells with unconcentrated light and 86% with concentrated light [129]. A useful strategy in which this problem can be alleviated is through multijunction or multi-absorbing layers, typically termed as tandem structures [26]. Tandem OPV devices are made of two or more active layers which are stacked on top of each other (Figure 2.22). Therefore, the absorbing layers consist of different materials with different bandgaps, so that one layer absorbs high energy photons whilst lower energy photons are transmitted to the other layer [130].
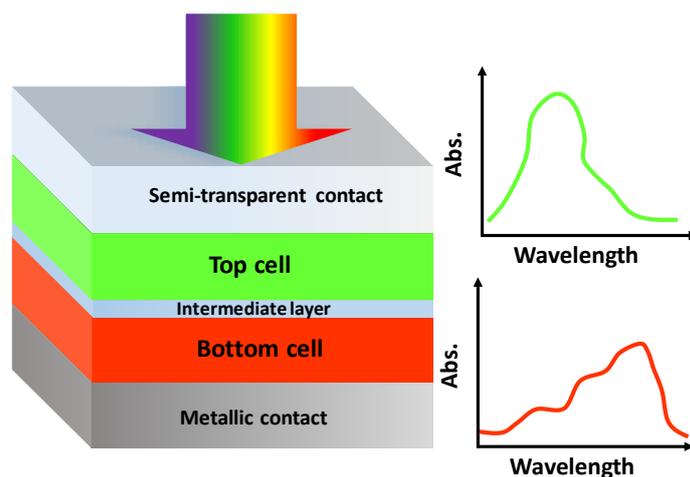
Figure 2.22. Basic schematic of an OPV tandem structure, adapted from [26].

Further, these active layers are separated by an intermediate (or recombination) layer, allowing holes of one layer to recombine with electrons from the other layer [130]. Consequently, due to the complementary light harvesting, tandem structures offer more flexibility to tune the absorption characteristics. In addition, to attain high performances is desirable that the individual active layers contribute with similar currents for series connected tandems [130]. Although in practice, achieving a current balance model can prove to be difficult considering all the different types of materials and processing conditions one can use to fabricate devices [131]. Theoretically, considering a detail balanced limit, a tandem cell of two junctions can attain a 42% efficiency whilst a triple junction tandem cell a 49% mostly due to enhancement in the extraction of charge carriers [129]. At present, however, a PCE of ~17% has been achieved experimentally with a double junction tandem and ~15% with triple junction fabricated of organic semiconductors [23, 132]. Though impressive, these results are still not high enough to compete with established PV technologies, yet, they demonstrate promising potential in the development of novel OPVs. So, a combination of techniques and new materials which can aid to cover more efficiently the solar spectrum is normally sought by the OPV community.

In Chapter 7, a novel tandem architecture is investigated with advanced modelling to understand how it works, consisting of two separate BHJ layers and a recombination layer. The objective is to show that a high efficiency can be achieved even if there is a current mismatch between sub-cells, which can be an important efficiency limiting factor as stated above.

In addition, this model is also examined under varied illumination conditions to better understand how tandems perform in the real world. Another relevant approach is also considered in this Chapter, consisting of the tandem structure but with no intermediate layer, resulting in overall the same outcome, thus showing the robustness of the method proposed. To wrap up this section, the development of new architectures and device engineering is of paramount relevance, because in that way, OPVs will continue to reach higher efficiencies and certainly commercialisation.

Finally, with the contextual background covered, the structure of the rest of the thesis is as follows: in Chapter 3, the experimental, modelling and characterisation methods used throughout the thesis will be covered. The results derived from this thesis are included in Chapters 4 through 7 and are based on the methods to improve efficiency as stated in section 2.11. Specifically, Chapter 4 comprises preparatory work necessary to optimise binary blends and further understand the performance when a third component is added. Thus, the formulation approach is introduced in Chapter 5 by fabricating ternary blends based on novel polymers and fullerenes. Novel electron acceptors materials made of NFA, hybrid fullerenes and fullerenes are investigated in Chapter 6 to elucidate electron transport properties. In Chapter 7, new architectures are explored by engineering tandem and double BHJ OPVs with advance modelling. At last, Chapter 8 summarises the findings from this study and provides suggestions for future work.

2.12 References

1. MacKay, D.J., *Part I: Numbers not adjectives*, in *Sustainable Energy - Without the Hot Air*. 2009, UIT Cambridge Ltd.: England. p. 1-21.

2. Darling, S.B. and F. You, *The Case for Organic Photovoltaics.* RSC Adv., 2013. **3**(39): p. 17633-17648.

3. Krebs, F.C., *Chapter 1: Introduction*, in *Polymer Photovoltaics: A Practical Approach*. 2008, SPIE: United States of America. p. 1-10.

4. Zhang, T., M. Wang, and H. Yang, *A Review of the Energy Performance and Life-Cycle Assessment of Building-Integrated Photovoltaic (BIPV) Systems.* Energies, 2018. **11**(11).

5. Cao, W. and J. Xue, *Recent Progress in Organic Photovoltaics: Device Architecture and Optical Design.* Energy Environ. Sci., 2014. **7**(7): p. 2123-2144.

6. Cengiz, M.S. and M.S. Mamiş, *Price-Efficiency Relationship for Photovoltaic Systems on a Global Basis.* Int. J. Photoenergy, 2015. **2015**: p. 1-12.

7. Thompson, B.C., et al., *Polymer-Based Solar Cells: State-of-the-Art Principles for the Design of Active Layer Components.* Green, 2011. **1**(1).

8. Xiao, S., Q. Zhang, and W. You, *Molecular Engineering of Conjugated Polymers for Solar Cells: An Updated Report.* Adv. Mater., 2017. **29**(20).

9. Poelking, C. and D. Andrienko, *Design Rules for Organic Donor-Acceptor Heterojunctions: Pathway for Charge Splitting and Detrapping.* J. Am. Chem. Soc., 2015. **137**(19): p. 6320-6326.

10. M. Ramrakhiani, S.D., Hemraj Waxar, Kamal Kumar Kushwaha, Pranav Singh, *Chapter 2: Basic Principles and Theory of the Photovoltaic Effect*, in *Recent Advances in Photovoltaics*, M. Ramrakhiani, Editor. 2017, Materials Research Forum LLC: United States of America. p. 37-57.

11. Sonal P. Ghawade, A.D.D., Kavita Abhay Deshmukh, S. J. Dhoble, *Chapter 1: The Rise of Solar Cells*, in *Recent Advances in Photovoltaics*, M. Ramrakhiani, Editor. 2017, Materials Research Forum LLC: United States of America. p. 1-36.

12. Arno Smets, K.J., Olindo Isabella, René Van Swaaij, Miro Zeman, *Chapter 11: A Short History of Solar Cells*, in *Solar Energy, The Physics and Engineering of Photovoltaic Conversion, Technologies and Systems*. 2015, UIT Cambdrige Ltd: England. p. 149-152.

13. Hideki Shirakawa, E.J.L., Alan G. MacDiarmid, Chwan K. Chiang and Alan J. Heeger, *Synthesis of Electrically Conducting Organic Polymers: Halogen Derivatives of Polyacetylene, (CH)x.* J. Chem. Soc., Chem. Commun., 1977: p. 578-580.

14. Tang, C.W., *Two-layer organic photovoltaic cell.* Appl. Phys. Lett., 1986. **48**(2): p. 183-185.

15. N. S. Sariciftci, L.S., A. J. Heeger, F. Wudl, *Photoinduced Electron Transfer from a Conducting Polymer to Buckminsterfullerene.* Science, 1992. **258**(5087): p. 1474-1476.

16. J. J. M. Halls, C.A.W., N. C. Greenham, E. A. Marseglia, R. H. Friend, S. C. Moratti & A. B. Holmes *Efficient Photodiodes From Interpenetrating Polymer Networks.* Nature, 1995. **376**: p. 498-500.

17. G. Yu, J.G., J. C. Hummelen, F. Wudl, A. J. Heeger, *Polymer Photovoltaic Cells: Enhanced Efficiencies via a Network of Internal Donor-Acceptor Heterojunctions.* Science, 1995. **270**(5243): p. 1789-1791.

18. F. Padinger, R.S.R., N. S. Sariciftci, *Effects of Postproduction Treatment on Plastic Solar Cells.* Adv. Funct. Mater., 2003. **13**(1): p. 85-88.

19. Peet, J., et al., *Efficiency Enhancement in Low-Bandgap Polymer Solar Cells by Processing with Alkane Dithiols.* Nat. Mater., 2007. **6**(7): p. 497-500.

20. Liang, Y., et al., *For the Bright Future-Bulk Heterojunction Polymer Solar Cells with Power Conversion Efficiency of 7.4%.* Adv. Mater., 2010. **22**(20): p. E135-8.

21. He, Z., et al., *Enhanced Power-Conversion Efficiency in Polymer Solar Cells Using an Inverted Device Structure.* Nat. Photonics, 2012. **6**(9): p. 591-595.

22. Xiao, Z., X. Jia, and L. Ding, *Ternary Organic Solar Cells Offer 14% Power Conversion Efficiency.* Sci. Bull., 2017. **62**(23): p. 1562-1564.

23. Lingxian Meng, Y.Z., Xiangjian Wan, Chenxi Li, Xin Zhang, Yanbo Wang, Xin Ke, Zuo Xiao, Liming Ding, Ruoxi Xia, Hin-Lap Yip, Yong Cao, Yongsheng Chen, *Organic and Solution-Processed Tandem Solar Cells with 17.3% Efficiency.* Science, 2018. **361**(6407): p. 1094-1098.

24. Upama, M.B., et al., *Trendsetters in High-Efficiency Organic Solar Cells: Toward 20% Power Conversion Efficiency.* Sol. RRL., 2019. **4**(1).

25. Li, G., W.-H. Chang, and Y. Yang, *Low-Bandgap Conjugated Polymers Enabling Solution-Processable Tandem Solar Cells.* Nat. Rev. Mater., 2017. **2**(17043).

26. Ameri, T., et al., *Organic Tandem Solar Cells: A Review.* Energy Environ. Sci., 2009. **2**(4): p. 347-363.

27. Conibeer, G., *Third-Generation Photovoltaics.* Mater. Today, 2007. **10**(11): p. 42-50.

28. Arno Smets, K.J., Olindo Isabella, René Van Swaaij, Miro Zeman, *Chapter 12: Crystalline Silicon Solar Cells*, in *Solar Energy, The Physics and Engineering of Photovoltaic Conversion, Technologies and Systems*. 2015, UIT Cambridge Ltd: England. p. 153-176.

29.   Arno Smets, K.J., Olindo Isabella, René Van Swaaij, Miro Zeman, *Chapter 1: Energy*, in *Solar Energy, The Physics and Engineering of Photovoltaic Conversion, Technologies and Systems*. 2015, UIT Cambdrige Ltd: England. p. 1-12.

30.   Bilgili, M., et al., *An Overview of Renewable Electric Power Capacity and Progress in New Technologies in the World.* Renew. Sust. Energ. Rev., 2015. **49**: p. 323-334.

31.   Lee, H.S., et al., *Enhanced Efficiency of Crystalline Si Solar Cells Based on Kerfless-Thin Wafers with Nanohole Arrays.* Sci. Rep., 2018. **8**(1): p. 3504.

32.   Kitai, A., *Chapter 1: Semiconductor Physics*, in *Principles of Solar Cells, LEDs and Diodes: The Role of the PN Junction*, L. John Wiley & Sons, Editor. 2011, John Wiley & Sons, Ltd.: Malaysia. p. 1-68.

33.   Arno Smets, K.J., Olindo Isabella, René Van Swaaij, Miro Zeman, *Chapter 13: Thin-Film Solar Cells*, in *Solar Energy, The Physics and Engineering of Photovoltaic Conversion, Technologies and Systems*. 2015, UIT Cambdrige Ltd: England. p. 177-216.

34.   Shen, K., et al., *High Efficiency CdTe Solar Cells with a Through-Thickness Polycrystalline CdTe Thin Film.* RSC Adv., 2016. **6**(57): p. 52326-52333.

35.   Wang, W., et al., *Device Characteristics of CZTSSe Thin-Film Solar Cells with 12.6% Efficiency.* Adv. Energy Mater., 2014. **4**(7).

36.   Qu, Y., G. Zoppi, and N.S. Beattie, *The Role of Nanoparticle Inks in Determining the Performance of Solution Processed Cu2ZnSn(S,Se)4 Thin Film Solar Cells.* Prog. Photovolt: Res. Appl., 2016. **24**(6): p. 836-845.

37.   Wang, Q., et al., *Progress in Emerging Solution-Processed Thin Film Solar Cells – Part I: Polymer Solar Cells.* Renew. Sustain. Energy Rev., 2016. **56**: p. 347-361.

38.   Lee, T.H., Sue, H.J. & Cheng, X., *Solid-State Dye-Sensitized Solar Cells based on ZnO Nanoparticle and Nanorod Array Hybrid Photoanodes.* Nanoscale Res. Lett., 2011. **6**(517).

39.   Jung, E.H., et al., *Efficient, Stable and Scalable Perovskite Solar Cells Using Poly(3-hexylthiophene).* Nature, 2019. **567**(7749): p. 511-515.

40.   Rajagopal, A., et al., *Highly Efficient Perovskite-Perovskite Tandem Solar Cells Reaching 80% of the Theoretical Limit in Photovoltage.* Adv. Mater., 2017. **29**: p. 1702140.

41.   C. J. Brabec, J.A.H., P. Schilinsky & C. Waldauf, *Production Aspects of Organic Photovoltaics and Their Impact on the Commercialization of Devices.* MRS Bulletin, 2005. **30**: p. 50-52.

42.   Al-Busaidi, Z., et al., *Enhanced Lifetime of Organic Photovoltaic Diodes Utilizing a Ternary Blend Including an Insulating Polymer.* Sol. Energy Mater. Sol. Cells, 2017. **160**: p. 101-106.

43. Brabec, C.J., *Organic Photovoltaics: Technology and Market.* Sol. Energy Mater. Sol. Cells, 2004. **83**(2-3): p. 273-292.

44. A.J Nozik, *Quantum Dot Solar Cells.* Phys. E: Low-Dimens. Syst. Nanostructures, 2002. **14**(1-2): p. 115-120.

45. Arno Smets, K.J., Olindo Isabella, René Van Swaaij, Miro Zeman, *Chapter 16: Third generation concepts*, in *Solar Energy, The Physics and Engineering of Photovoltaic Conversion, Technologies and Systems*. 2015, UIT Cambdrige Ltd: England. p. 239-252.

46. Durrant, T.M.C.a.J.R., *Charge Photogeneration in Organic Solar Cells.* Chem. Rev., 2010. **110**(11): p. 6736-6767.

47. Cui, Y., et al., *Over 16% Efficiency Organic Photovoltaic Cells Enabled by a Chlorinated Acceptor with Increased Open-Circuit Voltages.* Nat. Commun., 2019. **10**(1): p. 2515.

48. Zhang, Y., et al., *Current Status of Outdoor Lifetime Testing of Organic Photovoltaics.* Adv. Sci., 2018. **5**(8): p. 1800434.

49. Espinosa, N., et al., *Solar Cells with One-Day Energy Payback for the Factories of the Future.* Energy Environ. Sci., 2012. **5**(1): p. 5117-5132.

50. Ma, W., et al., *Thermally Stable, Efficient Polymer Solar Cells with Nanoscale Control of the Interpenetrating Network Morphology.* Adv. Funct. Mater., 2005. **15**(10): p. 1617-1622.

51. Youjun He, H.-Y.C., Jianhui Hou, and Yongfang Li, *Indene−C60 Bisadduct: A New Acceptor for High-Performance Polymer Solar Cells.* J. Am. Chem. Soc., 2010. **132**: p. 1377-1382.

52. Chen, H.-C., et al., *Prominent Short-Circuit Currents of Fluorinated Quinoxaline-Based Copolymer Solar Cells with a Power Conversion Efficiency of 8.0%.* Chem. Mater., 2012. **24**(24): p. 4766-4772.

53. Zhang, H., et al., *Over 14% Efficiency in Organic Solar Cells Enabled by Chlorinated Nonfullerene Small-Molecule Acceptors.* Adv. Mater., 2018. **30**(28): p. 1800613.

54. Yuan, J., et al., *Single-Junction Organic Solar Cell with over 15% Efficiency Using Fused-Ring Acceptor with Electron-Deficient Core.* Joule, 2019. **3**(4): p. 1140-1151.

55. Lukas Schmidt-Mende, J.W., *Chapter 2: Semiconductors and Junctions*, in *Organic and Hybrid Solar Cells an Introduction*. 2016, De Gruyter: Berlin/Boston. p. 6-95.

56. Kitai, A., *Chapter 7: Organic Semiconductors, OLEDs, and Solar Cells*, in *Principles of Solar Cells, LEDs and related Devices: The Role of the PN Junction*, J.W. Sons, Editor. 2019, John Wiley & Sons: Singapore. p. 307-357.

57. Mikkel Jørgensen, E.B., Rémi de Bettignies and Frederik C. Krebs, *Chapter 2: The Polymer Solar Cell*, in *Polymer Photovoltaics: A Practical Approach*. 2008, SPIE: United States of America. p. 11-89.

58. Syed A. Moiz, I.A.K., Waheed A. Younis and Khasan S. Karimov, *Space Charge-Limited Current Model for Polymers*, in *Conducting Polymers*, F. Yilmaz, Editor. 2016, IntechOpen: Turkey.

59. Groves, C., *Simulating Charge Transport in Organic Semiconductors and Devices: A Review.* Rep. Prog. Phys., 2017. **80**(2): p. 026502.

60. Jenny Nelson, J.J.K., James Kirkpatrick, and Jarvist M. Frost, *Modeling Charge Transport in Organic Photovoltaic Materials.* Acc. Chem. Res., 2009. **42**(11): p. 1768-1778.

61. Jean-Luc Brédas, D.B., Veaceslav Coropceanu, and Jérôme Cornil, *Charge-Transfer and Energy-Transfer Processes in π-Conjugated Oligomers and Polymers: A Molecular Picture.* Chem. Rev., 2004. **104**(11): p. 4971-5004.

62. Coehoorn, R., et al., *Charge-Carrier Concentration Dependence of the Hopping Mobility in Organic Materials with Gaussian Disorder.* Phys. Rev. B., 2005. **72**(15): p. 155206.

63. Kitai, A., *Chapter 2: The PN Junction Diode*, in *Principles of Solar Cells, LEDs and Diodes: The Role of the PN Junction*, L. John Wiley & Sons, Editor. 2011, John Wiley & Sons, Ltd.: Malaysia. p. 70-122.

64. Lukas Schmidt-Mende, J.W., *Chapter 3: Working Mechanisms of Organic and Hybrid Solar Cells*, in *Organic and Hybrid Solar Cells an Introduction*. 2016, De Gruyter: Berlin/Boston. p. 97-192.

65. Yu, J., Y. Zheng, and J. Huang, *Towards High Performance Organic Photovoltaic Cells: A Review of Recent Development in Organic Photovoltaics.* Polymers, 2014. **6**(9): p. 2473-2509.

66. Muntwiler, M., et al., *Coulomb Barrier for Charge Separation at an Organic Semiconductor Interface.* Phys. Rev. Lett., 2008. **101**(19): p. 196403.

67. Mazzio, K.A. and C.K. Luscombe, *The Future of Organic Photovoltaics.* Chem. Soc. Rev., 2015. **44**(1): p. 78-90.

68. Kitai, A., *Chapter 4: The Solar Cell*, in *Principles of Solar Cells, LEDs and Diodes: The Role of the PN Junction*, L. John Wiley & Sons, Editor. 2011, John Wiley & Sons, Ltd.: Malaysia. p. 159-214.

69. Anthony, J.E., et al., *n-Type Organic Semiconductors in Organic Electronics.* Adv. Mater., 2010. **22**(34): p. 3876-3892.

70. Hoppe, H. and N.S. Sariciftci, *Organic Solar Cells: An Overview.* J. Mater. Res., 2011. **19**(7): p. 1924-1945.

71. Scully, S.R. and M.D. McGehee, *Effects of Optical Interference and Energy Transfer on Exciton Diffusion Length Measurements in Organic Semiconductors.* J. Appl. Phys., 2006. **100**(3).

72. Denis E. Markov, E.A., Paul W. M. Blom, Alexander B. Sieval, and Jan C. Hummelen, *Accurate Measurement of the Exciton Diffusion Length in a Conjugated Polymer Using a Heterostructure with a Side-Chain Cross-Linked Fullerene Layer.* J. Phys. Chem. A., 2005. **109**(24): p. 5266-5274.

73. Xu, X., et al., *The Prediction of the Morphology and PCE of Small Molecular Organic Solar Cells.* RSC Adv., 2015. **5**(87): p. 70939-70948.

74. Fukuhara, T., Y. Tamai, and H. Ohkita, *Nongeminate Charge Recombination in Organic Photovoltaics.* Sustain. Energy Fuels, 2020. **4**(9): p. 4321-4351.

75. Deibel, C. and V. Dyakonov, *Polymer–Fullerene Bulk Heterojunction Solar Cells.* Rep. Prog. Phys., 2010. **73**(9).

76. Albrecht, C.W.T.A.C., *Chlorophyll-a Photovoltaic Cells.* Nature, 1975. **254**: p. 507-509.

77. Park, S.H., et al., *Bulk Heterojunction Solar Cells With Internal Quantum Efficiency Approaching 100%.* Nat. Photonics, 2009. **3**(5): p. 297-302.

78. Liu, F., et al., *Characterization of the Morphology of Solution-Processed Bulk Heterojunction Organic Photovoltaics.* Prog. Polym. Sci., 2013. **38**(12): p. 1990-2052.

79. Arno Smets, K.J., Olindo Isabella, René Van Swaaij, Miro Zeman, *Chapter 5: Solar Radiation*, in *Solar Energy, The Physics and Engineering of Photovoltaic Conversion, Technologies and Systems*. 2015, UIT Cambdrige Ltd: England. p. 35-46.

80. Brabec, C.J., *Chapter 5: Semiconductor Aspects of Organic Bulk Heterojunction Solar Cells*, in *Organic Photovoltaics Concepts and Realization*, V.D. C. Brabec, J. Parisi, N. S. Sariciftci, Editor. 2003, Springer: Germany. p. 159-248.

81. Krebs, F.C., *Chapter 3: Characterization of Organic Solar Cells*, in *Polymer Photovoltaics: A Practical Approach*. 2008, SPIE: United States of America. p. 91-154.

82. Winder, C. and N.S. Sariciftci, *Low Bandgap Polymers for Photon Harvesting in Bulk Heterojunction Solar Cells.* J. Mater. Chem., 2004. **14**(7): p. 1077-1086.

83. Xu, T. and L. Yu, *How to Design Low Bandgap Polymers for Highly Efficient Organic Solar Cells.* Mater. Today, 2014. **17**(1): p. 11-15.

84. Elumalai, N.K. and A. Uddin, *Open Circuit Voltage of Organic Solar Cells: An in-Depth Review.* Energy Environ. Sci., 2016. **9**(2): p. 391-410.

85. Li, G., R. Zhu, and Y. Yang, *Polymer Solar Cells.* Nat. Photonics, 2012. **6**(3): p. 153-161.

86. Veldman, D., S.C.J. Meskers, and R.A.J. Janssen, *The Energy of Charge-Transfer States in Electron Donor–Acceptor Blends: Insight into the Energy Losses in Organic Solar Cells.* Adv. Funct. Mater., 2009. **19**(12): p. 1939-1948.

87. Qi, B. and J. Wang, *Fill Factor in Organic Solar Cells.* Phys. Chem. Chem. Phys., 2013. **15**(23): p. 8972-8982.

88. Brabec, C.J., et al., *Effect of LiF/Metal Electrodes on the Performance of Plastic Solar Cells.* Appl. Phys. Lett., 2002. **80**(7): p. 1288-1290.

89. Krückemeier, L., et al., *Developing Design Criteria for Organic Solar Cells Using Well-Absorbing Non-Fullerene Acceptors.* Commun. Phys., 2018. **1**(1).

90. Li, Y., *Molecular Design of Photovoltaic Materials for Polymer Solar Cells: Toward Suitable Electronic Energy Levels and Broad Absorption.* Acc. Chem. Res., 2012. **45**(5): p. 723-733.

91. Cowan, S.R., A. Roy, and A.J. Heeger, *Recombination in Polymer-Fullerene Bulk Heterojunction Solar Cells.* Phys. Rev. B., 2010. **82**.

92. Proctor, C.M., M. Kuik, and T.-Q. Nguyen, *Charge Carrier Recombination in Organic Solar Cells.* Prog. in Polym. Sci., 2013. **38**(12): p. 1941-1960.

93. Greenham, C.G.a.N.C., *Monte Carlo Simulations of Organic Photovoltaics*, in *Multiscale Modelling of Organic and Hybrid Photovoltaics*, J.C. David Beljonne, Editor. 2013, Springer: Berlin. p. 257-278.

94. Kurpiers, J., et al., *Probing the Pathways of Free Charge Generation in Organic Bulk Heterojunction Solar Cells.* Nat. Commun., 2018. **9**(1): p. 2038.

95. Nelson, J., *Polymer:Fullerene Bulk Heterojunction Solar Cells.* Mater. Today, 2011. **14**(10): p. 462-470.

96. Jones, M.L., et al., *Are Hot Charge Transfer States the Primary Cause of Efficient Free-Charge Generation in Polymer:Fullerene Organic Photovoltaic Devices? A Kinetic Monte Carlo study.* Phys. Chem. Chem. Phys., 2014. **16**(38): p. 20310-20320.

97. Groves, C., J.C. Blakesley, and N.C. Greenham, *Effect of Charge Trapping on Geminate Recombination and Polymer Solar Cell Performance.* Nano Lett., 2010. **10**(3): p. 1063-1069.

98. Credgington, D., et al., *Quantification of Geminate and Non-Geminate Recombination Losses Within a Solution-Processed Small-Molecule Bulk Heterojunction Solar Cell.* Adv. Mater., 2012. **24**(16): p. 2135-2141.

99. Lakhwani, G., A. Rao, and R.H. Friend, *Bimolecular Recombination in Organic Photovoltaics.* Annu. Rev. Phys. Chem., 2014. **65**: p. 557-581.

100. Göhler, C., A. Wagenpfahl, and C. Deibel, *Nongeminate Recombination in Organic Solar Cells.* Adv. Electron. Mater., 2018. **4**(10).

101. Huang, T.-Y., et al., *Efficient Ternary Bulk Heterojunction Solar Cells Based on Small Molecules Only.* J. Mater. Chem. A., 2015. **3**(19): p. 10512-10518.

102. Zhang, H., et al., *Effects of DIO on the Charge Recombination Behaviors of PTB7:PC71BM Photovoltaics.* Org. Electron., 2019. **67**: p. 50-56.

103. Hahn, T., et al., *Monomolecular and Bimolecular Recombination of Electron-Hole Pairs at the Interface of a Bilayer Organic Solar Cell.* Adv. Funct. Mater., 2017. **27**(1).

104. Groves, C. and N.C. Greenham, *Bimolecular Recombination in Polymer Electronic Devices.* Phys. Rev. B, 2008. **78**(15).

105. Cowan, S.R., et al., *Charge Formation, Recombination, and Sweep-Out Dynamics in Organic Solar Cells.* Adv. Funct. Mater., 2012. **22**(6): p. 1116-1128.

106. W. Graupner, G.L., G. Leising, and U. Scherf, *Shallow and Deep Traps in Conjugated Polymers of High Intrachain Order.* Phys. Rev. B, 1996. **54**.

107. Mandoc, M.M., et al., *Effect of Traps on the Performance of Bulk Heterojunction Organic Solar Cells.* Appl. Phys. Lett., 2007. **91**(26).

108. Mihailetchi, V., van Duren, J., Blom, P., Hummelen, J., Janssen, R., Kroon, J., Rispens, M., Verhees, W. and Wienk, M, *Electron Transport in a Methanofullerene.* Adv. Funct. Mater., 2003. **13**: p. 43-46.

109. Street, R.A., et al., *Interface State Recombination in Organic Solar Cells.* Phys. Rev. B, 2010. **81**.

110. Forrest, S.R., *The Path to Ubiquitous and Low-Cost Organic Electronic Appliances on Plastic.* Nature, 2004. **428**: p. 911-918.

111. Z. Zhu, D.M., M. Morana, M. Koppe, M. C. Scharber, D. Waller, G. Dennler, and C. J. Brabec, *Chapter 13: Design Rules for Efficient Organic Solar Cells*, in *High-Efficient Low-Cost Photovoltaics*, R.H. Vesselinka PEtrova-Koch, Adolf Goetzberger, Editor. 2009, Springer: Germany. p. 195-222.

112. Dang, M.T., et al., *Controlling the Morphology and Performance of Bulk Heterojunctions in Solar Cells. Lessons Learned From the Benchmark Poly(3-hexylthiophene):[6,6]-phenyl-C61-butyric Acid Methyl Ester System.* Chem. Rev., 2013. **113**(5): p. 3734-3765.

113. Weng, K., et al., *Optimized Active Layer Morphology Toward Efficient and Polymer Batch Insensitive Organic Solar Cells.* Nat. Commun., 2020. **11**(1): p. 2855.

114. Brinkmann, M., *Structure and Morphology Control in Thin Films of Regioregular Poly(3-hexylthiophene).* J. Polym. Sci. B Polym. Phys., 2011. **49**(17): p. 1218-1233.

115. Groves, C., L.J.A. Koster, and N.C. Greenham, *The Effect of Morphology Upon Mobility: Implications for Bulk Heterojunction Solar Cells with Nonuniform Blend Morphology.* J. Appl. Phys., 2009. **105**(9).

116. Xiaoniu Yang, J.L., Sjoerd C. Veenstra, Wiljan J. H. Verhees, Martijn M. Wienk, Jan M. Kroon, Matthias A. J. Michels, and René A. J. Janssen, *Nanoscale Morphology of High-Performance Polymer Solar Cells.* Nano Lett., 2005. **5**(4): p. 579-583.

117. Liao, H.C., et al., *Insights Into Solvent Vapor Annealing on the Performance of Bulk Heterojunction Solar Cells by a Quantitative Nanomorphology Study.* RSC Adv., 2014. **4**(12).

118. Ameri, T., et al., *Organic Ternary Solar Cells: A Review.* Adv. Mater., 2013. **25**(31): p. 4245-4266.

119. Lu, L., et al., *Status and Prospects for Ternary Organic Photovoltaics.* Nat. Photonics, 2015. **9**(8): p. 491-500.

120. Bi, P. and X. Hao, *Versatile Ternary Approach for Novel Organic Solar Cells: A Review.* Solar RRL, 2019. **3**(1).

121. Xie, Y., et al., *Morphology Control Enables Efficient Ternary Organic Solar Cells.* Adv. Mater., 2018. **30**(38): p. e1803045.

122. An, Q., et al., *Efficient Organic Ternary Solar Cells with the Third Component as Energy Acceptor.* Nano Energy, 2016. **26**: p. 180-191.

123. Liao, H.-C., et al., *Additives for Morphology Control in High-Efficiency Organic Solar Cells.* Mater. Today, 2013. **16**(9): p. 326-336.

124. Lou, S.J., et al., *Effects of Additives on the Morphology of Solution Phase Aggregates Formed by Active Layer Components of High-Efficiency Organic Solar Cells.* J. Am. Chem. Soc., 2011. **133**(51): p. 20661-20663.

125. Zhao, X., et al., *Impact of Alkyl Chain Length of 1,n-diiodoalkanes on PC71BM Distribution in Both Bulk and Air Surface of PTB7:PC71BM Film.* Org. Electron., 2016. **37**: p. 358-365.

126. He, Y. and Y. Li, *Fullerene Derivative Acceptors for High Performance Polymer Solar Cells.* Phys. Chem. Chem. Phys., 2011. **13**(6): p. 1970-1983.

127. Zhang, G., et al., *Nonfullerene Acceptor Molecules for Bulk Heterojunction Organic Solar Cells.* Chem. Rev., 2018. **118**(7): p. 3447-3507.

128. Shockley, W. and H.J. Queisser, *Detailed Balance Limit of Efficiency of p-n Junction Solar Cells.* J. Appl. Phys., 1961. **32**(3): p. 510-519.

129. Vos, A.d., *Detailed Balance Limit of the Efficiency of Tandem Solar Cells.* J. Phys. D: Appl. Phys., 1980. **13**: p. 839-846.

130. Li, N., et al., *Towards 15% Energy Conversion Efficiency: A Systematic Study of the Solution-Processed Organic Tandem Solar Cells Based on Commercially Available Materials.* Energy Environ. Sci., 2013. **6**(12).

131. Zhang, K., et al., *Toward Efficient Tandem Organic Solar Cells: From Materials to Device Engineering.* ACS Appl. Mater. Interfaces, 2020. **12**(36): p. 39937-39947.

132. Firdaus, Y., et al., *Efficient Double- and Triple-Junction Nonfullerene Organic Photovoltaics and Design Guidelines for Optimal Cell Performance.* ACS Energy Lett., 2020. **5**(12): p. 3692-3701.

CHAPTER 3

EXPERIMENTAL AND MODELLING METHODS

3.1 Introduction

The materials and fabrication processes used in this thesis are described in this Chapter. First, information about the architecture of OPVs, donor and acceptor materials are discussed followed by the fabrication processes of binary and ternary blend OPVs. Next, the characterisation of OPV devices is explained, including measurements techniques, and instrumentation with corresponding schematics. At the end of the Chapter, modelling and numerical procedures used in the optical and electrical simulations of Chapter 5, 6 and 7 are also provided.

3.2 Materials and device architecture

In this study, a standard device superstrate configuration was used for binary and ternary OPVs of Chapter 4, 5 and for electron-only devices of Chapter 6 respectively. In these type of architectures, the active layer is "sandwiched" between the cathode and anode, as it is depicted in Figure 3.1a for the binary devices. As stated in Chapter 2 of OPV fundamentals, one of the key requirements in the development of OPVs is that excitons fully dissociate into free holes and electrons which can be extracted through the external circuit [1]. Once these charges are separated, they can transport from molecule to molecule through a "hopping" process [2]. However, exciton dissociation and carrier extraction compete with recombination processes, so it is fundamental to identify these loss mechanisms [3, 4]. As such, materials and device engineering designed to reduce recombination and facilitate exciton dissociation and collection are essential to successful OPVs. How does one best optimise devices? in Chapter 4, we address this vital question by using two different processing methods that enable control over the morphology, a necessary foundation before adding a third component into the blend, which is investigated in Chapter 5. The use of a ternary blend system in Chapter 5, was proposed as a mean to reduce recombination and boost performance, whilst providing design insights/rules that are useful for the fabrication of efficient OPV. The third component that makes up a ternary blend was added to the binary solutions as exhibited in Figure

3.1b. In Chapter 6, the main objective was to investigate the electron transport properties in novel acceptor materials for the first time, since higher mobilities are fundamental to increase the efficiency. In Chapter 7 a tandem structure is examined with different thicknesses and illumination conditions in order to maximise the efficiency. At the end of this Chapter, modelling details are provided.
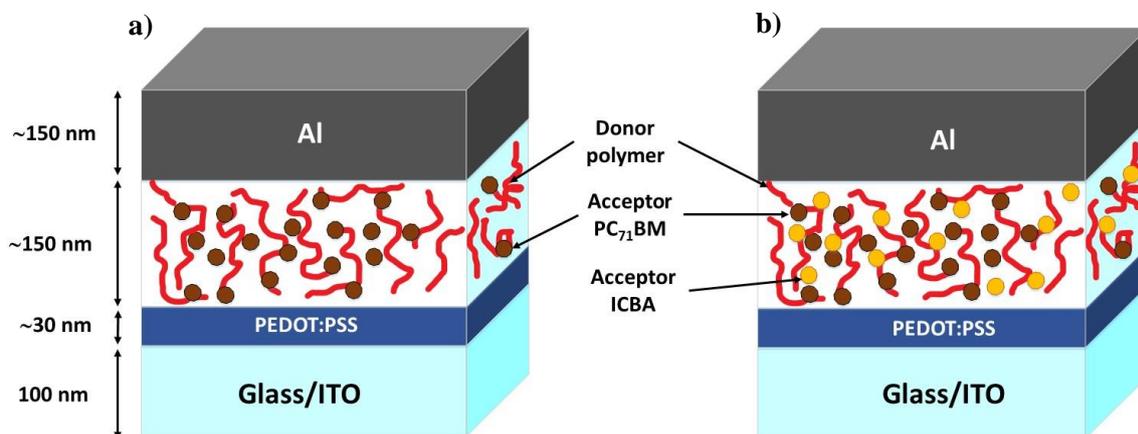
Figure 3.1. Device architecture of a) binary OPVs and b) ternary OPVs from this work. P3HT and PTB7 were used as polymer donors whereas $PC_{71}BM$ and ICBA were used as the acceptor materials in binary and ternary OPVs. In this device geometry, light enters from the glass/ITO side.

3.2.1 Active layers

To recap from the previous Chapter, the active layer is referred as the heart of the photovoltaic device. The advantage of being deposited by solution processing techniques holds promise for low-cost manufacturing as discussed before [5-8]. In this thesis, regio-regular poly (3-hexathiophine-2,5-diyl) (P3HT, from 1-material) and fullerene [6,6]-phenyl-C60-butyric-acid-methyl-ester (PCBM) (M111 C60 PCBM 911 g/mol from Ossila) were used to fabricate OPVs of Chapter 4. Further, P3HT, poly(4,8-bis[(2-ethylhexyl)-oxy]benzo[1,2-b:4,5-b0]dithiophene-2,6-diyl-alt-3-fluoro-2-[(2-ethylhexyl) carbonyl] thieno[3,4-b]thiophene-4,6-diyl)¬ (PTB7), [6,6]-phenyl-C71-butyric-acid-methyl-ester ($PC_{71}BM$) and 1′,1″,4′,4″-tetrahydro-di[1,4] methanonaphthaleno [1,2:2′,3′,56,60:2″,3″][5,6] fullerene-C60 (ICBA) (all purchased from 1-material) were used to produce the BHJ film of binary and ternary blends of Chapter 5. In Chapter 6, PCBM, non-fullerenes (NFA) NDI_2, *bis*-NDI, and hybrid fullerenes $NDI_{12}C_{60,}$ $Alk_{12}C_{60}$

(in-house synthesis) were used to produce the active layer of electron-only diodes. In the following sections, each material will be briefly explained.

3.2.2 Donor P3HT and PTB7 polymers

P3HT has been a central conjugated polymer in the field of OPVs and much of what is known about the fundamental working principles has been determined from P3HT-based blend systems [9, 10]. It is soluble in common organic solvents which offers the capability for low cost and solution processing of OPV devices [11-13]. P3HT has a tendency to crystallize, which is beneficial for morphology formation [10, 12, 14]. After thermal annealing, P3HT can reach hole and electron mobilities of 2×10^{-8} m^2 V^{-1} s^{-1} and 3×10^{-7} m^2 V^{-1} s^{-1} respectively [15]. Moreover, P3HT can harvest about ~22% of the photon energy because of its bandgap of ~1.9-2 eV (up to 650 nm) [16]. The molecular structure is presented on Figure 3.2a.

PTB7 is a promising novel low bandgap polymer which can absorb light with wavelengths over 650 nm [17, 18]. It was one of the first polymers to show a PCE over 7% when blended with $PC_{71}BM$ fullerene because it has a stronger absorption and suitable HOMO level [17, 19]. By thermal annealing, it has been demonstrated that polymer chains move into a more ordered arrangement which can have a favourable effect on the device properties [20]. OPVs based on PTB7:$PC_{71}BM$ can achieve a hole mobility of approximately 1×10^{-4} cm^2 V^{-1} s^{-1} and electron mobility of 1×10^{-5} cm^2 V^{-1} s^{-1} respectively [21]. Its bandgap is found around ~1.6 eV [19, 22], with an absorption ranging from 300-800 nm reaching its maximum between 700-800 nm. The chemical structure is depicted on Figure 3.2b.
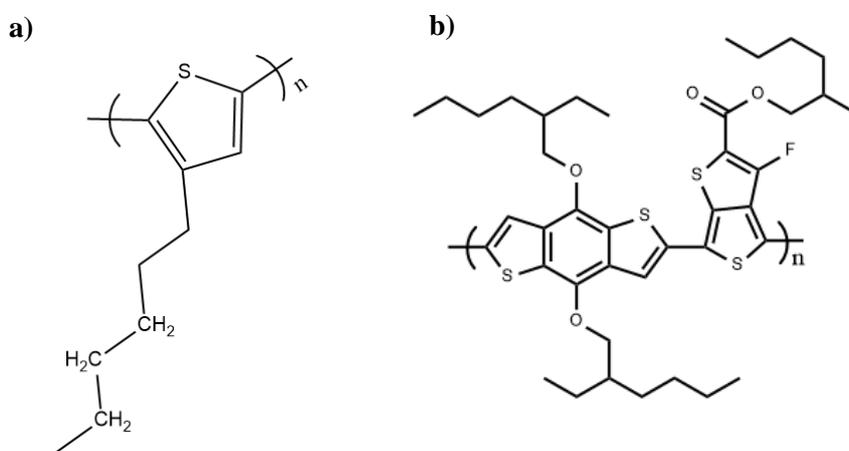
Figure 3.2. Chemical structure of a) P3HT and b) PTB7 semiconducting polymers.

3.2.3 Fullerenes PCBM, PC$_{71}$BM, ICBA and novel acceptor materials

The introduction of soluble PCBM to improve photoinduced electron transfer in photodiodes [23] represented a breakthrough in the progress of acceptor materials for OPVs and is still extensively used to date. PCBM has a good solubility with organic solvents, high electron mobility of 2 x 10^{-3} cm^2 V^{-1} s^{-1} and high electron affinity [24, 25]. However, it has a weak absorption in the visible region due to its high degree of symmetry and a low LUMO, that can result in a lower V$_{OC}$ [24]. PC$_{71}$BM on the other hand, has demonstrated higher performances over regular PCBM, which is in part attributed to a stronger visible absorption [24]. As such, PC$_{71}$BM can contribute to increase the photon harvesting and potentially increase photocurrent. This has led PC$_{71}$BM to be one of the most studied fullerenes in high efficiency blend systems [26]. PC$_{71}$BM is also soluble in most organic solvents and possess an electron mobility of 1 x 10^{-3} cm^2 V^{-1} s^{-1} [24, 27]. ICBA is another fullerene derivative with good solubility and is easier to synthesise than PCBM and PC$_{71}$BM [28]. Because of its 0.17 eV higher LUMO level than PCBM, when blended with P3HT it can increase V$_{OC}$ from .58 to .84 V, resulting in a PCE of 5.4% [28]. Figure 3.3 illustrates the chemical structures of fullerenes used in this study. In addition, an energy level diagram is included in Figure 3.4 depicting an OPV device from Chapter 4 with architecture: glass ITO/PEDOT:PSS:P3HT:PCBM/Al. From the image, P3HT is the donor (with higher energy levels) and PCBM the acceptor (with lower energy levels) that if brought into contact, electronic interactions are possible.
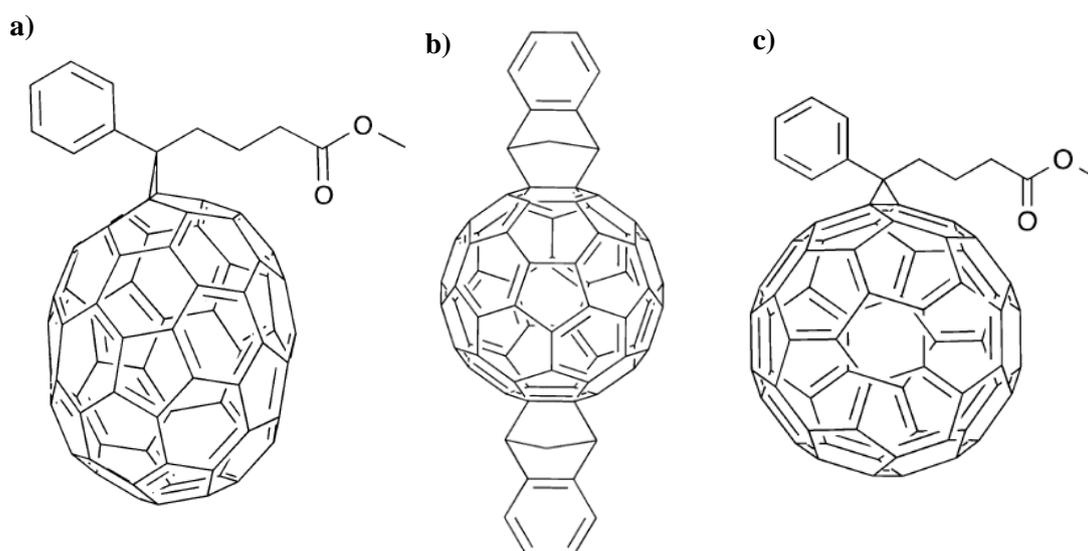
Figure 3.3. Fullerenes acceptors a) PC$_{71}$BM, b) ICBA and c) PCBM.
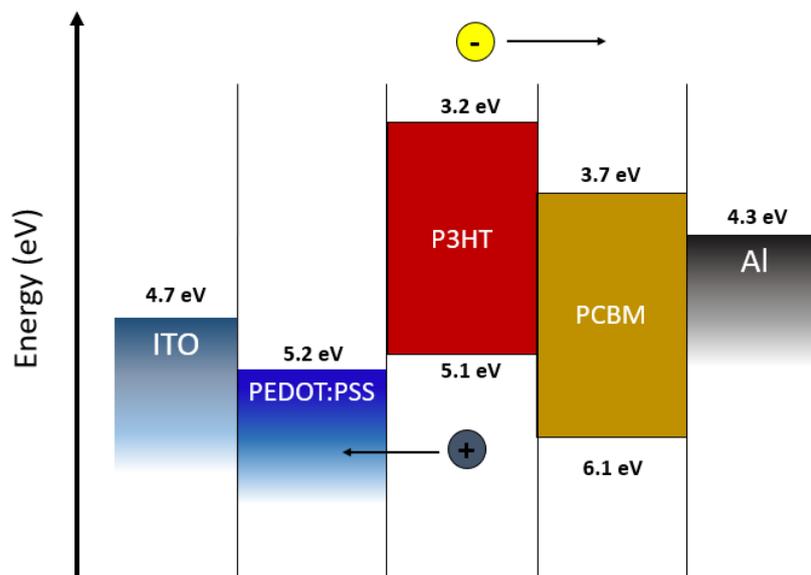
Figure 3.4. Energy band diagram of an OPV used in Chapter 4. Energy levels from: [25, 29, 30].

Developing novel acceptor materials is also a promising strategy to further optimise efficiency in OPVs. NFA and hybrid fullerene acceptors: NDI_2, *bis*-NDI, $NDI_{12}C_{60}$, and $Alk_{12}C_{60}$ used in this thesis were synthesised by Dr. Avestro and her team in the Chemistry Department. Figure 3.5 presents such components. Briefly, all reagents and solvents to fabricate the molecules were purchased from commercial suppliers (Merck, Acros Organics, Alfa Aesar, Fischer Scientific, Tokyo Chemical Industry or Fluorochem) and used without further purification unless stated otherwise.
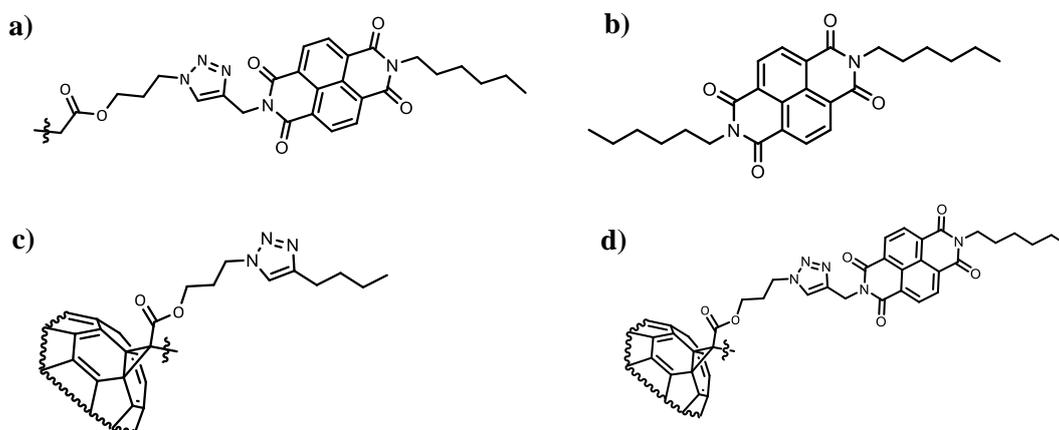
Figure 3.5. Compact representation of NFA and hybrid fullerene acceptors used in Chapter 6. a) NDI_2, b) *bis*-NDI, c) $Alk_{12}C_{60}$ and d) $NDI_{12}C_{60}$. Full structure shown in Chapter 6.

3.2.4 Hole-injection buffer layer (PEDOT:PSS)

Poly (3, 4-ethylene dioxythiophene): poly (4-styrene sulfonate) (PEDOT:PSS) (CLEVIOS P VP AI 4083 from Heraeus) was used to coat the ITO anode surface on all substrates in this thesis. PEDOT:PSS is highly transparent when spin coated into a film and serves to planarise and improve hole injection between ITO and the active layer [31-33]. Because of its high work function (~5.0-5.2 eV) it makes it compatible with ITO and provides a better match to the HOMO orbitals of the donor materials used in this study allowing efficient hole injection [31, 32]. Thusly, PEDOT:PSS represents a suitable choice compared to just ITO or other p-doped organic layers [34-36]. PEDOT:PSS is solution processed and offers mechanical flexibility and stability if used on flexible substrates during OPV fabrication, which makes it attractive from a manufacture point of view [31]. As such, PEDOT:PSS is a popular hole injecting layer in the field of OPVs. The chemical structure of PEDOT:PSS is shown in Figure 3.6.
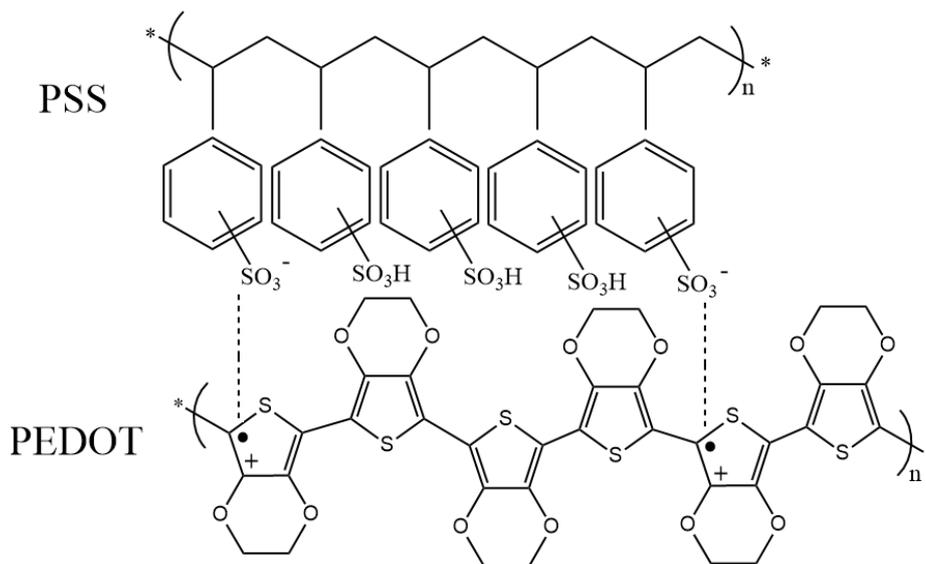
Figure 3.6. Chemical structure of PEDOT:PSS [31].

3.3 Electrodes

3.3.1 Indium Tin Oxide (ITO) anode

Two electrodes are used on OPV device fabrication irrespective of the architecture, the hole collecting anode (high work function) and the electron collecting cathode (low work function) to efficiently collect charges [16]. The electrode materials

are chosen to match their work functions with the donor HOMO and acceptor LUMO for hole and electron transfer respectively. In this study, a glass substrate coated with Indium Tin Oxide (ITO) (VisionTek systems LTD with a resistance sheet film of 10 Ω/sq) was used as the anode material in the device fabrication from Chapter 4, 5 and 6. ITO is normally used as the anode material with the buffer layer PEDOT:PSS because it is a transparent and electrically conducting material that offers ease of patterning (i.e. by etching) [33, 37]. It has a high work function of 4.7 eV, which allows holes to be injected to most donor polymers [30, 33]. It holds a high optical transparency of ~90% [37, 38] and electrical conductivity around $\sigma = 20$ Ω/sq [39].

3.3.2 Aluminium (Al) and Lithium/Fluoride aluminium (LiF/Al) cathode

Contrasting anode materials, the cathode contact is usually not transparent providing a broader range of material choices. Some of the requirements for the cathode contact are high conductivity, low work function and good adhesion to the active layer [13]. Here, Aluminium (Al) and Lithium Fluoride with Aluminium (LiF/Al) (purchased from Thermo Fisher Scientific and Sigma-Aldrich respectively) were used as the negative contacts in Chapter 4, 5 (Al) and 6 (LiF/Al) correspondingly. Aluminium has a lower work function of 4.3 eV [29] and is thermally evaporated on top of the active layer to form the negative electrode. One of the challenges with cathode layers is that they can chemically react with the adjacent organic layers [40]. A two-layer cathode such as LiF/Al is an approach widely used, where the LiF preserves the low work function of the cathode and protects the active layer from hot Al atoms during the evaporation [40]. Work function of LiF/Al is found to be around $3.6 - 3.8$ eV [13].

3.4. Deposition methods

Once solutions are prepared, PEDOT:PSS and active layers can be spin casted onto the ITO/glass substrate. In this work, spin coating was used to deposit PEDOT:PSS and the active layers whilst thermal evaporation was used for the deposition of the metal contact onto the organic layer. In the following section both deposition methods will be discussed.

(a) Spin coating

Spin coating is a technique widely used in university and research laboratories which can provide a highly uniform film to a planar substrate with a good control over film thickness reproducibility [41]. This technique is particularly attractive for research on the area of OPVs, since most layers are solution-processed and vacuum free. There are other methods, for example, knife coating [16], slot die [16], dip coating [41], spray coating etc., but the present study only focuses on spin coating. However, laboratory batch to batch processing may lead to slight variations in thin film thicknesses, that represents a downside when it comes to large-scale fabrication [16]. The steps involved with this technique are as follows: 1) placing of a substrate horizontally on top of a rotating chuck, 2) spreading a solution onto the substrate 3) accelerating the chuck to spread solution, 4) ejection and evaporation of the solvent leaving behind a thin-solid film. These steps (Figure 3.7) are of paramount importance, since the solvent evaporates during the spinning of the substrate which influences the morphology formation and thus the overall performance of devices [41]. Here, two spin coaters were used, one for the PEDOT:PSS layer (WS-650 B Laurell technologies corporation) at room temperature and the other one for the active layers (homemade system), which is a spin coater placed inside a N_2 ambient glovebox.
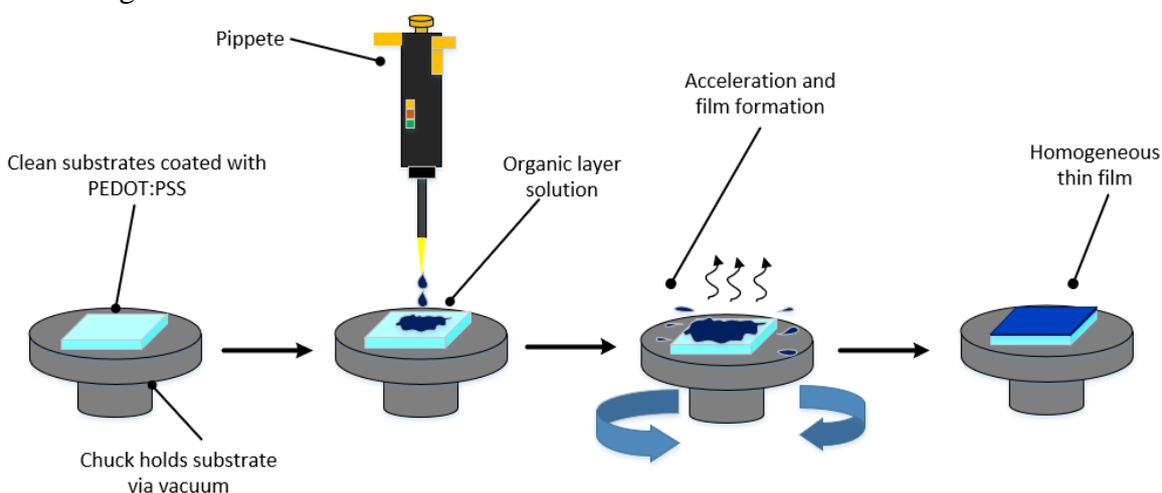
Figure 3.7. Schematic with the basic spin coating steps for the fabrication of devices.

(b) Thermal evaporation

The cathode contacts of the OPV devices fabricated in this study were vapour-deposited onto the solution processed active layers. Inside the evaporator and in high vacuum conditions ($<3\times10^{-6}$ mbar) the source material to be evaporated (Al or LiF/Al) is

placed over a tungsten filament melted by a current, which reaches the boiling point of the metal. The vapour travels upwards and condenses on top of the active layer surfaces. To decrease the possibility of collisions between particles and other molecules, the high vacuum increases the free path distance of the evaporating material. To determine the size of the active areas, a shadow mask was used. In this thesis, two Edwards 306 thermal evaporators were used, both of them inside N_2 glovebox: one for OPV devices of Chapter 4, 5 and the other for the electron-only devices of Chapter 6. Figure 3.8a presents an illustration of a thermal evaporator and main components and Figure 3.8b shows the shadow mask where samples are placed before putting them inside the evaporator. Section 3.6.5 and 3.6.6 include details about the thickness measurements.
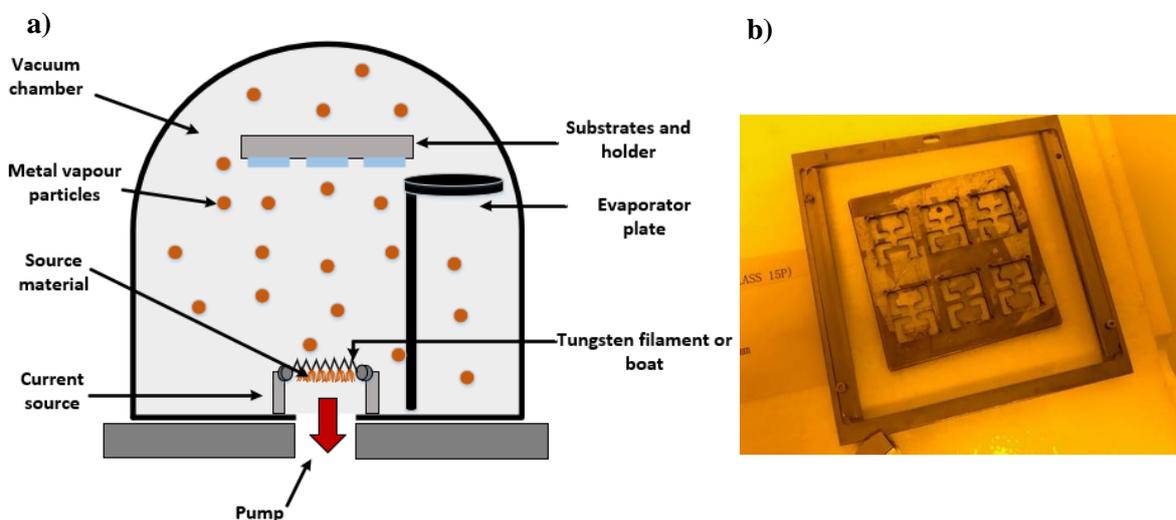
Figure 3.8. a) Basic thermal evaporator system. b) Shadow mask holder used for contact evaporation.

3.5 Fabrication process of OPVs

The fabrication of devices used in Chapter 4, 5 and 6 consisted of different steps which will be described in the following subsections. Each part exhibits pictures and details of the procedures involved. The following processes were conducted in a clean room laboratory at room temperature and ambient air unless otherwise specified.

3.5.1 Substrate preparation

Substrates were cut to dimensions of 19.5 mm x 16.5 mm a piece from a glass/ITO sheet (Figure 3.9a). The ITO conductive parts were patterned by masking a 6 mm strip on the centre of each substrate with Lacomit Varnish (G371, Agar Scientific Ltd) as shown in Figure 3.9b, allowing 30 min to dry. Alternatively, acid resistant tape can be used instead of the varnish, omitting the waiting time.

a) b)
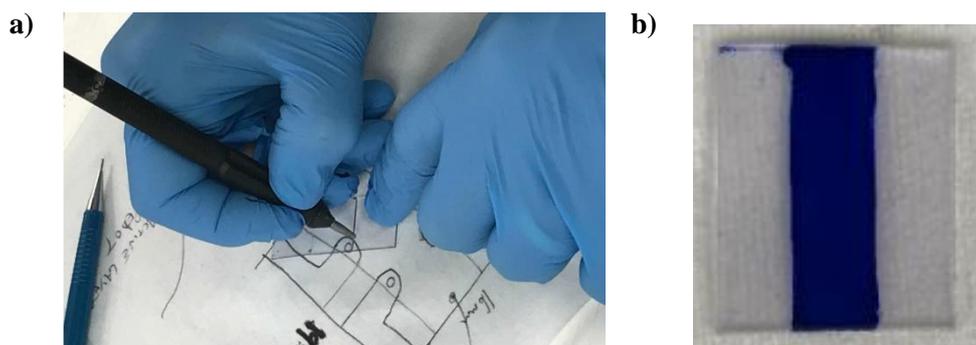
Figure 3.9. a) Cut of glass/ITO sheet to specified dimensions and b) substrate with patterned centre.

Following, an aqueous paste made by mixing deionized water (D.I. water) and Zinc powder (Sigma Aldrich) was prepared to paint with a brush the areas not covered by the varnish/tape, as indicated in Figure 3.10a. Then, substrates were immersed in Hydrochloric acid S.G. 1.18 (37%) (Fisher) for 3 seconds and subsequently in D.I water to clean (Figure 3.10b).

a) b)
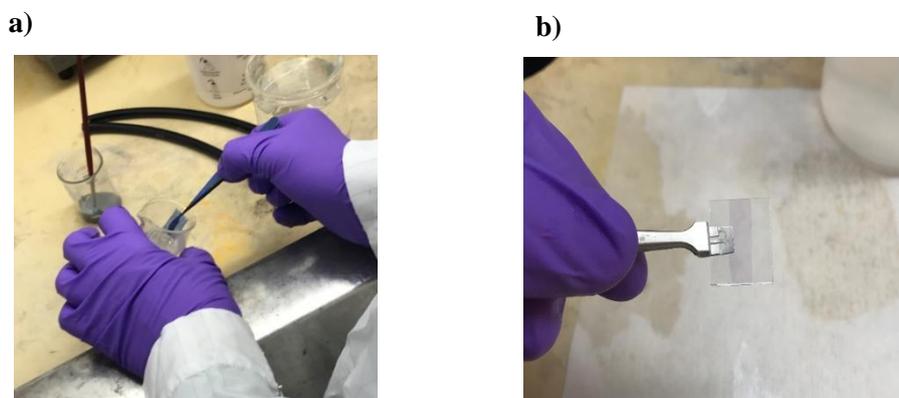
Figure 3.10. a) Zinc paste added to the areas not patterned then immersed in hydrochloric acid for 3 seconds. b) Removal of acid etching remnants.

Substrates were then sonicated in Propanol-2-ol, acetone, Decon 90 solution (2% aqueous) and D.I water for 15 minutes each (Figure 3.11). Decon 90 and all solvents were bought from Fisher.

Figure 3.11. Ultrasonic and sonication process used for all device fabrication in this study.

Finally, substrates were blown dry with N_2 gas. Cleaned substrates were treated by UV-oxygen plasma (Yield engineering systems Inc., YESR3, with radio frequency of 100 W) for 10 minutes, as shown in Figure 3.12. UV-oxygen irradiation produces ozone, which is an effective oxidizing agent to remove organic remnants from the ITO/substrate surface [42].

Figure 3.12. UV-oxygen plasma etcher used in this work.

3.5.2 Preparation and spin coating of the PEDOT:PSS layer

After substrate preparation, PEDOT:PSS was filtered through syringe filter (0.45 um pore size PFTE, Ossila) in a previously cleaned vial. Next, substrates were placed on

a chuck of a spin coater with 30 Psi vacuum to hold in place. A total of 200 µl of PEDOT:PSS solution was deposited on top of the conductive part of the substrate with a transfer electronic pippete (BrandTech 705323) before spin coating at 2500 rpm for 45 seconds to produce a thin homogeneous film of approximately ~30 nm. Thereafter substrates were thermally annealed at 140 °C for 10 min to remove any H_2O remnants.

3.5.3 BHJ blend solutions

(a) Binary and ternary BHJ solution preparation

Inside a nitrogen ambient glovebox, 30 mg per ml of P3HT, PTB7, PCBM, $PC_{71}BM$ and ICBA respectively were dissolved in 1 ml each of Chlorobenzene (PTB7, $PC_{71}BM$ and ICBA) and 1,2-dichlorobenzene (P3HT, $PC_{71}BM$, PCBM and ICBA) all chlorinated solvents from Sigma-Aldrich, and were left to stir for 30 min. To produce the binary and ternary solutions of Chapter 5, ICBA in concentrations from 0 to 30 wt.% was added into $P3HT:PC_{71}BM$ and $PTB7:PC_{71}BM$ blended solutions respectively, and were left to stir overnight inside nitrogen glovebox. Solvent additive 1,8-diiodooctane (Sigma-Aldrich) at 3% (1 ml, 97:3) was added to the solutions one hour prior to spin coating. OPVs from Chapter 4 were prepared the same as stated above, omitting the ICBA and DIO addition. Following, binary and ternary BHJ active layers were fabricated with a 1:1.5 donor and fullerenes acceptor ratios for PTB7-OPVs (Chapter 5) and 1:1 for P3HT-OPVs (Chapter 4 and 5) since these have been observed to be optimised optimum ratios for each type of blend, including the choice of solvents aforementioned [19, 43-45]. For preliminary results of Chapter 4, thermal annealing was conducted in P3HT:PCBM OPVs from 0 min to 20 min. For the solvent vapour annealing process, small amounts of DCB were added into a petri dish which contained the substrate and thin films of P3HT:PCBM to keep the active layer wet (inside N_2 glovebox) from 0 min to 60 min.

(b) Novel electron acceptors solution preparation

Solutions of PCBM and $NDI_{12}C_{60}$ were prepared with a combination of Chloroform (CHCl3) and o-DCB (90:10 ratio, dissolved in 600 µl) containing 18 mg and 10 mg to produce thick (~200 nm) and thin (~100 nm) films respectively. *bis*-NDI and $Alk_{12}C_{60}$ were prepared only with CHC13 containing 18 mg and 10 mg to produce thick (~200 nm) and thin (~100 nm) films respectively. NDI_2 was prepared with CHC13 using

18 mg dissolved in 1200 µl. $NDI_{12}C_{60}$, *bis*-NDI, $Alk_{12}C_{60}$ and NDI_2 solutions were heated in a hot plate at 50 °C while stirring for 4 hours before film deposition.

3.5.4 Active layer deposition of all devices

Under N_2 ambient inside the glovebox, a total of 150 µl of the active layer was spin coated at 1000 rpm for 60 seconds onto the PEDOT:PSS layer to achieve a uniform film for the binary and ternary OPVs described in Chapter 4 and 5. To accomplish desired thicknesses in electron-only diodes of Chapter 6, a 100 µl of active layer was spin coated at 1000 rpm for 60 seconds on top of the PEDOT:PSS buffer layer. For *bis*-NDI, 2000 rpm for 60 seconds were used (both for 18 mg and 10 mg) and for NDI_2, 1000 rpm for thin devices and 500 rpm for thick devices.

3.5.5 Al and LiF/Al cathode evaporation

Following film deposition, a ~150 nm layer of Al was thermally evaporated through a shadow mask to form an active area of .78 mm^2 (in high vacuum $<3x10^{-6}$ mbar) for binary and ternary composites of Chapter 4 and 5. All completed devices (Figure 3.13) received a thermal annealing of 120 °C for 10 minutes on a hot plate inside glovebox. A total of 8 nominally same repeats were fabricated for each type of blend of Chapter 4, i.e. 48 for thermal annealing, 48 for solvent vapour annealing totalling 96 OPVs. More details discussed in the next Chapter. Likewise, 8 nominally repeats were fabricated for ternary blends reported on Chapter 5 yielding 96 devices; 48 for each ternary blend system. Similar treatment was used for electron-only devices, however, a ~1 nm layer of LiF and ~100 nm of Al was thermally evaporated through a shadow mask to achieve an active area of 3.53 mm^2 to produce the cathode. A total of 20 nominally repeats were fabricated for each of the materials of Chapter 6, yielding 100 electron-only diodes.
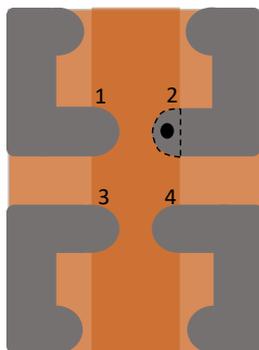
Figure 3.13. Example of a completed OPV consisting of 4 devices (dashed line). The dark circle represents the active area with light and the dashed line the active area under no light.

3.6. Device characterisation

3.6.1 Current voltage characteristics (J-V)

A fundamental OPV characterisation technique for any solar cell device is the current density-voltage (J-V) measurement. PCE, J_{SC}, FF and V_{OC} can be determined under illumination which shows how well a PV device achieves its purpose. Dark J-V measurements are also common because they reveal information about the diode quality and recombination losses of the device. Further, because an important part of OPV characterisation is the reproducibility of data, throughout this thesis only the values of typical devices are reported. The reason for this is to represent the ordinary or average trends obtained from a set of experiments rather than the top devices, giving confidence that our results are accurate and reproducible.

a) J-V under illumination

In this work, J-V measurements were carried out under 1000 W/m^2 illumination conditions using an Oriel Sol1A 94021A solar simulator with a mask to restrict the illumination area to .78 mm^2. A certified reference solar cell was used to calibrate at the abovementioned intensity. Figure 3.14a exhibits the set up for J-V measurements used in this study. An OPV device was appropriately placed inside a test chamber (Figure 3.14b) which has spring pins in contact with the cathodes and the common ITO anode. The test chamber has 4 holes of 1 mm diameter each that define the area that is subjected to light, as observed in Figure 3.14c. The device was illuminated by a Xenon lamp with filters so that the spectrum of light shining on the device simulate AM 1.5G sunlight. With these standardised parameters, the PCE of a device can be calculated. The test camber was connected to the test instruments (Keithley source meter 2400 and Lab View PC program) by two wires, one to the spring pin in contact with ITO and the other to a spring pin in contact with the metal cathode. The source meter applies a DC voltage sweep from -1.0 V to 1.0 V with step size of 200 mV between the front and back electrodes and measures the current. At this point, photo generated current measurements were produced and saved. An example of a J-V curve under illumination is presented in Figure 3.15.

Usually one is more interested in the current density voltage than just the current voltage. In order to calculate the current density "J", the absolute current "I" is divided by the active area of the OPV "A" impinged by light as follows [46]:

$$J = \frac{I}{A} \qquad\qquad (3.1)$$
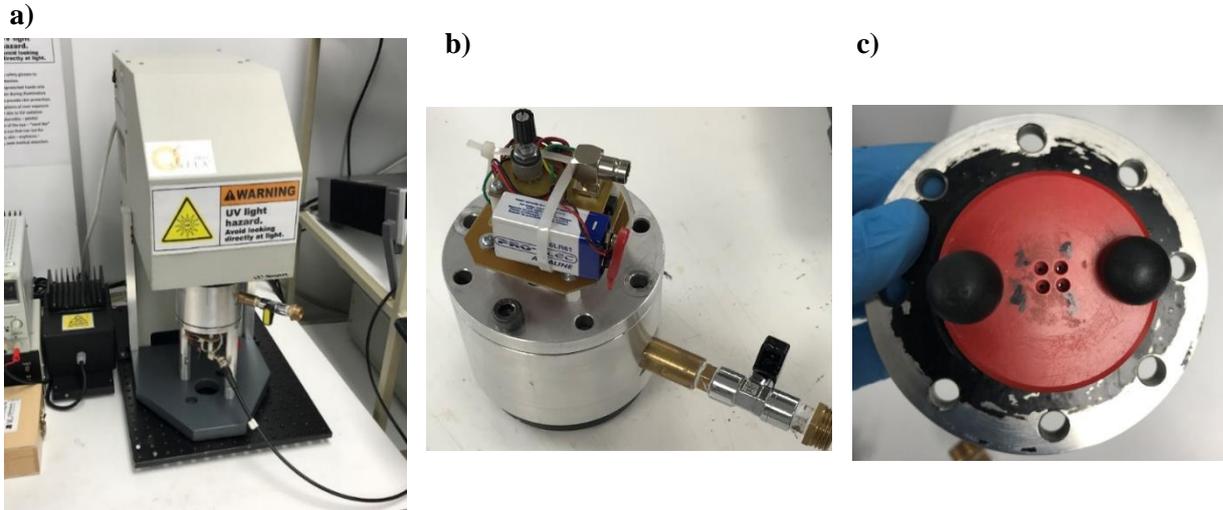
Figure 3.14. a) Solar simulator set up, b) test chamber and c) 4 holes of 1 mm of diameter where light enters the test chamber.
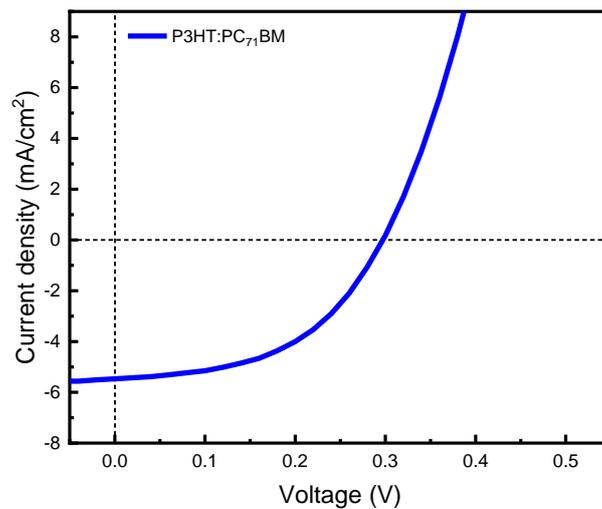
Figure 3.15. Example of a light J-V curve corresponding to a P3HT:PC$_{71}$BM based OPV.

b) J-V dark measurements

Keithley 2400 source was used to perform J-V dark measurements to assess the diode quality of the OPV device. For these dark J-V measurements, the active area is given by the overlap of the bottom and top electrodes [46]. Figure 3.16 depicts an example of a dark J-V response in a semi-logarithmic scale. A number of insights regarding shunt resistance (R_{SH}), series resistance (R_S) and recombination losses which arise from the

BHJ in the device can be assessed in these types of measurements. Briefly, the R_S is related to internal resistance of the device to current flow (from the active layer or electrodes), whereas the R_{SH} is attributed to leakage current throughout the device by pinholes that allow "parasitic" current to move directly between electrodes [47]. Three distinct regions (Figure 3.16) are normally found in a dark J-V. In the first region (low voltages), J-V characteristics are linear and mainly attributed to the R_{SH}, which limits the current. The second region (intermediate voltages) current increases exponentially and is controlled by the diode quality of the device. In the third region (higher voltages) J-V is also linear and the current limited by series resistances [47, 48]. In addition, the dark J-V reverse current (negative voltage) shows the amount of leakage current that may arise at the organic-metallic interface and its impact on V_{OC} [49].
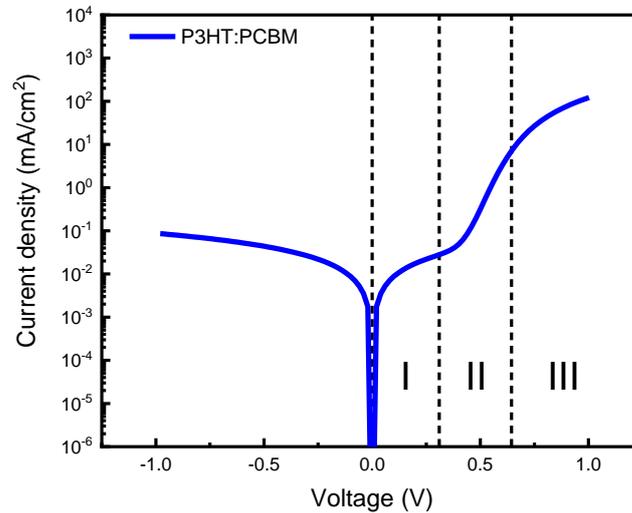
Figure 3.16. Semi-log dark J-V curve of P3HT:PCBM blend indicating the three regions (positive voltages) and reverse current.

3.6.2 External Quantum Efficiency (EQE)

EQE measurements reveal the quantum efficiency conversion of incident photons to electrons by a PV device, and which parts of the spectrum contribute to more photocurrent which is an important aspect to analyse when optimising OPVs [46]. In this work, the EQE spectra was measured on Oriel cornerstone 130 monochromator with a Xenon arc lamp. An important step before executing any measurements is the calibration, carried out with a silicon photodiode used as a reference cell. First, the photodiode is loaded onto the test chamber, which is placed in the EQE set up (Figure 3.17a), followed

by connecting two wires to the test chamber: one to the spring pin corresponding to the desired device to be calibrated and the other to the common. Then, a shadow mask is placed on the test chamber to allow illumination in just one of the four device's 'windows' (shown in Figure 3.14c) corresponding to the device receiving the calibration. Following, the program is run on "calibration mode" and the files are saved for reference. This last step is repeated just changing the shadow mask position until all four devices are calibrated. Now, to measure the EQE, the photodiode and shadow mask are removed from the test chamber and an actual OPV sample is loaded. Then, device 1 is selected by connecting the corresponding wires to the test chamber and the program is run under "test mode". After the first device is fully measured, a message on the test equipment will ask to select device 2 and so on, until the 4 devices are fully tested.

When measuring under calibration or test mode, the current is measured with the source meter for each wavelength position of the monochromator, and the device kept at short circuit conditions [46]. A Keithley source meter 2400 and MATLAB PC program were used to test the EQE spectra of binary and ternary composites of Chapter 4 and 5 (Figure 3.17b). To determine the EQE, the following equation is used [46]:

$$EQE = \frac{Number\ of\ photogenerated\ electrons}{Number\ incident\ photons} \qquad (3.2)$$

Normally, 10 nm steps were used ranging from 300 nm to 900 nm to test the OPVs in this thesis. Measurements were performed in a cleanroom under normal ambient temperature.
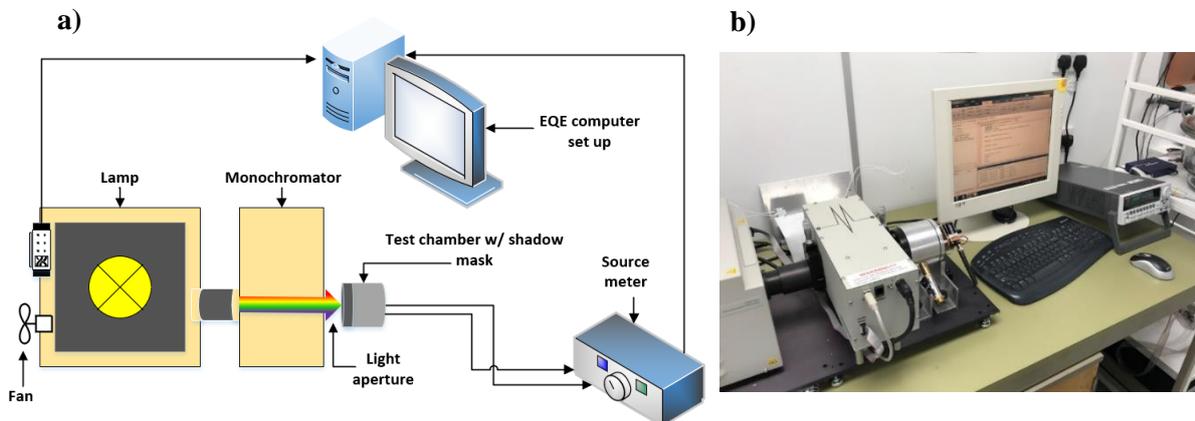
Figure 3.17. a) Basic schematic of the whole EQE experimental set up; b) Picture showing the test chamber, source meter and computer.

3.6.3 Space Charge Limited Current for hole and electron mobility measurements

Space charge limited current (SCLC) method is a commonly used technique to determine mobilities in OPVs [50, 51]. Unlike other methods such as Time of Flight (TOF) that requires thick devices or Current Extraction during Linear Increasing Voltage (CELIV) that utilises laser pulses, the main motives to choose SCLC is that the testing procedure is the same as a dark J-V, and the architecture of the devices that will be measured is equal to an OPV (including thickness), except that contacts are chosen to give injection of only one carrier type [51]. This means that only one type of carrier can be present and the other is neglected by a large injection barrier [52]. In this thesis, mobility measurements were carried out by measuring the dark J-V of devices with the ohmic contacts designed to be for electron or holes. Hole-only devices were fabricated to measure the hole mobility (μ_h) in binary and ternary blends of Chapter 5. Because of its high work function, gold (Au) was used to replace the aluminium metal contact. By replacing Au as the metal electrode, electron injection into the LUMO of $PC_{71}BM$ is essentially suppressed. Because P3HT HOMO is close to 5.1 eV [29], whilst for PEDOT:PSS is ~5.2 eV [31] and Au ~5.1 eV [53] respectively, the current measured is hole dominated. PEDOT:PSS forms an ohmic contact for hole injection and the mismatch between the LUMOs of Au and $PC_{71}BM$ strongly suppresses the injection of electrons into the fullerene. By fitting the Mott-Gurney equation with the thickness of the device (more details shown in Chapter 5 and 6), μ_h was calculated from the experimental dark J-V. Figure 3.18 presents an example of the energy diagram and injection of holes in the device.
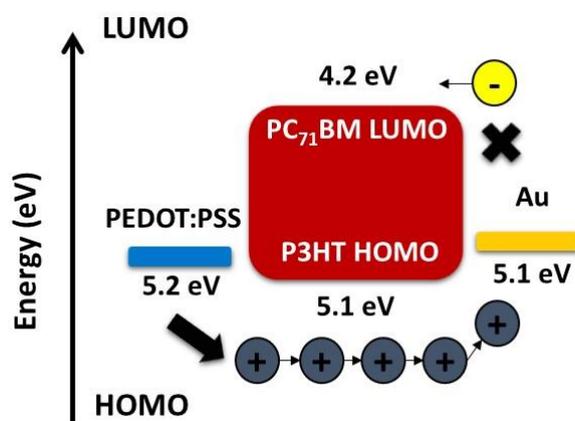
Figure 3.18. Example of an energy band diagram of hole-only devices based on binary and ternary P3HT OPVs under flat band conditions.

In addition, to probe the electron mobility (μ_e) in novel and hybrid acceptors of Chapter 6, electron-only devices were fabricated. From experimental dark J-V data, μ_e was calculated from the Mott-Gurney equation (shown in Chapter 6) and the results were fitted to the space charge limited current form [51]. For the fabrication of electron only devices, LiF was used with Al as the metal contact cathode. Because of the work functions, LiF is expected to form an Ohmic contact for electron injection on PCBM. PEDOT:PSS work function (5.2 eV) does not match the HOMO of PCBM (6.1 eV) so hole injection from PEDOT to PCBM was neglected, thus only electrons flow to PCBM in forward bias conditions [25] as observed in Figure 3.19. Complete details in Chapter 6.

.
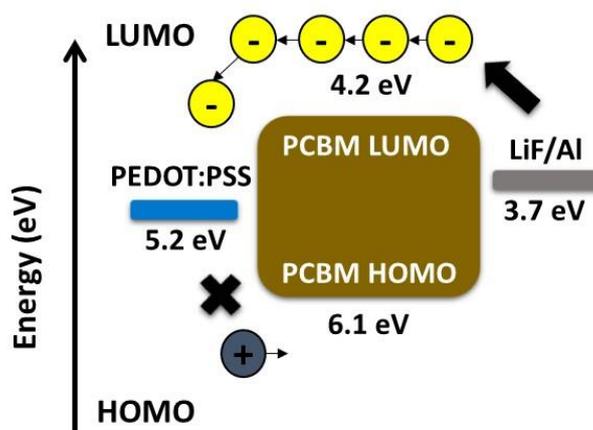
Figure 3.19. Energy band diagram of electron-only diodes under flat band conditions.

3.6.4 Ultraviolet-visible spectroscopy

The absorption of photons is one of the most important characteristics of PV materials. From a device engineering perspective, it is paramount that OPV materials are designed to absorb photons ideally in the UV, visible and near IR regions from the solar spectrum in accordance with the AM 1.5 spectrum. An important analysis technique is Ultraviolet-visible absorption spectroscopy (UV-vis), which probes the absorption of light in a sample [46]. In this work, absorption data was obtained with UV-1800 Shimadzu UV spectrophotometer, ranging from 190 to 1100 nm. Two lamps were used as the excitation source in this set up, an iodine (tungsten) lamp that emits mostly in the visible and a deuterium lamp for UV excitation. Figure 3.20 provides a basic schematic of the spectrophotometer and its components. When light passes through the OPV sample,

the difference between the incident (I_0) and transmitted light radiation (I) can be defined as transmittance or absorbance [54]:

$$T = {}^{I}/_{I_0} \ or \ \%T = \left({}^{I}/_{I_0}\right) x \ 100 \qquad \textbf{(3.3)}$$

Absorbance is measured by the UV-vis probe as the logarithmic ratio between incident and transmitted light radiation, as expressed by the Beer's law as follows [54]:

$$A = -log \ T \qquad \textbf{(3.4)}$$

Sufficient UV and visible light energy in regions of electronic transitions (HOMO-LUMO) cause an electron to move from a lower state to an excited state and the wavelength where this absorption occurs is recorded by the UV spectrophotometer [54]. Inside the measuring instrument, a diffraction grating splits light into different wavelengths. The photons that are transmitted through the film are measured by a detector. Before making the measurements, an important step is the calibration. To do this, a baseline is run without samples, which means that the spectrophotometer scans all the specified wavelengths (e.g. 190 nm – 1100 nm). This blank baseline is a necessary step carried out with the objective to cancel out any noise effect. Following, a clean substrate coated with PEDOT:PSS is placed on the first holder to use as the reference as depicted in the figure below. Next, a baseline correction is run in order to properly measure I_0 thus completing the calibration. To run the actual UV-vis test, a substrate coated with PEDOT:PSS is placed on the first holder to use as the reference and an additional substrate with PEDOT:PSS plus the active layer are placed in the second holder and the program is run.
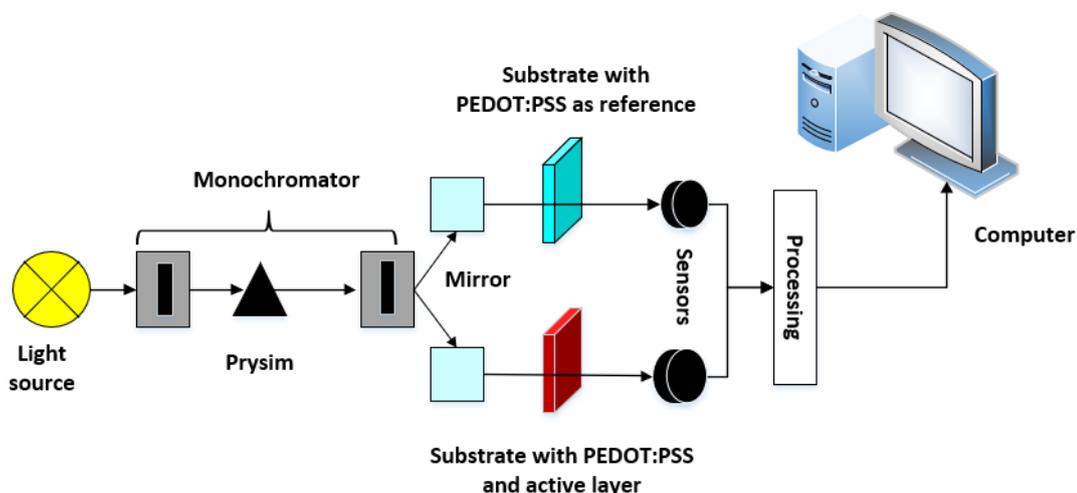
Figure 3.20. Basic schematic of UV-Vis spectrophotometer used in this study.

The resulting spectra is in arbitrary units since interference effects do not allow complete quantitative measurements. However, the shape of absorption profiles and peak positions can be investigated with this optical method, which provides important insights into the suitability of materials for OPV and optoelectronic applications [46].

3.6.5 Atomic Force Microscopy (AFM)

Atomic Force Microscopy (AFM) is a technique used to probe the topography of materials with high resolution and accuracy [55, 56]. In this work, a VEECO digital instruments AFM was used to examine the surface of OPVs and measurements were conducted by Dr. Chris Pearson accompanied by the author inside a laboratory cleanroom. Contrasting with other microscopy techniques, AFM does not form an image by focusing light or electrons onto the surface, rather it "feels" it with a sharp probe building a map of the height of the sample's topography [55]. Figure 3.21a, b exhibits a schematic with basic components and the AFM used in this study respectively. The basic principle of AFM is to scan the sample with a tip mounted to a cantilever spring. The force generated between the tip and the sample is measured by the deflection of the cantilever during the scanning. As the tip is scanning the sample, the deflected laser beam from the cantilever provides measurements of the difference in light intensities between the photodetectors (deflection vs position) and the image is obtained [57].

a)

b)
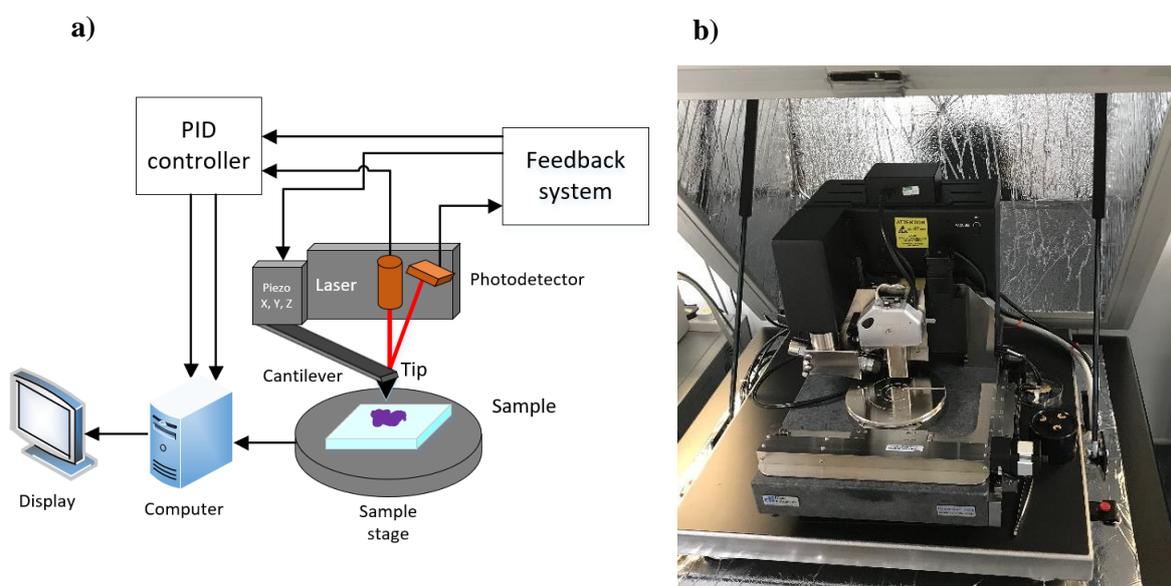
Figure 3.21. a) Basic components of a AFM microscopy, b) AFM used in this thesis.

There is a range of different AFM modes available such as: contact mode, non-contact mode, tapping mode, chemical force mode, conductive force mode, magnetic force mode, among others [58]. However, three main modes are typically used because of their capability for high resolution images, namely: non-contact mode, contact mode and tapping mode. Briefly, in non-contact mode the tip is not in contact with the surface but oscillating due to the interaction between probe and force field of the sample. As suggested by the name, in contact mode the tip is in constant contact with the sample's surface and deflection of the cantilever directly yields the topographic image. In tapping mode, because of the resonant frequency used with an amplitude of a few nm, the tip touches the surface moderately for a minimum amount of time [57, 58]. For this thesis, tapping mode was used to investigate the surface of OPVs.

a) Tapping mode

In this mode, the cantilever is oscillated by a piezoelectric element with a frequency close to its resonance leading to an excitation amplitude of typically (1-100 nm) [58]. The tip is moved towards the surface of the sample to lightly tap it to start scanning. Interactions between the surface and the tip (bumps and depressions) cause the amplitude of the cantilever oscillations to change, which are measured by the optical systems and controllers [57]. The piezoelectric element adjusts the separation between the sample and the tip to maintain a constant force on the surface. Finally, the surface's irregularities are expressed as a function of the tip's lateral position to generate the image of the sample [57]. Besides the topography scan, a phase-shift image can also be obtained with tapping mode. By moving the tip across regions of different composition on the surface the phase image is created. This is used to distinguish variations on the surface, such as adhesion, friction and viscoelasticity [58]. For this work, a typical scan size of 10 µm x 10 µm was used with a slow scan rate to obtain a high-quality topography image, root mean square (RMS), roughness (Rq) and the thicknesses of layers. The AFM model was a VEECO Microscope Dimension 3100 with Nano-scope 3A controller, VT103 acoustic enclosure and a spring constant of 0.2 Nm-1 from Budget sensors. In addition, Gwyddion software for scanning probe microscopy was used to visualise and analyse the data.

b) Active layer measurements

The surface topography of OPVs reported in Chapter 4 and Chapter 5 were measured by imaging the edge of a scratch in the active layer of a completed device. This cut was

done with a sharp tool (e.g. tweezers). Following this, the sample was placed on the sample stage of the AFM (Figure 3.21a, b) which is held with vacuum. To collect data, the sample was scanned at different locations, particularly where all the layers conforming the device could be clearly distinguished. The image is then flattened using AFM software. At this stage, the thickness of the PEDOT:PSS and active layer were acquired (separately). Figure 3.22 shows an example of a measurement of PEDOT:PSS in an OPV device, resulting in approximately a ~30 nm thick layer.
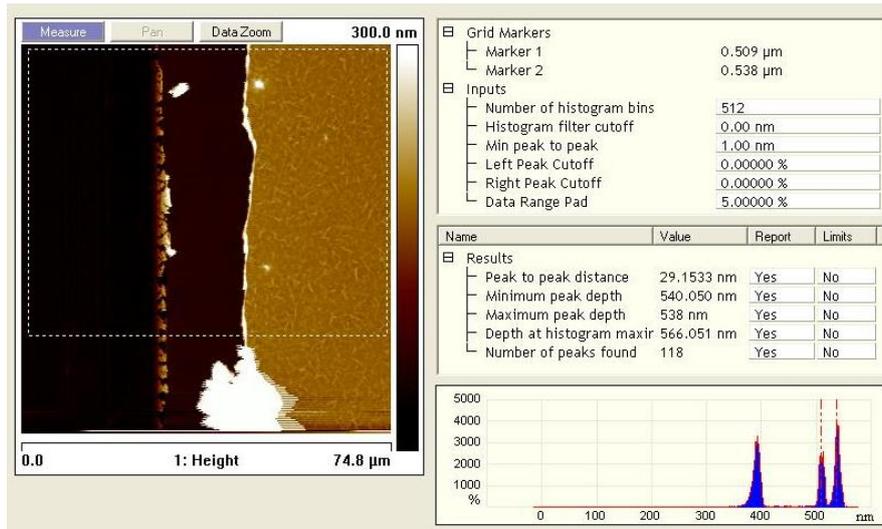
Figure 3.22. PEDOT:PSS layer thickness indicated by the "peak to peak distance" of ~30 nm.

3.6.6 Surface profilometer

For Chapter 6, electron-only diode thicknesses were measured with VEECO Dektak 3S high resolution surface profilometer, by Dr. Chris Pearson and Dr. Mike Cooke. The main objective of the profilometer is to measure the vertical profile of the samples, thickness and other topographical features [59]. The profilometer has a stylus which is used to measure the profile of the surface. First, the stylus is moved vertically into contact with the sample and then across the sample (laterally) for a specified distance. Usually the measurement ranges go from 100 Å to 650,000 Å for a 5" sample stage [59]. The complete diode was scratched to measure the corresponding layers. The electron-only diode measurements were carried out to obtain the thicknesses and not the topographical features, in order to characterise the electron transport properties with SCLC.

3.6.7 Transmission Electron Microscopy (TEM)

Understanding the relation between structural properties in OPV materials is considered of top importance to design new devices or improve present ones. On this note, Transmission Electron Microscopy (TEM) is a powerful technique that allows imaging of the bulk morphology in OPVs. For this work, TEM imaging was conducted in a collaborative work by Dr. Budhika Mendis and PhD fellow Faisal Alanazi. More details of the scans are included in Chapter 5 and its Appendixes. With TEM, high spatial resolution on crystallographic and chemical characterisation of materials can be obtained, reaching resolutions of 0.5 nm (i.e. the electron beam diameter) [60, 61]. A brief description of how TEM operates is that a beam of monochromatic electrons propagates through a sample held on a TEM grid (Figure 3.23) where patterns resulting from electron interactions are visualised on a screen [62, 63]. There are different TEM techniques such as: diffraction mode, bright-field mode, analytical mode, electron energy loss spectroscopy (EELS), energy filtered transmission electron microscopy (EFTEM) and others which help provide insights pertaining morphology, crystallinity and the structure of materials [62, 64, 65]. In this thesis, however, the main focus is on TEM bright field and diffraction measurements, which were used to study the bulk morphology of binary and ternary OPVs of Chapter 5. TEM measurements were carried out on a JEOL 2100F FEG with accelerating voltage of 200 kV.
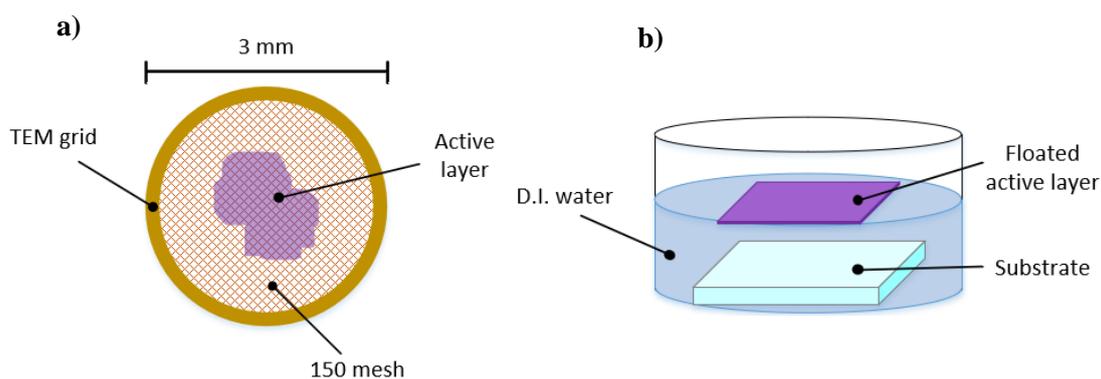
Figure 3.23. a) TEM grid mesh to deposit thin sample. b) Floating of active layer in D.I water.

Thin films for TEM measurements were fabricated with a combination of CB and o-DCB solutions of P3HT:$PC_{71}BM$ and PTB7:$PC_{71}BM$ with different concentrations of ICBA, with and without DIO. Films were prepared by first spin coating a thin layer of

PEDOT:PSS (~30 nm) onto a clean substrate followed by the active layer deposition. Then, samples were placed in D.I. water and the floated PEDOT:PSS/Active layer films (Figure 3.23b) were picked up with a mesh copper TEM grid. Figure 3.24 shows a picture of the actual TEM used in this work.
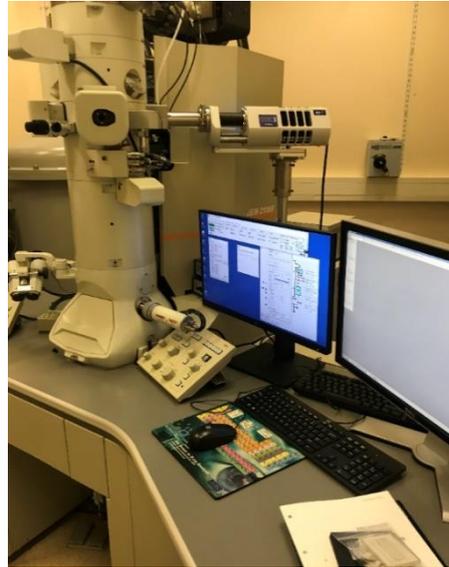
Figure 3.24. TEM used for bulk imaging of binary and ternary composites of Chapter 5.

3.7 OPV device modelling: GPVDM introduction

In this first section, a brief introduction to the General Purpose Photovoltaic Device Model (GPVDM) is given, followed by a more in-depth review in the subsequent sections: overview and model inputs.
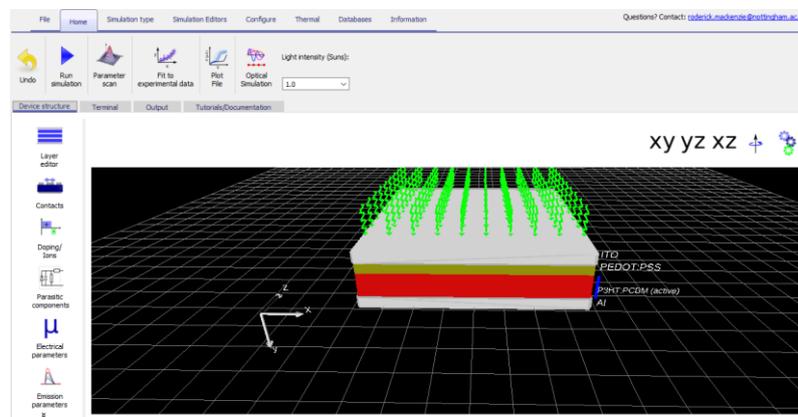
Figure 3.25. Main window and tabs available in GPVDM software.

GPVDM is a simulation tool for optoelectronic devices developed by Dr. Roderick Mackenzie, professor of Nottingham University, and it was used throughout the thesis, more specifically in results Chapters from 5 to 7 [66]. Thin films of OPVs, sensors, OFET, OLED, perovskite solar cells and many others can be simulated. GPVDM is available for use in both Windows and Linux operating systems. The main framework of the software is designed to be user friendly, with device parameters easy to access in the different tab windows and options offered (Figure 3.25).

3.7.1 Importance of PV modelling and GPVDM overview

This section contains a general outline on the importance of simulations, the different types of models to describe OPVs and briefly scrutinizes how the software runs before going into more technical detail regarding the electrical and optical inputs that govern drift diffusion simulations. Those are presented in the subsequent sections.

To start, the simulation of PVs has been widely used to design devices, predict, diagnose, and to interpret measurements by fitting experimental data [67, 68]. One of the benefits of using simulations is that they can provide valuable insights when analysing PVs that would otherwise be difficult to obtain. To name a few, simulations are useful to estimate the maximum J_{SC} a blend can provide, estimation of losses because of parasitic absorption (i.e. absorption from ITO, PEDOT:PSS), at what device thickness most of the light is absorbed in a specific layer (i.e. in the treatise of tandems) and the calculation of IQE [69-71]. In the case of inorganic PVs, mobilities can be measured with Hall effect measurements and the recombination rate is mostly proportional to the minority carrier concentration and light intensity. For instance, since devices are thicker, the generation rate can be determined by the Lambert-Beer law formulism [72]. On the other hand, in OPVs the mobilities are lower and a function of carrier density [72]. Since devices are very thin, both carrier types need to be accounted for and the optical generation rates rely on interference between the layers [72].

Thus, to describe solar cells, different approximations have been developed/adapted to OPVs in order to solve the main equations that govern semiconductors (Poisson's equation, continuity equations which are shown later) such as: Equivalent circuit models, Monte Carlo models, Mobility-lifetime models and drift diffusion models [69, 73]. Like so, drift diffusion models can be used to calculate the charge generation and transport mechanisms in a OPV device and have been thoroughly

76

utilised in the past, as demonstrated by high impact publications [74-76]. Although there are others drift diffusion programs such as TiberCAD [77], Setfos 4.6 FLUXIM AG [75, 78], the novelty with GPVDM is that it solves Shockley-Read-Hall (SRH) equations as a function of energy and position, thus enabling one to model effects of mobility, recombination rate as a function of carrier population [66, 76]. Further, GPVDM has been developed over the past 12 years and has been extensively validated in over 20 publications against experimental data, some of which can be reviewed here [66, 79, 80]. As such, GPVDM is a robust and reliable software to accurately simulate OPVs.

Now, focusing the attention on GPVDM, this software can simulate: light/dark J-Vs, EQE, PL, CELIV, fitting of experimental data, and more. An exhaustive list of software's features and full details can be reviewed elsewhere [81]. For the electrical part of the model, it uses a finite difference approach to solve electron and hole drift diffusion equations (shown later) in position space to describe the movement of charges in the OPV. At each point in position space, carrier trapping and escape equations are solved in energy space. Recombination by free to free (Langevin) or free to trap (Shockley-Read-Hall, SRH) are considered in the model. With this approach, carrier population can be resolved in position and energy space [76, 81]. For the optical part, there are three available models: The flat model, exponential model and the transfer matrix approach, the latter being the one used in this study unless otherwise specified [81]. Further details on the optical model are given in section 3.7.8. The aim of GPVDM was to investigate the influence of material parameters (mobility, recombination, absorption coefficients etc.) and to examine data with this simulation framework, by fitting experimental results into the model. Figure 3.26 presents a J-V curve for a P3HT:PCBM blend considering a AM 1.5G spectrum and device architecture of: ITO (100 nm)/PEDOT:PSS (30 nm)/P3HT:PCBM (150 nm)/Al (100 nm).
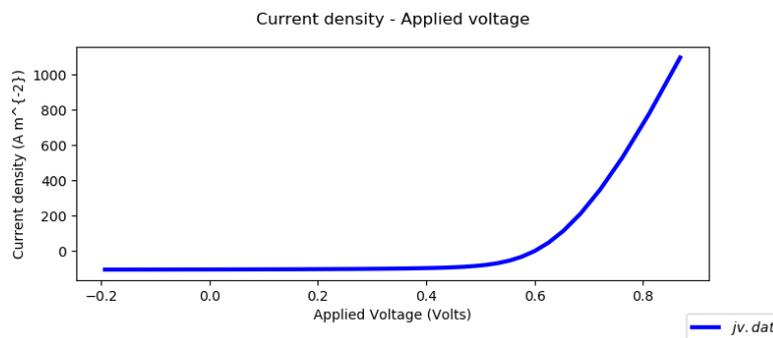
Figure 3.26. Example of a typical J-V curve of a P3HT:PCBM with a standard architecture as simulated with GPVDM.

Additionally, in the program each photoactive layer is configured in the electrical model tab, where recombination parameters and mobility are defined. Further, information about the R_{SH}, R_S, density of electrons and holes in the contacts can also be modified from the device tabs on the main window. Figure 3.27 presents a flow chart with the main characteristics and the inputs needed by users to run the simulations.
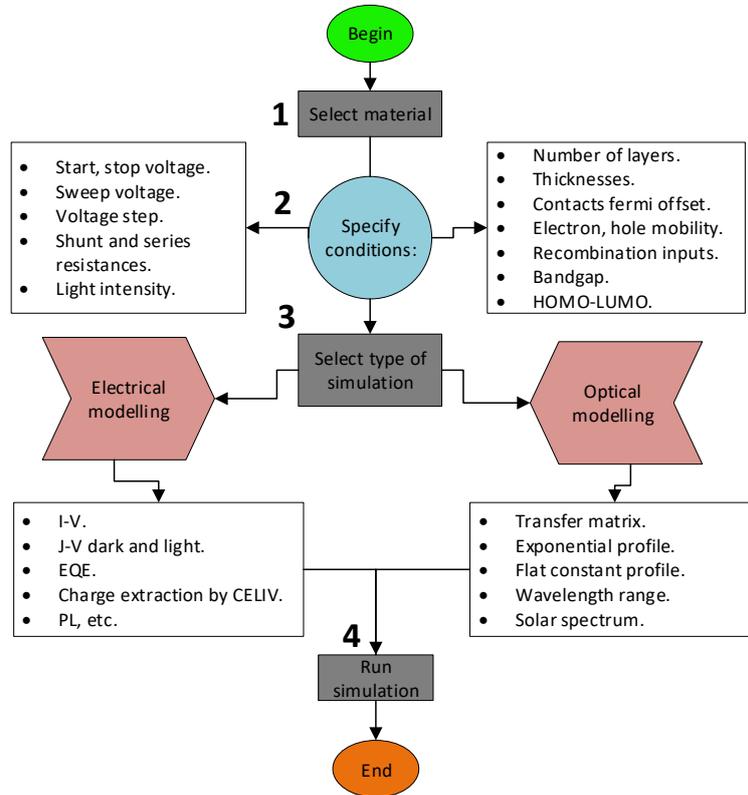
Figure 3.27. Flow chart of the main electrical and optical inputs when running a simulation.

3.7.2 Model Inputs

The GPVDM model requires parameters that determine how the different layers of an OPV model behave electrically and optically [82]. Each layer has a Density of States (DoS) tab in which electrical parameters that define carrier transport, mobility, type of recombination and trapping are set. If a device has two active layers, an additional DoS window needs to be completed as well. The layers in the device also need a refractive index spectrum, which includes the imaginary and real refractive index as a function of wavelength [82]. Some blend materials can readily be used and other materials can be manually added to the database. Table. 3.1 depicts main device parameters set in the electrical tab for a common P3HT:PCBM device.

Description	Parameter	DoS P3HT:PCBM
Electrical parameters:		
Electron trap density	$m^{-3} eV^{-1}$	3.80×10^{26}
Hole trap density	$m^{-3} eV^{-1}$	1.45×10^{25}
Electron tail slope	eV	4×10^{-2}
Hole tail slope	eV	6×10^{-2}
Electron mobility	$m^2 V^{-1} s^{-1}$	2.48×10^{-7}
Hole mobility	$m^2 V^{-1} s^{-1}$	2.48×10^{-7}
Relative permittivity	au	3.8
Number of traps	bands	20
Free electron to trapped electron	m^2	2.50×10^{-20}
Trapped electron to free hole	m^2	1.32×10^{-22}
Trapped hole to free electron	m^2	4.67×10^{-26}
Free hole to trapped hole	m^2	4.86×10^{-22}
Effective density of free electron states (@300k)	m^{-3}	1.28×10^{27}
Effective density of free hole states (@300k)	m^{-3}	2.86×10^{25}
X_i	eV	3.8
E_g	eV	1.1
Recombination constant	$m^{-3} s^{-1}$	0
Free carrier statistics	Maxwell boltzmann	
SRH capture escape rates:		
Electron capture rate, r_{ec}	$nV_{th}\sigma_n N_t(1-f)$	
Electron escape rate, r_{ee}	$e_n N_t f$	
Hole capture rate, r_{hc}	$pv_{th}\sigma_p N_t f$	
Hole escape rate, r_{he}	$e_p N_t(1-f)$	

Table 3.1. Device electrical parameters that can be modified to run simulations.

3.7.3 Electrical model

a) Energy levels

Having reviewed in the overview section the main features on how is it that the software runs, we take a closer look at the specifics. The model first calculates the built-in potential of the device. To do this, the software first needs to know the majority carrier concentrations on the negative ($_n$) and positive ($_p$) contacts, LUMO / HOMO and the effective band gap.

The energy of the LUMO and HOMO (i.e. conduction and valence band) of the of the device are defined as:

$$E_{LUMO} = -X \tag{3.5}$$

$$E_{HOMO} = -X - E_g \tag{3.6}$$

Where, *X* is the difference between LUMO and vacuum level and E_g the bandgap [66]. These parameters are already defined for standard materials (i.e. P3HT:PCBM, shown in Table 3.1) stored in the database. If new materials are added, these parameters need to be input before running a simulation [82].

Further, in the treatise of semiconductors, the Poisson's equation establishes the relationship between the density of electric charges and the electric potential [83]. Thusly, the internal potential distribution is obtained within the device with Poisson's equation:

$$\nabla \cdot \epsilon_0 \epsilon_r \nabla = q(n_f + n_t - p_f - p_t - N_{ad}) \qquad \textbf{(3.7)}$$

Where n_f, n_t are the carrier densities of free and trapped electrons; p_f and p_t are the carrier densities of free and trapped holes, N_{ad} is the doping density, q the elementary charge (1.60×10^{-19} Coulomb), ϵ_0 is the permittivity of free space and ϵ_r the relative permittivity of the blend (i.e. P3HT:PCBM) [66, 82].

b) Carrier trapping, de-trapping and recombination

In GPVDM, interaction of free carrier in energy space with a distribution of trap states is described with SRH theory. In Figure 3.28 which shows the energy space in the model, free electron and holes carrier distribution are labelled as n_f and p_f respectively. N_{trap} and P_{trap} denote trapped carrier populations, which are presented in the figure with the filled red and blue boxes. SRH theory describes the rates at which electrons and holes become captured and escape from the carrier traps. If a single electron trap is considered, the change in population of this trap can be described by four carrier capture and escape rates (Figure 3.28 and Table 3.1). The rate "r_{ec}" defines the rate at which electrons become captured into the electron trap; "r_{ee}" is the rate which electrons escape from the trap to the free electron population again; "r_{hc}" denotes the rate at which free holes get trapped and finally, "r_{he}" is the rate at which holes escape back to the free hole population. In short, the recombination is described by holes becoming captured into electron space slice through traps. Equivalent processes are also defined for the hole traps [81].
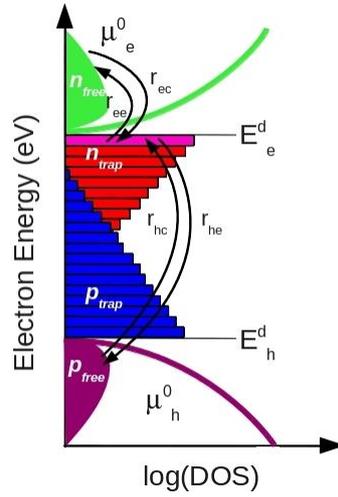
Figure 3.28. Diagram of DoS used by GPVDM. This image depicts the electron and hole capture and escape processes represented by the arrows going left and right for a single electron. Equivalent processes happen for all electron and hole traps. From [66, 81].

c) Free to free carrier recombination

In the model, free carrier to free carrier recombination is also accounted for. However, since most OPVs have many trap states and an ideality factor greater than 1, this suggests that free to free recombination is not a dominant mechanism. Nonetheless, this type of recombination is described by the equation:

$$R_{free} = K_r \left(n_f p_f - n_0 p_0 \right) \tag{3.8}$$

The methods to solve the equations are outlined at the end of the next section.

3.7.4 Carrier transport

In semiconductors, electrical conductivity is controlled by the hole and electron concentration and their ability to flow in a specific direction when influenced by an electric field [84]. Thusly, we momentarily dwell on the concepts of drift and diffusion which are the basic transport mechanisms in a semiconductor. To start, drift refers to the movement of charged particles in response to an electric field (ε) [85]. In an electric field, the force acts on charged particles where holes ($_p$) are accelerated in the direction of the electric field and electrons ($_n$) in the opposite direction, as shown in Figure 3.29. The motion of electrons and holes can be described by average drift velocities for electron (v_{dn}) and holes (v_{pn}), as shown by [85]:

$$V_{dn} = -\mu_n \varepsilon, \qquad \qquad \text{(3.9)}$$

$$V_{dp} = \mu_p \varepsilon, \qquad \qquad \text{(3.10)}$$

Where the mobility factor is represented by μ, and is a key parameter to investigate electron and hole transport because of drift. Further, the mobility represents how easily charge particles can move through a semiconducting material [85].
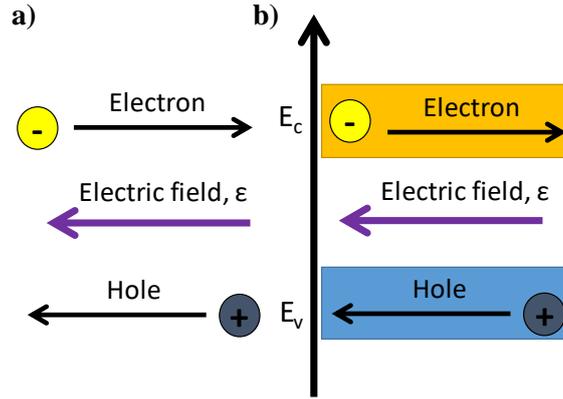
Figure 3.29. Schematic showing the a) direction of carriers because of an electric field and b) the complementary band diagram, where E_C and E_V are the conduction and valence band respectively. Adapted from [85].

The current densities of electron and holes are given by:

$$J_{n,drift} = -qnv_{dn} = qn\mu_n\varepsilon \qquad \qquad \text{(3.11)}$$

$$J_{p,drift} = qpv_{dp} = qp\mu_p\varepsilon \qquad \qquad \text{(3.12)}$$

Once these equations 3.11 and 3.12 are combined, they lead to the total drift current expressed as [85]:

$$J_{,drift} = q(p\mu_p + n\mu_n)\varepsilon \qquad \qquad \text{(3.13)}$$

On the other hand, diffusion is related to the gradient in particle concentration, which means that particles disperse from a region with high particle concentration into a lower particle concentration region in a random way [84]. A basic sketch of the diffusion mechanism is shown below (Figure 3.30).
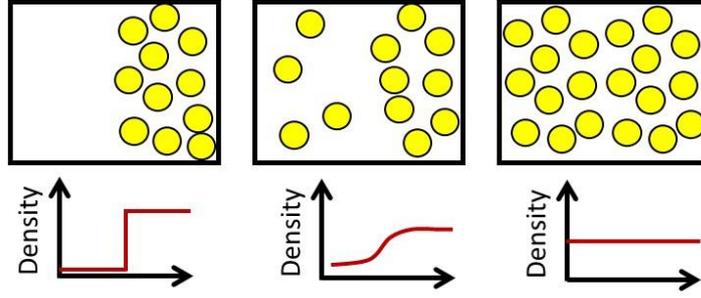
Figure 3.30. Schematic representing electron diffusion, redrawn from [85].

In diffusion mechanisms, electrons and holes are represented by the following equations:

$$J_{n,\ diff} = qD_n\ \nabla n \tag{3.14}$$

$$J_{p,\ diff} = -qD_p\ \nabla p \tag{3.15}$$

Where D_n, D_p represent the constants of electron and hole diffusion respectively. By combining equations 3.14 and 3.15 the total diffusion current is obtained:

$$J_{diff} = q(D_n\ \nabla n - D_p\ \nabla p) \tag{3.16}$$

And finally, combining equations 3.13 and 3.16 we obtain the drift + diffusion total current:

$$J = J_{drift} + J_{diff} = q(p\mu_p + n\mu_n)\varepsilon + q(D_n\nabla_n - D_p\nabla_p) \tag{3.17}$$

Having reviewed the basic concepts of drift and diffusion, we now focus on how transport is calculated by the software. For transport of carriers in GPVDM, the same drift diffusion equations are solved in position space for electrons and holes respectively:

$$J_n = q\mu_e nf\nabla E_C + qD_n\nabla n_f \tag{3.18}$$

$$J_p = q\mu_h pf\nabla E_V - qD_p\nabla p_f \tag{3.19}$$

In the above equations, J_n, J_p denote the electron and hole current density respectively. As such, these equations represent the carrier concentration across the device, which can be calculated now that the potential is known (from preceding sections). Now, in semiconductors, the continuity equations are used to take into account all carriers in terms of drift, diffusion, recombination and generation processes [85]:

$$\nabla J_n = q(R - G + \frac{\partial_n}{\partial_t})$$ (3.20)

$$\nabla J_p = -q(R - G + \frac{\partial_p}{\partial_t})$$ (3.21)

Where R and G are the recombination and generation rates per unit volume, ∂_n/∂_t and ∂_n/∂_t represent the time rate change in electron and hole concentration respectively. In addition, the spatial position of G comes from the optical model which is discussed next. As such, in GPVDM charge carrier conservation is forced by solving charge carrier continuity equations for both electrons and holes respectively.

To solve the equations, conditions are defined that fix the electrostatic potential of the contacts and a set of equations that connect the electron and hole currents flowing out of the device with the carrier concentrations [72]. Accordingly, such conditions specify the electron (hole) potential and the current densities of the electron (hole) in both contacts [72]. Thus, in order to solve equations simultaneously and consistently, GPVDM uses a Newton solver method which has been shown to offer suitable convergence. In the case of drift diffusion equations, these are solved with the Scharfetter-Gummel method to ensure stability [72, 76].

3.7.5 Optical model

From the optical part of the software, there are three main models: 1) The flat model, that considers the distribution of photons in the active layer(s) as uniform which in real life is not very realistic, since the optical properties change depending on the medium where light propagates (e.g. material properties and thickness). 2) The exponential model, in which light intensity decays exponentially as it traverses the device, as stated by the Beer-Lambert law that assumes constant absorption rate and no reflections. 3) The transfer matrix model, which considers reflections at the interfaces and where forward/backward propagating waves are solved [81, 82].

In OPV modelling, the absorption is normally modelled by the transfer matrix formalism, which represents the gold standard, since the very thin thicknesses are comparable to the wavelength of light and as such cannot be calculated by Beer-Lambert methods [72, 77, 86, 87]. With the transfer matrix method, the model calculates the absorption of each layer taking into account the interference, reflection and transmitted

effects at each of the interfaces within an OPV stack [71, 87] as shown in Figure 3.31. Hence, there have been many reports in literature describing optical models with the transfer matrix [77, 87].

Now a brief outline on how the transfer matrix works is presented below. In OPVs, light is incident on a glass (i.e. substrate) typically thicker than the light wavelength's, which is followed by other layers (i.e. photoactive layer, PEDOT:PSS) in which thicknesses are comparable or smaller than incident wavelengths.
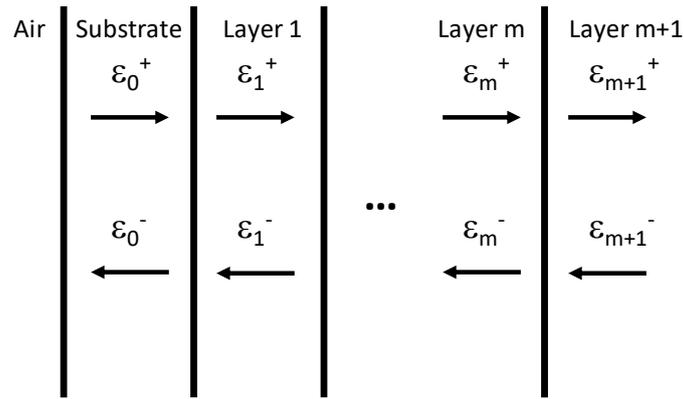
Figure 3.31. Electric fields (ε) in a stack that represents an OPV of *m* layers. The layers are characterised for their complex refractive index and thicknesses. From: [72].

Thus, to determine the electric fields in the OPV layers (going left or right) matrices are defined in the interfaces and for each layer. This formulism uses complex refractive index and thicknesses for the calculation. Hence, by using interface and layer matrices, the electric field on any point in the device can be determined as a function of incoming or outgoing electric field at the interface between layers with the following equation:

$$\begin{pmatrix} \varepsilon_0^+ \\ \varepsilon_0^- \end{pmatrix} = M_{01}^I M_1^L M_{12}^I \ldots M_m^L M_{mm+1}^I \begin{pmatrix} \varepsilon_{m+1}^+ \\ \varepsilon_{m+1}^- \end{pmatrix} \qquad (3.22)$$

Finally, once the electric field is known at any point in the device, it can be used to calculate the generation rate, G. For a detailed description of this optical model interested readers are referred here [71, 72, 87].

3.8 References:

1. Hoppe, H. and N.S. Sariciftci, *Organic solar cells: An overview.* Journal of Materials Research, 2011. **19**(7): p. 1924-1945.

2. Groves, C., *Simulating charge transport in organic semiconductors and devices: a review.* Rep Prog Phys, 2017. **80**(2): p. 026502.

3. Pivrikas, A., et al., *A review of charge transport and recombination in polymer/fullerene organic solar cells.* Progress in Photovoltaics: Research and Applications, 2007. **15**(8): p. 677-696.

4. Proctor, C.M., M. Kuik, and T.-Q. Nguyen, *Charge carrier recombination in organic solar cells.* Progress in Polymer Science, 2013. **38**(12): p. 1941-1960.

5. Darling, S.B. and F. You, *The case for organic photovoltaics.* RSC Advances, 2013. **3**(39).

6. Krebs, F.C., T. Tromholt, and M. Jorgensen, *Upscaling of polymer solar cell fabrication using full roll-to-roll processing.* Nanoscale, 2010. **2**(6): p. 873-86.

7. Baran, D., et al., *Reducing the efficiency-stability-cost gap of organic photovoltaics with highly efficient and stable small molecule acceptor ternary solar cells.* Nat Mater, 2017. **16**(3): p. 363-369.

8. Sun, C., et al., *A low cost and high performance polymer donor material for polymer solar cells.* Nat Commun, 2018. **9**(1): p. 743.

9. Berger, P.R. and M. Kim, *Polymer solar cells: P3HT:PCBM and beyond.* Journal of Renewable and Sustainable Energy, 2018. **10**(1).

10. Kleinschmidt, A.T., S.E. Root, and D.J. Lipomi, *Poly(3-hexylthiophene) (P3HT): fruit fly or outlier in organic solar cell research?* Journal of Materials Chemistry A, 2017. **5**(23): p. 11396-11400.

11. Serap Günes, H.N., and Niyazi Serdar Sariciftci, *Conjugated Polymer-Based Organic Solar Cells.* Chem. Rev., 2007. **107**(4): p. 14.

12. Hoppe, H. and N.S. Sariciftci, *Morphology of polymer/fullerene bulk heterojunction solar cells.* J. Mater. Chem., 2006. **16**(1): p. 45-61.

13. Kitai, A., *Chapter 7: Organic Semiconductors, OLEDs, and Solar Cells*, in *Principles of Solar Cells, LEDs and Related Devices: The Role of the PN Junction*. 2019, John Wiley & Sons Ltd. p. 307-357.

14. Brinkmann, M., *Structure and morphology control in thin films of regioregular poly(3-hexylthiophene).* Journal of Polymer Science Part B: Polymer Physics, 2011. **49**(17): p. 1218-1233.

15.   Mihailetchi, V.D., et al., *Charge Transport and Photocurrent Generation in Poly(3-hexylthiophene): Methanofullerene Bulk-Heterojunction Solar Cells.* Advanced Functional Materials, 2006. **16**(5): p. 699-708.

16.   Wang, Q., et al., *Progress in Emerging Solution-Processed Thin Film Solar Cells – Part I: Polymer Solar Cells.* Renew. Sust. Energ., 2016. **56**: p. 347-361.

17.   Lu, L. and L. Yu, *Understanding low bandgap polymer PTB7 and optimizing polymer solar cells based on it.* Adv Mater, 2014. **26**(26): p. 4413-30.

18.   Krebs, F.C., *The Polymer Solar Cell*, in *Polymer Photovoltaics: A Practical Approach*. 2008, SPIE Press. p. 11-89.

19.   Liang, Y., et al., *For the bright future-bulk heterojunction polymer solar cells with power conversion efficiency of 7.4%.* Adv Mater, 2010. **22**(20): p. E135-8.

20.   Savikhin, V., et al., *Morphological, Chemical, and Electronic Changes of the Conjugated Polymer PTB7 with Thermal Annealing.* iScience, 2018. **2**: p. 182-192.

21.   Foster, S., et al., *Electron Collection as a Limit to Polymer:PCBM Solar Cell Efficiency: Effect of Blend Microstructure on Carrier Mobility and Device Performance in PTB7:PCBM.* Advanced Energy Materials, 2014. **4**(14).

22.   Bencheikh, F., et al., *Study of Optical Properties and Molecular Aggregation of Conjugated Low Band Gap Copolymers: PTB7 and PTB7-Th.* The Journal of Physical Chemistry C, 2015. **119**(43): p. 24643-24648.

23.   Jan C. Hummelen, B.W.K., F. LePeq, and Fred Wudl, *Preparation and Characterization of Fulleroid and Methanofullerene Derivatives.* J. Org. Chem., 1995. **60**: p. 6.

24.   He, Y. and Y. Li, *Fullerene derivative acceptors for high performance polymer solar cells.* Phys Chem Chem Phys, 2011. **13**(6): p. 1970-83.

25.   V.D. Mihailetchi, J.K.J.v.D., P.W.M. Blom, J.C. Hummelen, R.A.J. Janssen, J.M. Kroon, M.T. Rispens, W.J.H. Verhees, M.M. Wienk, *Electron Transport in a Methanofullerene.* Adv. Funct. Mater., 2003. **13**: p. 4.

26.   He, Z., et al., *Single-junction polymer solar cells with high efficiency and photovoltage.* Nature Photonics, 2015. **9**(3): p. 174-179.

27.   Ebenhoch, B., et al., *Charge carrier mobility of the organic photovoltaic materials PTB7 and PC71BM and its influence on device performance.* Organic Electronics, 2015. **22**: p. 62-68.

28.   Youjun He, H.-Y.C., Jianhui Hou, and Yongfang Li, *Indene−C60 Bisadduct: A New Acceptor for High-Performance Polymer Solar Cells.* J. Am. Chem. Soc., 2010. **132**(4): p. 6.

29. Jin Young Kim, K.L., Nelson E. Coates, Daniel Moses, Thuc-Quyen Nguyen, Mark Dante, Alan J. Heeger, *Efficient Tandem Polymer Solar Cells Fabricated by All-Solution Processing.* Science, 2007. **317**(5835): p. 222-225.

30. Li, G., R. Zhu, and Y. Yang, *Polymer solar cells.* Nature Photonics, 2012. **6**(3): p. 153-161.

31. Sun, K., et al., *Review on application of PEDOTs and PEDOT:PSS in energy conversion and storage devices.* Journal of Materials Science: Materials in Electronics, 2015. **26**(7): p. 4438-4462.

32. Jeong, J., et al., *Wide range thickness effect of hole-collecting buffer layers for polymer:fullerene solar cells.* Organic Electronics, 2013. **14**(11): p. 2889-2895.

33. Wantz, G., et al., *Correlation between the Indium Tin Oxide morphology and the performances of polymer light-emitting diodes.* Thin Solid Films, 2005. **485**(1-2): p. 247-251.

34. Andreoli, E., et al., *PPy:PSS as Alternative to PEDOT:PSS in Organic Photovoltaics.* Synth. Met., 2013. **185-186**: p. 71-78.

35. Heeger, Y.Y.a.A.J., *Polyaniline as a Transparent Electrode for Polymer Light-Emitting Diodes: Lower Operating Voltage and Higher Efficiency.* Appl. Phys. Lett., 1994. **64**(10): p. 1245-1247.

36. Herrbach, J., et al., *P-Doped Organic Semiconductor: Potential Replacement for PEDOT:PSS in Organic Photodetectors.* Appl. Phys. Lett., 2016. **109**(7).

37. Bel Hadj Tahar, R., et al., *Tin doped indium oxide thin films: Electrical properties.* Journal of Applied Physics, 1998. **83**(5): p. 2631-2645.

38. Chen, Z., et al., *Fabrication of highly transparent and conductive indium-tin oxide thin films with a high figure of merit via solution processing.* Langmuir, 2013. **29**(45): p. 13836-42.

39. Brabec, C.J., et al., *Semiconductor Aspects of Organic Bulk Heterojunction Solar Cells*, in *Organic Photovoltaics: Concepts and Realization*. 2003, Springer Berlin Heidelberg. p. 159-248.

40. Brabec, C.J., et al., *Effect of LiF/metal electrodes on the performance of plastic solar cells.* Applied Physics Letters, 2002. **80**(7): p. 1288-1290.

41. Norrman, K., A. Ghanbari-Siahkali, and N.B. Larsen, *6 Studies of spin-coated polymer films.* Annual Reports Section "C" (Physical Chemistry), 2005. **101**.

42. So, S., Choi, W., Cheng, C. et al., *Surface preparation and characterization of indium tin oxide substrates for organic electroluminescent devices.* Appl Phys A, 1999. **68**: p. 447-450.

43. Padinger, F., Rittberger, R. and Sariciftci, N., *Effects of Postproduction Treatment on Plastic Solar Cells.* Adv. Funct. Mater., 2003. **13**: p. 4.

44. Li, G., et al., *High-efficiency solution processable polymer photovoltaic cells by self-organization of polymer blends.* Nature Materials, 2005. **4**(11): p. 864-868.

45. van Bavel, S., et al., *Relation between Photoactive Layer Thickness, 3D Morphology, and Device Performance in P3HT/PCBM Bulk-Heterojunction Solar Cells.* Macromolecules, 2009. **42**(19): p. 7396-7403.

46. Lukas Schmidt-Mende, J.W., *Characterization Techniques*, in *Organic and Hybrid Solar Cells: An Introduction*. 2016, De Gruyter. p. 193-243.

47. Servaites, J.D., M.A. Ratner, and T.J. Marks, *Organic solar cells: A new look at traditional models.* Energy & Environmental Science, 2011. **4**(11).

48. Qi, B. and J. Wang, *Fill factor in organic solar cells.* Phys Chem Chem Phys, 2013. **15**(23): p. 8972-82.

49. Potscavage, W.J., S. Yoo, and B. Kippelen, *Origin of the open-circuit voltage in multilayer heterojunction organic solar cells.* Applied Physics Letters, 2008. **93**(19).

50. Beiley, Z.M., et al., *Morphology-Dependent Trap Formation in High Performance Polymer Bulk Heterojunction Solar Cells.* Advanced Energy Materials, 2011. **1**(5): p. 954-962.

51. Mihailetchi, V.D., J. Wildeman, and P.W. Blom, *Space-charge limited photocurrent.* Phys Rev Lett, 2005. **94**(12): p. 126602.

52. Blom, P.W.M., et al., *Device Physics of Polymer:Fullerene Bulk Heterojunction Solar Cells.* Advanced Materials, 2007. **19**(12): p. 1551-1566.

53. Brabec, C.J., Cravino, A., Meissner, D., Sariciftci, N.S., Fromherz, T., Rispens, M.T., Sanchez, L. and Hummelen, J.C., *Origin of the Open Circuit Voltage of Plastic Solar Cells.* Adv. Funct. Mater., 2001. **11**: p. 374-380.

54. Owen, T., *Principles and applications of UV-visible spectroscopy*, in *Fundamentals of modern UV-visible spectroscopy*, A. Technologies, Editor. 2000. p. 2-28.

55. P. Eaton, P.W., *Introduction*, in *Atomic Force Microscopy*. 2010, Oxford University Press. p. 1-8.

56. Seo, Y. and W. Jhe, *Atomic force microscopy and spectroscopy.* Reports on Progress in Physics, 2008. **71**(1).

57. Jalili, N. and K. Laxminarayana, *A review of atomic force microscopy imaging systems: application to molecular metrology and biological sciences.* Mechatronics, 2004. **14**(8): p. 907-945.

58. P. Eaton, P.W., *AFM modes*, in *Atomic Force Microscopy*. 2010, Oxford University Press. p. 49-81.

59. I.N.R.F. *Dektak 3 Profilometer*. [Accessed: 04-Apr-2021]; Available from: https://www.inrf.uci.edu/facility/equipment/characterization/dektak-3-profilometer/.

60. Gauvin, R., *Review of transmission electron microscopy for the characterization of materials*, in *Materials Characterization and Optical Probe Techniques: A Critical Review*. 1997.

61. Rose, H.H., *Optics of high-performance electron microscopes.* Science and Technology of Advanced Materials, 2008. **9**(1).

62. Williams D.B., C.C.B., *The Transmission Electron Microscope*, in *Transmission Electron Microscopy A Textbook for Materials Science*. 2009, Springer: Boston, MA. p. 3-22.

63. Williams D.B., C.C.B., *Scattering and Diffraction*, in *Transmission Electron Microscopy A Textbook for Materials Science*. 2009, Springer: Boston, MA. p. 23-38.

64. Mendis, B.G., et al., *Plasmon-loss imaging of polymer-methanofullerene bulk heterojunction solar cells.* Applied Physics Letters, 2013. **102**(25).

65. Drummy, L.F., et al., *Molecular-Scale and Nanoscale Morphology of P3HT:PCBM Bulk Heterojunctions: Energy-Filtered TEM and Low-Dose HREM†.* Chemistry of Materials, 2011. **23**(3): p. 907-912.

66. MacKenzie, R.C.I., et al., *Extracting Microscopic Device Parameters from Transient Photocurrent Measurements of P3HT:PCBM Solar Cells.* Advanced Energy Materials, 2012. **2**(6): p. 662-669.

67. Wetzelaer, G.-J.A.H. and P.W.M. Blom, *Diffusion-Driven Currents in Organic-Semiconductor Diodes.* NPG Asia Mater., 2014. **6**(7): p. e110.

68. Groves, C., L.J.A. Koster, and N.C. Greenham, *The Effect of Morphology Upon Mobility: Implications for Bulk Heterojunction Solar Cells with Nonuniform Blend Morphology.* J. Appl. Phys., 2009. **105**(9).

69. Tress, W., K. Leo, and M. Riede, *Optimum Mobility, Contact Properties, and Open-Circuit Voltage of Organic Solar Cells: A Drift-Diffusion Simulation Study.* Phys. Rev. B., 2012. **85**(15): p. 155201.

70. Jenny Nelson, J.J.K., James Kirkpatrick, and Jarvist M. Frost, *Modeling Charge Transport in Organic Photovoltaic Materials.* Acc. Chem. Res., 2009. **42**(11): p. 1768-1778.

71. Burkhard, G.F., E.T. Hoke, and M.D. McGehee, *Accounting for Interference, Scattering, and Electrode Absorption to Make Accurate Internal Quantum Efficiency Measurements in Organic and Other Thin Solar Cells.* Adv. Mater., 2010. **22**(30): p. 3293-3297.

72.   Nelson, T.K.a.J., *Chapter 7: Device Modelling of Organic Bulk Heterojunction Solar Cells*, in *Multiscale Modelling of Organic and Hybrid Photovoltaics*, D.B.a.J. Cornil, Editor. 2013, Springer-Verlag: Berlin. p. 279-324.

73.   Groves, C., R.A. Marsh, and N.C. Greenham, *Monte Carlo Modeling of Geminate Recombination in Polymer-Polymer Photovoltaic Devices.* J. Chem. Phys., 2008. **129**(11): p. 114903.

74.   Min Nam, Y., J. Huh, and W.H. Jo, *A Computational Study on Optimal Design for Organic Tandem Solar Cells.* Sol. Energy Mater. Sol. Cells, 2011. **95**(4): p. 1095-1101.

75.   Altazin, S., et al., *Refined Drift-Diffusion Model for the Simulation of Charge Transport Across Layer Interfaces in Organic Semiconductor Devices.* J. Appl. Phys., 2018. **124**(13).

76.   MacKenzie, R.C.I., et al., *Modeling Nongeminate Recombination in P3HT:PCBM Solar Cells.* The Journal of Physical Chemistry C, 2011. **115**(19): p. 9806-9813.

77.   Fallahpour, A.H., et al., *Modeling and Simulation of Energetically Disordered Organic Solar Cells.* J. Appl. Phys., 2014. **116**(18).

78.   Firdaus, Y., et al., *Efficient Double- and Triple-Junction Nonfullerene Organic Photovoltaics and Design Guidelines for Optimal Cell Performance.* ACS Energy Lett., 2020. **5**(12): p. 3692-3701.

79.   Mäckel, H. and R.C.I. MacKenzie, *Determination of Charge-Carrier Mobility in Disordered Thin-Film Solar Cells as a Function of Current Density.* Phys. Rev. Appl., 2018. **9**(3): p. 03420.

80.   MacKenzie, R.C.I., et al., *Loss Mechanisms in High Efficiency Polymer Solar Cells.* Adv. Energy Mater., 2016. **6**(4).

81.   MacKenzie, R.C.I. *General Purpose Photovoltaic Device Model (GPVDM)*. [Accessed: 07-Apr-2021]; Available from: www.gpvdm.com.

82.   MacKenzie, R.C.I. *GPVDM user manual*. 2021 Accessed on: [07-Apr-2021]; Available from: https://www.gpvdm.com/docs.html.

83.   Arno Smets, K.J., Olindo Isabella, René Van Swaaij, Miro Zeman, *Chapter 4: Electrodynamic Basics*, in *Solar Energy The Physics and Engineering of Photovoltaic Conversion, Technologies and Systems*. 2015, UIT Cambdrige Ltd: England. p. 27-34.

84.   Kitai, A., *Chapter 2: Semiconductor Physics*, in *Principles of Solar Cells, LEDs and Related Devices: The Role of the PN Junction*. 2019, John Wiley & Sons Ltd. p. 37-110.

85.   Arno Smets, K.J., Olindo Isabella, René Van Swaaij, Miro Zeman, *Chapter 6: Basic Semiconductor Physics*, in *Solar Energy The Physics and Engineering of Photovoltaic Conversion, Technologies and Systems*. 2015, UIT Cambdrige Ltd: England. p. 47-64.

86.   Armin, A., et al., *Electro-Optics of Conventional and Inverted Thick Junction Organic Solar Cells.* ACS Photonics, 2015. **2**(12): p. 1745-1754.

87.   Sievers, D.W., V. Shrotriya, and Y. Yang, *Modeling Optical Effects and Thickness Dependent Current in Polymer Bulk-Heterojunction Solar Cells.* J. Appl. Phys., 2006. **100**(11).

CHAPTER 4

IMPACT ON MORPHOLOGY OF P3HT:PCBM BLENDS; PRECURSOR WORK TO BOOST EFFICIENCY ON OPVs

4.1 Introduction

This Chapter contains the first experimental results from this thesis. As noted from Chapter 2, the bulk morphology formation plays a key role that has a direct impact upon the performance of OPVs and a variety of methods have been elucidated in literature with the aim of maximising PV outcomes. In here, experimental data are presented in which the morphology of P3HT:PCBM blends are optimised. This work is necessary as a foundation for the work presented in Chapter 5, in which these optimal binary blends are further modified by the ternary components, thus enabling the effect of the ternary component to be discerned. To this end, binary P3HT:PCBM blends are subjected to thermal annealing (TA) and solvent vapour annealing (SVA), since these processing methods have demonstrated to improve the efficiency in OPVs [1, 2]. Figure 4.1 presents a sketch of the nanostructure in these blends when TA or SVA is utilised and their concepts are briefly recapped below.
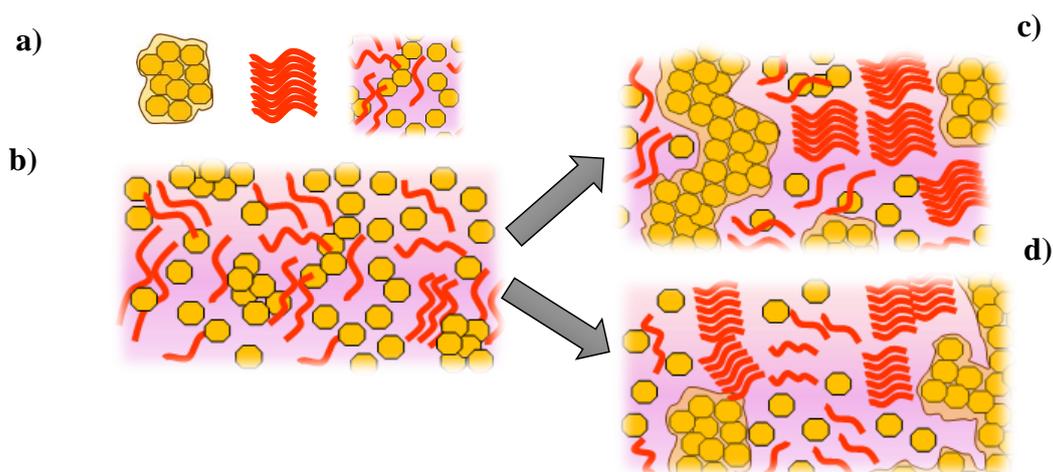
Figure 4.1. a) Representation of a fullerene aggregate (left), P3HT crystallite (middle) and amorphous region (right). Schematic of the morphologies in the b) as cast blend, c) with TA and d) SVA. Adapted from: [3, 4].

In TA, the temperature of the hotplate reorients isolated PCBM molecules into clusters and P3HT aggregates form crystallites [4]. The heat treatment is normally carried out below the melting point of the polymer (~<178 °C) [5]. SVA is a milder post treatment compared to TA, because is carried out in room temperature and in a closed container [1, 6]. During SVA, the solvent exposure creates a saturated ambient in which its molecules diffuse into the thin film and alter the microstructure during the slow evaporation of the solvent [1]. The reason behind the enhance performance and the similarity between these two strategies is that they can improve the crystallinity of the donor and promote fullerene aggregation, thereby enhancing absorption, transport properties and ultimately the efficiency [1].

4.2 Why is morphology control important?

Solution processed thin films are a key method of fabricating organic electronic devices such as OPVs [7, 8]. Generally, in solution processing, diluted electron and acceptor constituents are dissolved in a volatile solvent [9]. This solution can be casted into a substrate by a number of methods which include, spin coating, ink-jet printing and knife coating [7]. Spin coating is a lab-scale technique commonly used in universities because is vacuum free and can yield homogeneous thin films [10]. Following spin coating onto a substrate, the solvent starts to evaporate resulting in acceptor and donor rich regions [9]. Since the exciton diffusion length is around ~10 nm, the acceptor and donor constituents should ideally form numerous interfaces to maximise exciton dissociation, and suitable phase separation with continuous percolation channels to ensure charge collection at the contacts [11]. However, depending on the type of materials comprising the blend, D:A ratio and processing conditions in which the thin films are fabricated (i.e. spin coating time, type of solvent, type of substrate, inert atmosphere, etc.) distinct nanostructures are formed, thus rendering the control of the BHJ morphology a complex process [12].

As discussed in Chapter 2, several techniques have been introduced to this date in an effort to control the morphology to some extent in the pursuit of an "optimal design" that can maximise efficiency [12-15]. Among these strategies, TA and SVA have proved to be useful in the past to enhance polymer:fullerene blend systems, attributed to improved P3HT crystallinity, PCBM aggregation and enhanced optical absorption, resulting from a better organised morphology [2]. Thusly, this Chapter aims to reveal the

different PV outcomes by utilising two processing methods on OPVs and highlight the differences between the two. Firstly, TA was performed in P3HT:PCBM blends on a hotplate at 120 °C for a variety of annealing times. This temperature was chosen as it has been observed to be within an optimal range for P3HT:PCBM based blends [16-19]. Secondly, SVA was carried out by loading another set of P3HT:PCBM blends on a closed container (petri dish) holding the sample, and adding small amounts of DCB solvent to fill the space with a solvent vapour rich atmosphere [20]. A total of 8 nominal repeats for each type of blend were fabricated, totalling 96 for the complete set of experiments (48 for TA and 48 for SVA). Further, all OPVs were kept inside a N_2 atmosphere glovebox for the duration of either TA or SVA annealing times. Images of both processes are included in Appendix 4.1.

4.3 Morphology control by TA and SVA annealing in P3HT:PCBM composites

4.3.1 Surface topography

To start this section, an optimal morphology for a BHJ which maximises efficiency has been demonstrated to be largely dependent upon materials and processing conditions [21]. As a result, understanding and characterising the morphology and how is correlated to V_{OC}, J_{SC}, FF and PCE for particular donor-acceptor blends becomes vital. Hence, in here we fabricated P3HT:PCBM binary OPVs subjected to postprocessing TA and SVA. To understand the impact on the morphology by these methods, different annealing times were used for each blend system. The morphological effects of TA have been demonstrated to start more rapidly on thin films (~3 min) [22] compared to SVA, which generally requires more time for the thin film morphology to dry and reach equilibrium [23, 24]. Thus, TA times from 0 to 20 min and SVA exposure from 0 to 60 min was considered for the samples examined here, were the control is the as-cast film. Similar annealing times for both strategies have been used by other researchers [16, 24].

Figures 4.2 and 4.3 shows surface topography of P3HT:PCBM OPVs which received TA and SVA for varied annealing times respectively. These AFM scans were carried out in a controlled environment by Dr. Chris Pearson accompanied by the author (more details on the measurements are provided in Chapter 3). Considering first the TA samples, the control blend resulted in a surface with small phase separation, with a root

mean surface (RMS) roughness of 3.58 nm as depicted in Figure 4.2a. As thermal annealing time increases, the surface roughness of the annealed composites increased too, from ~5 nm to ~8 nm as observed in Figure 4.2b − f. These variations in the morphology are attributed to PCBM aggregation and P3HT molecule ordering, all of which occur concurrently during TA as shown in related studies [25]. Further, the thermally annealed samples show distinctive thin fibrillar structures which also increase with the annealing time, with widths of <100 nm and lengths between 500 nm and 2 µm that are observed throughout the film. These thin nanostructures are attributed to enhanced P3HT crystallinity with the heat treatment, which tends to form networks [11]. Because exciton diffusion length is ~10 nm, the resulting morphology may provide more interfaces between P3HT and PCBM for exciton dissociation and percolation paths for carrier collection that may increase efficiency [11].
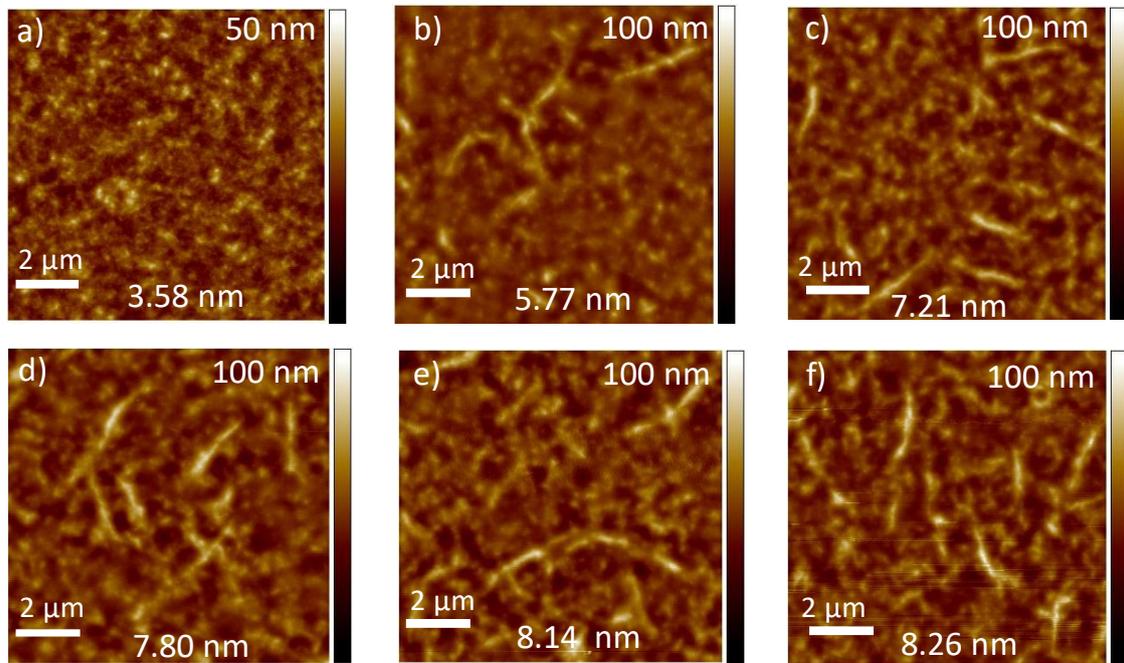
Figure 4.2. P3HT:PCBM with 120° C TA post processing at different annealing times: a) no annealing, b) 2 minutes, c) 5 minutes, d) 10 minutes, e) 15 minutes and f) 20 minutes.

These results are consistent with previous reports on the bulk structure as determined by X-ray diffraction [3, 11, 26, 27], where a P3HT crystallite in a film as cast has been found to have lengths of ~9 nm that are further increased to ~21 nm with TA [3], showing higher possibility of forming connections [20]. Going a step further, Yang and co-workers [11] also demonstrated that TA could yield higher efficiencies owing it to a more crystalline morphology as observed with TEM imaging, that could improve

hole mobility up to ~0.1 cm^2 V^{-1} s^{-1}. Nonetheless, TA has been also found to cause degradation when higher temperatures (>130° C) are used [26, 28, 29]. Additionally, extended periods of heat treatment time may result in a coarser morphology in P3HT:PCBM blends with PCBM clusters up to 100 µm in size, that are not beneficial for exciton diffusion into D:A interfaces, increasing exciton recombination and lowering PCE [17, 27, 29, 30].

On the other hand, AFM measurements on P3HT:PCBM with SVA evidenced that the control blend (Figure 4.3a) realised a surface roughness of ~3 nm with a small phase separation, comparable to the control blend of TA. However, AFM imaging also reveals less coarse morphologies and seemingly smaller nanofibers (Figure 4.3b – 4.3f) when compared to TA, yielding RMS between ~1 nm – 5 nm when blends were exposed to increasing vapour annealing time, as seen elsewhere [31]. Although nano fibrillar domains are also visible in SVA samples, widths are in the order of ~<50 nm with smaller lengths of ~200 nm throughout the films, thus yielding less developed crystalline features in contrast to TA samples.
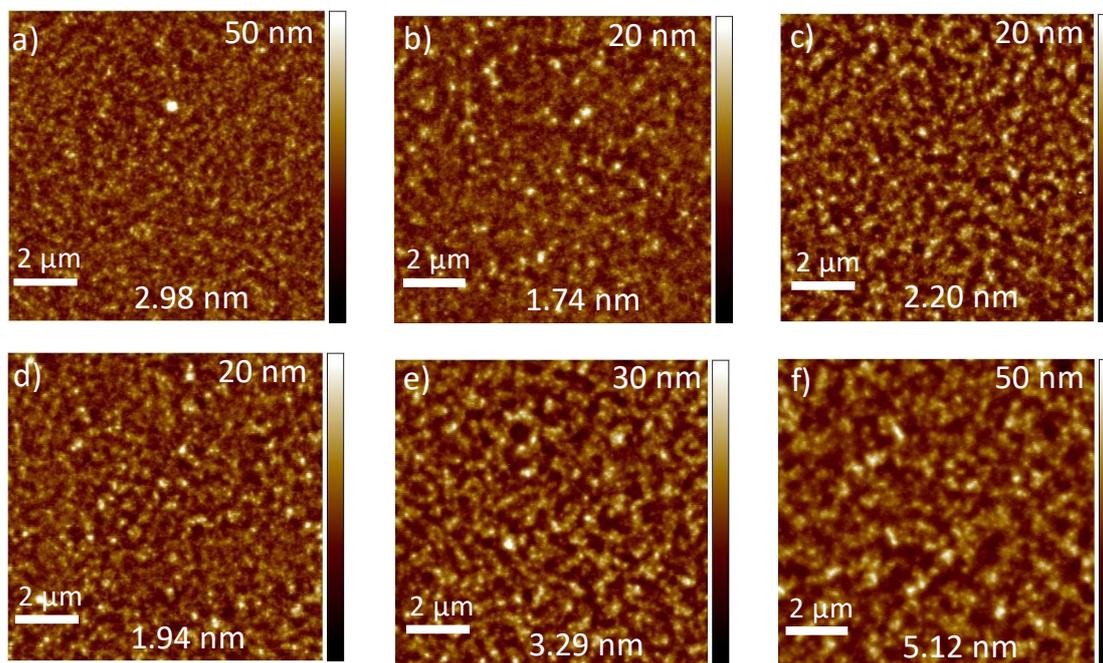
Figure 4.3. P3HT:PCBM with SVA post processing at different exposure times: a) no annealing, b) 3 minutes, c) 5 minutes, d) 15 minutes, e) 30 minutes and f) 60 minutes.

Since AFM focuses on the surface, several authors have shown with X-ray scattering in P3HT:PCBM blends, that SVA promotes P3HT crystallites to increase in

length from ~9 nm to ~11 nm [3, 20] in agreement with the results presented here. Further, a detailed characterisation on the morphology of P3HT:PCBM was also carried out by Verploegen et al [6] with the aim of understanding the structural changes undergoing with TA and SVA processing methods. X-ray diffraction measurements on P3HT:PCBM with vapour exposure yielded crystal domain sizes of <60 Å in contrast to TA samples yielding domain sizes of >130 Å, in line with the topography imaging recollected here.

Therefore, larger crystal sizes would have more possibility to form crystallite networks, thus reducing gaps between crystalline regions that can improve carrier transport [20]. In addition, factors that ultimately play a key role for the effectiveness of SVA are the solubility of the donor and acceptor constituents and the time solvent vapour exposure [32]. Having established the morphology differences, we now take a closer look at the performance of the devices.

4.3.2 Electrical characterisation: J-Vs and EQE

Figure 4.4a, c depicts J-V characteristics under dark and illumination for TA treatment of 120 °C with varied annealing times. For the parameters described here, the dark rectification ratios of all samples are close to 10 at 0.5 V bias, depicting series resistance (R_S) in the 0.5 V regime as well, which can be an indication of unfavourable interface between the active layer and the contacts [33]. Padinger et al [30] reported similar dark rectification trends for the control and TA devices, in which the poorer performance of the control was attributed to be partly limited by shunt resistance whilst the increase in J_{SC} observed in light J-Vs was presumed to be related to increased mobility. In the results presented here, the optimum outcome for TA processing was realised with a 10 min heat treatment, yielding a J_{SC} of ~6 mA/cm^2 accompanied by a 48% FF and 0.38 Voc. These results represented a considerable improvement compared to the control blend, which achieved a J_{SC} of 2 mA/cm^2. Overall the efficiency increased by ~3 times upon TA of 10 min, in line with other publications [16, 17, 30, 34].

Turning now to the SVA composites (Figure 4.4b, d), the control device showed a moderate J_{SC} of ~3 mA/cm^2, V_{OC} of 0.38 and FF of 46% yielding a PCE of 0.57%. A reasonable explanation for the small difference in J_{SC} between both controls, could be attributed to a more homogeneous morphology when no processing treatment was used,
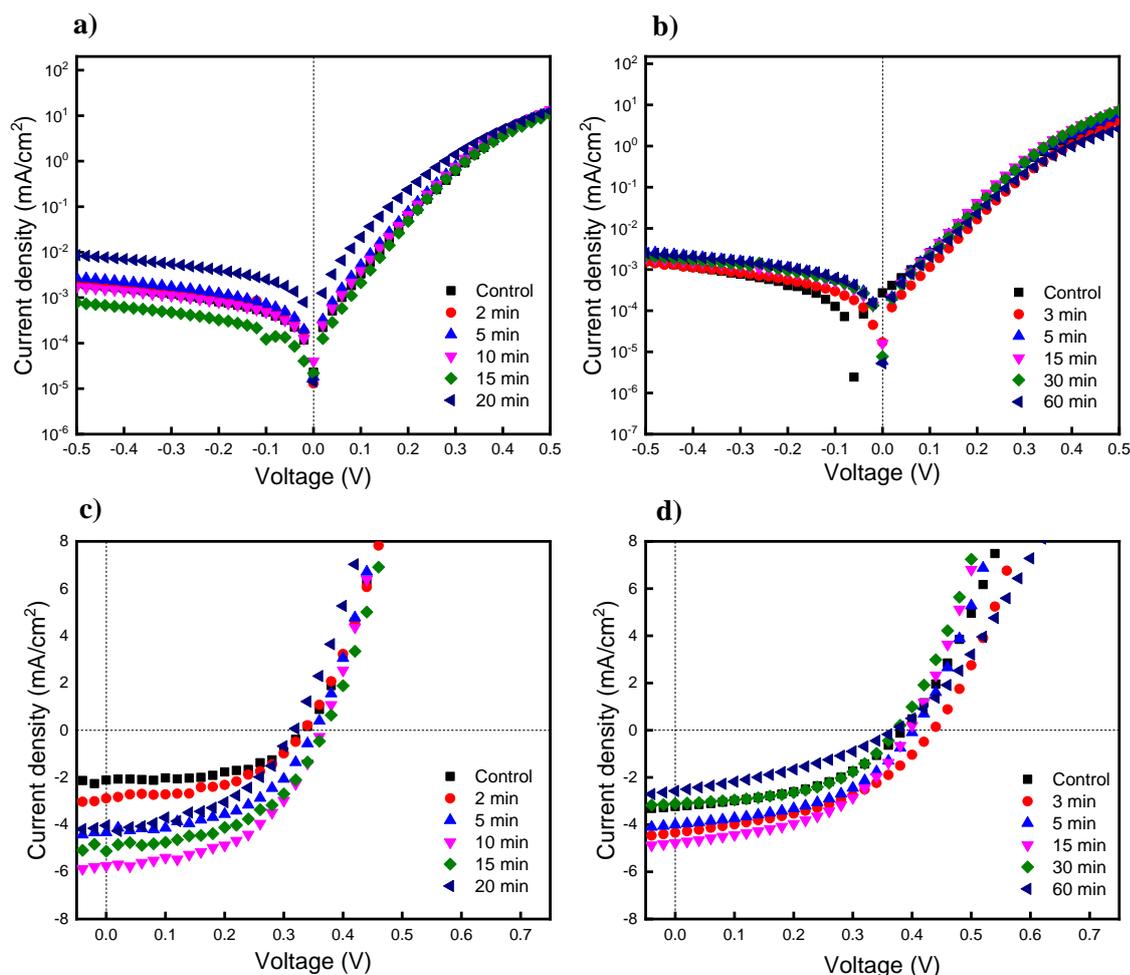
Figure 4.4. Dark (top) and light (bottom) characteristics for a-c) TA and b-d) SVA in P3HT:PCBM blends.

which can have an impact in the percolation pathways for carrier collection, contrary to the enhanced crystallinity and aggregation caused by the two annealing methods (as seen in the previous section) [34]. Further, the shallow slope observed in the dark J-V curves at the 0.5 V regime depicts R_S attributed also to the resistance of current flow between the organic layer and the electrode [33]. In addition, shunt resistances (R_{SH}) are evident in the <0.15 V region of the dark J-V (i.e. the control device with J value not at V=0), which may be due to pinholes and cracks in the active layer, a plausible reason since SVA method yielded thinner films compared to TA (see Appendix 4.2). The blend with 15 min of SVA treatment achieved a higher J_{SC}, with 4.33 mA/cm^2 delivering a PCE near ~1%, in agreement with similar results published by Onojima and colleagues for comparable SVA times [35]. Further, the PCE starts to drop after increasing the SVA exposure over 15 min, as evidenced by the poor PV values obtained for the 30 min and

60 min devices. As observed elsewhere [31], these lower PV values can be attributed to how the different vapour annealing times may result in distinct crystalline and disordered regions, in line with the surface topography imaging. All PV data related to J_{SC}, FF, V_{OC} and PCE for P3HT:PCBM BHJs with either TA or SVA are included in the Appendix 4.3.

Now, to further investigate the J_{SC} gains observed in J-Vs, EQE measurements were made on both sets of devices. Figure 4.5a shows the EQE spectra corresponding to devices that received TA for 2 min, 5 min, 10 min and 20 min respectively, plus the reference control.
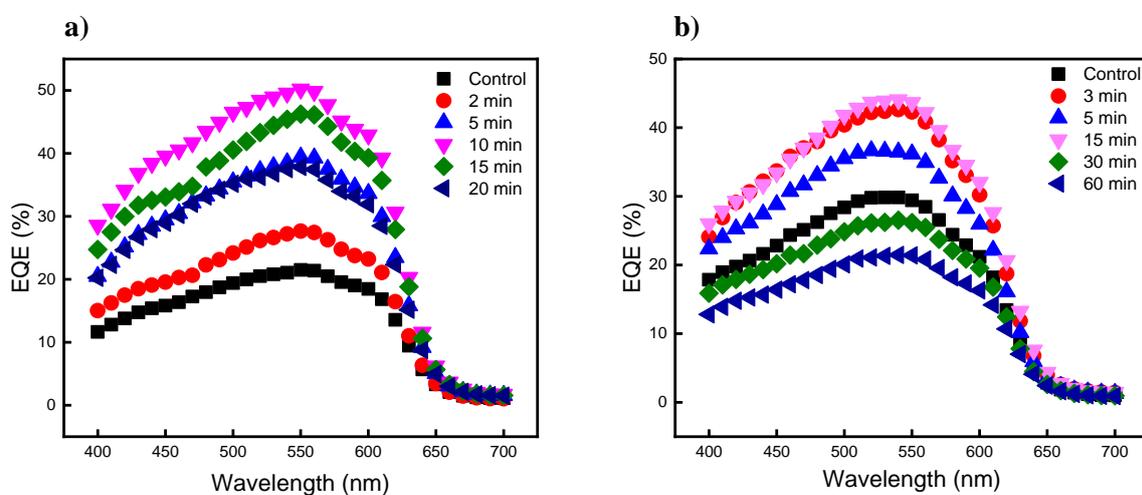
Figure 4.5. EQE measurements for P3HT:PCBM blends subjected to TA (a) and SVA (b) with varied annealing times of both strategies, as indicated in the inset.

The sample with a heat treatment of 2min attained a EQE of ~27% ranging from 450 nm to 600 nm wavelength, whilst the EQE increased by almost two-fold for the 10 min sample. A maximum EQE of ~44% is realised for this 10 min sample between 450 nm – 500 nm wavelengths which is consistent with the EQE increments observed elsewhere [11, 17, 30]. In these studies [16, 17], it was found that an enhanced crystallinity and orientation of the polymer chains caused an improvement in hole mobility, from 6×10^{-11} m^2 V^{-1} s^{-1} to 2×10^{-8} m^2 V^{-1} s^{-1} which is the main reason for the efficiency enhancement in these types of blends. Further, Li et al [17] investigated P3HT:PCBM blends under different TA times, from 0 min – 30 min, demonstrating that 10 min is the optimal choice and extending it may reduce the efficiency. Thus, the results presented here are in agreement with has been reported in literature, whereby this thermal

postproduction method can enable control over the morphology by tuning parameters like the amount of time of heat treatment.

Turning the attention into the SVA samples, the enhancement of J_{SC} for SVA treated P3HT:PCBM blends is also in agreement with EQE responses for varied vapour annealing times as depicted in Figure 4.5b. Overall, 3 – 15 min treated samples showed an enhancement in EQE after SVA for the entire spectrum range between 400 nm – 700 nm attaining a maximum EQE peak over 40% for the 15 min device. Indeed, extending the solvent exposure times also appears to be detrimental to SVA samples [32]. Further, the lower EQE attained by the 5 min sample compared to the 3 min and 15 min is attributed to the different crystalline features and disordered regions that result from varied vapour annealing times, and the optical spectra proves this conclusion as we shall see in the next section. To wrap up this section, Miao et al [36] reported in their paper an increase in absorption with SVA which can contribute to enhance EQE. Thus, to understand the origin of the EQE improvement, optical absorption spectra are investigated next.

4.3.3 Optical absorption spectra

Focusing on the optical profiles, Figure 4.6a exhibits a typical absorption profile of a P3HT:PCBM blends that received TA from 0 (control) to 20 min with film thicknesses of ~<150 nm as indicated in the Appendix 4.2. From the figure, the highest absorption was achieved with the 10 min sample. Two distinctive peaks are shown in the image; one between 330 nm – 340 nm corresponding to PCBM and other main peak at 500 nm – 550 nm with the P3HT contribution [16]. Additionally, two absorption shoulders located at 550 nm and 600 nm are attributed to interchain interactions of the P3HT molecules as observed here [37]. In agreement with reported data in literature, other authors have demonstrated that $110 - 120$ °C is the optimum thermal annealing for P3HT:PCBM blends, which red-shifts the optical absorption owing it to a more ordered crystalline structure [16-19]. Further, the increase in crystallinity degree contributes to enhance hole transport on P3HT, reaching hole carrier mobilities of 10^{-8} m^2 V^{-1} s^{-1} which is consistent with an increment in the efficiency in the blend as previously stated [16]. Moreover, in the 10 min blend, the red-shifted curve improves the spectral overlap with the solar emission and thus increasing the absorption in this blend, compared to the control sample. Nonetheless, the enhancement in optical absorption is around ~10%

compared to the EQE enhancement, demonstrating that mobility plays an important role [30].
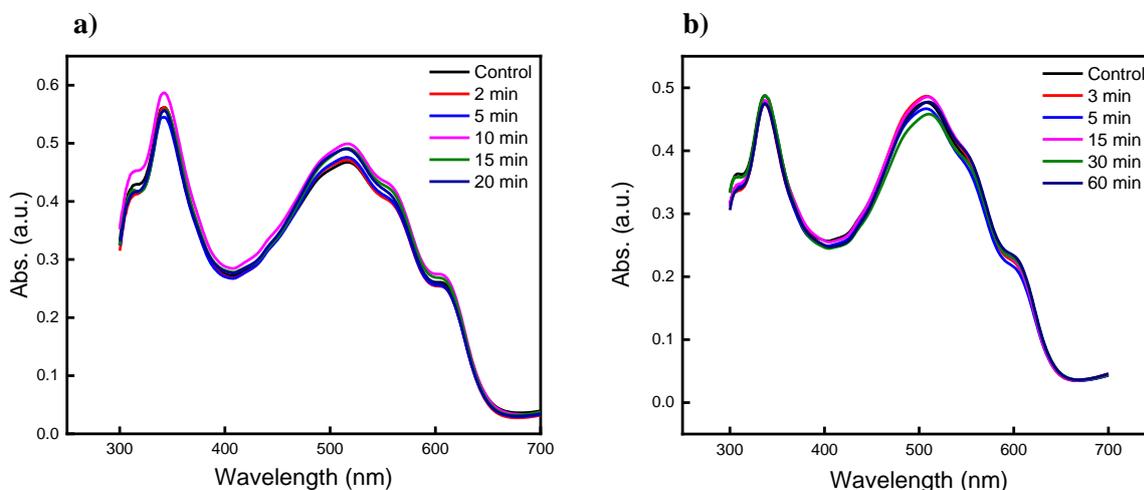
Figure 4.6. UV-vis absorption spectra of P3HT:PCBM composite with a) TA treatment and b) SVA treatment considering different annealing times respectively. Film thicknesses are ∼<150 nm.

UV-vis measurements were also carried out for the P3HT:PCBM SVA treated samples (Figure 4.6b). Similar shape and vibronic features are observed for these samples, displaying one shoulder between 600 nm – 607 nm, a second shoulder around 550 nm along with an ample peak at 508 nm. These results agree well with conclusions deduced from previous studies, where the absorption coefficient of the blend increases with increasing SVA time [24] but decreases with extended periods of annealing time, attributed to fullerene molecules interrupting the ordering of the P3HT chains [35]. Comparable optical profile structures were also observed by Onojima et al [35, 38] on P3HT:PCBM BHJ with SVA treatment across the entire spectrum. In agreement with their study, increasing the SVA time slightly reduces the absorption spectra. In addition, the optical spectra of the 5 min blend displays lessened vibronic features between 500 nm – 600 nm, which may result from less crystalline fibrils as seen in section 4.3.1, that can reduce EQE and thus efficiency.

To close this section, the experimental evidence presented here is congruent with what has been reported in literature, that the morphology may be greatly influenced depending on the post processing method used, choice of solvents, ratios, etc. which have a direct impact in the PV results.

4.4 Conclusion

As observed in this Chapter, the control of morphology remains one of the most essential issues in the field of OPVs. As previously discussed, high efficient OPVs require a systematic consideration and understanding of three key areas: formulation (device design), material development (novel materials) and new device architectures. In here two methods are shown to impact the morphology and the overall PV characteristics: TA and SVA for P3HT:PCBM binary blends. It is demonstrated that these two techniques can enable control over the morphology resulting in distinct topography and also in increased PV values. Indeed, although TA and SVA displayed enhanced crystallinity compared to as cast films, the evolution of the crystallization is found to be different, with TA exhibiting larger fibrils. Therefore, as a route to increase efficiency, the 10 min sample with TA at 120 °C showed a more profound impact in the performance of OPVs, in agreement with what has been reported in literature for this type of blend systems. Thusly, going forward, TA will continue to be used as it is a proved method to benefit the formation of a more suitable morphology. In the next Chapter, the formulation aspect of device design is investigated, in the form of adding a third component to the active layer and the usage of other processing methods such as co-solvents, to discern the impact of the additional component in the performance of OPVs.

4.5 References

1. Berger, P.R. and M. Kim, *Polymer Solar Cells: P3HT:PCBM and Beyond.* J. Renew. Sustain. Energy, 2018. **10**(1).

2. Huang, Y., et al., *Bulk Heterojunction Solar Cells: Morphology and Performance Relationships.* Chem. Rev., 2014. **114**(14): p. 7006-7043.

3. Liao, H.C., et al., *Quantitative Nanoorganized Structural Evolution for a High Efficiency Bulk Heterojunction Polymer Solar Cell.* J. Am. Chem. Soc., 2011. **133**(33): p. 13064-13073.

4. Erb, T., et al., *Correlation Between Structural and Optical Properties of Composite Polymer/Fullerene Films for Organic Solar Cells.* Adv. Funct. Mater., 2005. **15**(7): p. 1193-1196.

5. Yue Zhao, G.Y., Philippe Roche, Mario Leclerc, *A Calorimetric Study of the Phase Transitions in Poly(3-hexylthiophene).* Polymer, 1995. **36**(11): p. 2211-2214.

6. Verploegen, E., et al., *Manipulating the Morphology of P3HT–PCBM Bulk Heterojunction Blends with Solvent Vapor Annealing.* Chem. Mater., 2012. **24**(20): p. 3923-3931.

7. Wang, Q., et al., *Progress in Emerging Solution-Processed Thin Film Solar Cells – Part I: Polymer Solar Cells.* Renew. Sust. Energ., 2016. **56**: p. 347-361.

8. Brabec, C.J., Sariciftci, N.S. and Hummelen, J.C., *Plastic Solar Cells.* Adv. Funct. Mater., 2001. **11**: p. 15-26.

9. Wodo, O. and B. Ganapathysubramanian, *Modeling Morphology Evolution During Solvent-Based Fabrication of Organic Solar Cells.* Comput. Mater. Sci., 2012. **55**: p. 113-126.

10. Norrman, K., A. Ghanbari-Siahkali, and N.B. Larsen, *6 Studies of Spin-Coated Polymer Films.* Annu. Rep. Prog. Chem., Sect. C: Phys. Chem, 2005. **101**: p. 174-201.

11. Xiaoniu Yang, J.L., Sjoerd C. Veenstra, Wiljan J. H. Verhees, Martijn M. Wienk, Jan M. Kroon, Matthias A. J. Michels, and René A. J. Janssen, *Nanoscale Morphology of High-Performance Polymer Solar Cells.* Nano Lett., 2005. **5**(4): p. 579-583.

12. Min, J., et al., *Gaining Further Insight into the Effects of Thermal Annealing and Solvent Vapor Annealing on Time Morphological Development and Degradation in Small Molecule Solar Cells.* J. Mater. Chem. A, 2017. **5**(34): p. 18101-18110.

13. Liping Zheng, Q.Z., Xianyu Deng, Min Yuan, Gang Yu, and Yong Cao, *Methanofullerenes Used as Electron Acceptors in Polymer Photovoltaic Devices.* J. Phys. Chem. B, 2004. **108**(32): p. 11921-11926.

14.   Karagiannidis, P.G., et al., *Thermal Annealing Effect on the Nanomechanical Properties and Structure of P3HT:PCBM Thin Films.* Thin Solid Films, 2011. **519**(12): p. 4105-4109.

15.   Jin, S.-H., et al., *Optimization of Process Parameters for High-Efficiency Polymer Photovoltaic Devices Based on P3HT:PCBM System.* Sol. Energy Mater. Sol. Cells, 2007. **91**(13): p. 1187-1193.

16.   Mihailetchi, V.D., et al., *Charge Transport and Photocurrent Generation in Poly(3-hexylthiophene): Methanofullerene Bulk-Heterojunction Solar Cells.* Adv. Funct. Mater., 2006. **16**(5): p. 699-708.

17.   Li, G., et al., *High-Efficiency Solution Processable Polymer Photovoltaic Cells by Self-Organization of Polymer Blends.* Nat. Mater., 2005. **4**(11): p. 864-868.

18.   Shrotriya, V., et al., *Absorption Spectra Modification in Poly(3-hexylthiophene):Methanofullerene Blend Thin Films.* Chem. Phys. Lett., 2005. **411**(1-3): p. 138-143.

19.   Kim, Y., et al., *A Strong Regioregularity Effect in Self-Organizing Conjugated Polymer Films and High-Efficiency Polythiophene:Fullerene Solar Cells.* Nat. Mater., 2006. **5**(3): p. 197-203.

20.   Liao, H.C., et al., *Insights into Solvent Vapor Annealing on the Performance of Bulk Heterojunction Solar Cells by a Quantitative Nanomorphology Study.* RSC Adv., 2014. **4**(12): p. 6246-6253.

21.   Xiao, S., Q. Zhang, and W. You, *Molecular Engineering of Conjugated Polymers for Solar Cells: An Updated Report.* Adv. Mater., 2017. **29**(20): p. 1601391.

22.   Karagiannidis, P.G., et al., *Evolution of Vertical Phase Separation in P3HT:PCBM Thin Films Induced by Thermal Annealing.* Mater. Chem. Phys., 2011. **129**(3): p. 1207-1213.

23.   Lan, S., et al., *Importance of Solvent Removal Rate on the Morphology and Device Performance of Organic Photovoltaics with Solvent Annealing.* ACS Appl. Mater. Interfaces, 2017. **9**(24): p. 20679-20685.

24.   Yun, M.H., et al., *Towards Optimization of P3HT:bisPCBM Composites for Highly Efficient Polymer Solar Cells.* J. Mater. Chem., 2010. **20**(36).

25.   Shih, C.-F., et al., *In Situ Monitoring of Photovoltaic Properties in Organic Solar Cells During Thermal Annealing.* Org. Electron., 2012. **13**(3): p. 373-376.

26.   Kadem, B., A. Hassan, and W. Cranton, *Efficient P3HT:PCBM Bulk Heterojunction Organic Solar Cells; Effect of Post Deposition Thermal Treatment.* J. Mater. Sci.: Mater. Electron, 2016. **27**(7): p. 7038-7048.

27.   Swinnen, A., et al., *Tuning the Dimensions of C60-Based Needlelike Crystals in Blended Thin Films.* Adv. Funct. Mater., 2006. **16**(6): p. 760-765.

28. Hoppe, H. and N.S. Sariciftci, *Morphology of Polymer/Fullerene Bulk Heterojunction Solar Cells.* J. Mater. Chem., 2006. **16**(1): p. 45-61.

29. Savenije, T.J., et al., *The Effect of Thermal Treatment on the Morphology and Charge Carrier Dynamics in a Polythiophene-Fullerene Bulk Heterojunction.* Adv. Funct. Mater., 2005. **15**(8): p. 1260-1266.

30. Padinger, F., Rittberger, R. and Sariciftci, N., *Effects of Postproduction Treatment on Plastic Solar Cells.* Adv. Funct. Mater., 2003. **13**: p. 85-88.

31. Li, G., et al., *"Solvent Annealing" Effect in Polymer Solar Cells Based on Poly(3-hexylthiophene) and Methanofullerenes.* Adv. Funct. Mater., 2007. **17**(10): p. 1636-1644.

32. Babics, M., et al., *Solvent Vapor Annealing-Mediated Crystallization Directs Charge Generation, Recombination and Extraction in BHJ Solar Cells.* Chem. Mater., 2018. **30**(3): p. 789-798.

33. Servaites, J.D., M.A. Ratner, and T.J. Marks, *Organic Solar Cells: A New Look at Traditional Models.* Energy Environ. Sci., 2011. **4**(11): p. 4410-4422.

34. Aloui, W., et al., *Effect of Thermal Annealing on the Electrical Properties of P3HT:PC 70BM Nanocomposites.* Mater. Sci. Semicond. Process., 2015. **39**: p. 575-581.

35. Onojima, N., et al., *Raman Study of Bulk-Heterojunction Morphology in Photoactive Layers Treated with Solvent-Vapor Annealing.* Jpn. J. Appl. Phys., 2018. **57**(3S2).

36. Miao, J., et al., *Efficiency Enhancement in Solution-Processed Organic Small Molecule: Fullerene Solar Cells Via Solvent Vapor Annealing.* Appl. Phys. Lett., 2015. **106**(18).

37. Brown, P.J., et al., *Effect of Interchain Interactions on the Absorption and Emission of Poly(3-hexylthiophene).* Phys. Rev. B, 2003. **67**(6).

38. Kim, Y.J., T.K. An, and C.E. Park, *Morphological Studies of Small-Molecule Solar Cells: Nanostructural Engineering Via Solvent Vapor Annealing Treatments.* J. Mater. Sci., 2017. **52**(22): p. 13173-13182.

CHAPTER 5

DESIGN RULES FOR TERNARY BLEND OPVs FABRICATED WITH FULLERENE ACCEPTOR ALLOYS

5.1 Introduction

As discussed in Chapter 4, the performance of an OPV device is strongly related to the BHJ morphology, which ultimately dictates the main PV figures of merit. In this Chapter, the formulation method is introduced, in which a third component is added to the active layer of binary OPVs in order to discern the impact on the performance.

In ternary blends, the third component offers the opportunity to optimise electrical properties beyond which is possible in binary blends. Considering all the different choice of materials and processing conditions that ternary blends can display, how can one best design and optimise an OPV? In recent past different approaches have been explored to fabricate ternary blends, for example: by blending two donors and one acceptor [1], three donor (polymeric) materials [2] and more recently one donor and two acceptors [3]. Although valuable results have been derived from these studies, to date, a methodology which compares insights across different blend systems is still lacking. Thus, in order to use ternary blends as a methodology to improve the efficiency of OPVs, understanding of material selection and device fabrication is of great interest to OPV researchers.

In this Chapter, this question is examined by fabricating two ternary systems, specifically PTB7:$PC_{71}BM$ and P3HT:$PC_{71}BM$ in which ICBA is added as a third component, both with and without the processing additive 1,8-diiodooctane (DIO). To begin, we first recapitulate on fundamental concepts of ternary blends, different types of ternaries and novel advances from literature. Secondly, we describe the fullerene alloy model consisting of one polymer donor and two fullerene derivatives. Following, experimental results are outlined which include electrical characterisation, molecular schematics, modelling and morphological studies on the bulk and surface of OPVs.

Lastly, the results from this Chapter provide vital information about the morphology and performance of these blends, which can assist OPV engineers to design future ternary OPVs with fullerene alloys.

5.2 Ternary blends and fundamental principles

We begin this section by summarising what are ternary blends and why is it relevant to study them. Over the past years, binary BHJ have become the gold standard of OPV fabrication because of the high efficiencies that can be achieved [4]. In principle, to further increase the PCE in binary OPVs the V_{OC}, J_{SC} and FF should be enhanced [5]. Nonetheless, binary OPVs are limited by a narrow absorption since the photoactive layers can only harvest photons from equal or greater energies than their bandgap [5]. Further, as stated in previous Chapters, organic semiconductors normally yield low charge carrier mobilities [6], which can also limit OPV devices to <200 nm thicknesses to ensure efficient charge collection [7]. Unfortunately, this means that because of such thin films, not all incoming light is absorbed. A promising strategy to tackle these binary OPV bottlenecks, is through the addition of a third component into the active layer -the ternary blend- which can be another donor or acceptor component [8].
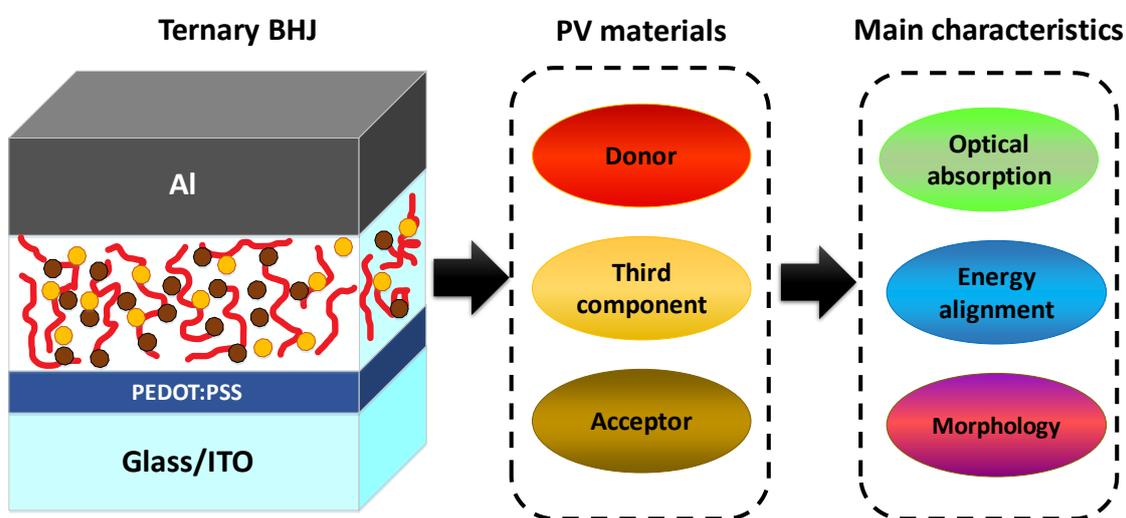
Figure 5.1. Representation of a conventional ternary blend (left) where the red lines denote polymer chains, the yellow circles an acceptor (i.e. fullerene) and the brown circles the third component. The PV materials used to fabricate ternary blends are shown in the centre and some of the key characteristics that can be optimised with this strategy on the right. Schematic adapted from: [9].

In recent past, ternary blends have demonstrated to be an effective method to increase efficiency compared to binary OPVs since they can display a number of advantages which include: 1) It retains the fabrication conditions used in binary blends plus broadening the absorption bandwidth of the active layer as in a multi-junction device [10]. 2) Strategies that have been used to optimise binary blends can also be applied to ternary blends (thermal annealing, solvent additives, different D:A ratios, and more) [11]. 3) Appropriate material selection can provide efficient exciton dissociation, charge transfer and assist in reducing recombination [12]. 4) The morphology can be improved which may facilitate a suitable molecular organisation to improve charge generation, transport and collection [13]. Figure 5.1 presents a general schematic of a ternary blend OPV and some of the key characteristics that can be enhanced. Inspiringly, ternary OPVs have almost exceeded 17% in efficiency thus showing great potential for this method to fabricate high performing solar cells [14]. Ternary blends are generally made up of a dominating D:A constituents, plus an additional component added to the active layer which can be other: polymers [2], fullerenes [15], Non-fullerenes (NFA) [16], dyes [17], small molecules [18], quantum dots [19] and nanoparticles [20].

Although many authors have demonstrated that ternary blend OPVs can effectively be used to increase the main PV parameters and ultimately PCE [21-23], however, many aspects remain to be understood, to name a few, the location of the third component in the blend, recombination mechanisms, and the tuneability of V_{OC} and J_{SC}. To address these issues, several classifications and models have been developed which are discussed next.

5.3 Operating methodologies of ternary blends

Due to the incorporation of an additional material in the active layer, the governing PV mechanisms in ternary blends are different from that of their binary counterparts, and is more than just the superposition of PV processes of the individual OPV blends [11]. Based on the functionality or design approach, ternary blends are generally classified into four different categories, namely: the charge transfer, energy transfer, parallel-like model and the alloy model (Figures 5.2 and 5.3). Since the objective of adding an additional component to make up the active layer is to enhance PCE of the OPV device, it is normally reported in literature that it can be done through electronic and/or structural changes [11]. Electronically, the additional component can assist in

energy charge transfer, and structurally, it can contribute by facilitating an optimised molecular assembly in the film, which can favour charge dissociation and charge transport [13]. These mechanisms which are related to where the additional component is located in the BHJ, are briefly explained below. For a full in-depth review on these mechanisms, readers are referred elsewhere [5, 8, 11].

5.3.1 Charge and energy transfer mechanisms

In ternary OPVs where a charge transfer mechanism governs, the energy levels of the third component should ideally be in between the LUMO and HOMO of the main donor and acceptor to form an energy cascade alignment [10, 13]. To illustrate an example, considering the third component as an acceptor in Figure 5.2a, excitons generated in D_1 or A_1 can dissociate into charge carriers at the D:A_1 or D:A_2 interfaces and holes can travel through the channels formed of the donor and the electrons via the acceptors domains [10, 11]. Since holes are collected by the channel made by the donor (higher HOMO level) the V_{OC} in these ternary blends is close to the smaller V_{OC} of the binary analogues [10].
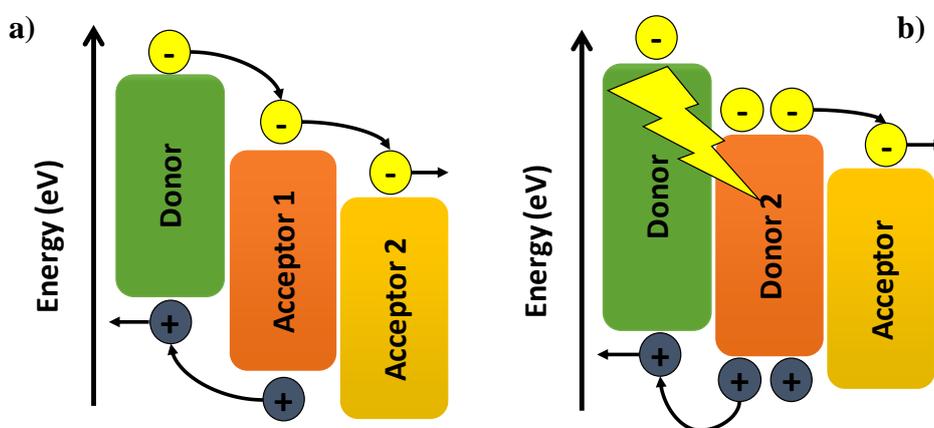
Figure 5.2. Ternary OPV mechanisms: charge transfer a) and energy transfer b). Adapted from: [13]. Note that these models can also be represented by D_1:D_2:A and D:A_1:A_2 systems.

The second model is the energy transfer model, otherwise known as Förster or Dexter Resonance Energy Transfer [11, 24]. In order to achieve an efficient energy transfer with this model, ternary blends require a short distance (<10 nm) between the third component and the D_1 (or A_1), as well as overlap with the emission spectrum of D_1 (or A_1) and the absorption spectrum of the third component [25]. Considering a system

of D_1:D_2:A as shown in the Figure 5.2b, exciton energy from D_1 can be transferred via "energy transfer" to D_2, and the excitons that are generated in D_2 can dissociate into charge carriers at D_2:A interface. Then, electrons are transported to the cathode via the acceptor channels whilst holes in D_2 can directly transport to the anode or transfer to D_1 and then to the anode via channels formed by D_1. As observed elsewhere, the charge transfer and energy transfer mechanism can occur concurrently in ternary blends [10].

5.3.2 Parallel-like and alloy model mechanisms

To explain the parallel linkage mechanism in ternary OPVs, let us consider a ternary structure of D_1:D_2:A as depicted in Figure 5.3a. In here, excitons generated in donor domains can dissociate at the D_1:A or D_2:A interfaces into free carriers. Then, holes would be transported to the anode by the two-donor parallel formed channels whilst electrons are transported only via the acceptor channel to the cathode [11]. In this ternary mechanism, the energy transfer or charge transfer is absent between two donors or two acceptors, which is similar to a parallel connection of individual OPVs and hence the name [11]. To describe this model in a few words, complementary donors absorb light, split excitons and transport holes, meaning that each donor forms its own transport pathways [13].
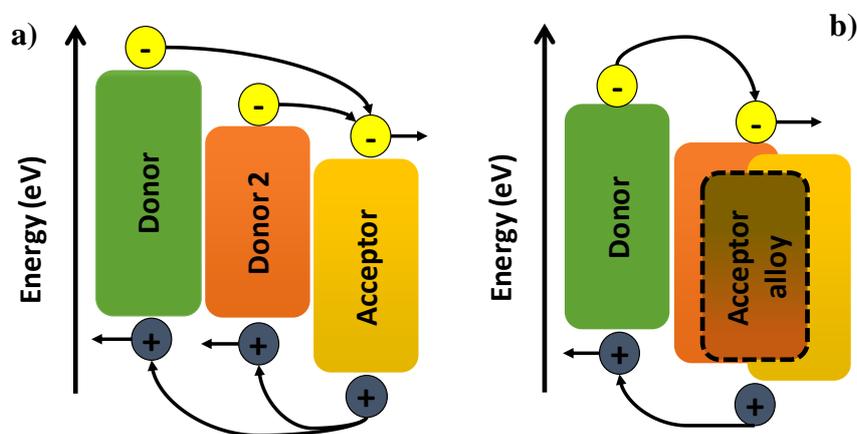
Figure 5.3. Ternary OPV mechanisms: parallel-linkage a) and an acceptor alloy model b). Adapted from: [13]. Note that these models can also be represented by D_1:D_2:A and D:A_1:A_2 systems.

In contrast, in the alloy model mechanism, instead of each component forming its own transport channel as in a parallel linkage, two electronically similar materials (two donors or two acceptors) form an electronic 'alloy' (Figure 5.3b) such that they become

111

electronically coupled to form a new state [10, 11, 13]. However, these two acceptors or donors still retain individual molecular properties and the HOMO and LUMO levels of the alloy are dependent on the composition of the third component in the blend. Hence, V_{OC} depends on the composition of the acceptor or donors in the blend [13]. Additionally, J_{SC} may be increased by complementary absorption via the third component [10]. In these ternary blends, the main and host donors or acceptors are required to have good miscibility and similar electronic properties for the alloy formation [10].

To wrap up this section, there is no strict limitation that says that one's blend will fall into a certain category, and in practice, it is commonplace to have these mechanisms intertwined and having different models occur in a ternary blend, thus complicating the prediction of governing PV mechanisms [25]. Further, some aspects of these models are still debated in literature, specifically, the alloy model which has been unable to explain the raise in V_{OC} in fullerene based OPVs with increasing ratios of the third component [13]. Thusly, in the upcoming sections, the main focus will be on ternary blends with organic alloys.

5.4 P3HT and PTB7-based OPVs blended with fullerene alloys

As observed from the previous sections, the role of the third component in ternary blends is still matter of debate and many studies have been published recently to underpin the underlying physics [13, 25]. Why is there a raise in V_{OC} in ternary blends with alloy? How do the effects of a ternary component generalise to a specific morphology? In this Chapter, we resolve these pressing questions by systematically examining two blend systems with fullerene alloys in which the donor material is different. But before we move onto the experimental data, first we present relevant literature comprising ternary blends with fullerene alloys.

To start, among the different strategies to fabricate ternary blends, fullerene alloys which include polymers mixed with a combination of fullerene acceptors (i.e. PCBM:ICBA) have recently emerged as an effective route to further improve PV properties in OPVs [26-28]. Thompson et al. [26, 27] first proposed the alloy model in P3HT with PCBM:ICBA, where the V_{OC} could be effectively tuned in ternary solar cells by varying the composition of fullerenes. For instance, a ~40 wt% ICBA resulted in a ~64 mV increase in V_{OC} compared to the P3HT:PCBM binary blend, however, J_{SC}

decreased for all ICBA combinations [26]. Now, in ternary blends it was generally predicted that V_{OC} would be pinned down to the smaller V_{OC} of the corresponding binary blend components [29]. However, these results demonstrated experimentally that ternary OPVs could maximise V_{OC} and exceed binary BHJ efficiencies.

Further, Angmo et al. [30] verified that mixed fullerenes form an alloy in ternary blends of P3HT:ICBA:PCBM with solid-state nuclear magnetic resonance (NMR). Following device optimisation, a PCE of 2.37% was realised with the ternary blend alloy exceeding its binary equivalents. Similarly, other authors have proved that ternary OPVs with and acceptor alloy and low band gap polymers can indeed lead to higher performing OPVs [28, 31]. For instance, the usability of the alloy comprised of ICBA:PC_{71}BM was tested with 5 different polymers in which all of them showed increased in performance of ~12% in contrast to devices fabricated with PC_{71}BM [32]. Cheng et al [33] fabricated ternary blends with ICBA:PC_{71}BM and low bandgap PTB7 polymer. Contrarily to P3HT, the enhancement of V_{OC} was moderate with PTB7 as the donor, yet J_{SC} improved until a certain threshold (~20% - 30% ICBA content) prior to reducing. Further, although hole and electron mobilities remained relatively unchanged between the binary and ternary blends, ICBA enhanced the external quantum efficiency (EQE) which was attributed due to a cascade formation all of which resulted in an overall 12% PCE enhancement. Similarly, Sharma et al [34] introduced ICBA as a third component in PTB7:PC_{71}BM blend to elucidate critical information for OPV design. In their study, 10 wt% ICBA increased EQE which was correlated to improved charge dissociation as revealed by transient absorption studies, while higher concentrations of ICBA yielded more recombination.

More recently, blends of NFAs have also demonstrated encouraging results in state-of-the art OPVs [16, 35, 36]. Lu et al. [37] presented a ternary blend of PPBDTBT donor with ITIC:PC_{71}BM as the acceptor materials, in which ITIC extended the light absorption whilst PC_{71}BM reduced the aggregation of ITIC as seen with TEM images. Despite an increase in J_{SC} and PCE with the ternary blends, V_{OC} progressively decreased with the increasing weight ratio of the fullerene, thus evidencing no intimate acceptor alloy. Although these papers have shed light on how specific ternary blend systems operate, it remains unclear how the effects of a third component in OPVs generalise to specific morphologies in new blend systems. The novelty of this Chapter is that we seek to provide insights into this question by comparing two ternary blend systems based on

different donor materials but with the same fullerene acceptor and concentrations of ternary components. In the next section, we discuss the fabrication conditions of the OPVs investigated in this Chapter.

5.5 Fabrication of binary and ternary OPVs

In order to investigate how can one best optimise ternary OPVs, blends of PTB7:ICBA:PC$_{71}$BM and P3HT:ICBA:PC$_{71}$BM were fabricated, and as the control references the binary blends of PTB7:PC$_{71}$BM and P3HT:PC$_{71}$BM. Further, as discussed in the previous section, ICBA:PC$_{71}$BM have shown to form a fullerene alloy under certain circumstances, and hence the selected ternary blend systems may display a wide range of behaviours that may occur in ternary OPV blends in general.
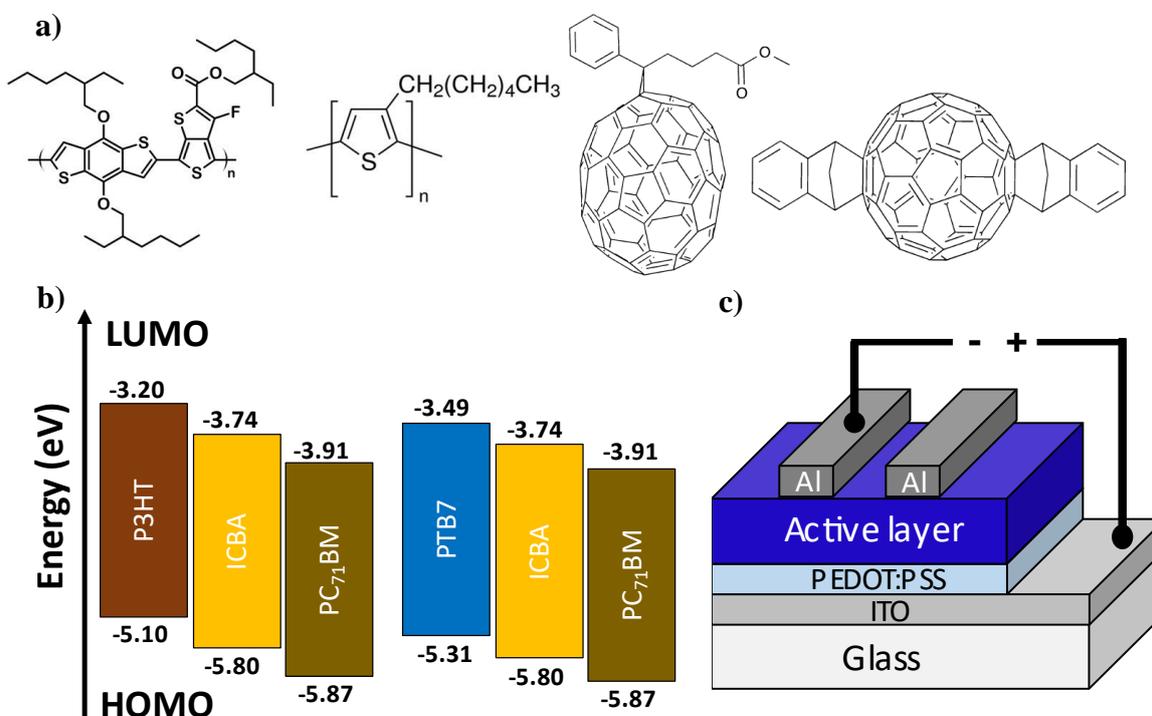
Figure 5.4. a) Molecular structure of materials used: PTB7, P3HT, PC$_{71}$BM and ICBA (from left to right), b) energy levels and c) OPV device configuration. Energy levels from [33, 38].

The molecular structure of materials and energy levels are depicted in Figure 5.4a, b. The architecture of all OPVs discussed in this Chapter was glass/ITO/PEDOT:PSS/Active layer/Al as shown in Figure 5.4c. The active layers were fabricated with a 1:1.5 donor and fullerenes acceptor ratios for PTB7-OPVs and 1:1 for P3HT-OPVs since these have been observed to be the optimum ratios for each type of

114

blend [39-43]. A total of 8 nominally same repeats of each type of blend were fabricated yielding 96 OPV devices; 48 for each ternary blend system in which the wt% of ICBA was increased from 0% to 30%. All measurements were carried down on a cleanroom environment and to ensure repeatability, typical devices rather than hero devices are reported. The impact of morphology was examined by fabricating devices both with and without the additive DIO, since previous investigations have demonstrated that 3 vol% DIO when used as a co-solvent in PTB7 and P3HT blends can assist in achieving higher performances [44-46]. We now turn to the full characterisation of binary and ternary OPVs.

5.6 Photovoltaic trends: Open-circuit voltage (V_{OC})

To set all of the upcoming analysis into context, we will begin by discussing the variation in PV parameters for P3HT and PTB7-based OPVs as a function of ICBA and DIO. For reference, the J-V curves and PV statistics are included in the Appendix 5.1 and 5.2 respectively. We start by rationalising the increase in V_{OC} of P3HT-blends (Figure 5.5a) which interestingly, stands out abruptly with the addition of ICBA. It can be seen that at 25 wt% of ICBA, V_{OC} is enhanced by 200 mV and 100 mV without and with DIO respectively compared to its reference counterpart. On the other hand, V_{OC} decreases 40 mV with no DIO and increases 20 mV when added into PTB7-blends for the same ICBA concentrations. Indeed, our results also demonstrate that V_{OC} appears to be determined by the mixing ratio of the fullerene compounds, rather than being pinned down to the lowest acceptor energy level [26, 27, 30]. Now, the difference in V_{OC} shift for the same change in fullerene composition between different blend systems has not been elucidated in literature and our contribution is to explain this difference.

To rationalise why, we begin by hypothesising that the formation of an alloy implies intimate mixing of the two fullerene components somewhere in the blend. Like so, the differing morphology of the two blend systems may hold some proof as to why the alloying behaviour is different. Although PCBM has been shown to be miscible in PTB7 [47] and in amorphous P3HT [48], leading to an amorphous polymer:fullerene phase in both blend systems, we note that the side-chain density of P3HT is high compared to other donor:acceptor polymers [49].
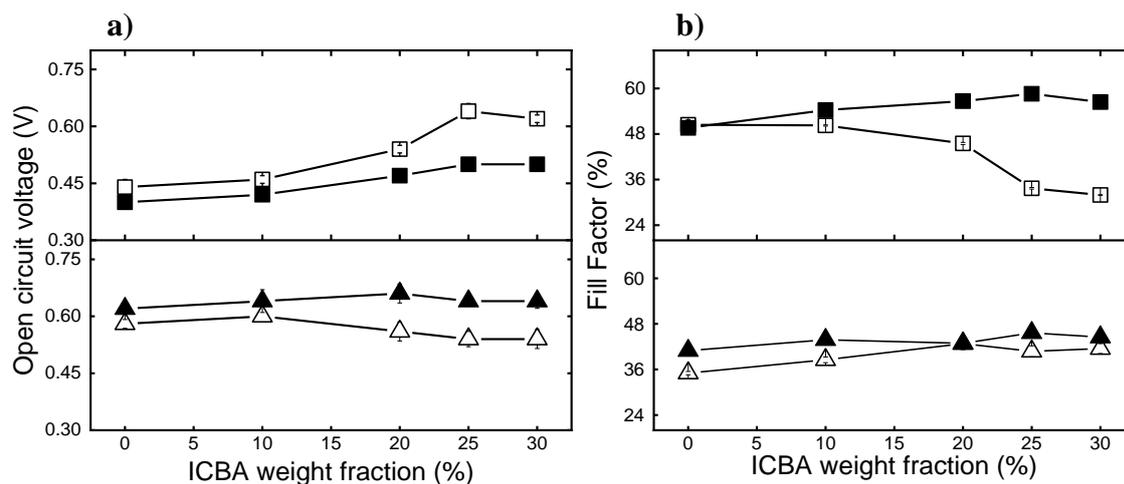
Figure 5.5. Variation of a) V_{OC} and b) FF as a function of ICBA added to the P3HT:PC$_{71}$BM (black square) and PTB7:PC$_{71}$BM blends (black triangle) in 0%, 10%, 20%, 25% and 30%. Open figures denote OPVs without DIO and solid figures with 3% of DIO respectively.

A result of this high side-chain density is that PCBM does not intercalate into P3HT crystalline regions [43, 48]. Consequently, we propose that fullerene molecules do not readily interpose between P3HT side-chains (Figure 5.6a) in either the crystalline or amorphous phases, and that as a consequence, fullerenes are excluded to other regions in the blend where they form an alloy.
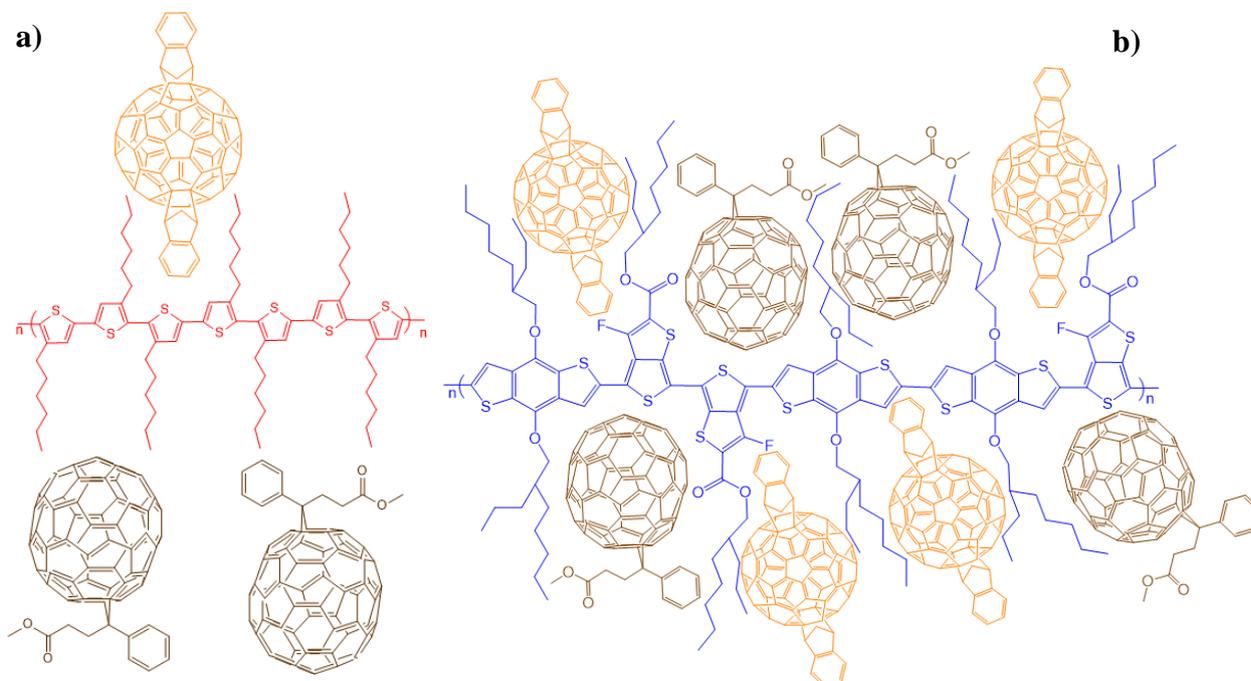
Figure 5.6. Molecular schematics on a planar conformation configuration of how polymers may interpose PC$_{71}$BM (brown) and ICBA (orange) between side-chains, showing a) P3HT (red) and b) PTB7 (blue). As a reference, fullerene diameter ~10 Å [50] and a PTB7 monomer length ~16 Å [51].

Conversely, we argue that the impact of alloying is less strong in the PTB7 blends as fullerenes can more easily interpose between the side-chains, which we define as molecular intermixing (Figure 5.6b). There is indirect evidence of molecular intermixing in PTB7:fullerene blends as optimised blends require an excess of fullerene [43], side-chains have weak orientational uniformity [52, 53], and that PCBM molecules disrupt π-π stacking in PTB type polymers generally [54]. To investigate this claim, we conducted a survey on literature regarding ternary blends utilising ICBA:PCBM alloy as acceptors and similar processing conditions that is included in the Appendix 5.3. From this table, we found that polymer donors that support molecular intermixing (i.e. PTB7 and PBTTT-C14) had similar small increases in V_{OC} when $30-40$wt% of ICBA was added, compared to the binary control [28, 33, 34], which is in agreement with our hypothesis. Conspicuously, we believe PBTTT-C14 is an interesting comparison to the current data as it is both crystalline (as P3HT) and has a structure that permits PCBM molecules to site between side-chains (as argued for PTB7) [55], and also describes modest increases in V_{OC} with the addition of ICBA (as observed for PTB7) [28]. On the other hand, P3HT was the only example of a polymer that was not favourable to molecular intermixing which has been used in ICBA:PCBM ternary blends, but what evidence has been reported also agrees with our observation of a larger V_{OC} with the addition of ICBA [26, 27].

In addition, we also investigated literature on more widely reported binary blends and whether the donor polymer supported or not molecular intermixing (Table 5.1) by numerous techniques. This analysis further corroborates that P3HT is unusual in its high side-chain density, since numerous systems do support intercalation, to name a few: PTT, PQT, PBTTT, PCDTBT, and PFBT-T20TT [43, 56, 57], whereas P3HT does not. Hence, it appears that the degree of molecular mixing is a key element to a full benefit of V_{OC} provided by a fullerene alloy.

5.6.1 Fill Factor (FF)

Momentarily going back to Figure 5.5, we observe that the FF is not largely affected by the addition of ICBA in all cases with the exception of the P3HT ternaries without DIO. As noted, the devices with DIO maintained a similar FF to the binary control. Since reduction in FF for P3HT-based ternaries with more than 20 wt% ICBA may be due to poor charge transport, we take a closer look at the surface and bulk morphologies to elucidate any crystalline structures or their absence.

Donor	Acceptor	Intercalation or molecular intermixing	Additive	Evidence of intercalation or molecular intermixing	Ref.
P3HT	PCBM	No	-	Schematics[50, 43]	43, 50, 55
	ICBA	No	-	-	58
PATBT	PCBM	No	-	PL	59
BisOC$_{10}$-PPV	PCBM	No	-	Schematics	43
PTB1	PCBM	Yes	-	X-ray	60
PTB7	PCBM	Yes	2% DIO	X-ray	61
PTB7	PC$_{71}$BM	Yes	3% DIO	Schematic[62], X-ray,[47, 63] PL[45]	45, 47, 62, 63
PTB7-Th	PC$_{71}$BM	Yes	3% DIO	PL[32, 64, 65], X-ray[32, 64, 65], Raman[65]	32, 64, 65
MDMO-PPV	PCBM	Yes	-	Schematics[43, 66] PL[66], SEM[66]	43, 66
	PC$_{71}$BM	Yes	-	SEM, PL	66
PTT	PCBM	Yes	-	Schematics, X-ray	43
PQT	PCBM	Yes	-	Schematics, X-ray	43
PBTTT	PC$_{71}$BM	Yes	-	Schematics, X-ray	43
	PCBM	Yes	-	X-ray[43], PL[59]	43, 59
	ICBA	Yes	-	Schematics, X-ray	58
PBTCT	PCBM	Yes		PL	59
PBTTT-C14	PCBM	Yes	5.3% Me12	Schematics, X-ray, PL	67
	PC$_{71}$BM	Yes	-	Schematics	55
PCDTBT	PC$_{71}$BM	Yes	-	Schematics[43], PL[56]	43, 56
PFBT-T20TT	PC$_{71}$BM	Yes	-	X-ray	57

Table 5.1. Materials with evidence of intercalation or intermixing reported by various methods. Schematics stand for chemical drawings, PL for Photoluminescence, X-ray for X-ray studies (i.e. GIXS), SEM for Scanning Electron Microscopy and Raman for Raman Spectroscopy. PTB7-Th is also known as PBDTTT-EFT. Ref. from table: [32, 43, 45, 47, 50, 55-67].

In this study, we used a combination of AFM and TEM because of the complementary data obtained: with AFM surface features can be observed whilst TEM reveals a projection of the bulk structure [68, 69]. First, the P3HT:PC$_{71}$BM control blend with no DIO presented a smooth surface roughness of ~1.1 nm which was further reduced to ~0.68 nm considering a 30 wt% ICBA as observed in Figure 5.7a, b. In these blends, adding the ICBA did not significantly modify the surface topography and a low phase separation is clear between the components. Contrarily, binary and ternary P3HT blends with DIO (Figure 5.7c, d) revealed a more crystalline and coarser surface with root mean square (RMS) roughness in the order of 7 nm for all ICBA combinations. In agreement with surface topography, TEM imaging reveals an extensive P3HT crystalline network in high ICBA wt% OPVs with DIO (Figure 5.7h), whilst such structure is not found on OPVs prepared with no additive (Figure 5.7e, f).
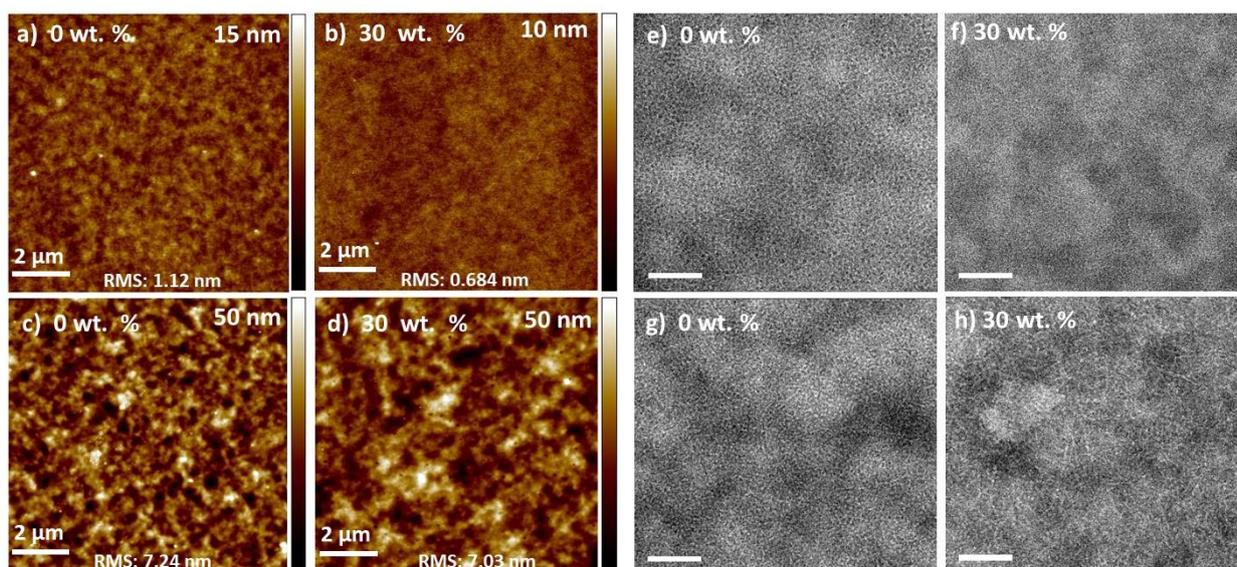
Figure 5.7. AFM topography and TEM morphology images of P3HT:PC$_{71}$BM binary blends without (a, e,) and with (c, g,) DIO, and ternary P3HT:ICBA:PC$_{71}$BM (30 wt%) without (b, f) and with (d, h) DIO. On TEM images, scale bar represents 200 nm.

Interestingly, this lack of crystalline structure on devices with no DIO provides good evidence to the reduction in FF observed in the PV trends, attributed to poor charge transport [70], further validated by the reduced dark diode current (Appendix 5.1a). However, it is also possible that P3HT-based ternaries with more than 20wt% ICBA are impacted by a poor interface between the film surface and cathode, as the J-V curves for these devices have an S-shaped characteristic. Further, the morphologies depicted in here are accurate since similar trends have been reported by previous authors [46, 71]. Additional scans of AFM, TEM with corresponding film thicknesses are provided in Appendixes 5.4 − 5.7.

5.7 Photovoltaic trends: Short-circuit current (J$_{SC}$)

Let us now turn the attention towards the variations of J$_{SC}$ for each type of blend. It can be observed from Figure 5.8a that increasing the content of ICBA reduces the J$_{SC}$ for all combination of devices, with the exception of PTB7-blends in which J$_{SC}$ is largely enhanced. For instance, in the PTB7:PC$_{71}$BM reference blend with no DIO, a J$_{SC}$ of 4.3 mA/cm^2 was attained, which was drastically increased to 8.4 mA/cm^2 with DIO and even further to 9.1 mA/cm^2 when a 25 wt% ICBA was added in the blend. This improvement in J$_{SC}$ was sufficient to yield a higher PCE (Figure 5.8b) compared to its binary counterpart.
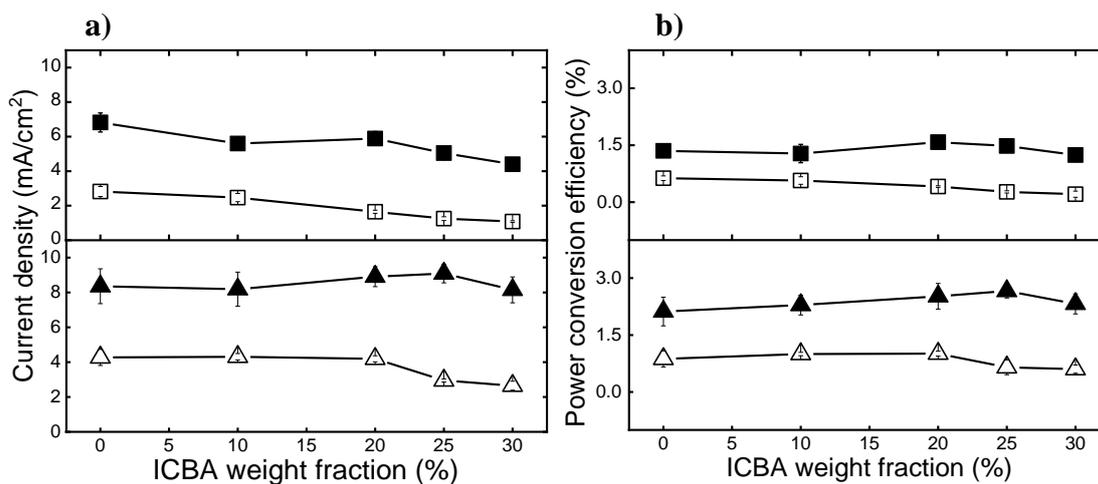
Figure 5.8. Variation of a) J_{SC} and b) PCE as a function of the amount of ICBA added to the P3HT:PC$_{71}$BM (black square) and PTB7:PC$_{71}$BM blends (black triangle) in 0%, 10%, 20%, 25% and 30%. Open figures denote OPVs without DIO and solid figures with 3% of DIO respectively.

Again, experimental results showed a different behaviour for P3HT-blends, whereby DIO improved the PV characteristics but J_{SC} decreased for all combinations with ICBA compared to the corresponding control. Having compared the J_{SC} between both blend systems, an important question arises which is why is it that J_{SC} increases in PTB7-based OPVs with DIO, but decreases for all other combinations?

To further understand the difference in J_{SC} behaviour when ICBA and DIO are added, we measured the EQE spectra. This is a relevant measurement because it tells us about the ratio of collected photo generated charges to the number of incident photons [72] and is the product of four efficiencies: $\eta_{absorption}(\lambda) * \eta_{exciton\ diffusion}(\lambda) * \eta_{charge\ separation}(\lambda) * \eta_{charge\ collection}(\lambda)$ [72, 73], thus revealing important insights about recombination mechanisms competing with charge extraction. Figure 5.9 presents the EQE profiles for both ternary systems, showing the spectral response ranging from 400 nm to 700 nm. In the case of PTB7-blends with ICBA and DIO, the EQE spectra demonstrated efficient photo conversion from 400 nm extending to 700 nm, with a maximum EQE of ~50% at 600 nm. The overall result was an EQE improvement in the order of 20% compared to the binary equivalent. We also notice that the trends reported here for both blend systems are in agreement with high cited papers from literature [33, 34, 45, 74-78].
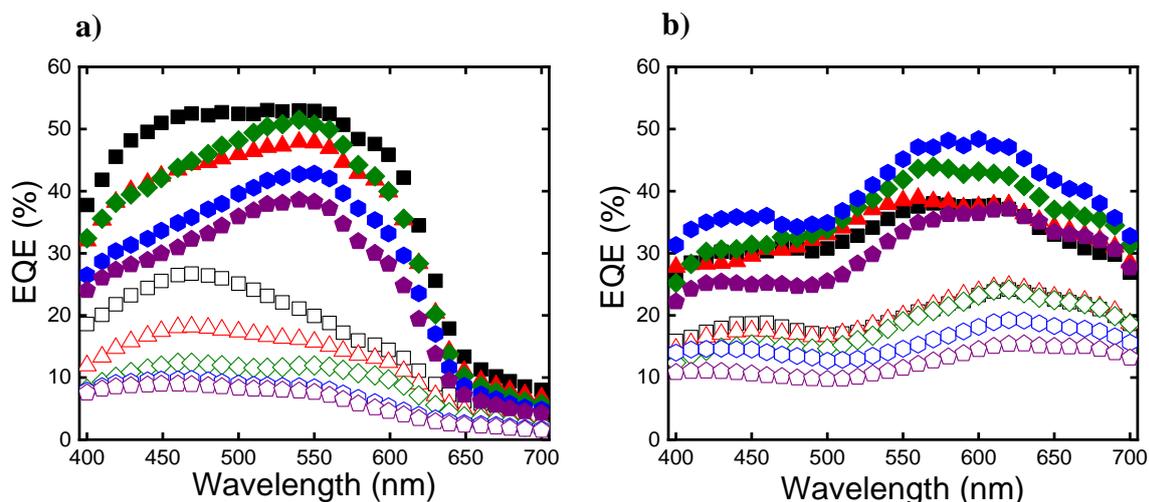
Figure 5.9. EQE spectra of a) P3HT:PC$_{71}$BM and b) PTB7:PC$_{71}$BM prepared with 0% (black) and an additional 10% (red), 20% (green), 25% (blue) and 30% (purple) concentration of ICBA with and without 3% of DIO. Solid figures represent OPVs with DIO and open figures represent OPVs without DIO.

Regarding the P3HT-blends contribution, the binary EQE was much higher than that of its ternary counterparts, that is attributed to a more crystalline order of P3HT fibrils because of the additive [46, 79], which is in agreement with TEM and AFM images shown previously on Figure 5.7. On the other hand, we note that in PTB7-based OPVs (Figure 5.10), the surface and bulk morphologies reveal large agglomerates (>150 nm) which increase in size as ICBA is added onto blends with no additive.
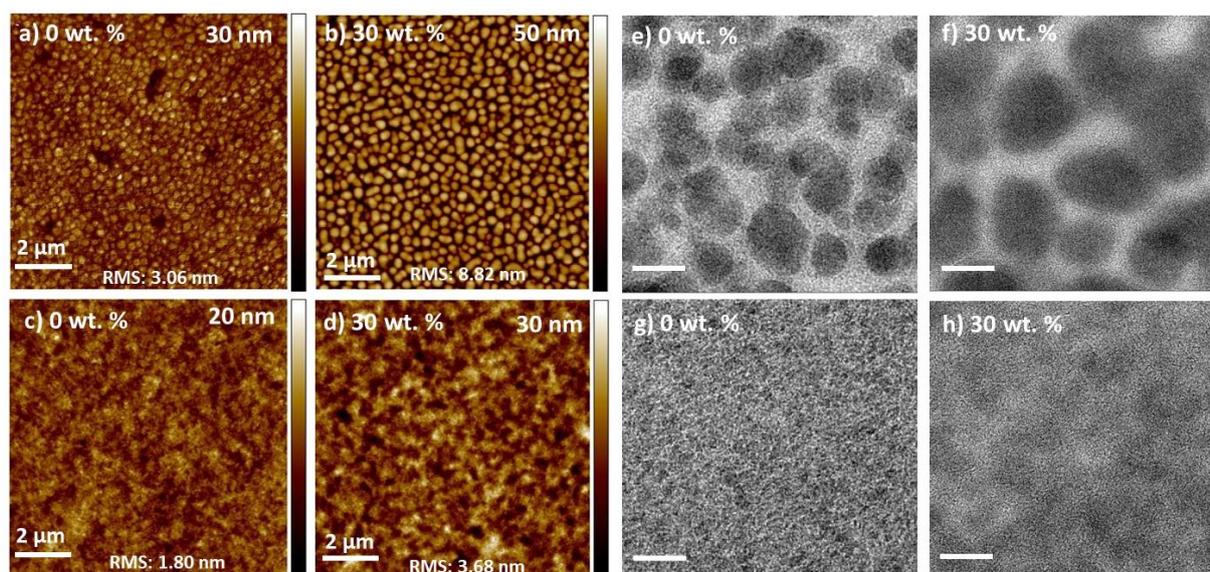
Figure 5.10. AFM topography and TEM morphology images of PTB7:PC$_{71}$BM binary blends without (a, e,) and with (c, g,) DIO, and ternary PTB7:ICBA:PC$_{71}$BM (30 wt%) without (b, f) and with (d, h) DIO. On TEM images, scale bar represents 200 nm.

Thus, PTB7 based blends are improved by adding DIO as it limits the size of fullerene aggregates (<20 nm) that would otherwise reduce exciton dissociation [47, 63] as observed with both AFM and TEM scans. Again, the morphology results described in this section are in full agreement with what has been reported in literature [47, 63, 69], though it is demonstrated here that DIO also supresses the size of ICBA. Since the EQE data allowed us to examine J_{SC} trends and it is shown there must be a reduction in recombination or possibly an increase in absorption, we now take a closer look at the absorption characteristics between both blends systems.

5.7.1 Ultraviolet-visible (UV-vis) spectroscopy

To further understand the impact of increasing ICBA on EQE, we focus on the optical properties of both blend systems analysed with UV-vis spectroscopy (Figure 5.11) to determine how much light is absorbed by each blend system and at what wavelengths.
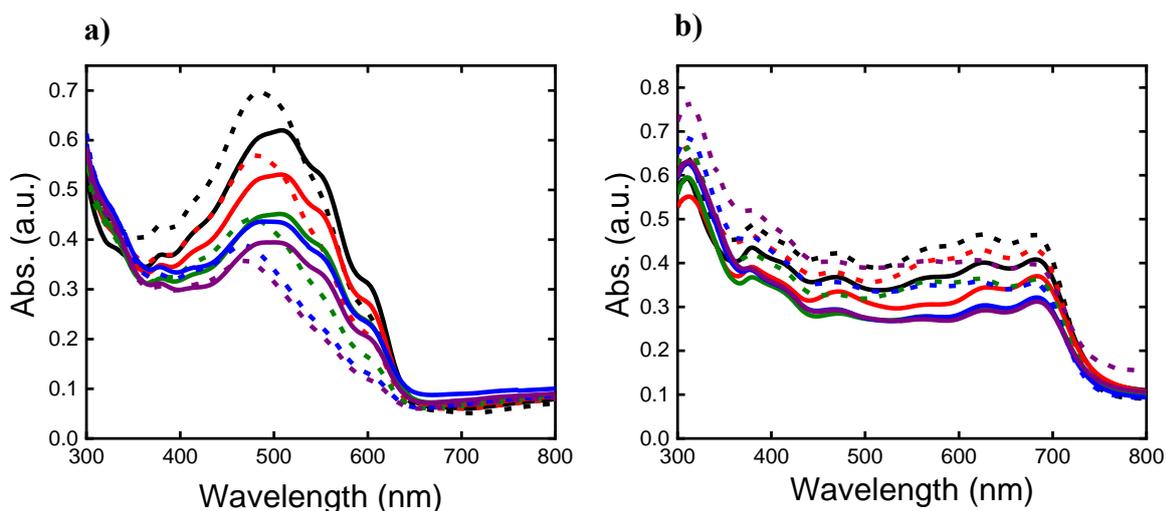
Figure 5.11. Optical absorption spectra of a) P3HT:PC$_{71}$BM and b) PTB7:PC$_{71}$BM blends with 0% (black), 10% (red), 20% (green), 25% (blue) and 30% (purple) ICBA loading, with and without 3% of DIO. Solid lines denote OPVs with DIO and short-dot lines denote OPVs without DIO.

Evidently, as the amount of ICBA increased in both blends, the absorption reduced. This is attributed to a weaker absorption of ICBA (Appendix 5.8) compared to the other active materials [26, 34, 80]. Further, DIO reduces absorption in PTB7-based blends, and at short wavelengths (<~525 nm) in P3HT-based blends. DIO is also shown to increase absorption at longer wavelengths (> ~525 nm) in P3HT-based blends due to an increase in coherence length of P3HT crystallites, since DIO promotes more ordered

crystalline packing compared to untreated devices as observed here [46, 79]. Because all devices were fabricated with a similar thickness (Appendix 5.7), ICBA reduced the light absorption which decreased EQE and ultimately J_{SC}. However, this was not the case for PTB7 blends with DIO as EQE is enhanced up to a ~20% of ICBA content before reducing, notwithstanding the decrease in absorption. Thus, these results indicate that charge generation and transport must be more efficient in PTB7-blends. To quantify the difference in recombination, the IQE is examined in the next section.

5.7.2 Internal Quantum Efficiency (IQE)

In contrast to EQE, the IQE tells us about the number of collected photo generated carriers to the number of photons absorbed in the active layer [81]. To account for the effect of changing absorption shown in Figure 5.11, the IQE is estimated by dividing EQE by the simulated absorption of the active layer using the transfer matrix method [81].
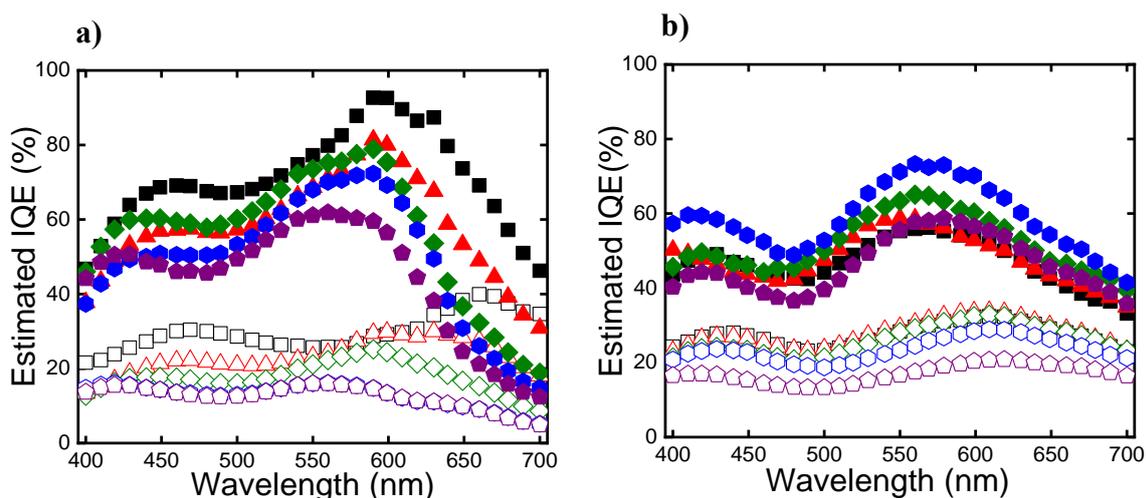
Figure 5.12. Estimated IQE curves of a) P3HT:PC$_{71}$BM and b) PTB7:PC$_{71}$BM prepared with 0% (black) and an additional 10% (red), 20% (green), 25% (blue) and 30% (purple) concentration of ICBA with and without 3% of DIO. Solid figures represent OPVs with DIO and open figures represent OPVs without DIO.

This transfer matrix formulism utilised, considers the reflection/transmission at the air/glass interfaces and contemplates the IQE as: IQE=EQE/(1-R) in addition to scattering, interference and parasitic absorption of all layers including the electrodes [81]. Briefly, the objective of probing IQE measurements was to reveal valuable information regarding exciton generation, dissociation, recombination, transport and collection in

competition with the incident photon energy [81]. In this Chapter, only relevant wavelengths where the active layer significantly absorbs are considered and a device structure of glass/ITO/PEDOT:PSS/Active layer/Al. Full details on the transfer matrix method outlined by Burkhard and colleagues can be found here [81]. The estimated IQE for P3HT and PTB7 based OPVs is shown in Figure 5.12a and b respectively.

Starting with the P3HT based devices, addition of DIO enhances the IQE particularly in the region of 600 nm, which is associated with absorption from P3HT fibrils as stated previously. In particular, DIO leads to a substantial increase in P3HT fibrils for ICBA concentrations up to 30 wt%. However, notwithstanding the improvement in the fibril density when DIO is used, addition of ICBA leads to a reduction in IQE. Further, estimated IQE for P3HT:ICBA:PC$_{71}$BM ternaries reduces with increasing ICBA without DIO. In contrast to the EQE trends, IQE peaks observed at higher wavelengths for P3HT based devices are due because of the differences in exciton harvesting efficiency, whereby P3HT has a stronger absorption between 500 nm – 600 nm in contrast to PCBM [81]. In blend systems where exciton harvesting is equally efficient, the IQE trends result flatter [81]. Now, focusing on the PTB7:ICBA:PC$_{71}$BM ternaries it can be observed that IQE increases with the addition of ICBA up to 25 wt% when DIO is used, and is largely constant up to 20 wt% without DIO prior to reducing. Thus, although absorption changes with composition, the IQE data suggests that ICBA is acting to reduce recombination in the PTB7-based blends.

5.7.3 Recombination loss mechanism

In this section, we examine the recombination mechanisms as a possible explanation for J_{SC} and IQE trends observed with the addition of ICBA. First, let us ponder on the possibility of changing exciton dissociation. TEM images (Figure 5.7, 5.10) suggest fine intermixing of the donor and acceptor constituents (<20 nm) for P3HT OPVs with and without DIO, and in PTB7 OPVs with DIO even with 30 wt% ICBA. Contrarily, PTB7 devices with no DIO depict large fullerene domains (>150 nm) which increase in size when ICBA is added (Figure 5.10e, f) that would be expected to reduce IQE through reduced exciton dissociation efficiency, which is observed in our data. As such, although changing the exciton dissociation efficiency seems to explain reducing IQE as ICBA is increased for PTB7 ternaries without DIO, we note that the reduction in IQE up to 25 wt% ICBA is minor (~4%) compared to the increase in fullerene-rich aggregates (~100

nm) which is many times larger than the exciton diffusion length (~10 nm) [82-85]. Thus, these results in total suggest that charge recombination reduces in PTB7-blends with no DIO as well in PTB7-blends with DIO, and it is more noticeably in the latter.

5.7.4 Carrier transport with GPVDM and hole mobility measurements

In this section, we investigate whether changed mobility is the reason for the improved J_{SC} and IQE trends observed with ICBA for PTB7 blends by utilising modelling to fit experimental data whilst varying electron mobility and by fabricating hole-only diodes. Previously, studies on ternary blends with changes in IQE have been attributed to be due to improvements or otherwise in charge transport through the blend [2, 86]. In here, by adding an acceptor as a third component into the binary blends, the overall acceptor content is increased whilst the donor content is reduced. Indeed, from a charge transport standpoint, the binary blends have an optimal D:A ratio for each type of blend system, and thus it may be the case that adding ICBA pushes the blend away from the optimum and reduces efficiency.
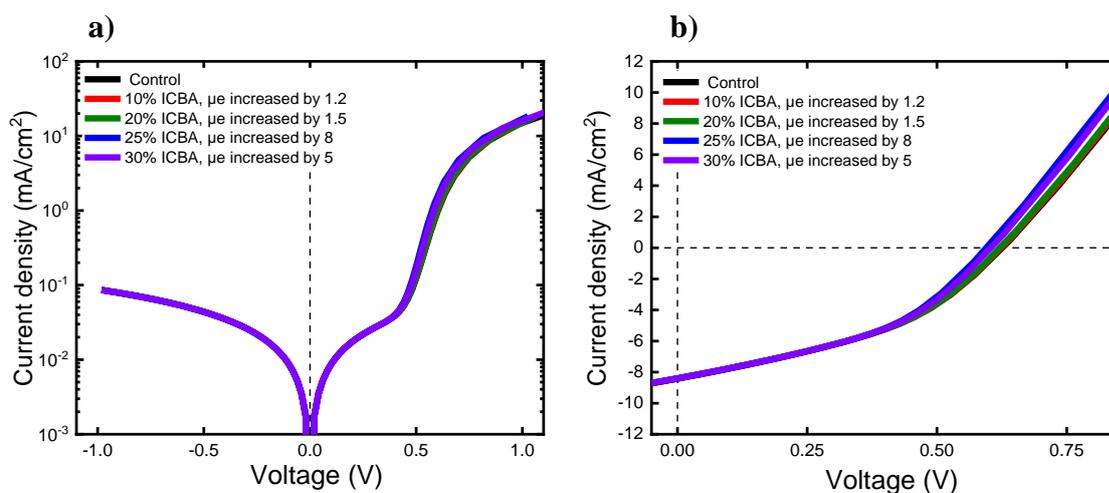
Figure 5.13. a) Dark and b) light J-V fits of PTB7-based OPVs varying electron mobility in a range of factors of 1-8 in an attempt to recreate J-V characteristics with modelling.

To shed more light on this balance, charge transport simulations were carried out with advance GPVDM modelling [87]. For this Chapter, a device structure of ITO (100 nm)/ PEDOT:PSS (30 nm) / Active layer (150 nm) / Al (100 nm) was considered. First, fits of the dark J-V curves for PTB7-based bends were carried out for all ICBA compositions by varying the electron mobility alone (Figure 5.13a). As observed, this

approach enabled to recreate the increase in diode current, however, this approach did not recreate the observed increase in photocurrent (Figure 5.13b). Like so, we view it unlikely that the improvement in IQE observed on PTB7-blends with ICBA is due to changes in mobility alone.

Moreover, charge carrier hole mobility (μ_h) was examined by fabricating single carrier devices with the architecture ITO/PEDOT:PSS/Active layer/Au and using space charge limited current (SCLC). This method was utilised as it has been shown to be the dominant mechanism with this type of blends [33, 34] and it is typically used to examine transport properties in low mobility, disordered organic semiconductors [6]. In here, under diode conditions, the dark characteristics of OPVs and mobility were derived from the Mott-Gurney equation [88, 89] and the results were fitted to the space charge limited form [90].

$$J = \frac{9}{8}\, \varepsilon_0\, \varepsilon_r\, \mu_h\, \frac{V^2}{L^3} \tag{5.1}$$

Where J is the current, ε_0 represents the permittivity of vacuum (8.85×10^{-12} F.m^{-1}), ε_r the organic dielectric constant (~3-4), μ_h the estimated hole mobility, L the active layer thickness (Appendix 5.7), and V the internal voltage. SCLC fits of binary and ternary blends are included in the Appendixes 5.9 and 5.10 with simulation fits for the same architecture. In short, our results are in agreement with what little data has been reported in literature for fullerene alloys with these blends [33, 34] in which mobilities with the addition of ICBA and DIO remain relatively alike when compared to the control devices. Thus, we ruled out that the improvement in IQE for PTB7 OPVs with ICBA was due to hole mobility changes.

5.7.5 Energy cascade heterojunctions on PTB7-based blends

In this last section, we investigate if the energy cascade heterojunctions are the cause of reduced recombination which led to increases of IQE and J_{SC} in PTB7-blends. In recent past, ternary blends have been shown to reduce recombination if the energy levels of the constituent materials form a 'staircase' in which separation of the charge pair is energetically favoured, similar to photosynthesis [91-94]. This 'cascade' effect, and a consequent reduction in recombination has been observed directly in some evaporated systems [95-97]. Figure 5.14 depicts a representation of the energy cascade landscape

formed due to the energy levels of materials that can assist in facilitating charge transfer at donor and acceptor interfaces by three different routes in ternary blends: $D:A_1$, $D:A_2$, $A_1:A_2$ compared to $D:A_1$ in binary blends.

However, we are still faced with the question as to why is there an enhancement in IQE for PTB7 based blends with increasing ICBA, but not for P3HT based blends. It is proposed that this difference can be attributed to the alloying effect discussed previously on section 5.6.
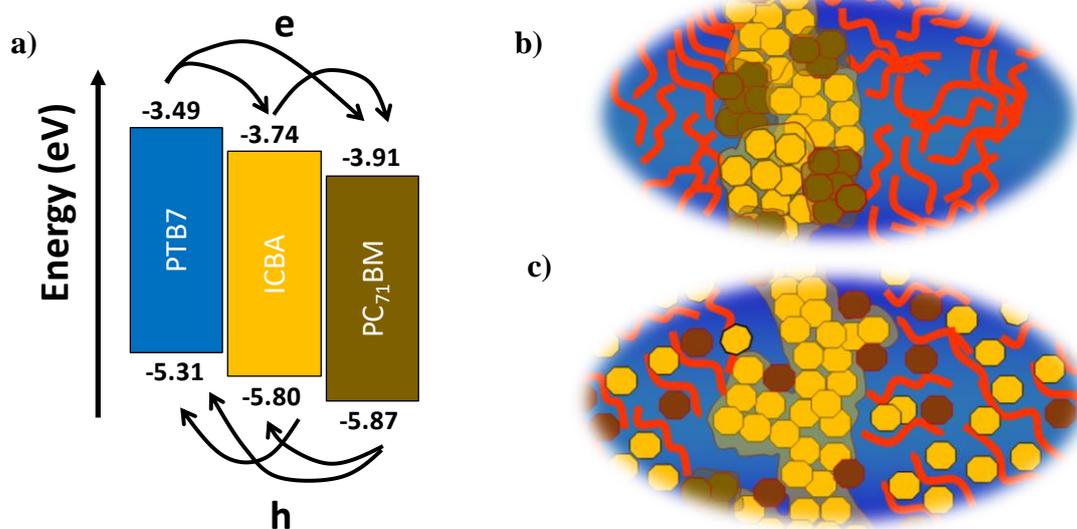
Figure 5.14. a) Cascade energy alignment in PTB7-blends a) where e represents the electrons and h the holes. b) Morphology representation of fullerene alloying between two different acceptors (yellow and brown circles) and a polymer donor (red lines) whereby the different acceptors intimately mix to form an alloy. c) Morphology representation of molecular intermixing between donor and the acceptors that leads to the possibility of cascade heterojunctions.

On the one hand, in P3HT based blends, the fullerene alloying appears to occur readily whereby we may expect that any possible advantage from a cascade heterojunction to be lost. On the other hand, PTB7 based blends appear to show fullerene alloying to a lesser degree, suggesting that electronically distinct fullerene domains may be more prevalent, in turn leading to the possibility of cascade heterojunctions. As such, these cascade structures in PTB7-blends were effective to reduce recombination losses, resulting in a substantial enhancement of J_{SC} that ultimately increased the efficiency.

5.8 Conclusion

In conclusion, in this Chapter the formulation method to increase efficiency was introduced and for the first time, the utility of a ternary blend is investigated by comparing J_{SC} and V_{OC} and relating it to the morphology. Two blend systems made of P3HT:ICBA:PC$_{71}$BM and PTB7:ICBA:PC$_{71}$BM were characterised and compared to binary blends, with and without 3% of processing additive DIO with the aim of understanding how a ternary system works and how to best optimise it. The third component ICBA was found to have a substantial impact between the two different polymers. In P3HT-based OPVs, ternaries showed a considerable increase in V_{OC} of 200 mV and 100 mV without and with DIO, whilst a major increase in J_{SC} from 4.3 mA/cm^2 to 9.1 mA/cm^2 was achieved on PTB7-based ternaries with DIO, regardless of the same concentrations of ternary and acceptor components in each series. Quantum efficiency measurements revealed in PTB7-based blends with DIO an increase of 20% when ICBA was added to the blends whilst it was reduced in the P3HT-based system for all ICBA combinations.

It was hypothesised that the differences stem from the molecular morphology on both systems, whereby fullerene molecules are found to intermix between PTB7 side-chains but they do not intercalate in between P3HT side-chains. It is argued that this leads to larger gains in V_{OC} for P3HT-based blends because the fullerene alloys occur readily. On the other hand, a greater reduction in recombination due to cascade heterojunctions in PTB7-based OPVs arises attributed to more electronically distinct fullerene domains which yielded IQE improvements in the order of 25% that increased J_{SC} and ultimately the efficiency.

Thusly, with the data provided in here we demonstrate that ternary blends can indeed outperform binary blends with differing impacts upon the physical operation of the OPV, which depends on the donor polymer. The findings reported in this Chapter provide vital information to engineer ternary OPVs and for future experiments, in which the molecular morphology is chosen to intercalate or not, with current or novel materials and thus choosing the impact that a ternary component will have.

5.9 References

1. Lu, L., et al., *Ternary Blend Polymer Solar Cells with Enhanced Power Conversion Efficiency.* Nat. Photonics, 2014. **8**(9): p. 716-722.

2. Li, Z., et al., *9.0% Power Conversion Efficiency From Ternary All-Polymer Solar Cells.* Energy Environ. Sci., 2017. **10**: p. 2212-2221.

3. Khlyabich, P.P., et al., *Optimization and simplification of polymer–fullerene solar cells through polymer and active layer design.* Polymer, 2013. **54**(20): p. 5267-5298.

4. Thompson, B.C., et al., *Polymer-Based Solar Cells: State-of-the-Art Principles for the Design of Active Layer Components.* Green, 2011. **1**(1): p. 29-54.

5. Huang, H., L. Yang, and B. Sharma, *Recent Advances in Organic Ternary Solar Cells.* J. Mater. Chem. A, 2017. **5**: p. 11501-11517.

6. Groves, C., *Simulating charge transport in organic semiconductors and devices: a review.* Rep. Prog. Phys., 2017. **80**(2): p. 026502.

7. Hoppe, H. and N.S. Sariciftci, *Organic solar cells: An overview.* J. Mater. Res., 2011. **19**: p. 1924-1945.

8. Ameri, T., et al., *Organic Ternary Solar Cells: A Review.* Adv. Mater., 2013. **25**: p. 4245-4266.

9. Liu, X., et al., *Ternary Blend Strategy for Achieving High-Efficiency Organic Solar Cells with Nonfullerene Acceptors Involved.* Adv. Funct. Mater., 2018. **28**(29).

10. Bi, P. and X. Hao, *Versatile Ternary Approach for Novel Organic Solar Cells: A Review.* Sol. RRL, 2019. **3**: p. 1800263.

11. An, Q., et al., *Versatile Ternary Organic Solar Cells: A Critical Review.* Energy Environ. Sci., 2016. **9**: p. 281-322.

12. Lami, V., et al., *Energy Level Alignment in Ternary Organic Solar Cells.* Adv. Electron. Mater., 2020. **6**(8).

13. Lu, L., et al., *Status and prospects for ternary organic photovoltaics.* Nat. Photonics, 2015. **9**(8): p. 491-500.

14. Pan, M.-A., et al., *16.7%-Efficiency Ternary Blended Organic Photovoltaic Cells with PCBM as the Acceptor Additive to Increase the Open-Circuit Voltage and Phase Purity.* J. Mater. Chem. A, 2019. **7**: p. 20713-20722.

15. Chen, Y., et al., *From Binary to Ternary: Improving the External Quantum Efficiency of Small-Molecule Acceptor-Based Polymer Solar Cells with a Minute Amount of Fullerene Sensitization.* Adv. Energy Mater., 2017. **7**(17).

16. Liu, T., et al., *Ternary Organic Solar Cells Based on Two Compatible Nonfullerene Acceptors with Power Conversion Efficiency >10%.* Adv. Mater., 2016. **28**: p. 10008-10015.

17. Honda, S., et al., *Selective Dye Loading at the Heterojunction in Polymer/Fullerene Solar Cells.* Adv. Energy Mater., 2011. **1**(4): p. 588-598.

18. Punzi, A., et al., *Designing Small Molecules as Ternary Energy-Cascade Additives for Polymer:Fullerene Solar Cell Blends.* Chem. Mater., 2018. **30**(7): p. 2213-2217.

19. Litvin, A.P., et al., *Ternary Composites with PbS Quantum Dots for Hybrid Photovoltaics.* J. Phys. Chem. C., 2019. **123**(5): p. 3115-3121.

20. Stylianakis, M.M., et al., *Efficient ternary organic photovoltaics incorporating a graphene-based porphyrin molecule as a universal electron cascade material.* Nanoscale, 2015. **7**(42): p. 17827-35.

21. Xu, C., et al., *Ternary blend organic solar cells with a non-fullerene acceptor as a third component to synergistically improve the efficiency.* Org. Electron., 2018. **62**: p. 261-268.

22. An, Q., et al., *Efficient Organic Ternary Solar Cells with the Third Component as Energy Acceptor.* Nano Energy, 2016. **26**: p. 180-191.

23. Xie, Y., et al., *Morphology Control Enables Efficient Ternary Organic Solar Cells.* Adv. Mater., 2018. **30**(38): p. e1803045.

24. Zhang, L. and W. Ma, *Morphology optimization in ternary organic solar cells.* CHINESE J POLYM SCI, 2016. **35**(2): p. 184-197.

25. Gasparini, N., et al., *The role of the third component in ternary organic solar cells.* Nat. Rev. Mater., 2019. **4**(4): p. 229-242.

26. Khlyabich, P.P., B. Burkhart, and B.C. Thompson, *Efficient Ternary Blend Bulk Heterojunction Solar Cells with Tunable Open-Circuit Voltage.* J. Am. Chem. Soc., 2011. **133**: p. 14534-14537.

27. Street, R.A., et al., *Origin of the Tunable Open-Circuit Voltage in Ternary Blend Bulk Heterojunction Organic Solar Cells.* J. Am. Chem. Soc., 2013. **135**: p. 986-989.

28. Khlyabich, P.P., et al., *Formation of Organic Alloys in Ternary-Blend Solar Cells with Two Acceptors Having Energy-Level Offsets Exceeding 0.4 eV.* ACS Energy Lett., 2017. **2**: p. 2149-2156.

29. Khlyabich, P.P., et al., *Structural Origins for Tunable Open-Circuit Voltage in Ternary-Blend Organic Solar Cells.* Adv. Funct. Mater., 2015. **25**(34): p. 5557-5563.

30. Angmo, D., et al., *Fullerene Alloy Formation and the Benefits for Efficient Printing of Ternary Blend Organic Solar Cells.* J. Mater. Chem. C, 2015. **3**: p. 5541-5548.

31.   Peng, Z., et al., *A Dual Ternary System for Highly Efficient ITO-Free Inverted Polymer Solar Cells.* J. Mater. Chem. A, 2015. **3**: p. 18365-18371.

32.   Cheng, P., et al., *Alloy Acceptor: Superior Alternative to PCBM toward Efficient and Stable Organic Solar Cells.* Adv. Mater., 2016. **28**: p. 8021-8028.

33.   Cheng, P., Y. Li, and X. Zhan, *Efficient Ternary Blend Polymer Solar Cells with Indene-C60 Bisadduct as an Electron-Cascade Acceptor.* Energy Environ. Sci., 2014. **7**: p. 2005-2011.

34.   Sharma, R., et al., *Photo-Physics of PTB7, PCBM and ICBA Based Ternary Solar Cells.* Org. Electron., 2016. **34**: p. 111-117.

35.   Chen, Y., et al., *Tuning Voc for High Performance Organic Ternary Solar Cells with Non-Fullerene Acceptor Alloys.* J. Mater. Chem. A, 2017. **5**: p. 19697-19702.

36.   Baran, D., et al., *Reducing the Efficiency-Stability-Cost Gap of Organic Photovoltaics with Highly Efficient and Stable Small Molecule Acceptor Ternary Solar Cells.* Nat. Mater., 2017. **16**: p. 363-369.

37.   Lu, H., et al., *Ternary-Blend Polymer Solar Cells Combining Fullerene and Nonfullerene Acceptors to Synergistically Boost the Photovoltaic Performance.* Adv. Mater., 2016. **28**: p. 9559-9566.

38.   Jin Young Kim, K.L., Nelson E. Coates, Daniel Moses, Thuc-Quyen Nguyen, Mark Dante, Alan J. Heeger, *Efficient Tandem Polymer Solar Cells Fabricated by All-Solution Processing.* Science, 2007. **317**: p. 222-225.

39.   Liang, Y., et al., *For the Bright Future-Bulk Heterojunction Polymer Solar Cells with Power Conversion Efficiency of 7.4%.* Adv. Mater., 2010. **22**: p. E135-E138.

40.   Padinger, F., Rittberger, R. and Sariciftci, N., *Effects of Postproduction Treatment on Plastic Solar Cells.* Adv. Funct. Mater., 2003. **13**: p. 85-88.

41.   van Bavel, S., et al., *Relation Between Photoactive Layer Thickness, 3D Morphology, and Device Performance in P3HT/PCBM Bulk-Heterojunction Solar Cells.* Macromolecules, 2009. **42**: p. 7396-7403.

42.   Li, G., et al., *High-Efficiency Solution Processable Polymer Photovoltaic Cells by Self-Organization of Polymer Blends.* Nat. Mater., 2005. **4**: p. 864-868.

43.   Mayer, A.C., et al., *Bimolecular Crystals of Fullerenes in Conjugated Polymers and the Implications of Molecular Mixing for Solar Cells.* Adv. Funct. Mater., 2009. **19**: p. 1173-1179.

44.   Zhao, X., et al., *Impact of Alkyl Chain Length of 1,n-diiodoalkanes on PC71BM Distribution in Both Bulk and Air Surface of PTB7:PC71BM Film.* Org. Electron., 2016. **37**: p. 358-365.

45. Kim, W., et al., *Conflicted Effects of a Solvent Additive on PTB7:PC71BM Bulk Heterojunction Solar Cells.* J. Phys. Chem. C, 2015. **119**: p. 5954-5961.

46. Fan, X., et al., *Nano Structure Evolution in P3HT:PC61BM Blend Films Due to the Effects of Thermal Annealing or by Adding Solvent.* Chin. Phys. B, 2015. **24**: p. 078401.

47. Collins, B.A., et al., *Absolute Measurement of Domain Composition and Nanoscale Size Distribution Explains Performance in PTB7:PC71BM Solar Cells.* Adv. Energy Mater., 2013. **3**: p. 65-74.

48. Collins, B.A., et al., *Molecular Miscibility of Polymer–Fullerene Blends.* J. Phys. Chem. Lett., 2010. **1**(21): p. 3160-3166.

49. Kleinschmidt, A.T., S.E. Root, and D.J. Lipomi, *Poly(3-hexylthiophene) (P3HT): Fruit Fly or Outlier in Organic Solar Cell Research?* J. Mater. Chem. A., 2017. **5**(23): p. 11396-11400.

50. Koppe, M., et al., *Polyterthiophenes as Donors for Polymer Solar Cells.* Adv. Funct. Mater., 2007. **17**: p. 1371-1376.

51. Savikhin, V., et al., *Morphological, Chemical, and Electronic Changes of the Conjugated Polymer PTB7 with Thermal Annealing.* iScience, 2018. **2**: p. 182-192.

52. Szarko, J.M., et al., *Photovoltaic Function and Exciton/Charge Transfer Dynamics in a Highly Efficient Semiconducting Copolymer.* Adv. Funct. Mater., 2014. **24**(1): p. 10-26.

53. Matthew R. Hammond, R.J.K., Andrew A. Herzing, Lee J. Richter, David S. Germack, Hyun-Wook Ro, Christopher L. Soles, Daniel A. Fischer, Tao Xu, Luping Yu, Michael F. Toney, and Dean M. DeLongchamp, *Molecular Order in High-Efficiency Polymer/Fullerene Bulk Heterojunction Solar Cells.* ACS Nano, 2011. **5**(10): p. 8248-8257.

54. Szarko, J.M., et al., *When Function Follows Form: Effects of Donor Copolymer Side Chains on Film Morphology and BHJ Solar Cell Performance.* Adv. Mater., 2010. **22**(48): p. 5468-5472.

55. Miller, N.C., et al., *Factors Governing Intercalation of Fullerenes and Other Small Molecules Between the Side Chains of Semiconducting Polymers Used in Solar Cells.* Adv. Energy Mater., 2012. **2**: p. 1208-1217.

56. Beiley, Z.M., et al., *Morphology-Dependent Trap Formation in High Performance Polymer Bulk Heterojunction Solar Cells.* Adv. Energy Mater., 2011. **1**: p. 954-962.

57. Xiao, T., et al., *Molecular Packing and Electronic Processes in Amorphous-Like Polymer Bulk Heterojunction Solar Cells with Fullerene Intercalation.* Sci. Rep., 2014. **4**: p. 5211.

58. Miller, N.C., et al., *Molecular Packing and Solar Cell Performance in Blends of Polymers with a Bisadduct Fullerene.* Nano Lett., 2012. **12**: p. 1566-1570.

59. Tom J. Savenije, W.J.G., Martin Heeney, Steve Tierney, Iain McCulloch, and Laurens D. A. Siebbeles, *Photoinduced Charge Carrier Generation in Blends of*

Poly(Thienothiophene) Derivatives and [6,6]-Phenyl-C61-butyric Acid Methyl Ester: Phase Segregation versus Intercalation. J. Phys. Chem. C, 2010. **114**(35): p. 15116-15120.

60. Jianchang Guo, Y.L., Jodi Szarko, Byeongdu Lee, Hae Jung Son, Brian S. Rolczynski, Luping Yu, and Lin X. Chen, *Structure, Dynamics, and Power Conversion Efficiency Correlations in a New Low Bandgap Polymer: PCBM Solar Cell.* J. Phys. Chem. B, 2010. **114**(2): p. 742-748.

61. Chen, W., et al., *Hierarchical Nanomorphologies Promote Exciton Dissociation in Polymer/Fullerene Bulk Heterojunction Solar Cells.* Nano Lett., 2011. **11**: p. 3707-3713.

62. Lu, L. and L. Yu, *Understanding Low Bandgap Polymer PTB7 and Optimizing Polymer Solar Cells Based on it.* Adv. Mater., 2014. **26**: p. 4413-4430.

63. Liu, F., et al., *Understanding the Morphology of PTB7:PCBM Blends in Organic Photovoltaics.* Adv. Energy Mater., 2014. **4**: p. 1301377.

64. Huang, W., et al., *Impact of Fullerene Mixing Behavior on the Microstructure, Photophysics, and Device Performance of Polymer/Fullerene Solar Cells.* ACS Appl. Mater. Interfaces, 2016. **8**: p. 29608-29618.

65. Komilian, S., O. Oklobia, and T. Sadat-Shafai, *Controlling Intercalations of PBDTTT-EFT Side Chain to Initiate Suitable Network for Charge Extraction in PBDTTT-EFT:PC71BM Blended Bulk Heterojunction Solar Cell.* Sol. Energy Mater. Sol. Cells, 2018. **175**: p. 35-40.

66. Cates, N.C., et al., *Effects of Intercalation on the Hole Mobility of Amorphous Semiconducting Polymer Blends.* Chem. Mater., 2010. **22**: p. 3543-3548.

67. Kassar, T., et al., *Real-Time Study on Structure Formation and the Intercalation Process of Polymer: Fullerene Bulk Heterojunction Thin Films.* Sol. RRL, 2020. **4**: p. 1900508.

68. Gao, H.L., et al., *Quantitative Characterization of Phase Separation in the Photoactive Layer of Polymer Solar Cells by the Phase Image of Atomic Force Microscopy.* Thin Solid Films, 2015. **576**: p. 81-87.

69. Alekseev, A., et al., *Morphology and Local Electrical Properties of PTB7:PC71BM Blends.* J. Mater. Chem. A, 2015. **3**(16): p. 8706-8714.

70. Qi, B. and J. Wang, *Fill Factor in Organic Solar Cells.* Phys. Chem. Chem. Phys., 2013. **15**(23): p. 8972-8982.

71. Hsiang-Yu Chen, H.Y., Guanwen Yang, Srinivas Sista, Ruben Zadoyan, Gang Li, and Yang Yang, *Fast-Grown Interpenetrating Network in Poly(3-hexylthiophene): Methanofullerenes Solar Cells Processed with Additive.* J. Phys. Chem. C, 2009. **113**(18): p. 7946-7953.

72. Li, G., R. Zhu, and Y. Yang, *Polymer Solar Cells.* Nat. Photonics, 2012. **6**: p. 153-161.

73. Mazzio, K.A. and C.K. Luscombe, *The Future of Organic Photovoltaics.* Chem. Soc. Rev., 2015. **44**: p. 78-90.

74. Das, S., et al., *Correlating High Power Conversion Efficiency of PTB7:PC71BM Inverted Organic Solar Cells with Nanoscale Structures.* Nanoscale, 2015. **7**: p. 15576-15583.

75. Zheng, Y., et al., *Binary Solvent Additives Treatment Boosts the Efficiency of PTB7:PCBM Polymer Solar Cells to Over 9.5%.* Sol. RRL, 2018. **2**: p. 1700144.

76. Guo, X., et al., *High Efficiency Polymer Solar Cells Based on poly(3-hexylthiophene)/indene-C70 Bisadduct With Solvent Additive.* Energy Environ. Sci., 2012. **5**: p. 7943-7949.

77. Arca, F., M. Loch, and P. Lugli, *Enhancing Efficiency of Organic Bulkheterojunction Solar Cells by Using 1,8-Diiodooctane as Processing Additive.* IEEE J. Photovolt., 2014. **4**: p. 1560-1565.

78. Zhang, H., et al., *Effects of DIO on the Charge Recombination Behaviors of PTB7:PC71BM Photovoltaics.* Org. Electron., 2019. **67**: p. 50-56.

79. Park, M.S. and F.S. Kim, *Synergistic Effects of Processing Additives and Thermal Annealing on Nanomorphology and Hole Mobility of Poly(3-hexylthiophene) Thin Films.* Polymers, 2019. **11**: p. 112.

80. Xu, B., et al., *Improving Photovoltaic Properties of P3HT:IC60BA through the Incorporation of Small Molecules.* Polymers, 2018. **10**: p. 121.

81. Burkhard, G.F., E.T. Hoke, and M.D. McGehee, *Accounting for Interference, Scattering, and Electrode Absorption to Make Accurate Internal Quantum Efficiency Measurements in Organic and Other Thin Solar Cells.* Adv. Mater., 2010. **22**: p. 3293-3297.

82. Scully, S.R. and M.D. McGehee, *Effects of Optical Interference and Energy Transfer on Exciton Diffusion Length Measurements in Organic Semiconductors.* J. App. Phys., 2006. **100**: p. 034907.

83. Peumans, P., Uchida, S. & Forrest, S., *Efficient Bulk Heterojunction Photovoltaic Cells Using Small-Molecular-Weight Organic Thin Films.* Nature, 2003. **425**: p. 158-162.

84. Denis E. Markov, E.A., Paul W. M. Blom, Alexander B. Sieval, and Jan C. Hummelen, *Accurate Measurement of the Exciton Diffusion Length in a Conjugated Polymer Using a Heterostructure with a Side-Chain Cross-Linked Fullerene Layer.* J. Phys. Chem. A, 2005. **109**(24): p. 5266-5274.

85. Dang, M.T., et al., *Controlling the Morphology and Performance of Bulk Heterojunctions in Solar Cells. Lessons Learned from the Benchmark Poly(3-hexylthiophene):[6,6]-phenyl-C61-butyric Acid Methyl Ester System.* Chem. Rev., 2013. **113**: p. 3734-3765.

86.   Fan, R., et al., *Enhanced Performance of Polymer Solar Cells Based on PTB7-Th:PC71BM by Doping with 1-Bromo-4-Nitrobenzene.* J. Mater. Chem. C, 2017. **5**: p. 10985-10990.

87.   MacKenzie, R.C.I., et al., *Modeling Nongeminate Recombination in P3HT:PCBM Solar Cells.* J. Phys. Chem. C, 2011. **115**: p. 9806-9813.

88.   Carbone, A., B.K. Kotowska, and D. Kotowski, *Space-Charge-Limited Current Fluctuations in Organic Semiconductors.* Phys. Rev. Lett., 2005. **95**(23): p. 236601.

89.   G. G. Malliaras, J.R.S., P. J. Brock, and C. Scott, *Electrical Characteristics and Efficiency of Single-Layer Organic Light-Emitting Diodes.* Phys. Rev. B, 1998. **58**: p. R13411(R).

90.   Mihailetchi, V., van Duren, J., Blom, P., Hummelen, J., Janssen, R., Kroon, J., Rispens, M., Verhees, W. and Wienk, M., *Electron Transport in a Methanofullerene.* Adv. Funct. Mater., 2003. **13**: p. 43-46.

91.   Tan, Z.K., et al., *Suppressing Recombination in Polymer Photovoltaic Devices Via Energy-Level Cascades.* Adv. Mater., 2013. **25**: p. 4131-4138.

92.   Groves, C., *Suppression of Geminate Charge Recombination in Organic Photovoltaic Devices with a Cascaded Energy Heterojunction.* Energy Environ. Sci., 2013. **6**: p. 1546-1551.

93.   Izawa, S., et al., *Dominant Effects of First Monolayer Energetics at Donor/Acceptor Interfaces on Organic Photovoltaics.* Adv. Mater., 2015. **27**: p. 3025-3031.

94.   Nakano, K., et al., *Roles of Energy/Charge Cascades and Intermixed Layers at Donor/Acceptor Interfaces in Organic Solar Cells.* Sci. Rep., 2016. **6**: p. 29529.

95.   Schlenker, C.W., et al., *Cascade Organic Solar Cells.* Chem. Mater., 2011. **23**: p. 4132-4140.

96.   Sista, S., et al., *Enhancement in Open Circuit Voltage Through a Cascade-Type Energy Band Structure.* Appl. Phys. Lett., 2007. **91**: p. 223508.

97.   Kinoshita, Y., T. Hasobe, and H. Murata, *Control of Open-Circuit Voltage in Organic Photovoltaic Cells by Inserting an Ultrathin Metal-Phthalocyanine Layer.* Appl. Phys. Lett., 2007. **91**: p. 083518.

CHAPTER 6

ELECTRON TRANSPORT IN EMERGENT NON-FULLERENE AND HYBRID FULLERENES ACCEPTORS

6.1 Introduction

Over the past decades, fullerene derivatives have been extensively studied for OPV fabrication due to their high electron mobility, high electron affinity and good solubility which allows them to be spin casted in thin films [1]. To date, efforts to improve fullerenes have mostly focused on three main areas: changing the electron affinity, increasing light harvesting and influencing the blend morphology [2]. However, because of the lack in synthesis flexibility, researchers now seek other novel alternatives.

Non-fullerene acceptors (NFA) have risen as a promising route due to their higher flexibility which ensues tuneable electronic properties [3]. Indeed, reports in literature have shown that NFAs may yield a broad absorption, high electron mobility and good device stability compared to fullerenes, which is a main driving force behind their study [4, 5]. Among them, naphthalene diimide (NDI) has emerged as an encouraging candidate, because of a low lying LUMO and is an electron deficient molecule, which allows it to behave like a n-type acceptor [6]. As discussed in the OPV fundamentals Chapter, the charge carrier mobility is a vital parameter in semiconductors, that ultimately plays an important role to determine whether a PV device is efficient or not. From a design standpoint, higher mobilities are desired since it means that carriers will be collected in less time and hence, less energy lost to recombination.

This Chapter presents experimental results of a work in collaboration with Dr. Alyssa Avestro and fellow PhD Phil Hope, who developed a family of novel electron acceptors comprised of NFA and hybrid fullerenes. Since new PV materials may benefit from high mobilities, this work is relevant because the electron transport properties were probed for the first time. Our role was to fabricate electron-only diodes, characterise the electron mobility, and to compare it with PCBM fullerene. But to put all of this into context, first the importance of PCBM and the development of n-type semiconductors is detailed, followed by approaches one can take to modify fullerenes to enhance electron

transport and why there is need for new materials. Next, a discussion on NFAs is described and finally, electron mobility measurements with Space Charge Limited Current (SCLC) formulism are presented. This Chapter provides vital information about electron charge transport in emergent materials, which can aid to further develop novel n-type organic semiconductors for PV applications.

6.2 N-type semiconductors: Fullerene PCBM and development

In recent past, organic semiconductors have been thoroughly researched by academia and industry due to their potential application for solar energy harvesting and commercial devices have successfully begun to enter niche markets [2, 7, 8]. Nonetheless, much of this progress has been focused on p-type semiconductors because usually most of the light absorption is harvested in this component. Thus, although high efficiencies have been attained with novel p-type semiconductors in OPVs [9-12], less effort has been focused to n-type semiconductors. Due to their high electron affinity, fullerenes have been an excellent choice for electron transport in organic materials [1]. Indeed, some of the highest efficiency OPVs have been achieved by a solution processed BHJ made of a donor:acceptor (D:A) blend, in which fullerenes form part of the acceptor component (i.e. $PC_{60}BM$ or $PC_{71}BM$) [13, 14].

In earlier literature, buckminsterfullerene C60 cage demonstrated potential for solar cells and optoelectronics field after charge transfer from polymer MEH-PPV was first identified by Sariciftci et al [15]. Following this milestone, a soluble PCBM derivative in a BHJ OPV device was introduced by Yu and colleagues [16]. Their studies demonstrated that the higher solubility of PCBM enhanced charge separation, carrier mobility and PCE because of continuous D:A pathways compared to C60. Because pristine C60 is more difficult to deposit (i.e. it needs to be vacuum deposited), soluble PCBM presented an advantage towards optimisation of solution processed OPVs [2, 17]. As such, PCBM was one of the first soluble acceptor materials used with MEH-PPV [16], which itself is one of the earliest conjugated polymers for organic semiconductor devices. With MEH-PPV:fullerene blend systems, efficiencies of up to 3% − 4% were attained following device optimisation [18, 19]. However, the narrow light absorption and generally low hole mobilities hampered their further progress. Researchers then turned into conjugated P3HT polymer as the donor material, due to its higher hole mobility and broader coverage of the solar spectrum, making P3HT:PCBM better blend systems for

OPVs applications [20-22]. Indeed, single junction BHJ devices made of P3HT and fullerenes have attained higher efficiencies, ranging in 5% − 7% [23, 24] in recent times. Even though PCBM resulted in increased PCE and electron mobility compared to C60, only some approaches have been detailed in literature to further develop fullerene-based acceptor materials. The fabrication of new fullerenes by increasing the LUMO energy levels with multi-adducts, modifying the phenyl groups, changing the alkyl chain length and varying the fullerene cage have been some of such efforts to boost performance and electron mobility [25], which will be discussed in the following section. Figure 6.1 presents a basic schematic of a fullerene molecule and some of the main possible modifications aforementioned that have been considered to fabricate novel and hybrid acceptor materials. From the image, *Ar* denotes the aryl group, *R* the end group and *n* the times the chain is repeated
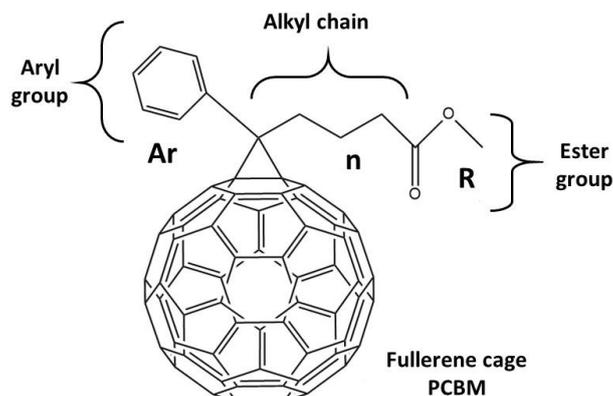
Figure 6.1. PCBM and some approaches one can take to make novel acceptors.

6.3 Modifications to PCBM acceptor molecule and hybrid fullerenes

6.3.1 Phenyl group modifications (aryl and ester)

The importance of phenyl group modification was investigated by Troshin et al [26]. It was found that modifying the phenyl ring (*Ar* and *R* from Figure 6.1) of PCBM could affect physical properties i.e. solubility, which has a direct impact in the performance of devices. In a similar way, Zhang and colleagues [27] altered the phenyl group of PCBM to make two derivatives: TPA-PCBM and MF-PCBM which resulted in a more amorphous nature compared to PCBM. The TPA-PCBM derivative realised an electron mobility of 1.2×10^{-2} cm^2 V^{-1} s^{-1} which was similar to that of PCBM in the same

study with 1.6×10^{-2} cm^2 V^{-1} s^{-1}. Considering a comparable approach, Kim et al [28] reported a series of fullerene derivatives with modified phenyl groups, namely: NCBM, PyCBM, ACBM in addition to the PCBM control (Figure 6.2), which were blended with conjugated P3HT donor. Out of the three new molecules, NCBM reported the highest efficiency of 4.09% as compared to 3.80% of PCBM. Electron transport measurements yielded comparable mobilities of 2.27×10^{-4} cm^2 V^{-1} s^{-1} and 2.39×10^{-4} cm^2 V^{-1} s^{-1} for these two respectively. The higher performance of NCBM was associated to improved LUMO levels that achieved higher V_{OC} and FF values compared to that of control PCBM, in addition to a high Photoluminescence (PL) quenching. Briefly, PL measurements are a convenient tool to investigate energy transfer processes (i.e. between fullerene and polymers) and it takes place when excitons recombine emissively before splitting at a D:A interface, as such, a high PL quenching evidences electron transfer from fullerene to the polymer [29]. Thus, the aforesaid references demonstrated that modifying the phenyl group in fullerene molecules can be a potential approach to develop hybrid and new acceptor materials.
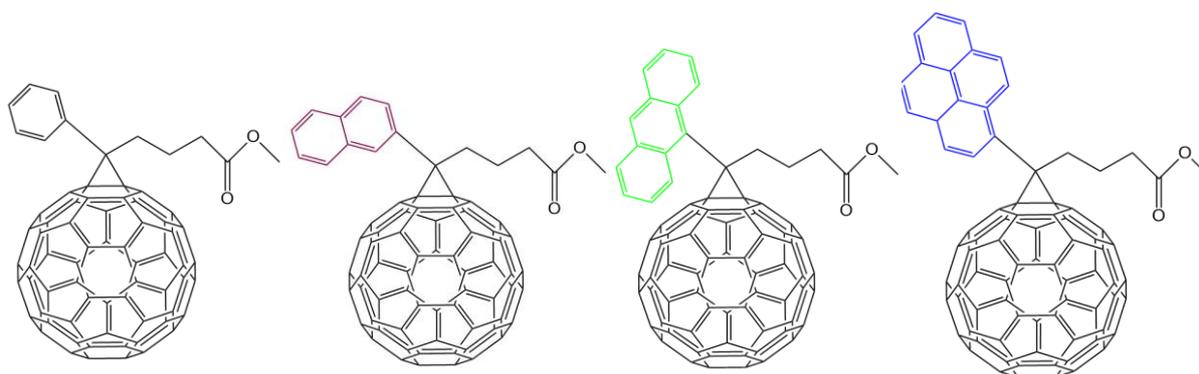
Figure 6.2. Schematic of phenyl group modifications (*Ar*) in a fullerene molecule showing PCBM, NCBM, ACBM and PyCBM from left to right respectively (modification marked with different colours). Redrawn from: [28].

6.3.2 Alkyl chain modifications

The alkyl chain modification (Figure 6.3) can also have an impact in the solubility as detailed by Troshin [26] and Zheng et al [30]. In a study of the former, reducing the chain length drastically decreased the PCE from 3.70% to 0.40% [26]. Based upon this insight, Zhao and co-workers [31] varied the alkyl chain length from 3 to 7 carbon atoms to study the optical, electron mobility and photovoltaic properties in new fullerene

molecules. Their results demonstrated that absorption and LUMO remained almost unchanged, thus indicating that the alkyl chain influenced the absorption and energy levels very little. However, the alkyl chain had an impact in the morphology as revealed by their AFM measurements, showing suitable aggregates and nanostructures for exciton dissociation and transport channels [31]. As a consequence, the electron transport and overall PV properties were slightly higher. For example, the electron mobility attained by a chain length of 3 carbon atoms was 2.2×10^{-3} cm^2 V^{-1} s^{-1} compared to reference PCBM with 1.3×10^{-3} cm^2 V^{-1} s^{-1} respectively. In addition, the fullerene with an alkyl chain of 3 carbon atoms achieved a PCE of 3.7% when blended with P3HT, in contrast to the 3.5% of the PCBM control.
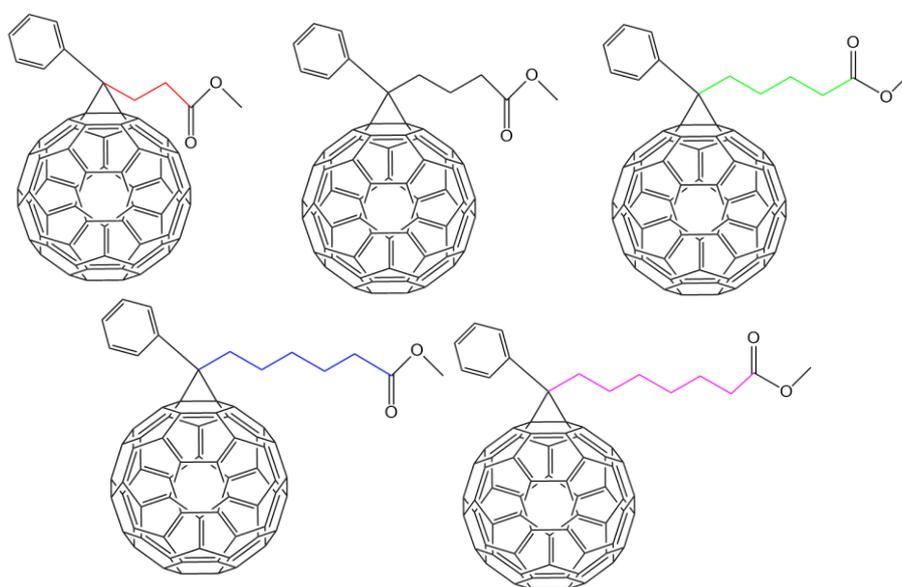
Figure 6.3. Schematic depicting different chain lengths used in a fullerene. Modifications are marked with colours and PCBM remains unchanged (black). Top row shows increase from 3 to 5 carbon atoms whilst the bottom row 6 and 7 respectively. Adapted from: [31].

Thus, changes to the alkyl chain length have only shown improvements in the morphology that achieve comparable or slightly better performances to fullerene PCBM, and little changes to the absorption and energy levels. In the next section the focus will be on modifications to the fullerene cage.

6.3.3 Multi-adduct and fullerene cage derivatives

As laid out above, one of the ways to further develop fullerene acceptors was to attach more soluble electron donating groups (i.e. alkyl chain) or by modifying the phenyl

groups. In here, the focus is now shifted towards modifications in the fullerene cage. Bis-PCBM and Tris-PCBM (Figure 6.4a, b) are soluble in organic solvents as PCBM with a LUMO level higher by 0.1 V and 0.2 V respectively [17]. Further, in recent past bis-adducts have been more favoured because they could realise optimal V_{OC} and electron mobility. For instance, examination by Lenes and colleagues [32] on these blends revealed that electron mobility of bis-PCBM, $7x10^{-4}$ cm^2 V^{-1} s^{-1}, was similar to the $2x10^{-3}$ cm^2 V^{-1} s^{-1} PCBM mobility, but tris-PCBM suffered from a mobility of 5 orders of magnitude lower. Benefitting from a higher V_{OC}, P3HT:bis-PCBM devices enhanced the PCE by 18% compared to regular PCBM [33]. Although V_{OC} of P3HT:Tris-PCBM was higher, J_{SC} and FF were lessened, resulting from a poor electron mobility [32].

Now, because PCBM does not absorb very well in the visible region of the spectrum due to the symmetry of its C60 molecule that leads to lower energy transitions [20], another choice is utilising [6,6]-Phenyl-C71-butyric acid methyl ester, known as $PC_{70}BM$ or $PC_{71}BM$ [2]. In this fullerene (Figure 6.4c), the molecular shape is slightly different, with the symmetry broken compared to PCBM allowing a broader absorption in the visible range [2, 20]. As a downside, it is more expensive due to its purifications processes that may limit its application [20]. Another higher fullerene analogue is [6,6]-Phenyl-C84-butyric acid methyl ester, termed $PC_{84}BM$ (Figure 6.4d), that was synthesised for OPVs by Hummelen et al [34]. In their study, the V_{OC} of MDMO-PPV:$PC_{84}BM$ was ~0.5 V lower to that obtained with PCBM. It has a stronger absorption in the visible (longer than $PC_{71}BM$) and it extends towards the NIR, along with an electron mobility of 10^{-3} cm^2 V^{-1} s^{-1} comparable to PCBM devices. However, it was found that the hole mobility is not strongly enhanced leading to space charge effects and efficiencies less than 1%. In addition, because of the fullerene cage size increase, its solubility becomes compromised, outweighing some of the benefits [34].

As such, although the previous sub-sections provided important guidelines to further develop PCBM and other derivatives, because of the inherently restricted flexibility for synthesis, researchers now look for new acceptor materials to address these limitations that will be discussed in the following section.
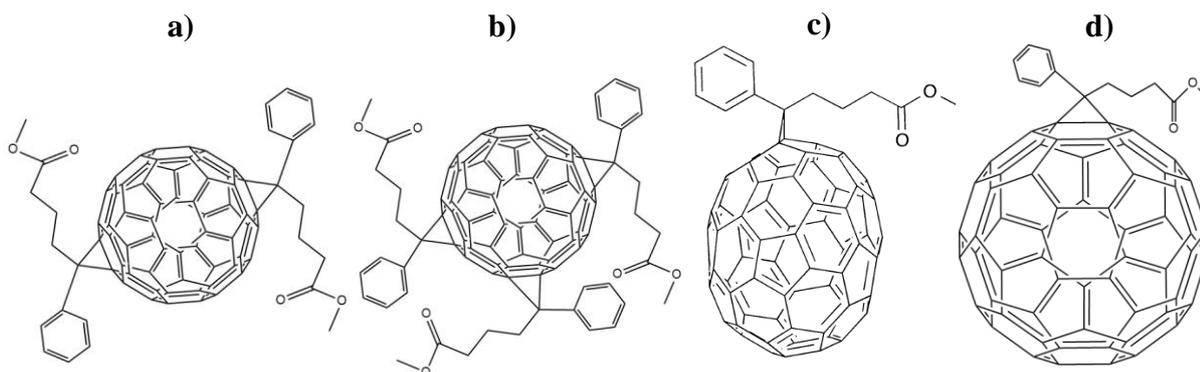
Figure 6.4. Example of multi adducts on PCBM (a-b) showing Bis-PCBM and Tris-PCBM. Schematic of fullerene cage derivatives (c-d) showing $PC_{71}BM$ and $PC_{84}BM$.

6.4 Emerging Non-fullerene acceptors and recent advances

As observed from the preceding sections, fullerene acceptors have continued to be used until recently as electron acceptor materials in OPVs, because of their electron affinity, good mobilities and tendency to form percolation pathways [25, 35, 36]. These characteristics have allowed them to produce high efficient OPVs when blended with low band gap donor counterparts [9, 37, 38]. Despite these valuable properties, as discussed previously, PCBM possess some limitations like incomplete absorption in the visible region, that chemical modifications are not straight forward (rendering low flexibility) and some difficulty in tuning optical/electronic properties [3, 17]. In addition, when fabricated in OPV devices, fullerenes have shown considerable degradation [39, 40].

Thus, demand for replacing fullerenes have acted as a strong leverage in the research community to develop NFAs. Contrarily to fullerenes, NFA possess excellent synthetic flexibility with readily available source materials, easy tuneable electronic/optical properties and improved stability [3]. As such, NFAs can work paired with donor materials in terms of electronic and optical complementarity and energetic compatibility to attain broader solar spectrum [41]. Besides, easier synthesis and simplified purification processes can substantially reduce the cost of NFAs manufacturing [3, 42]. As expected, important progress has been made with NFA, as PCEs of over 14%-16% have been achieved for single junction devices [43, 44] and over 20% have been predicted for tandem structures with modelling [45, 46].

However, despite these appealing results, many challenges remain to be addressed in this field. For example, in NFAs molecular twisting is introduced to prevent over aggregation but this can hamper charge transport [3, 47]. Moreover, NFAs do not have three-dimensional charge transport capability (like spherical fullerenes), so a scrutinized understanding of the interactions in pristine NFAs and blended NFAs is still needed [3]. Furthermore, morphological studies to underpin morphology process and device physics are still lacking, which are considered vital issues to further advance in progress. More recently, rylene imide dyes such as perylenediimide (PDI) and naphthalene diimide (NDI) have emerged as promising alternatives to replace fullerene acceptors for OPV application [6, 48]. Because they have low lying HOMOs and are electron deficient molecules, it is believed they can behave as n-type semiconductors [6]. To verify this claim, OFET devices have been examined with NDI which resulted in charge mobilities of 4.7×10^{-3} cm^2 V^{-1} s^{-1} in vacuum [6] attributed to more ordered structures as observed with XRD and AFM studies. In a recent work by Liu and co-workers [49], NDI with PTB7 achieved a PCE of 2.41%, demonstrating high promise for this NFA in OPV devices.

6.5 Novel materials synthesised for this work

In this Chapter, novel NFA and hybrid fullerenes are examined. These are NDI$_2$, *bis*-NDI plus NDI$_{12}$C$_{60}$ and Alk$_{12}$C$_{60}$ respectively, which were synthesised by Dr. Avestro and fellow PhD Phil Hope in a collaborative work. Figure 6.5 depicts the full chemical structure of the materials investigated in this Chapter. From the figure, the two NFAs exhibit a planar and shortened conjugated backbone in contrast to the spherical structure of fullerenes [3]. On the other hand, hybrid fullerenes exhibit a C60 core in which NDI$_{12}$C$_{60}$ has 12 NDI "arms" and similarly Alk$_{12}$C$_{60}$ but it bears no NDI units. As observed with the success of fullerenes, implementing a strategy which incorporates a 3D structure in both hybrid fullerenes may lead to interesting transport properties [3].
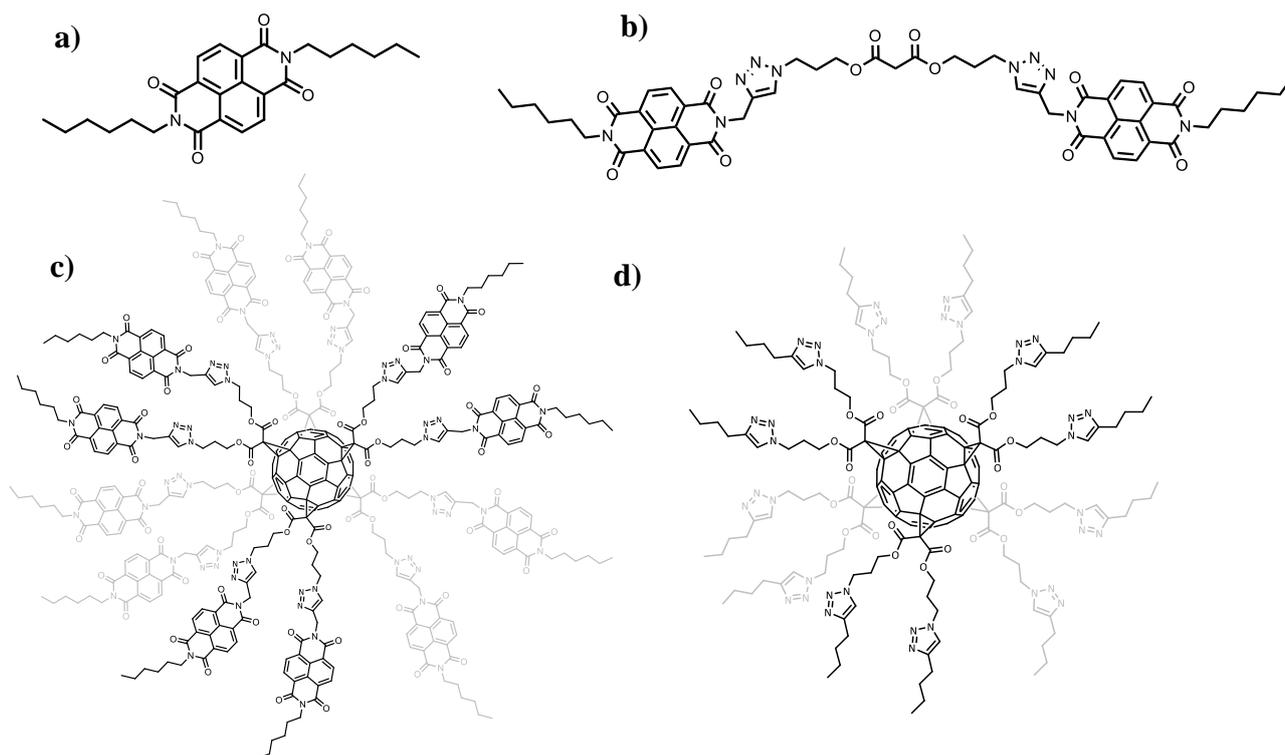
Figure 6.5. Molecular structure of novel materials showing on the top row (a-b) *bis*-NDI, NDI_2 and the bottom row (c-d) $NDI_{12}C_{60}$ and $Alk_{12}C_{60}$ respectively.

Figure 6.6 presents optical measurements in the form of absorption (solid lines) and emission (dashed lines) that were carried out on the novel acceptors to examine intermolecular π-aggregation and possibly the presence of charge transport pathways. These studies were performed in thin films drop cast from DCB solutions by the Chemistry colleagues.
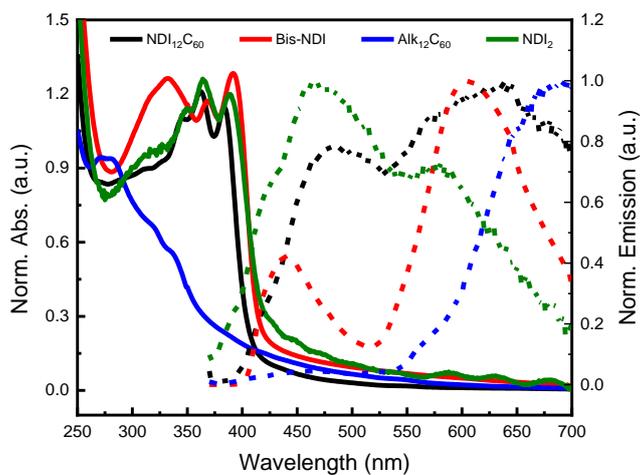
Figure 6.6. Absorption (solid lines) and emission (dashed lines) of novel acceptors used in this work.

We begin this part by first discussing the absorption and emission spectra of the two NFAs. *Bis*-NDI and NDI_2 exhibit a red shifted absorption profile with a maximum energy at ~400 nm, which suggests favourable NDI-NDI interactions may be more predominant in smaller molecules, in agreement with previous absorption studies on NDI derivatives [50, 51]. In addition, both NFA constituents depict a red shifted emission at ~550 nm – 600 nm which suggests molecular interaction and possibly self-assembly ordering [50]. Focusing the attention on the hybrid fullerene materials, $NDI_{12}C_{60}$ describes a broader absorption than that of $Alk_{12}C_{60}$ and a wider, featureless emission profile (~635 nm) which indicates intramolecular μ-aggregation [3]. Indeed, for $Alk_{12}C_{60}$ which has no NDI units in its structure, a weak absorption in the visible region is observed, particularly between 300 nm – 400 nm which extends towards 600 nm due to its fullerene core. Its emission profile is broad but centred towards the near infra-red (NIR) region extending over ~ 670 nm, and red-shifted from $NDI_{12}C_{60}$ which may be in part due to a higher solubility as seen with C60 core fullerenes [52].

To gain further insight regarding the molecular ordering hinted by absorption and emission measurements, the morphology of novel acceptors was examined using Scanning Electron Microscopy (SEM) and scans are presented in Figure 6.7. Starting with the NFAs, *bis*-NDI (Figure 6.7a) revealed a large crystalline morphology with some ordering present and features longer than 10 μm, whereas scans of NDI_2 revealed semi-crystalline and fibrillar aggregates (Figure 6.7b). This is in agreement with the absorption measurements presented before since red-shifted absorption points to crystallinity in the materials [53]. In addition, crystalline systems have been found to enhance electronic coupling and charge transport in other polymer:fullerenes [54], and polymer:NFAs [55] systems, which suggests that these novel NFAs may promote electron transport.

In hybrid fullerenes -$NDI_{12}C_{60}$ and $Alk_{12}C_{60}$- the morphology was very different. $NDI_{12}C_{60}$ (Figure 6.7c) resulted in no noticeable morphology in the resolution examined, which may be expected due to its molecular shape that could hinder packing into crystalline domains. Even though the absorption of $NDI_{12}C_{60}$ was not much enhanced if compared with the NFAs, due to the NDI 'arms' and adjacent $NDI_{12}C_{60}$ molecules, it is possible that it could provide a 3D network of favourable π-interactions once spin casted into a thin film. $Alk_{12}C_{60}$ on the other hand, realised a similar morphology but with some particles of varying sizes (Figure 6.7d).
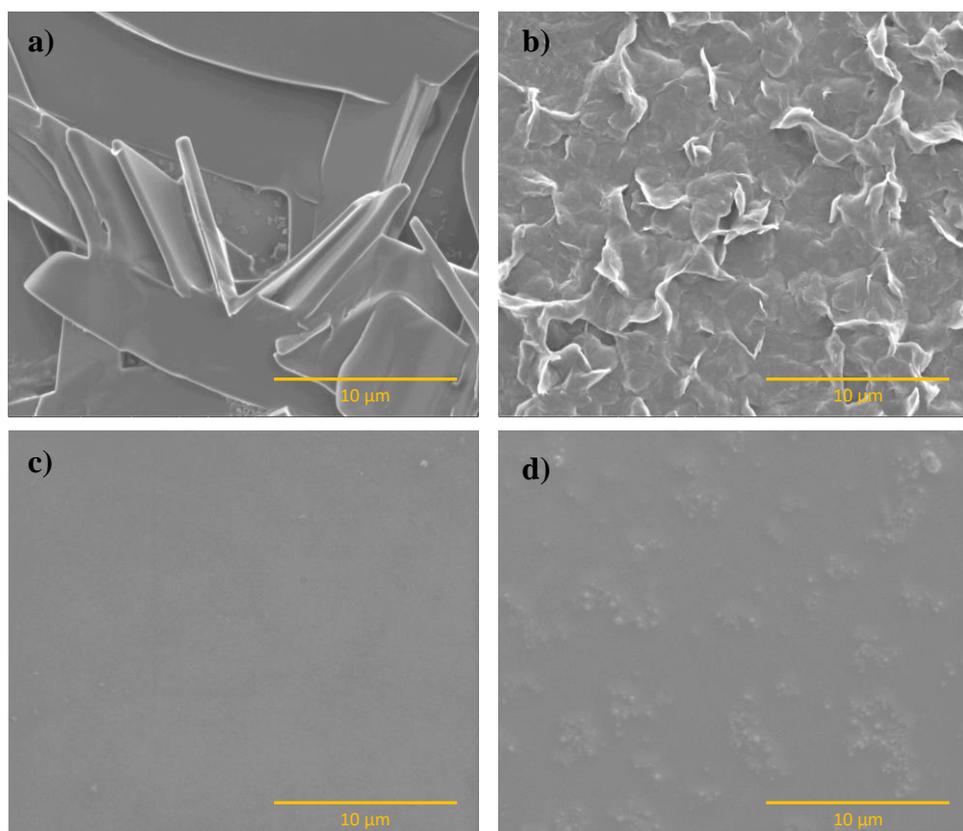
Figure 6.7. SEM scans of a, b) *bis*-NDI, NDI_2, and c, d) $NDI_{12}C_{60}$ and $Alk_{12}C_{60}$ respectively.

However, the behaviour of $Alk_{12}C_{60}$ might be expected to be different in terms of the molecular interactions between neighbouring molecules, since its 'arms' are NDI deficient in contrast to $NDI_{12}C_{60}$ which possibly exhibits a wider range of interactions due to its NDI arms. Thus, from these absorptions and morphology studies, it was determined that $NDI_{12}C_{60}$ and $Alk_{12}C_{60}$ could potentially extend charge transport pathways in three-dimensional space due to their spherical molecular structure. NDI_2 and *bis*-NDI on the other hand, share some of the physical properties but their structures are much more compact.

In order to rationalise whether these materials could facilitate charge transport, organic diodes were fabricated to probe electron transport in single-carrier devices. Additionally, a blend of $NDI_{12}C_{60}$ with NDI_2 at 1:1 and 1:2 ratios were fabricated to understand the relationship between these blended compounds; one with a fullerene core and the other deficient of fullerene.

6.6 Electron transport probed by Space Charge Limited Current method

Before the mobility measurements are discussed, basic concepts on charge transport are first reviewed. To further design and optimise new materials, the study of charge transport properties is necessary to inform OPV device engineers [56-58]. There are a number of techniques to study carrier mobility, notably time of flight (TOF), the use of field effect transistors (FETs), current extraction during linear increasing voltage (CELIV) and space charge limited current (SCLC), all which are well established methods with advantages and drawbacks [54, 58, 59]. Amongst them, SCLC is suited to determine mobilities of both types of carriers on OPV materials and in the context of an OPV structure as briefly introduced in the experimental and modelling methods Chapter. A major advantage of this technique is that the same process used to fabricate OPVs is used for the single carrier measurements except for the contacts [58, 60-62]. By using specific contacts with work functions near the HOMO or LUMO of the material under study, the device is dominated by one type of carrier. For example, to probe electron mobility, contacts are selected which have poor efficiencies for hole injection and do not constitute barriers for electron extraction. This approach has been used to study a range of single carrier OPVs, including polymers [54, 63], fullerenes [64, 65] and more recently NFAs [48, 49].

In this work, single carrier devices with two suitable electron injecting contacts were used to characterise electron transport properties. When a forward bias is applied, the free carrier concentration increases because of the injected carriers. In such devices, the J-V characteristics depend entirely on the majority carrier properties since only one type of carrier is injected [66]. In this situation, when the current is dominated by the injected charge, the J-V characteristics become quadratic and will depend only on the mobility and dielectric constant. This is known as the SCLC, and in the absence of traps, is characterised by the Mott-Gurney law [62, 66]. In this regime, the SCLC current varies as $J \propto V^2$, as per the following equation [62]:

$$J = \frac{9}{8} \varepsilon_0 \varepsilon_r \mu_e \frac{V^2}{L^3} \tag{6.1}$$

Here, ε_0 represents the permittivity of vacuum (8.85×10^{-12} F.m^{-1}), ε_r the novel fullerene materials dielectric constant ($\sim$3.9 V), μ_e the electron mobility, L the active layer thickness ($<$250 nm), and V the internal voltage (1.5 V) [62, 64, 67]. In this thesis, because the contacts have two different work functions there is a built-in voltage whilst still being a single carrier device. This means that one contact injects electrons well and one contact has a lightly larger barrier for electron injection and extraction, but still does not inject or extract holes, as observed in Figure 6.8 [66].
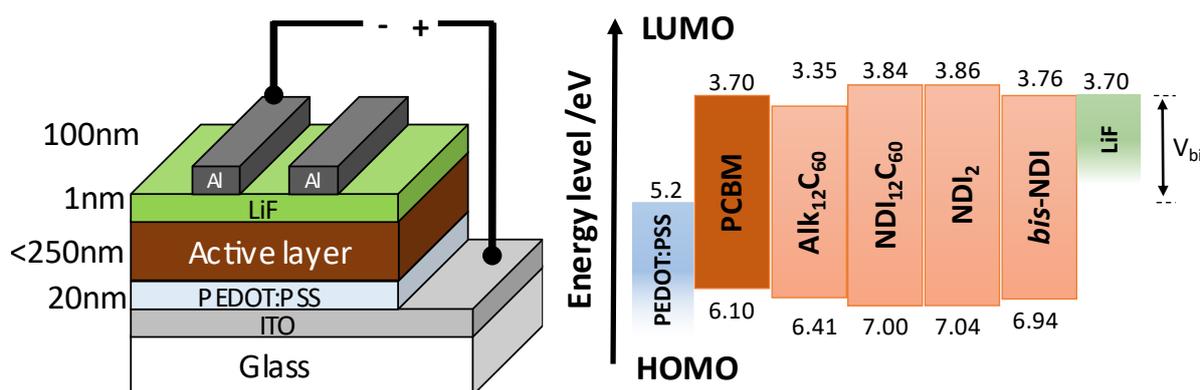
Figure 6.8. Device architecture of diodes used in this work (left) and energy levels (right).

For the fabrication of electron-only devices, the novel materials were sandwiched between PEDOT:PSS and Lithium fluoride (LiF)/ Aluminium (Al) cathode (Figure 6.8). A total of 20 nominally same repeats were fabricated for each of the compounds yielding a total of 100 diodes. Also, the results reported herein depict the typical behaviour rather than "champion" diodes. For comparisons, PCBM was also fabricated into an electron-only diode and mobility measurements were carried out as a control sample. Measurements were performed in cleanroom under room temperature conditions and thicknesses were obtained with Dektak 3S high resolution profilometer. The materials used here are soluble in common organic solvents (see experimental Chapter) and were spin casted on a patterned bottom ITO electrode. Figure 6.8 presents the energy band diagram (flat band) condition. It can be observed that because of the work functions, the LiF/Al contact forms an ohmic contact for electron injection with PCBM. PEDOT:PSS has a work function of 5.2 eV that does not match the HOMO of the materials used here, hence, hole injection is supressed from the anode contact to the active layer [64]. As a result, charge transport is dominated by electrons under forward bias [64]. This approach is the same as that used elsewhere [64, 68, 69]. The built-in voltage stems from the work

function difference (i.e. V_{bi} = PEDOT:PSS – LiF/Al) resulting in ~1.5 V. To obtain the internal voltage (V_{int}) the applied voltage is subtracted from the V_{bi} as follows: $V_{int} = V_{app} - V_{bi}$. By fitting the Mott-Gurney equation to the experimental dark J-V_{int} curves, the electron mobility is estimated. A challenge in obtaining reliable fits to mobility in such devices can be the influence of injected charge into the disordered organic semiconductor. Fabricating a range of SCLC diodes with a range of active layer thicknesses and performing a global fit to these data can mitigate this concern.

6.7 Electron mobility in thick and thin fullerene and hybrid fullerene acceptors

6.7.1 PCBM

First, measurements were performed with PCBM to use as control and to validate the architecture selected to study all materials. The electron-only diode structure utilised was glassITO/PEDOT:PSS/PCBM/LiF/Al as depicted in Figure 6.8. Current-voltage measurements were performed by applying positive bias from 0 V to 5 V between the contacts. The reason for a higher bias (larger than V_{bi}) is to provide enough confidence that fits depict a quadratic behaviour, characteristic of SCLC [70]. Also, once the current becomes limited by the uncompensated electron injection, it results in a space charge limited current that can be described by Eq. 6.1 [70]. Experimental dark J-V characteristics of PCBM with thicknesses of 120 nm and 240 nm are shown in Figure 6.9. Because of the energy levels presented in Figure 6.8, a built-in voltage of ~1.5 V is anticipated in these devices [64]. It is clear from Figure 6.9a, b that in thin PCBM diodes, the J scales linearly with the voltage, a consequence of series resistance, whilst in thick PCBM (Figure 6.9c, d) the slope of J versus V depends quadratically on the voltage, more so at lower voltages (<1.5 V), which is indicative that the current depends only on the mobility also known as the space charge region. This type of behaviour is common in low mobility organic semiconductors, which allows for direct single-carrier measurements as reported elsewhere [54]. To demonstrate the quadratic behaviour under the SCLC regime, a fit was included in Figure 6.9d (red curve) for the thick device. In addition, blue-dashed lines are provided as guidelines to depict the $J \propto V$ and $J \propto V^2$ trends for the same device [71].
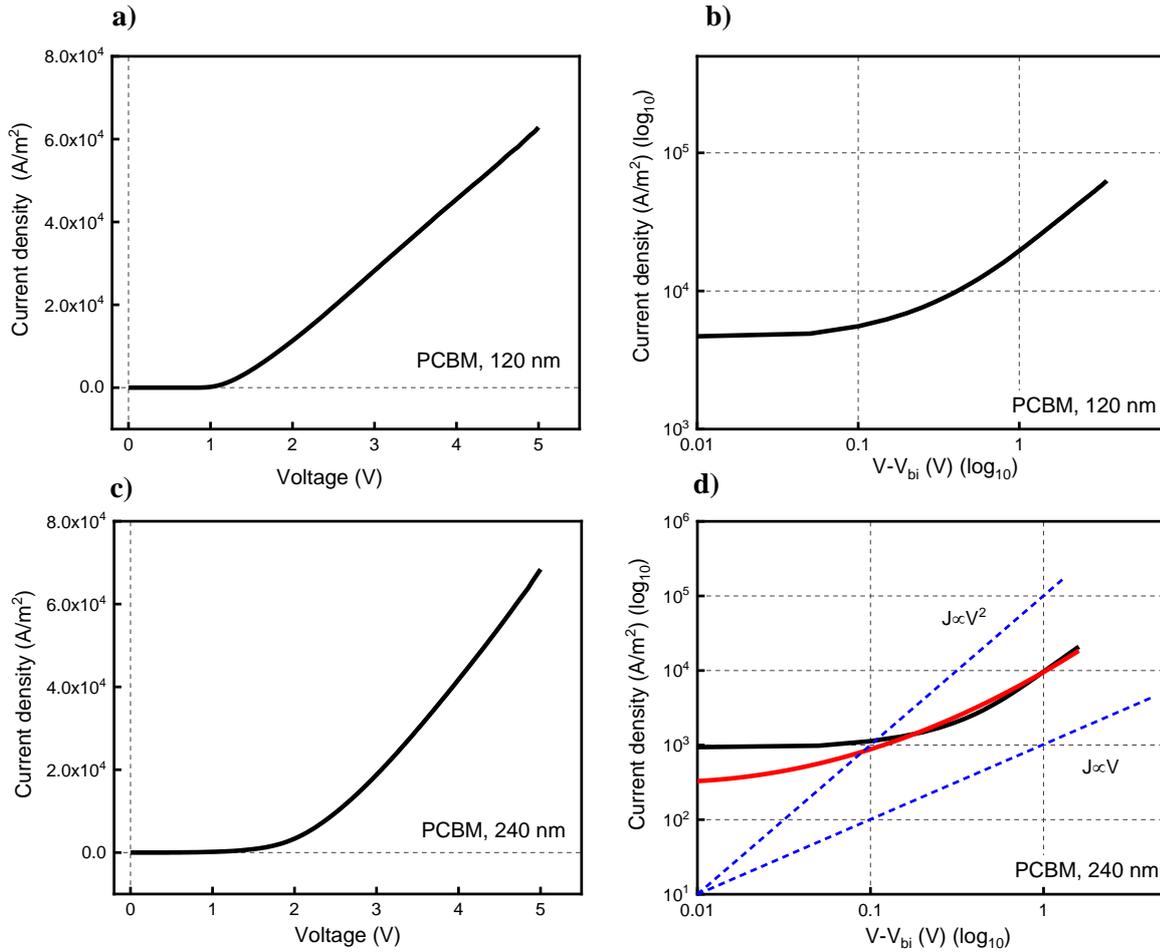
Figure 6.9. Experimental dark J-V curves of ITO/PEDOT:PSS/PCBM/LiF/Al electron-only devices with thicknesses of a, b) 120 nm and c, d) 240 nm.

Further, the current densities in the linear-linear plots of parts a, c span to several orders of magnitude which may hide some of the data and present V_{bi} effects, whereas in semi-log parts b, d is easier to observe the quadratic behaviour of the curve with the effect of V_{bi} corrected [32, 70]. Also, the difference in V_{bi} between a and c is attributed to contact effects in a thin device [67]. As such, Mott-Gurney's equation was used to determine the electron mobility in thick PCBM. Herein, PCBM dielectric's constant was considered as 3.9, with a $L = 240$ nm, and V_{bi} of 1.5 V. Because of the linear dependence of J with V of the thin electron-only device, mobility could not be determined by SCLC fitting. The experimental data of thick PCBM devices was fitted using equation 6.1 and the results are observed in the Figure 6.10. In addition, because the thick PCBM fit looks somewhat linear at higher voltages, the electron mobility was measured at 1.5 V_{bi} to ensure the current depends only on the mobility as observed by the quadratic behaviour.

An electron mobility of 2.90×10^{-6} m^2 V^{-1} s^{-1} was obtained, comparable to the results published in a study of Mihailetchi et al [64] and to those of Armin et al [72]. Furthermore, the mobility results obtained here are on par with neat PC$_{71}$BM mobilities observed elsewhere [73]. From previous literature reports, differences in mobilities with PCBM are generally attributed to energetic disorder in the bulk as compared to C60's single crystals, which can play an important role for electron transport [64]. Thus, there are two important observations from these results: 1) Similar mobilities have been realised by highly quoted papers and, 2) the results obtained confirm that the measurements/device geometry used are valid. As such, we now turn the attention to the novel electron acceptors.
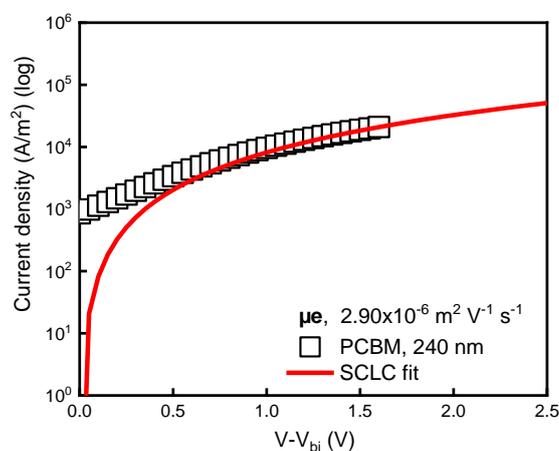
Figure 6.10. Electron transport in PCBM device with thickness of 240 nm and V$_{bi}$ of 1.5 V, as described by SCLC.

6.7.2. Hybrid fullerene acceptors NDI$_{12}$C$_{60}$ and Alk$_{12}$C$_{60}$

To begin the examination of novel materials, NDI$_{12}$C$_{60}$ and Alk$_{12}$C$_{60}$ are discussed together as these hybrid acceptor components have a fullerene core in their molecular structure as shown at the beginning of section 6.5. Unlike PCBM, the NDI$_{12}$C$_{60}$ acceptor has 12 NDI derivatives distributed around the exterior. If the molecular packing is similar to what has been observed for other NDI derivatives [3, 74], then there is potential to facilitate electron transport. To test this theory, electron-only diodes were fabricated. Figure 6.11 shows the thin and thick dark J-V-V$_{bi}$ curves in semi-log scale for NDI$_{12}$C$_{60}$ respectively. Figure 6.11a, b confirms that in the J-V slope (semi-log), the current J depends quadratically on the voltage V which is indication of SCLC regime. By using an

acceptor dielectric constant of $\varepsilon = 3.9$ and $L = 139$ nm and 189 nm, it is found that the J-V characteristics are well described by the equation 6.1 considering 0.82×10^{-11} m^2 V^{-1} s^{-1} and 2.47×10^{-11} m^2 V^{-1} s^{-1} as electron mobilities respectively (Figure 6.11c, d). In addition, the obtained mobilities are similar for both thicknesses, which means that the transport characteristics in the device are bulk limited and that contact effects are minor [75].
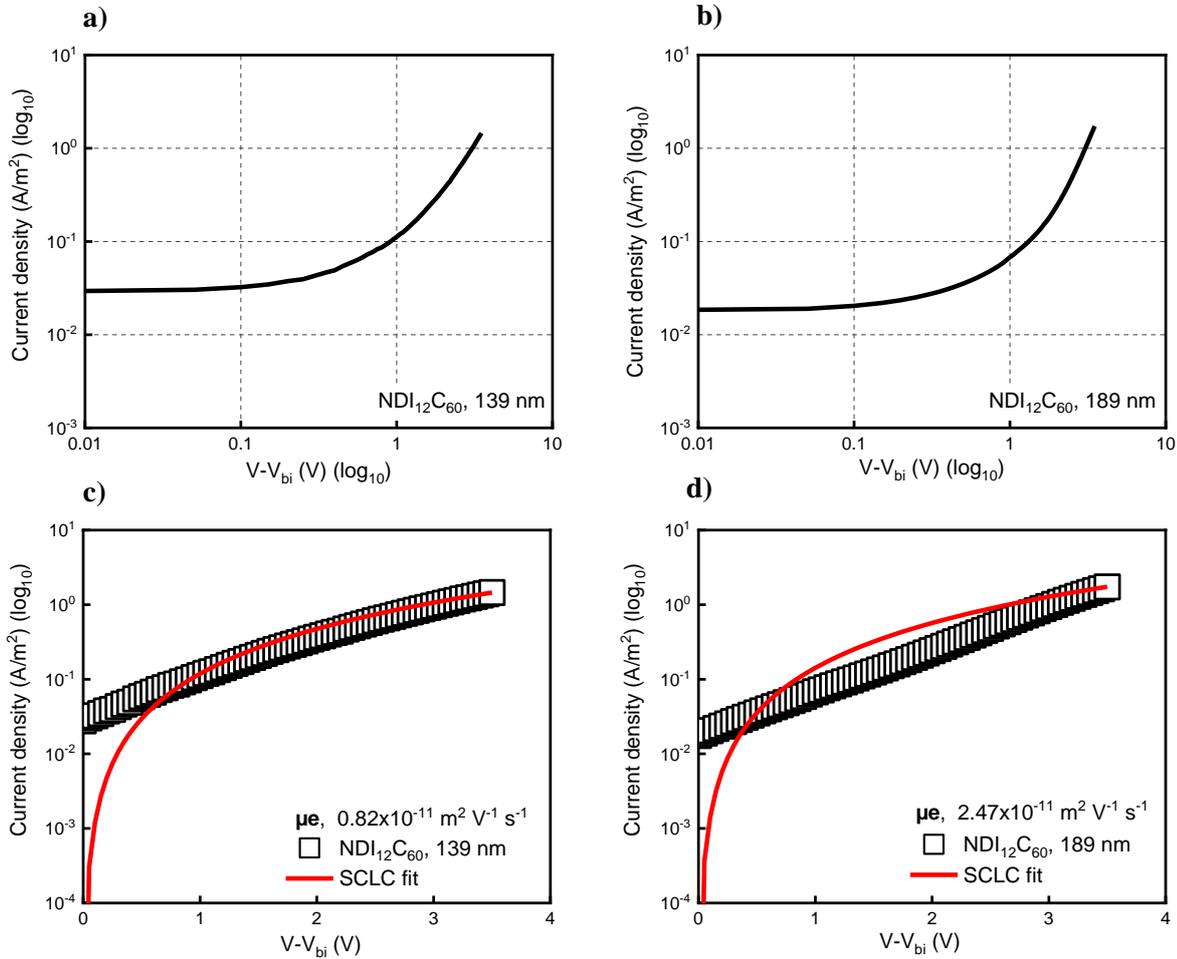
Figure 6.11. a, b) Experimental dark J-Vs with semi-log scale for thin and thick diodes respectively. c, d) Electron transport in thin and thick $NDI_{12}C_{60}$ devices under SCLC regime.

Contrasting to PCBM, $Alk_{12}C_{60}$ has a deeper LUMO as depicted on Figure 6.8 and no NDI derivatives in its molecule as with $NDI_{12}C_{60}$. To verify the potential for electron transport J-V dark curves of $Alk_{12}C_{60}$ are presented in Figure 6.12a, b. A quadratic relationship between J and V is also evident from both thin and thick devices which was fitted into the SCLC model. Thicknesses were measured yielding $L = 145$ nm and $L = 200$ nm and the electron mobility of diodes was 1.43×10^{-11} m^2 V^{-1} s^{-1} and 1.03×10^{-11} m^2 V^{-1} s^{-1} as shown in Figure 6.12c, d. Again, similar mobilities for the thick and thin

diodes considered here reflect that electron transport is limited by bulk effects and not contact dominated [75].
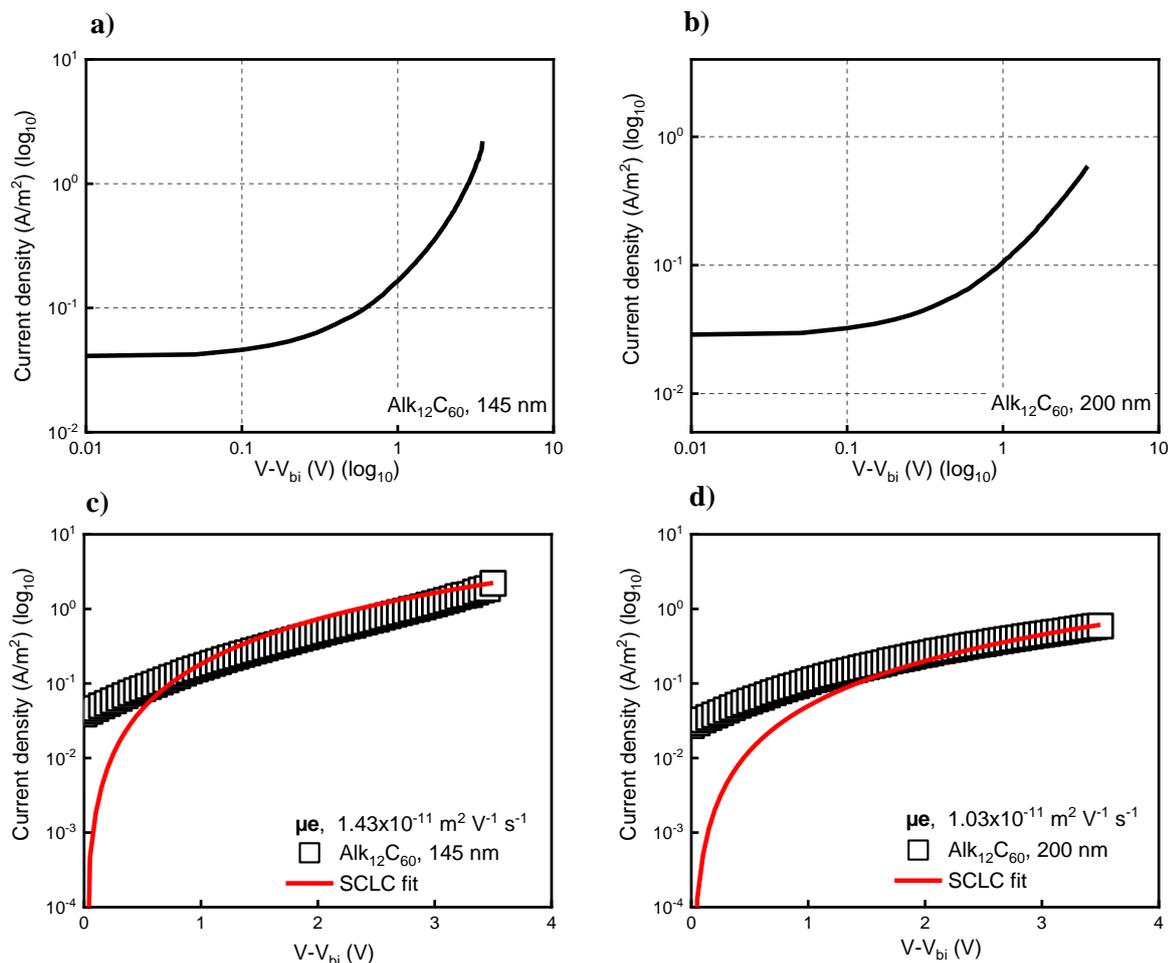
Figure 6.12. a, b) Experimental dark J-Vs with semi-log scale for thin and thick diodes respectively. c, d) Electron transport in thin and thick $Alk_{12}C_{60}$ devices under SCLC regime.

Interestingly, the mobility of thick $Alk_{12}C_{60}$ device was slightly lower compared to thick $NDI_{12}C_{60}$ with electron mobility of 2.47×10^{-11} m^2 V^{-1} s^{-1} whereas the thin $Alk_{12}C_{60}$ was barely higher (by a factor of 0.6) to thin $NDI_{12}C_{60}$. However, in comparison to PCBM, these two components have a lower mobility by ~5 orders of magnitude. These results also suggest that the strategy of NDI 'arms' in $NDI_{12}C_{60}$ did not facilitate the formation of charge transport pathways, but that instead transport was via the fullerene core as the results were similar to $Alk_{12}C_{60}$. To shed light on the possible reasons why the mobility was low, it is noted that a report by Volker et al [76] on hybrid solar cells, a molecule with a fullerene core was used as an electron blocking contact whilst twelve

153

triaryl units were added to improve hole transport properties. By taking a closer look at their molecule design and comparing it to $NDI_{12}C_{60}$ molecule, the similarities are evident between the two. Thus, it may be that increasing the length of the linker between the fullerene core and NDI derivatives could impact carrier mobility in $NDI_{12}C_{60}$ as observed in their study. Contrarily to PCBM, the $Alk_{12}C_{60}$ modifications on the fullerene molecule clearly impacted the electron transport properties and presumably the molecule packing as observed with the SEM analysis, which ultimately affected the charge transport. These results highlight the importance of studying electron mobility in novel electron acceptor materials, suggesting that in OPV fabrication $NDI_{12}C_{60}$ and $Alk_{12}C_{60}$ would suffer from poor charge transport. In addition, it invites to further investigation of the fullerene-free compounds.

6.7.3 Non-fullerene acceptors NDI$_2$ and *bis*-NDI

Novel NF acceptors, NDI$_2$ and *bis*-NDI were also investigated by fabricating electron-only diodes. To recap from previous sections, the presence of charge transport pathways through crystals was hinted from absorption and emission measurements as shown in Figure 6.6. Crystalline domains were observed in morphological images of *bis*-NDI (Figure 6.7) which have been demonstrated to be beneficial for charge transport in other systems [54, 77]. The electron-only architecture fabricated consisted in the same geometry as explained previously. Dark J-V data for *bis*-NDI is shown in Figure 6.13 for $L=$ 100 nm and $L=$ 248 nm devices. Indeed, the slope of the curves exhibited a quadratic behaviour of J with V, which allowed the data to be fitted with the SCLC equation (Figure 6.13c, d).

Thin and thick devices yielded mobilities of 1.50×10^{-8} m^2 V^{-1} s^{-1} and 0.73×10^{-8} m^2 V^{-1} s^{-1} respectively, which are remarkably higher in contrast to $Alk_{12}C_{60}$ and $NDI_{12}C_{60}$. Because these electron mobilities attained similar values for different thickness, it demonstrates that the current is bulk limited and not by contact effects as seen elsewhere [75]. Hence, these measurements further corroborated that *bis*-NDI is a better candidate to facilitate electron transport in comparison with the fullerene core hybrid fullerenes. Although in literature NDI and derivatives have attained similar or higher mobilities [3, 49], our results are promising since the device structure used here can be further optimised (i.e. different interlayers, solvent additives, different thermal annealing times, etc).
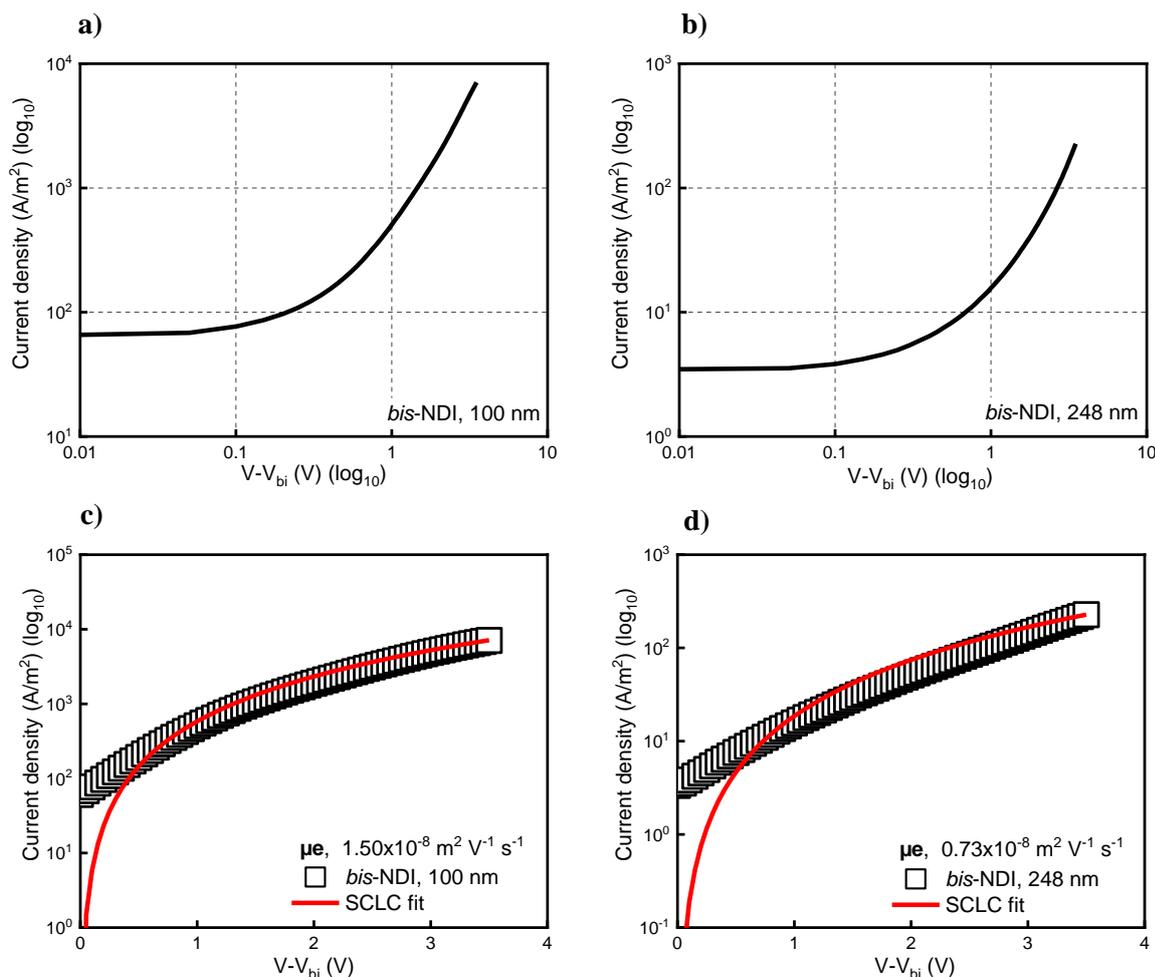
Figure 6.13. a, b) Experimental dark J-Vs with semi-log scale for thin and thick diodes respectively. c, d) Electron transport in thin and thick *bis*-NDI devices under SCLC regime.

Now, turning to NDI₂, the morphological analysis outcome revealed a fibrillar and semi-crystalline assembly in contrast to *bis*-NDI. To probe electron transport in this NFA, single carrier diodes were fabricated. Experimental dark J-V-V_{bi} data for NDI₂ is shown in Figure 6.14a, b for thin and thick devices. Unlike *bis*-NDI, only thick NDI₂ presented a quadratic behaviour, as the thin device exhibited a linear current-voltage dependence which did not allowed mobility to be measured by SCLC. A high electron mobility of 0.80×10^{-6} m² V⁻¹ s⁻¹ was obtained for the thick diode (Figure 6.14c).
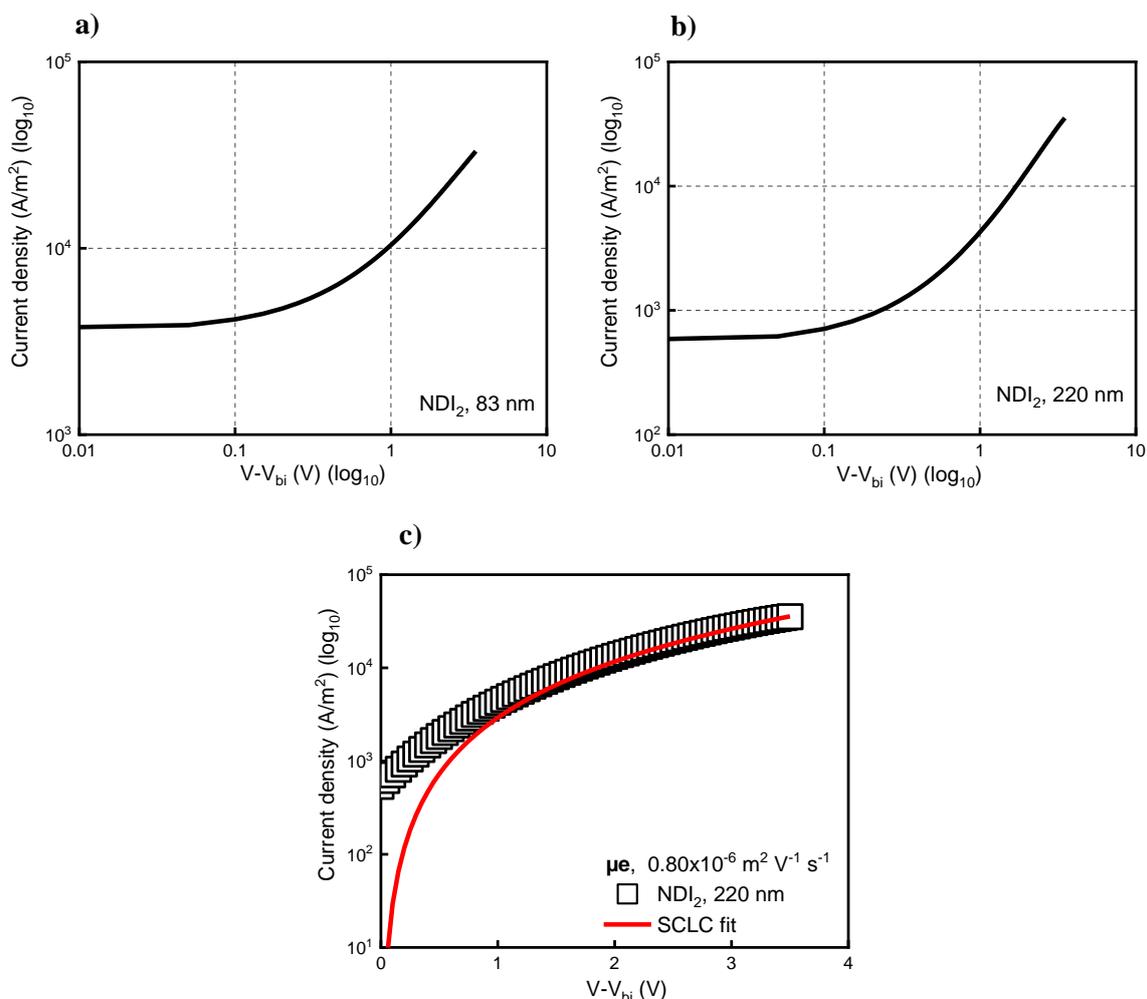
Figure 6.14. a, b) Experimental dark J-Vs with semi-log scale for thin and thick diodes respectively. c) Electron transport of thick NDI$_2$ diode with SCLC method.

The electron mobility achieved was amongst the highest for the novel acceptors described in this thesis, remarkably close to benchmark PCBM control. After NDI$_2$, *bis*-NDI came the closest to PCBM by just over ~2 orders of magnitude lower. Even though SEM characterisation revealed a more semi-crystalline nature in NDI$_2$ rather than crystalline as in *bis*-NDI, it is likely that the suitable fibrillar networks provided sufficient transport pathways to achieve a higher mobility [78]. Indeed, a recent paper by Kumari et al [50], electron only diodes of NDI derivatives were fabricated with different mg/ml. A 40 mg/ml solution achieved an electron mobility of 1.8×10^{-3} cm^2 V^{-1} s^{-1} comparable to the results obtained here. Further, it was demonstrated that by increasing the annealing time the conductivity improved. Similarly, Avinash et al [74] fabricated thicker NDI derivatives devices (1 µm) to measure electron mobility which was in the order of 10^{-8} cm^2 V^{-1} s^{-1}. The mobility achieved was attributed to π-π stacking direction and ordering as displayed by XRD studies. Likewise, in a recent communication by Liu and co-workers

156

[51] NDI derivatives 'NDI-NI and NDI-CI' were used as a cathode interlayers (from 8 nm to 37 nm) enhancing electron transport properties attributed to a reduction of Schottky barriers at the contact. Notably, the net effect was an improvement in efficiency with a maximum of 16.9% for a range of fullerene, NFA and ternary-based devices. Thus, these encouraging results also demonstrate potential for these novel NFAs to be used as interlayers in organic electronics.

In agreement with these data, the NDI_2 probed here obtained comparable electron mobilities which can be further optimised. As proposed for *bis*-NDI, further device optimisation could also be achieved with NDI_2 by using different ratios, blending with another material, the use of additives to tune morphology and by increasing the annealing temperature as hinted in the previous references. Thus, these emergent NFA acceptors demonstrate potential for OPV fabrication.

6.7.4 Electron transport in blends of $NDI_{12}C_{60}$:NDI_2

Going a step further, the impact of blending two compounds in different ratios to understand its effect on mobility was also investigated. As observed in their molecular structures, $NDI_{12}C_{60}$ has 12 NDI which are distributed in three-dimensional space. If molecular packing is similar to NDI_2 (which resembles one of the $NDI_{12}C_{60}$ 'arms'), it is likely that charge transport could be facilitated in these blended composites. In the preceding sections, it was observed that $NDI_{12}C_{60}$ attained a lower mobility as the NDI units did not facilitate charge transport. On the other hand, NDI_2 realised a high mobility in part attributed to a more ordered structure in the film.

To further determine whether if NDI to NDI pathways are the reason for low mobility on $NDI_{12}C_{60}$, electron only-diodes with architecture of ITO/PEDOT:PSS/$NDI_{12}C_{60}$:NDI_2/LiF/Al were fabricated. Because of the presence of NDIs in the mixture, it is expected that it will have an impact in the measured electron mobility. Dark J-V curves are presented on Figure 6.15a, b for 1:1 and 1:2 blend ratios of $NDI_{12}C_{60}$:NDI_2 respectively. Due to the quadratic slope of J with V, data was also fitted to the SCLC method to probe electron mobility (Figure 6.15c, d). Typical electron mobilities achieved were 3×10^{-9} m^2 V^{-1} s^{-1} and 1.75×10^{-8} m^2 V^{-1} s^{-1} for 1:1 and 1:2 ratios respectively, considering nominally similar diode thicknesses of $L = 191$ nm and $L = 167$ nm. From Figure 6.15d, the 1:2 ratio mobility came slight closer to fullerene PCBM.
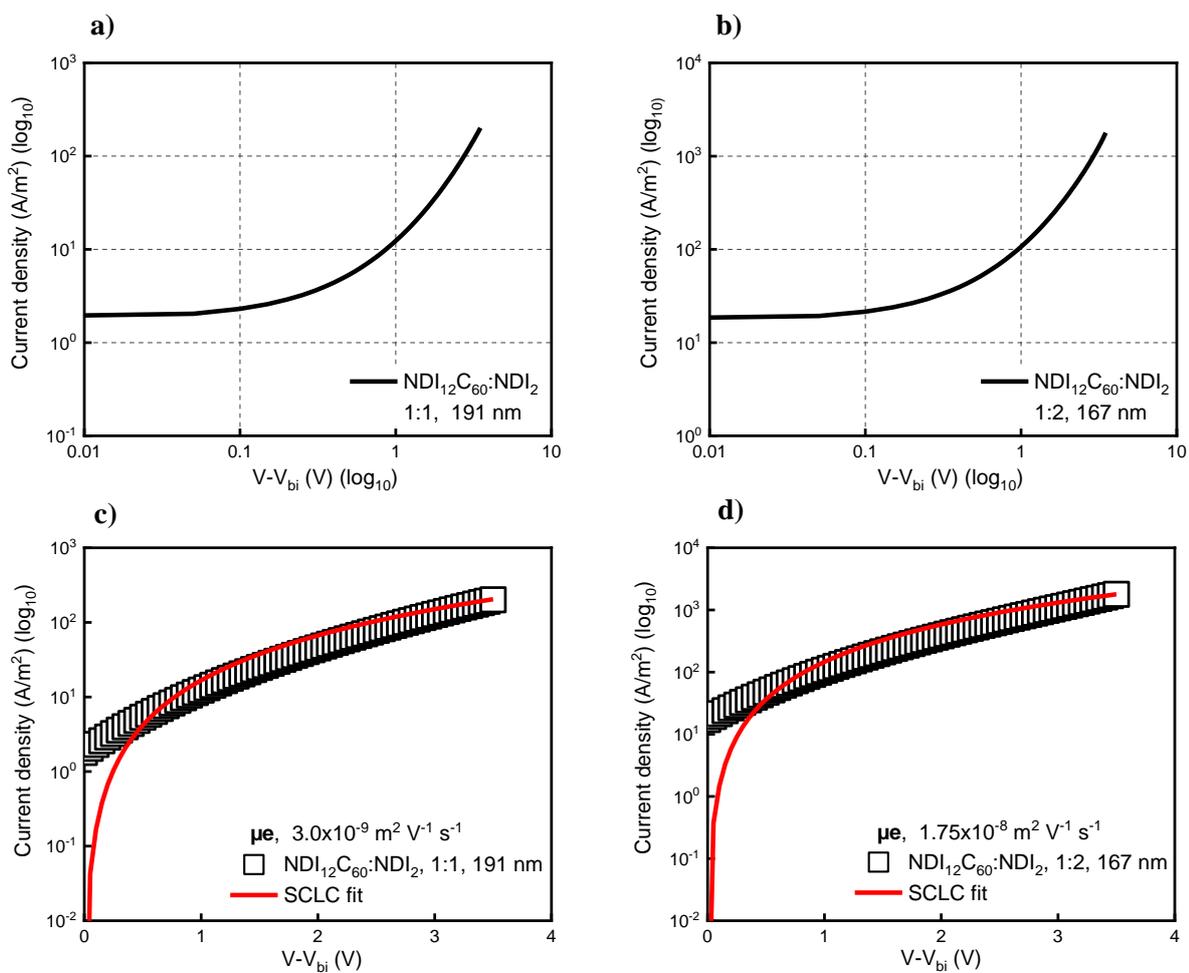
Figure 6.15. a, b) Experimental dark J-Vs with semi-log scale for 1:1 and 1:2 of $NDI_{12}C_{60}:NDI_2$ diodes respectively. c, d) Electron transport in $NDI_{12}C_{60}:NDI_2$ for the same ratios under SCLC.

Indeed, as the doping of NDI_2 was added into the mixture (Figure 6.16a), the electron transport was enhanced. The typical mobilities obtained with a 1:2 ratios are a factor of ~2 less compared to neat films of high performing ITIC NFA, as reported by Lin et al [79] with SCLC measurements. Similarly, Holliday and colleagues [80] achieved ~3-6x10^{-6} cm^2 V^{-1} s^{-1} electron mobilities on a blend of P3HT with novel IDTBR NFA, which is close to the values obtained here. Interestingly, although the electron mobility in single compound for thick $NDI_{12}C_{60}$ was lower (Figure 6.16b) by more than two orders of magnitude, when blended with NDI_2 electron mobility rose depicting a power law trend. Therefore, the data suggests that $NDI_{12}C_{60}$ was insulating whereas NDI_2 was not. From the percolation theory, the information presented suggests that by adding more NDI_2 content the electron mobility would increase until certain critical concentration (or percolation threshold) followed by a plateauing [81, 82]. In addition, the strong influence of NDI_2 on the mobility might also suggest that $NDI_{12}C_{60}$ was acting as a 'trap' material

(i.e. by the C60 core), whereby NDI$_2$ dilutes and eventually replaces the effect of these traps. Although this last is just speculation, further morphology characterisation may shed light into understanding the electron transport in this blend.

a)

b)

Acceptor	Ratio	μe mobility, V_{bi}1.5V $(m^2V^{-1}s^{-1})$
NDI$_{12}$C$_{60}$:NDI$_2$	1:0	2.47×10^{-11}
NDI$_{12}$C$_{60}$:NDI$_2$	1:1	3.00×10^{-9}
NDI$_{12}$C$_{60}$:NDI$_2$	1:2	1.75×10^{-8}
NDI$_{12}$C$_{60}$:NDI$_2$	0:1	0.80×10^{-6}
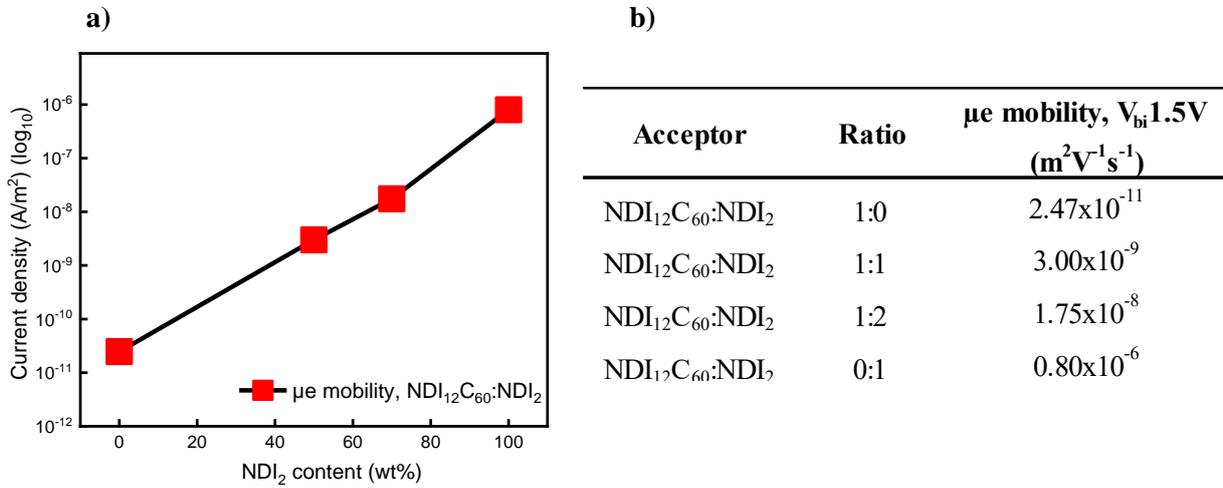
Figure 6.16. a) Electron mobility in NDI$_{12}$C$_{60}$:NDI$_2$ with increasing NDI$_2$ content and b) summary of electron mobility in NDI$_{12}$C$_{60}$:NDI$_2$ blend.

To wrap up this section, a summary table showing the electron mobility of all the novel materials is shown in Table 6.1.

Acceptor material	Thickness (nm)	Experimental μe mobility $(m^2V^{-1}s^{-1})$	Simulations μe mobility $(m^2V^{-1}s^{-1})$
PCBM	240	2.90×10^{-6}	4.00×10^{-8}
NDI$_{12}$C$_{60}$	189	2.47×10^{-11}	1.50×10^{-10}
NDI$_{12}$C$_{60}$	139	0.82×10^{-11}	3.85×10^{-11}
Alk$_{12}$C$_{60}$	200	1.03×10^{-11}	5.73×10^{-11}
Alk$_{12}$C$_{60}$	145	1.43×10^{-11}	7.05×10^{-11}
bis-NDI	248	0.73×10^{-8}	1.52×10^{-8}
bis-NDI	100	1.50×10^{-8}	1.75×10^{-8}
NDI$_2$	220	0.80×10^{-6}	2.44×10^{-8}
NDI$_{12}$C$_{60}$:NDI$_2$(1:1)	191	3.00×10^{-9}	2.70×10^{-9}
NDI$_{12}$C$_{60}$:NDI$_2$(1:2)	167	1.75×10^{-8}	9.05×10^{-9}

Table 6.1. Summary with novel materials and electron mobility measurements attained by SCLC and GPVDM modelling. Modelling fits are included in the Appendix section.

Furthermore, we used a drift diffusion model to fit the experimental J-V curves of all compounds and obtained largely the same results which are included in the Appendix section.

6.7 Conclusions

In this Chapter, electron-only diodes were fabricated using a family of novel acceptors synthesised by Dr. Avestro and fellow PhD Phil Hope to probe electron mobility, a critical factor to acquire higher efficiencies in new PV materials. NFA diodes fabricated of NDI_2 and *bis*-NDI attained the highest mobilities, revealing the capability of these components to mediate electron transport. Due to their semi-crystalline and crystalline nature respectively, NDI_2 achieved an electron mobility of 0.80×10^{-6} m^2 V^{-1} s^{-1} and thick *bis*-NDI of 0.73×10^{-8} m^2 V^{-1} s^{-1} which were close to PCBM control with 2.90×10^{-6} m^2 V^{-1} s^{-1}. Further optimisation techniques sought by OPV engineers could be utilised on these NFAs to potentially achieve higher mobilities. In terms of the hybrid fullerenes, the electron transport was drastically reduced in $NDI_{12}C_{60}$ and $Alk_{12}C_{60}$ with mobilities in the order of 10^{-11} m^2 V^{-1} s^{-1}. From the experimental data of this Chapter, we demonstrate that the synthetic strategy of adding NDI units and molecular moieties as 'arms' to C60 cores did not work to enhance electron mobility, ensuing further investigation. To rationalise on the possible reasons for the low mobility, a blend of $NDI_{12}C_{60}$:NDI_2 with the different ratios was also examined. A power law increase in mobility with higher contents of NDI_2 suggested $NDI_{12}C_{60}$ was acting as insulator and that increasing content of NDI_2 facilitated such raise in mobility. Further, experimental results were fitted with drift diffusion modelling and the trends obtained were largely the same, enabling accurate interpretation of our data.

Overall, the results presented here indicate that NDI_2 and *bis*-NDI could potentially be used in the fabrication of OPVs. On the other hand, hybrid fullerenes $NDI_{12}C_{60}$ and $Alk_{12}C_{60}$ could possibly perform better in other types of experiments like photoelectric water splitting, where fullerenes are highly compromised due to their low water stability. Lastly, these results demonstrate that novel compounds which are more flexible to manufacture have the potential to achieve electron mobilities comparable to well-established fullerenes. Thus, this Chapter presented data that is valuable for synthetic chemists and OPV design engineers, to further assist in the development of novel materials.

6.8 References

1.   Thompson, B.C., et al., *Polymer-Based Solar Cells: State-of-the-Art Principles for the Design of Active Layer Components.* Green, 2011. **1**(1).

2.   Anthony, J.E., et al., *n-Type Organic Semiconductors in Organic Electronics.* Adv. Mater., 2010. **22**(34): p. 3876-3892.

3.   Zhang, G., et al., *Nonfullerene Acceptor Molecules for Bulk Heterojunction Organic Solar Cells.* Chem. Rev., 2018. **118**(7): p. 3447-3507.

4.   Gurney, R.S., D.G. Lidzey, and T. Wang, *A Review of Non-Fullerene Polymer Solar Cells: From Device Physics to Morphology Control.* Rep. Prog. Phys., 2019. **82**(3): p. 036601.

5.   Zhang, S., et al., *Efficient Ternary Organic Solar Cells With Small Aggregation Phases and Low Bimolecular Recombination Using ICBA: ITIC Double Electron Acceptors.* IEEE J. Photovolt., 2018. **8**(1): p. 171-176.

6.   Sakai, N., et al., *Core-Substituted Naphthalenediimides.* Chem. Commun., 2010. **46**(24): p. 4225-4237.

7.   Krebs, F.C., et al., *Strategies for incorporation of polymer photovoltaics into garments and textiles.* Solar Energy Materials and Solar Cells, 2006. **90**(7-8): p. 1058-1067.

8.   Chang, S.-Y., et al., *Transparent Polymer Photovoltaics for Solar Energy Harvesting and Beyond.* Joule, 2018. **2**(6): p. 1039-1054.

9.   Winder, C. and N.S. Sariciftci, *Low bandgap polymers for photon harvesting in bulk heterojunction solar cells.* Journal of Materials Chemistry, 2004. **14**(7).

10.   Murali, M.G., et al., *Narrow band gap conjugated polymer for improving the photovoltaic performance of P3HT:PCBM ternary blend bulk heterojunction solar cells.* Polymer Chemistry, 2015. **6**(6): p. 962-972.

11.   Pratyusha, T., et al., *Novel Ternary Blend of PCDTBT, PCPDTBT and PC 70 BM for the Fabrication of Bulk Heterojunction Organic Solar Cells.* Materials Today: Proceedings, 2017. **4**(4): p. 5067-5073.

12.   Liu, T., et al., *Ternary Organic Solar Cells Based on Two Highly Efficient Polymer Donors with Enhanced Power Conversion Efficiency.* Advanced Energy Materials, 2016. **6**(6).

13.   Xiao, Z., X. Jia, and L. Ding, *Ternary organic solar cells offer 14% power conversion efficiency.* Science Bulletin, 2017. **62**(23): p. 1562-1564.

14.   Pan, M.-A., et al., *16.7%-efficiency ternary blended organic photovoltaic cells with PCBM as the acceptor additive to increase the open-circuit voltage and phase purity.* Journal of Materials Chemistry A, 2019. **7**(36): p. 20713-20722.

15. N. S. Sariciftci, L.S., A. J. Heeger, F. Wudl, *Photoinduced Electron Transfer from a Conducting Polymer to Buckminsterfullerene.* Science, 1992. **258**(5087): p. 1474-1476.

16. G. Yu, J.G., J. C. Hummelen, F. Wudl, A. J. Heeger, *Polymer Photovoltaic Cells: Enhanced Efficiencies via a Network of Internal Donor-Acceptor Heterojunctions.* Science, 1995. **270**(5243): p. 1789-1791.

17. He, Y. and Y. Li, *Fullerene derivative acceptors for high performance polymer solar cells.* Phys Chem Chem Phys, 2011. **13**(6): p. 1970-83.

18. Brabec, C.J., et al., *Effect of LiF/metal electrodes on the performance of plastic solar cells.* Applied Physics Letters, 2002. **80**(7): p. 1288-1290.

19. Wienk, M.M., et al., *Efficient methano[70]fullerene/MDMO-PPV bulk heterojunction photovoltaic cells.* Angew Chem Int Ed Engl, 2003. **42**(29): p. 3371-5.

20. Berger, P.R. and M. Kim, *Polymer Solar Cells: P3HT:PCBM and Beyond.* J. Renew. Sustain. Energy, 2018. **10**(1).

21. Kleinschmidt, A.T., S.E. Root, and D.J. Lipomi, *Poly(3-hexylthiophene) (P3HT): fruit fly or outlier in organic solar cell research?* Journal of Materials Chemistry A, 2017. **5**(23): p. 11396-11400.

22. Chi, D., et al., *High efficiency P3HT:PCBM solar cells with an inserted PCBM layer.* Journal of Materials Chemistry C, 2014. **2**(22).

23. Ma, W., et al., *Thermally Stable, Efficient Polymer Solar Cells with Nanoscale Control of the Interpenetrating Network Morphology.* Advanced Functional Materials, 2005. **15**(10): p. 1617-1622.

24. Guo, X., et al., *High efficiency polymer solar cells based on poly(3-hexylthiophene)/indene-C70 bisadduct with solvent additive.* Energy & Environmental Science, 2012. **5**(7).

25. Ganesamoorthy, R., G. Sathiyan, and P. Sakthivel, *Review: Fullerene based acceptors for efficient bulk heterojunction organic solar cell applications.* Solar Energy Materials and Solar Cells, 2017. **161**: p. 102-148.

26. Troshin, P.A., et al., *Material Solubility-Photovoltaic Performance Relationship in the Design of Novel Fullerene Derivatives for Bulk Heterojunction Solar Cells.* Advanced Functional Materials, 2009. **19**(5): p. 779-788.

27. Zhang, Y., et al., *A Simple and Effective Way of Achieving Highly Efficient and Thermally Stable Bulk-Heterojunction Polymer Solar Cells Using Amorphous Fullerene Derivatives as Electron Acceptor.* Chemistry of Materials, 2009. **21**(13): p. 2598-2600.

28. Kim, H.U., et al., *Naphthalene-, Anthracene-, and Pyrene-Substituted Fullerene Derivatives as Electron Acceptors in Polymer-Based Solar Cells.* ACS Appl. Mater. Interfaces, 2014. **6**(23): p. 20776-20785.

29. Cates, N.C., et al., *Effects of Intercalation on the Hole Mobility of Amorphous Semiconducting Polymer Blends.* Chem. Mater., 2010. **22**(11): p. 3543-3548.

30. Liping Zheng, Q.Z., Xianyu Deng, Min Yuan, Gang Yu, and Yong Cao, *Methanofullerenes Used as Electron Acceptors in Polymer Photovoltaic Devices.* J. Phys. Chem. B, 2004. **108**(32): p. 11921-11926.

31. Zhao, G., et al., *Effect of Carbon Chain Length in the Substituent of PCBM-like Molecules on Their Photovoltaic Properties.* Adv. Funct. Mater., 2010. **20**(9): p. 1480-1487.

32. Lenes, M., et al., *Electron Trapping in Higher Adduct Fullerene-Based Solar Cells.* Advanced Functional Materials, 2009. **19**(18): p. 3002-3007.

33. Lenes, M., et al., *Fullerene Bisadducts for Enhanced Open-Circuit Voltages and Efficiencies in Polymer Solar Cells.* Advanced Materials, 2008. **20**(11): p. 2116-2119.

34. Floris B. Kooistra, V.D.M., Lacramioara M. Popescu, David Kronholm, Paul W. M. Blom, and Jan C. Hummelen, *New C84 Derivative and Its Application in a Bulk Heterojunction Solar Cell.* Chem. Mater., 2006. **18**(13): p. 3068-3073.

35. Hoppe, H. and N.S. Sariciftci, *Morphology of polymer/fullerene bulk heterojunction solar cells.* J. Mater. Chem., 2006. **16**(1): p. 45-61.

36. Bartelt, J.A., et al., *The Importance of Fullerene Percolation in the Mixed Regions of Polymer-Fullerene Bulk Heterojunction Solar Cells.* Advanced Energy Materials, 2013. **3**(3): p. 364-374.

37. Koppe, M., et al., *Near IR Sensitization of Organic Bulk Heterojunction Solar Cells: Towards Optimization of the Spectral Response of Organic Solar Cells.* Advanced Functional Materials, 2010. **20**(2): p. 338-346.

38. Chen, J.D., et al., *Single-junction polymer solar cells exceeding 10% power conversion efficiency.* Adv Mater, 2015. **27**(6): p. 1035-41.

39. Al-Busaidi, Z., et al., *Enhanced lifetime of organic photovoltaic diodes utilizing a ternary blend including an insulating polymer.* Solar Energy Materials and Solar Cells, 2017. **160**: p. 101-106.

40. Mateker, W.R. and M.D. McGehee, *Progress in Understanding Degradation Mechanisms and Improving Stability in Organic Photovoltaics.* Adv Mater, 2017. **29**(10).

41. Fu, H., Z. Wang, and Y. Sun, *Advances in Non-Fullerene Acceptor Based Ternary Organic Solar Cells.* Solar RRL, 2018. **2**(1).

42. Zhang, X., et al., *Additive-Free Non-Fullerene Organic Solar Cells.* ChemElectroChem, 2019. **6**(22): p. 5547-5562.

43. Cui, Y., et al., *Over 16% efficiency organic photovoltaic cells enabled by a chlorinated acceptor with increased open-circuit voltages.* Nat Commun, 2019. **10**(1): p. 2515.

44. Zhang, H., et al., *Over 14% Efficiency in Organic Solar Cells Enabled by Chlorinated Nonfullerene Small-Molecule Acceptors.* Adv Mater, 2018. **30**(28): p. e1800613.

45. Firdaus, Y., et al., *Key Parameters Requirements for Non-Fullerene-Based Organic Solar Cells with Power Conversion Efficiency >20.* Adv Sci (Weinh), 2019. **6**(9): p. 1802028.

46. Firdaus, Y., et al., *Efficient Double- and Triple-Junction Nonfullerene Organic Photovoltaics and Design Guidelines for Optimal Cell Performance.* ACS Energy Letters, 2020. **5**(12): p. 3692-3701.

47. Lin, H., et al., *Reduced Intramolecular Twisting Improves the Performance of 3D Molecular Acceptors in Non-Fullerene Organic Solar Cells.* Adv Mater, 2016. **28**(38): p. 8546-8551.

48. Fernando, R., et al., *Tuning the Organic Solar Cell Performance of Acceptor 2,6-Dialkylaminonaphthalene Diimides by Varying a Linker between the Imide Nitrogen and a Thiophene Group.* The Journal of Physical Chemistry C, 2014. **118**(7): p. 3433-3442.

49. Liu, Y., et al., *NDI-Based Small Molecule as Promising Nonfullerene Acceptor for Solution-Processed Organic Photovoltaics.* Advanced Energy Materials, 2015. **5**(12).

50. Kumari, N., S. Naqvi, and R. Kumar, *Naphthalene Diimide Self-Assembled Ribbons with High Electrical Conductivity and Mobility Without Doping.* J. Mater. Sci., 2017. **53**(6): p. 4046-4055.

51. Liu, M., et al., *Naphthalene-Diimide-Based Ionenes as Universal Interlayers for Efficient Organic Solar Cells.* Angew. Chem. Int. Ed. Engl., 2020. **59**(41): p. 18131-18135.

52. Saraswati, T.E., et al., *The Study of the Optical Properties of C60 Fullerene in Different Organic Solvents.* Open Chem., 2019. **17**(1): p. 1198-1212.

53. Xiaoniu Yang, J.L., Sjoerd C. Veenstra, Wiljan J. H. Verhees, Martijn M. Wienk, Jan M. Kroon, Matthias A. J. Michels, and René A. J. Janssen, *Nanoscale Morphology of High-Performance Polymer Solar Cells.* Nano. Lett., 2005. **5**(4): p. 579-583.

54. Mihailetchi, V.D., et al., *Charge Transport and Photocurrent Generation in Poly(3-hexylthiophene): Methanofullerene Bulk-Heterojunction Solar Cells.* Adv. Funct. Mater., 2006. **16**(5): p. 699-708.

55. Li, W., et al., *Molecular Order Control of Non-fullerene Acceptors for High-Efficiency Polymer Solar Cells.* Joule, 2019. **3**(3): p. 819-833.

56.   Groves, C., *Simulating charge transport in organic semiconductors and devices: a review.* Rep Prog Phys, 2017. **80**(2): p. 026502.

57.   Pivrikas, A., et al., *A review of charge transport and recombination in polymer/fullerene organic solar cells.* Progress in Photovoltaics: Research and Applications, 2007. **15**(8): p. 677-696.

58.   Karl, N., *Charge carrier transport in organic semiconductors.* Synthetic Metals, 2003. **133-134**: p. 649-657.

59.   López Varo, P., et al., *Space-charge and injection limited current in organic diodes: A unified model.* Organic Electronics, 2014. **15**(10): p. 2526-2535.

60.   Schauer, F., *Space-charge-limited currents for organic solar cells optimisation.* Solar Energy Materials and Solar Cells, 2005. **87**(1-4): p. 235-250.

61.   Carbone, A., B.K. Kotowska, and D. Kotowski, *Space-charge-limited current fluctuations in organic semiconductors.* Phys Rev Lett, 2005. **95**(23): p. 236601.

62.   Mihailetchi, V.D., J. Wildeman, and P.W. Blom, *Space-charge limited photocurrent.* Phys Rev Lett, 2005. **94**(12): p. 126602.

63.   Blom, P.W.M., M.J.M. de Jong, and J.J.M. Vleggaar, *Electron and hole transport in poly(p-phenylene vinylene) devices.* Applied Physics Letters, 1996. **68**(23): p. 3308-3310.

64.   Mihailetchi, V., van Duren, J., Blom, P., Hummelen, J., Janssen, R., Kroon, J., Rispens, M., Verhees, W. and Wienk, M. , *Electron Transport in a Methanofullerene.* Adv. Funct. Mater.,, 2003. **13**: p. 43-46.

65.   Foster, S., et al., *Electron Collection as a Limit to Polymer:PCBM Solar Cell Efficiency: Effect of Blend Microstructure on Carrier Mobility and Device Performance in PTB7:PCBM.* Advanced Energy Materials, 2014. **4**(14).

66.   Nelson, T.K.a.J., *Device Modelling of Organic Bulk Heterojunction Solar Cells*, in *Multiscale Modelling of Organic and Hybrid Photovoltaics*, J.C. David Beljonne, Editor. 2013, Springer. p. 279-324.

67.   Wang, Z.B., et al., *Carrier Mobility of Organic Semiconductors Based on Current-Voltage Characteristics.* J. Appl. Phys., 2010. **107**(3).

68.   Mandoc, M.M., B. de Boer, and P.W.M. Blom, *Electron-only diodes of poly(dialkoxy-p-phenylene vinylene) using hole-blocking bottom electrodes.* Physical Review B, 2006. **73**(15).

69.   Steyrleuthner, R., S. Bange, and D. Neher, *Reliable electron-only devices and electron transport in n-type polymers.* Journal of Applied Physics, 2009. **105**(6).

70.   Wetzelaer, G.-J.A.H. and P.W.M. Blom, *Diffusion-Driven Currents in Organic-Semiconductor Diodes.* NPG Asia Materials, 2014. **6**(7): p. e110-e110.

71. Palumbo, M., et al., *Electrical investigations of layer-by-layer films of carbon nanotubes.* J. Phys. D: Appl. Phys., 2006. **39**(3077).

72. Armin, A., et al., *On the Unipolarity of Charge Transport in Methanofullerene Diodes.* npj Flex. Electron., 2017. **1**(13).

73. Ebenhoch, B., et al., *Charge carrier mobility of the organic photovoltaic materials PTB7 and PC71BM and its influence on device performance.* Organic Electronics, 2015. **22**: p. 62-68.

74. Avinash, M.B. and T. Govindaraju, *Engineering Molecular Organization of Naphthalenediimides: Large Nanosheets with Metallic Conductivity and Attoliter Containers.* Advanced Functional Materials, 2011. **21**(20): p. 3875-3882.

75. Sandberg, O.J., M. Nyman, and R. Österbacka, *Effect of Contacts in Organic Bulk Heterojunction Solar Cells.* Phys. Rev. Applied, 2014. **1**(2): p. 024003.

76. Volker, S.F., et al., *Fullerene-Based Materials as Hole-Transporting/Electron-Blocking Layers: Applications in Perovskite Solar Cells.* Chemistry, 2018. **24**(34): p. 8524-8529.

77. Alberga, D., et al., *Morphological and charge transport properties of amorphous and crystalline P3HT and PBTTT: insights from theory.* Phys Chem Chem Phys, 2015. **17**(28): p. 18742-50.

78. Schrader, M., et al., *Charge transport in amorphous and smectic mesophases of dicyanovinyl-substituted oligothiophenes.* Journal of Materials Chemistry, 2012. **22**(41).

79. Lin, Y., et al., *An electron acceptor challenging fullerenes for efficient polymer solar cells.* Adv Mater, 2015. **27**(7): p. 1170-4.

80. Holliday, S., et al., *High-efficiency and air-stable P3HT-based polymer solar cells with a new non-fullerene acceptor.* Nat Commun, 2016. **7**: p. 11585.

81. Ye, L., et al., *Quenching to the Percolation Threshold in Organic Solar Cells.* Joule, 2019. **3**(2): p. 443-458.

82. K. D. Benkstein, N.K., J. van de Lagemaat, and A. J. Frank, *Influence of the Percolation Network Geometry on Electron Transport in Dye-Sensitized Titanium Dioxide Solar Cells.* J. Phys. Chem. B, 2003. **107**(31): p. 7759-7767.

CHAPTER 7

DESIGN STRATEGIES FOR THE FABRICATION OF TANDEM OPVs WITH IMPERFECT CURRENT MATCHING

7.1 Introduction

Recent advances in efficiency and development have been derived from a combination of fabrication processes, i.e. ternary blends as discussed in Chapter 5 and novel materials in electron-only diodes examined in Chapter 6. Another relevant approach to further advance the efficiency proposed in this work is through device engineering [1]. One way to do so is by multi stacking photoactive layers in a multijunction device, otherwise known as tandem PV cells [2]. With this architecture, different absorber layers are utilised with the aim of addressing the dominant losses that limit the efficiency in single junction cells, as briefly explained in section 2.11 of Chapter 2. However, the additional flexibility provided by a tandem structure to effectively harvest photons is balanced by the challenge in matching photocurrent from the front and back cells to provide the best performance [3]. Further, considering all the types of materials with varied properties and many ways in which these can be combined, it is not trivial to design OPVs that make best use of the tandem concept. In practice, arduous experimental optimisation is often required to extract the best performance of a specific tandem OPV. In addition, tandem cells with balanced current matching under AM1.5G spectra may not remain balanced considering real-world illumination conditions which may be affected by pollution, dust and diffuse light [4, 5].

In this Chapter, a tandem OPV structure is presented to understand how they work so that we can provide device insights and achieve a higher flexibility in the development of tandem OPVs. Since current matching is challenging to achieve in practice due to the diverse properties of materials, in here we utilised modelling with GPVDM to investigate how can one effectively design high performing tandem devices when there is a mismatch in charge photogeneration between the two photoactive cells. Specifically, we aim to provide simple design criteria which can be used by researchers and engineers to lessen this issue and demonstrate that tandem OPVs can still deliver higher performances even

with significant unbalance in current matching. Because the introduction to tandems was described on Chapter 2, we begin this Chapter with a brief recap, followed by recent advances in literature and why is it that research on tandem is important. Next, the tandem models used in this thesis will be discussed alongside simulation results, comprised of different electrical and optical characteristics. Finally, we take a step forward and present the behaviour of such tandem OPVs under real life conditions including diffuse light. This Chapter demonstrates the outcome of high performing tandems and offers a useful methodology that can expand the design space and performance to fabricate tandems beyond current matching.

7.2 Recent advances in Tandem OPVs

We begin this section by briefly dwelling on what tandems are and then we focus the attention on the most recent literature about their development. In the BHJ blend structures discussed so far, an important limitation is the incomplete light absorption and low carrier mobility, which is inherent to disorder organic semiconductors [6]. A blend comprising of a donor and acceptor in which both materials have all attributes required for an "ideal" OPV (i.e. high absorption, good electron and hole mobilities) is still lacking, considering that at present the donors usually do most of the absorption [7, 8]. A way in which device engineers can address these constraints is through tandem OPVs. As discussed at the end of Chapter 2, single junction devices are limited by the Schockley and Queisser (SQ) limit, and tandem structures allows us to overcome this (note that single junction devices have yet to reach that limit) [9]. Thus, tandem cells are devices in which different photoactive layers harvest photons from different regions of the solar spectrum, and represent an active area with current developments [6]. The geometry of these structures is generally conceived of two absorber layers with distinct energy band gaps, where each cell can complement each other and thus absorb more light [10].

Although series-connected tandems have been successful to attain high efficiencies due to increased photon harvesting compared to single junction cells, it is balanced by the challenge of matching the photocurrent between the front and back cells [3, 11-13]. This is because in serially-connected tandems, the J_{SC} of the device is controlled by the sub-cell having lower J_{SC}, as such, in practice judicious device engineering and control of thicknesses is required to obtain balanced currents [2, 13]. In previous studies, Janssen et al [14] used modelling combined with experiments to

highlight the role of bandgap optimisation, in order to realise tandems that exceeded the performance of single junctions. Likewise, the same group developed a tandem consisting in three BHJs to boost PCE over 9%, whereby one sub-cell was separated into two as a method to improve the performance due to unbalanced current [15]. In addition, modelling data allowed them to determine optimum thicknesses for each photoactive layer. More recently, Nam and colleagues [16] developed an optical and drift diffusion model to optimise tandem solar cells by varying the sub-cell thicknesses. A front and back cell of 150 nm and 120 nm yielded a PCE of 6.51% in agreement with previous papers [17]. The drift diffusion methodology to optimise and characterise devices has also been subject to comprehensive studies by other authors [18-20]. For example, Da Silva et al [21] examined the role of interfaces in multijunction OPV, and revealed that with careful device engineering combined with modelling, PCEs of 9% could be achieved contrasting to 7% attained by a single junction device.

The development of NFA as introduced in the previous Chapter, has also paved the way to further advance studies on tandem OPVs [12, 22-24]. Firdaus et al [25] in particular, modelled a novel NFA tandem OPVs using optical simulations to develop design rules which predicted that a high PCE of 25% could be achieved if balanced mobilities ($>10^{-3}$ cm^2 V^{-1} s^{-1}) and low bimolecular recombination rate were considered. In agreement with these results, the same authors fabricated a multijunction OPV based on low bandgap polymers and NFA yielding efficiencies of almost 17%, which were in good agreement with their simulation predictions [26].

Despite that numerous studies have demonstrated the reliability of modelling to better fabricate and design tandem OPVs, a complete picture of the underlying processes is still lacking. For instance, it is not clear the impact that balanced or imbalanced charge generation between the cells will have on charge carrier extraction when mobilities are balanced or imbalanced. Thus, it is important to fully understand these perquisites in order to design and fabricate high efficiency tandem OPVs.

7.3 Tandem structure utilised on modelling

In this section, the tandem structure models are introduced. Then, the simulation parameters discussed followed by the results. The reason to utilise device simulations is to examine the design space for this tandem OPV by varying the electron-hole mobilities, optical absorption properties and cell thicknesses. Fundamentally, this would represent

the approach an OPV engineer can take when selecting materials for each cell layer and their tuneability. As stated before, the objective is to closely examine the impact on performance when the top and bottom cells charge generation is not matched. As such, with this model, suitable design criterions may be derived which can be used to fabricate high performing tandem OPVs so that they are more robust to non-ideal current matching on the top and bottom cells. Hence, the device structure we are looking at (depicted in Figure 7.1a) comprises an architecture of ITO (100 nm) / PEDOT:PSS (30 nm) / Front cell (x_F <500 nm) / ZnO (30 nm) / PEDOT:PSS (15 nm) / Back cell (x_B <500 nm) / Al (100 nm). To account for the absorption characteristics, representative blend systems based on PCDTBT:PC$_{70}$BM and PTB7-TH:PC$_{70}$BM (Figure 7.1b, c) were considered for the front and back cell respectively, which have also been utilised in other high performing tandems [14, 27] and thus, are relevant for OPVs. It is worth mentioning that important milestones in the field of OPVs have been achieved with such blend systems, as observed in Chapter 2, further supporting our choice for these materials.
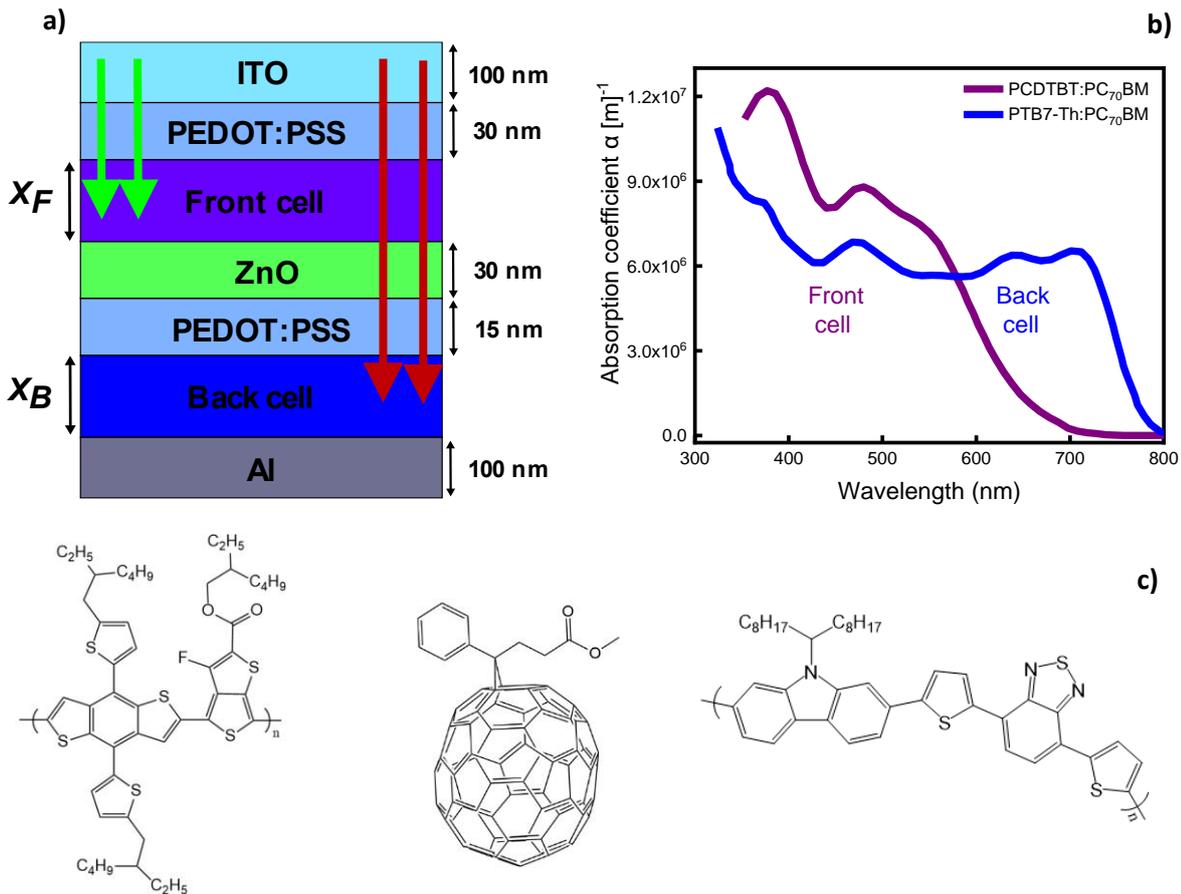
Figure 7.1. a) Tandem device used in this thesis; b) absorption profile spectrum of the front and back cells, from [28, 29]; c) molecular structure of the materials considered: PTB7-Th, PC$_{70}$BM and PCDTBT from left to right.

Moving on, the PEDOT:PSS / ZnO layer was used as recombination layer [11, 30, 31]. As our aim is to understand the physics which underpins tandem OPV devices in general, rather than a specific set of materials (as for example in [19, 32-36]), thus we selected electrical and optical properties of the front and back cells that are generally representative of organic semiconductors. Therefore, we selected electron and hole mobilities of 10^{-7} m^2 V^{-1} s^{-1} for both cells and a free-carrier recombination rate of 10^{-18} m^{-3} s^{-1} which represent typical values observed in other simulation papers [25, 28]. Details of the electrical parameters used are shown in Appendix 7.1.

7.4 Standard tandem model and PV predictions

In this section, the first model experiments are discussed, in which charge carrier mobilities are balanced on both the top and back cells and thus considered as the base or control. The prediction of main PV figures of merit is shown by a series of contour plots (Figure 7.2) considering a tandem structure with a range of thicknesses between 50 nm – 500 nm. The purpose of these simulations is to understand the performance of OPVs as a function of layer thickness, an aspect that designers can vary during manufacture.

For the parameters considered here, V_{OC} did not change significantly and plots of these are shown in Appendix 7.2. Now, as observed from the J_{SC} contour, three main peaks occur with (x_F, x_B) values of (200 nm, 125 nm), (200 nm, 300 nm) and (50 nm, 300 nm), that are associated with the optical field overlapping favourably with the absorbing material in the front and back cells as shown in Figure 7.2d for the optimal (200 nm, 125 nm) device. In this photon map the front cell exhibits a considerable absorption of photons of $\lambda < 600$ nm that are balanced by the thinner back cell, with a narrower absorption range between 600 nm $< \lambda < \sim$800 nm. The Appendix 7.3a, b further shows the photon absorption maps of (200 nm, 300 nm) and (50 nm, 300 nm) devices correspondingly. We then calculated the integrated absorption in the front (A_1) and back (A_2) cells by accounting the photon distribution in each layer of the device for the specified thicknesses. This analysis revealed a ratio of $A_1/A_2 = 1.3$, 1.0 and 0.32 in the (200 nm, 125 nm), (200 nm, 300 nm) and (50 nm, 300 nm) devices respectively, thus showing that peaks in J_{SC} performance can be obtained in tandem cells without strict current matching.
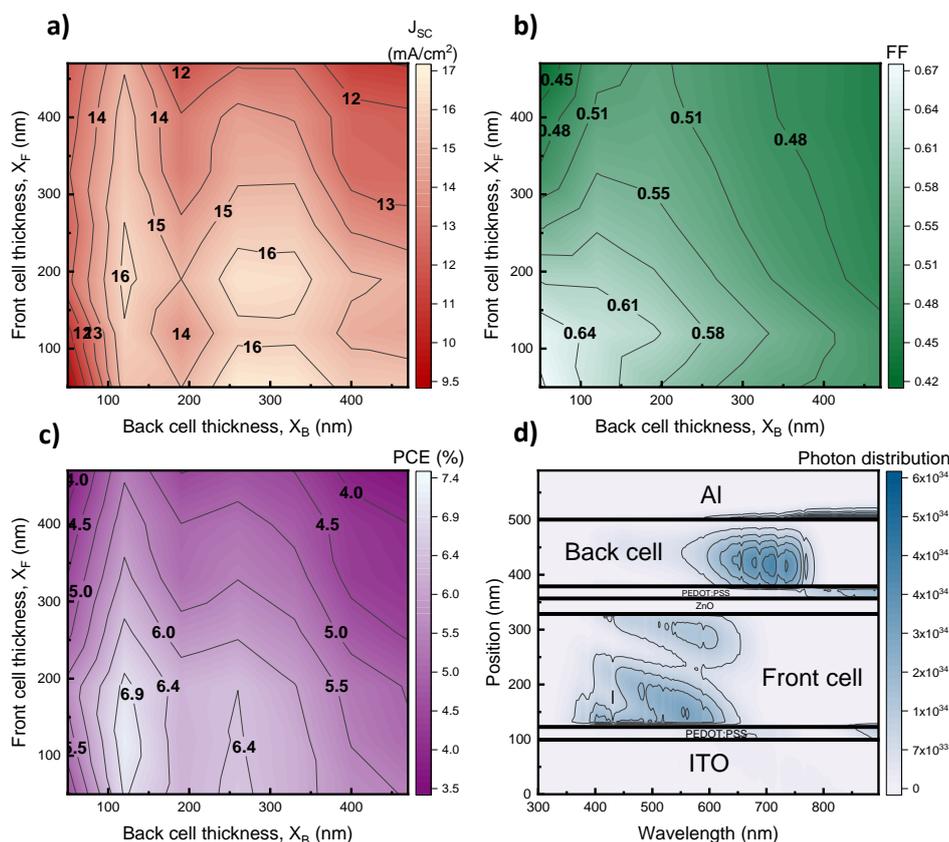
Figure 7.2. PV predictions of a) J_{SC}, b) FF and c) PCE for a tandem cell as a function of front (x_F) and back (x_B) cell thickness. d) Shows distribution of photon absorption in the device (photons/m^3) within a region of optimal J_{SC} x_F = 200 nm and back x_B = 125 nm.

Further, the peak J_{SC} values for the x_B = 300 nm devices do not carry through into peak PCE due to the rapid decrease in FF as either front or back cell increase. Certainly, we note that the (200 nm, 300 nm) device has matched absorption in the front and back cells, but is not predicted to be optimal due to non-geminate recombination in the (relatively) thick active layers in this case [37]. The thicknesses for which absorption of charge is matched in tandem OPVs will be a function of the absorption in the relative layers. However, in the case examined here at least, the broad absorption in the top cell means that matching absorption in the back cell would need an unpractical large back cell thicknesses.

The results presented here are also in agreement with modelling reports in literature. For instance, Fallahpour et al [32] demonstrated with modelling the influence of energetic disorder and cell thicknesses on the performance of OPVs. The FF contour map in their study describes a similar trend as the control model shown here, in which values were reduced as both cells thicknesses increased. With the same modelling methodology, Li and co-workers [38] characterised a tandem OPV based on materials

which had complementary absorption. Optical modelling was used to provide guidelines for the optimal thicknesses in sub-cells. Although the predicted J_{SC} realised a similar tendency to the one described here, their maximum J_{SC} of 12 mA/cm^2 was found at ~125 nm for both cells.

Returning to Figure 7.2, we note that from a practical standpoint the tolerance for variations in layer thickness is predicted to be small, as is the overlap between regions of high FF and J_{SC}. Hence, we ask ourselves what choices are available to an engineer if one wishes to widen the tolerance for layer thickness and materials properties while maintaining a high PCE. Since, one can choose from an ample variety of materials that could result in a different range of mobilities, to fully represent this idea two modifications were done to the base model shown in the next section.

7.5 PV predictions in mobility enhanced tandem OPVs

In this section, we examine methods to overcome the challenges in tandem OPVs with unbalanced current matching. Hence, by changing the mobility (Figure 7.3), we represent the selection of a different material. In the first intervention, the hole mobility was enhanced in the top cell (termed as hole-enhanced) and in the second intervention, the electron mobility was enhanced on the back cell (termed as electron-enhanced). According to the PV predictions the electron enhanced model (Figure 7.3 left) is remarkably different from the standard base model (Figure 7.2) and the hole enhanced model (Figure 7.3 right). It is observed in the electron enhanced model that the region of optimal J_{SC} is extended towards higher front cell thicknesses which in turn also extends the PCE maximum. On the other hand, increasing the hole mobility in the front cell does not substantially change J_{SC} nor PCE when compared to the base model of Figure 7.2. Considering that the mobilities are the only parameters changed in the model, it seems plausible that the differences must originate from the total of photons absorbed on each cell and the charge carrier generation.

To further understand the reasons for this, we examined the recombination, potential and charge carrier densities for the (300 nm, 350 nm) device presented in Figure 7.4.
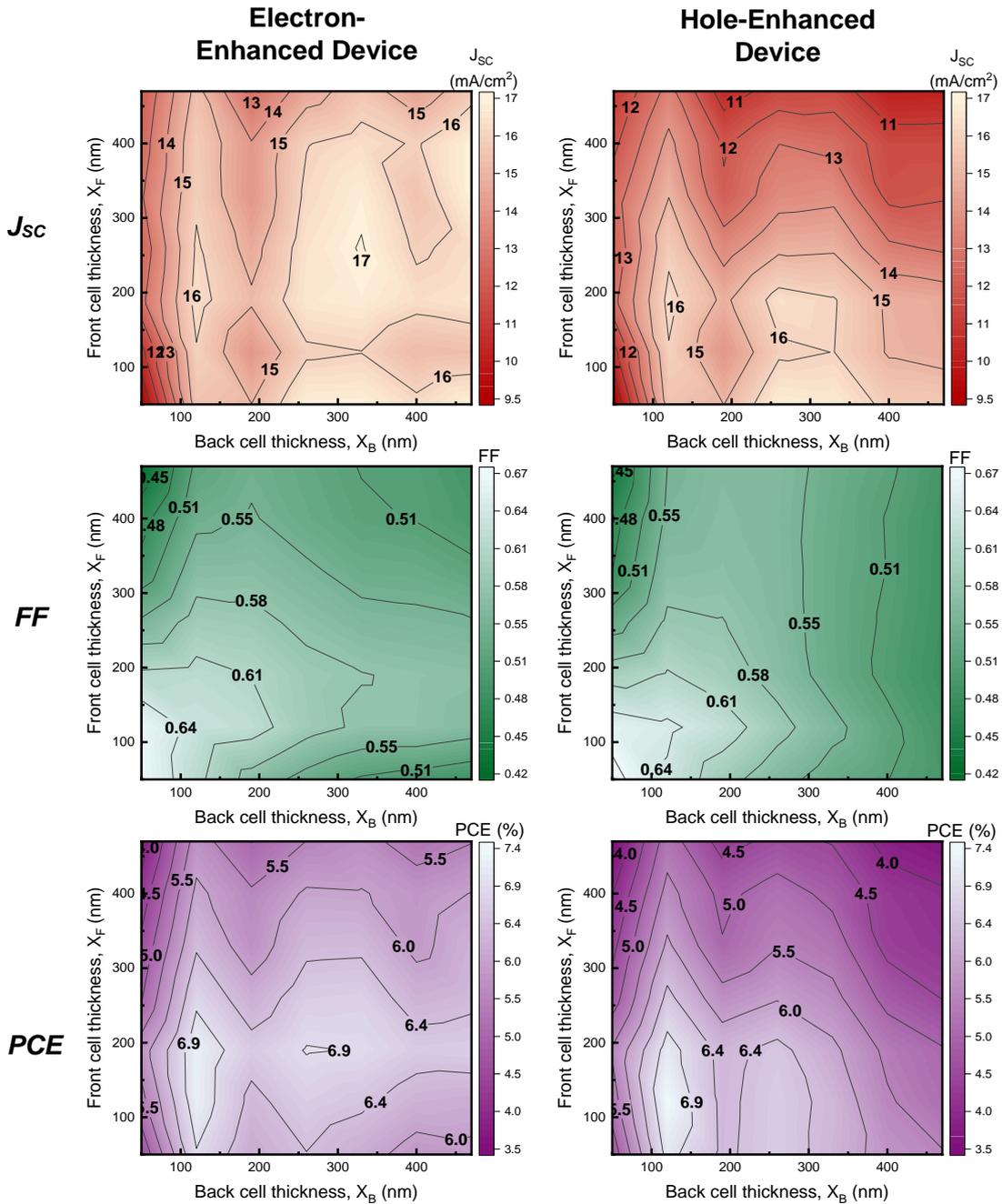
Figure 7.3. Predictions of J_{SC}, FF and PCE (top, middle and bottom respectively) for both the electron- and hole-enhanced devices (left and right respectively) as a function of cell geometry.

This geometry was considered since it shows a significant increase in J_{SC} when electron mobility is enhanced, whereas increasing the hole mobility was shown to have minimal effect in J_{SC}. The photon map for this tandem structure is shown in Figure 7.4d.
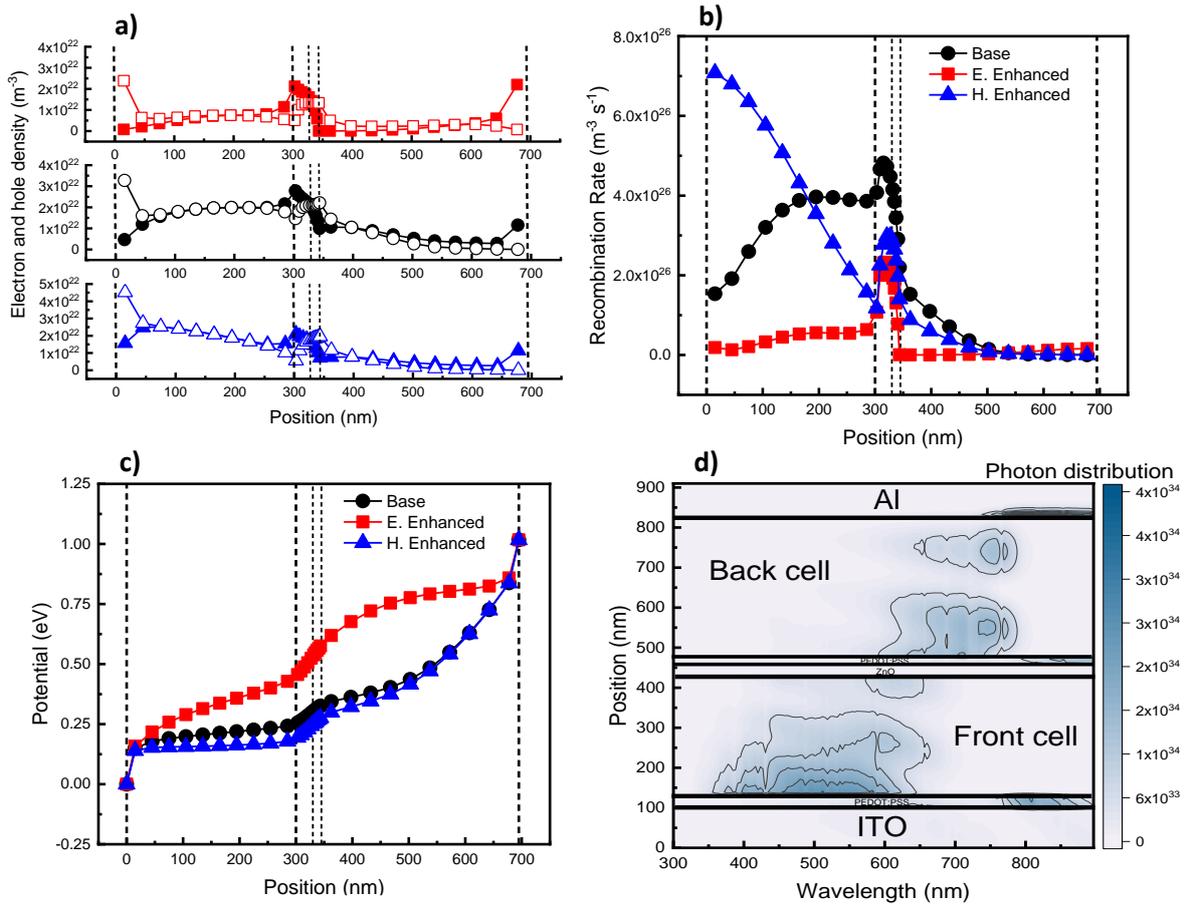
Figure 7.4. Electron and hole densities a), recombination rate b) and potential c) measured at short-circuit. d) Photon map (photons/m^3) with $A_1/A_2 = 1.4$ for the $x_F = 300$ nm $x_B = 350$ nm tandem device. On all figures, black circles represent the base model, red squares the electron-enhanced model and blue triangles the hole-enhanced model. From a) the solid symbols denote the electron density and the open symbols the hole density. The dashed lines on a-c represent the different layers.

Starting with charge carrier densities, the base model in Figure 7.4a shows a build-up of charge in the front cell with balanced mobilities, which is related to surplus of absorption on the front cell ($A_1/A_2 = 1.4$). In addition, because of this photocarrier accumulation in the front cell, a clear increase in recombination for the same positions is observed in Figure 7.4b. Now, when the electron mobility is enhanced in the back cell the extraction of electrons is more efficient, as observed with the lessened recombination near the cathode which contrasts to the hole enhanced model near the anode. Further, from Figure 7.4c, enhancing the electron mobility redistributes the electric field so that the potential is dropped in the front cell, where most charge is generated as observed in Figure 7.4a. Contrarily, for the hole enhanced model the electric field is concentrated in the back cell, where little charge is being generated. As such, because the field is flattened in the

175

front cell (where charge is generated) this reduces the photocurrent because of increased recombination. An important point to emphasise derived from these data, is that balanced absorption favours balanced mobilities but when the absorption is unbalanced, it requires enhanced mobility in one of the cells, more specifically efficient extraction of carriers which are passing through the cell doing less of the absorption.

Interestingly, investigation of varied mobilities has also been reviewed in other high impact studies [34]. To illustrate this, Armin et al [28] used three model systems with different mobility ratios ($\mu_h / \mu_e \ll 1$, $\mu_h / \mu_e \gg 1$, $\mu_h / \mu_e = 1$) considered in a conventional and inverted structure. Their simulations and experiments evidenced that in thick junction devices with balanced mobilities, the conventional and inverted architectures should deliver equivalent efficiencies. In addition, when the electron is the faster carrier, their modelling predicted that an inverted structure would compensate for imbalanced mobilities that would otherwise cause more recombination. Similarly, Shieh et al [35] utilised three different carrier mobilities in simulations, namely: 10^{-1} cm^2 /V s, 10^{-2} cm^2 /V s and 10^{-3} cm^2 /V s, in order to establish a model which could describe microscopic properties and electrical characteristics in OPVs. It was demonstrated that the recombination rate increased due to accumulation in the bulk of the lower mobility carriers (10^{-3} cm^2 /V s) in agreement with the trends discussed here.

Indeed, while such strategies of balanced and unbalanced mobilities with varied thicknesses in modelling have been proved to be useful in the design of more appropriate tandem devices, OPV engineers may also be inclined to change the absorption characteristics, as shown in the next section.

7.6 Shifted absorption characteristics in a tandem OPV

In this section, to further understand the effects that impact the ratio of charges being generated, the absorption of the front cell is shifted towards higher and lower photon energies (-200 nm to 100 nm) compared to the base PCDTBT:PC$_{70}$BM front cell, as indicated on Figure 7.5a, as this may reflect the selection of different absorber materials. Further, the measured absorption characteristic was padded with a value of 1.18×10^7 m^{-1} below 350 nm, which was the extent of the measurement, so that no unphysical gap in absorption at high photon energies is introduced when the absorption profile was shifted to higher wavelengths. These profiles were used to simulate the performance of a tandem cell with $x_F = 300$ nm, $x_B = 350$ nm, as in Figure 7.4. This

geometry is selected as this position is in the region of several maxima, and therefore may be expected to yield interesting outcomes. Note that a thin 100 nm structure for both cells is also discussed later. Figure 7.5b depicts the main PV figures compared to the fraction of total photons distributed in the front (A_1) and back cell (A_2) respectively. The degree of absorption in the PEDOT:PSS / ZnO recombination layer was less than 5% (and 2.6% on average) of the total absorption in the tandem cell, and thus much smaller than A_1 and A_2. In addition, Appendix 7.4 shows the change in A_1 / A_2 ratios when the absorption is shifted, to illustrate more clearly where balanced absorption occurs, whereas Appendix 7.5 replots the same information as Figure 7.5b but considering the absorption shift.
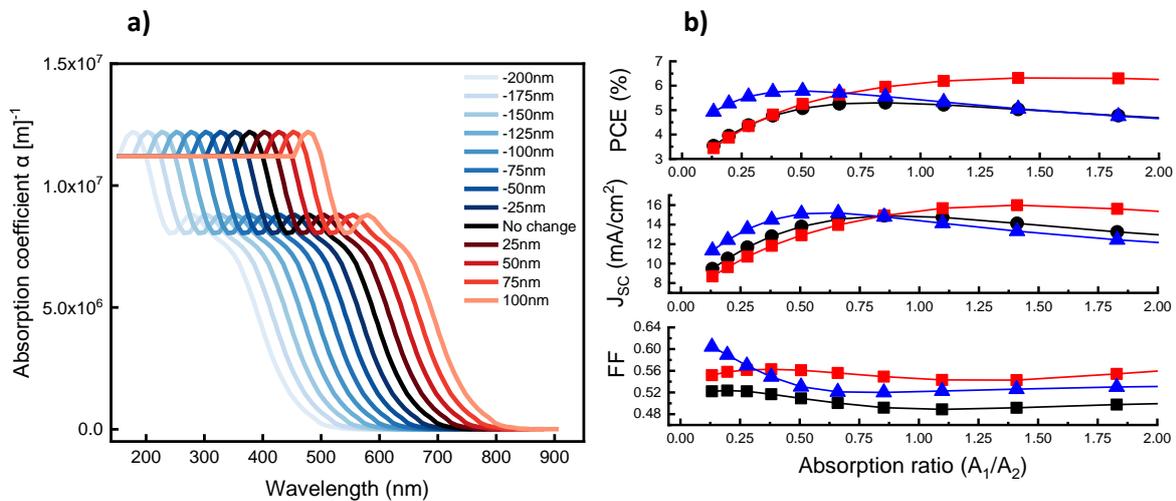
Figure 7.5. a) Range of top cell absorption characteristics simulated. b) PCE, J_{SC} and FF as a function of relative absorption in the top (A_1) and back (A_2) cells. Black circles denote the base model, red squares the electron-enhanced, and blue triangles the hole-enhanced.

Now, Figure 7.5b shows that an excess of charge in the front cell (i.e. A_1 / A_2 >> 1) favours enhanced electron mobility in the back cell. On the other hand, an excess of charge in the back cell (i.e. A_1 / A_2 << 1) favours the hole mobility in the top cell. From a design point of view, these demonstrates that high performing tandem OPVs can be fabricated even when charge generation is unmatched on both cells, considering that the mobility of photo generated charges transiting across the less absorbing cell is sufficiently enhanced. Moreover, it is observed that the peak in performance of the tandem with equal mobilities did not occur for balanced injection (A_1 / A_2 = 1), but the peak predicted performance of devices with balanced mobilities when A_1 / A_2 = ~0.85 e.g. when there is a minor increase in absorption in the back cell. This is correlated to the relative position

of charges injected in the top and back cells as observed on Figure 7.4d. For example, in the top cell, charges are generated near the ITO anode which leads to efficient extraction of holes. Contrastingly, in the back cell charges are generated near the junction between both cells which results on longer transport paths for both holes and electrons to the contacts.

Further, we also consider the sensitivity of the above results to assumed materials parameters and device structure. We investigated the relative importance of charge generation with respect to recombination on the trends observed above by predicting J_{SC}, FF and PCE for differing x_F and x_B values for increased recombination rate (Appendix 7.7) and doubled absorption (Appendix 7.8) in both layers, whilst keeping all other parameters the same. In both cases, the same trends are observed indicating that the underlying device physics are not sensitive to variations in parameters over this range. But first, we show the plots of the double absorption profiles in both absorbing layers as a reference in the Appendix 7.6. Also, we highlight that the $x_F = 300$ nm $x_B = 350$ nm device was considered as the focus of Figure 7.5 as it was expected that shifts in absorption of the top cell would yield large changes in J_{SC} for this geometry. By contrast, contour plots of the standard (Figure 7.2) and electron- and hole-enhanced devices (Figure 7.3) show that the PV parameters of thinner devices (e.g. $x_F = 100$ nm $x_B = 100$ nm) change relatively little when electron or hole mobility are enhanced. The effect of shifted absorption on predicted J_{SC} and PCE for the $x_F = 100$ nm $x_B = 100$ nm device is shown below (Figure 7.6).
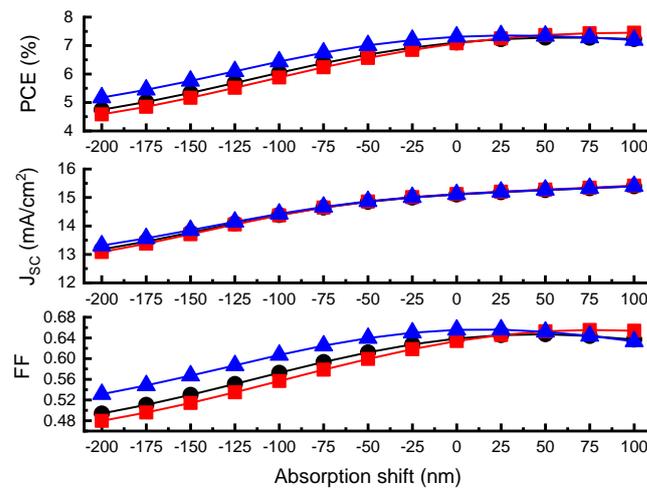
Figure 7.6. Effect of shifted absorption on PCE, J_{SC} and FF for a tandem cell with $x_F = 100$ nm and $x_B = 100$ nm. Black circles denote the base model, red squares the electron-enhanced and blue triangles the hole-enhanced.

Contrarily to the thicker device in Figure 7.4, and mobility enhanced models shown in Figure 7.3, the thinner device is shown to have enhanced J_{SC} as absorption shifts to higher wavelengths. This is attributed to the less complete absorption in the thinner device, thus, changing the absorption in the front cell to higher wavelengths increases the absorption of low-energy photons and consequently the efficiency.

To wrap up this section, we also investigated the role of the recombination layer by repeating the simulations without it. This approach has been investigated experimentally by Ghasemi et al [39] whereby two binary BHJs were deposited sequentially, resulting in a similar tandem structure as presented here, but with no recombination layer that could yield higher J_{SC} as revealed by their EQE. Based upon these results, Wang [40] and Huang [27] also fabricated double BHJ OPVs that could realise larger J_{SC} gains. Again, we find that the trends presented in this Chapter are reproduced but with minor differences in the values obtained, as shown in Appendixes 7.9 and 7.10.

7.7 Tandem cells under varied illumination conditions

In the last section of this Chapter, we centre the discussion on the implications for the tandem of Figure 7.4 (300 nm, 350 nm) operating on environments with different illumination conditions.
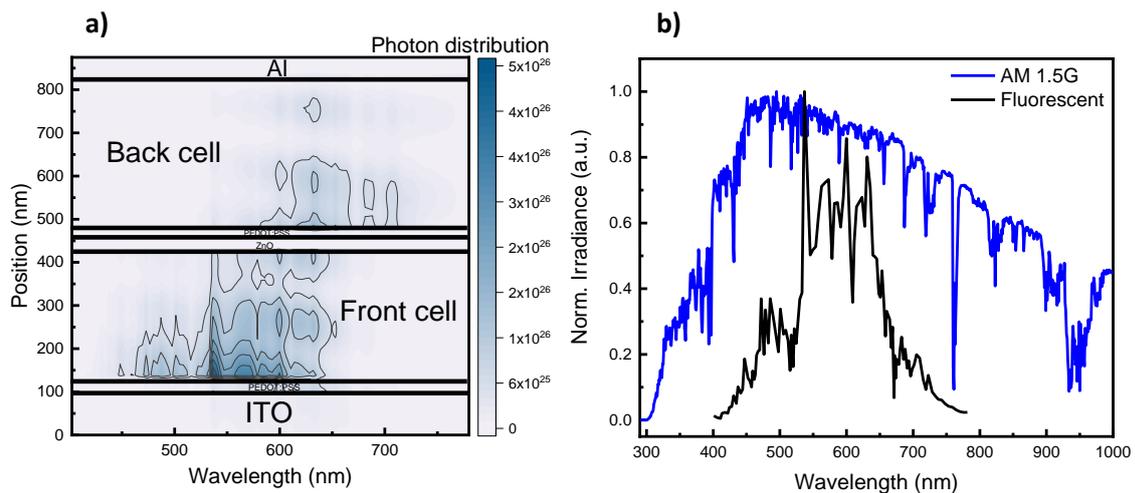
Figure 7.7. a) Distribution of photon absorption in tandem device (photons/m^3) with thickness of $x_F = 300$ nm and $x_F = 350$ nm considering fluorescent irradiance and A_1/A_2 ratio of 2.0. b) Shows the fluorescent spectrum compared to the AM 1.5G (normalised) as a reference.

If the spectrum of incident radiation changes, for example via dust accumulation, pollution, cloud cover or reflection, we may expect that the relative degree of absorption in the front and back cells would change. This effect is particularly abrupt if the source of illumination changes. To present a clear example, a fluorescent light is predicted to lead to a ratio of $A_1/A_2 = 2.0$ (Figure 7.7a), as compared to $A_1/A_2 = 1.4$ under AM1.5 that was presented in Figure 7.4d. However, significant changes in A_1/A_2 can also be realised through dust, smoke and pollutant accumulation in the atmosphere. A convenient way to characterise the consequent changes in the spectra at ground level is via the aerosol optical depth (AOD) [41]. Figure 7.8a plots three solar spectra generated with the SPECTRAL2 model [42] with different values of AOD, namely values which represent a city with clean air like Freiburg in Germany ($0.15 – 0.71$ cm^{-1}) and Beijing in China (1.4-3.7 cm^{-1}).
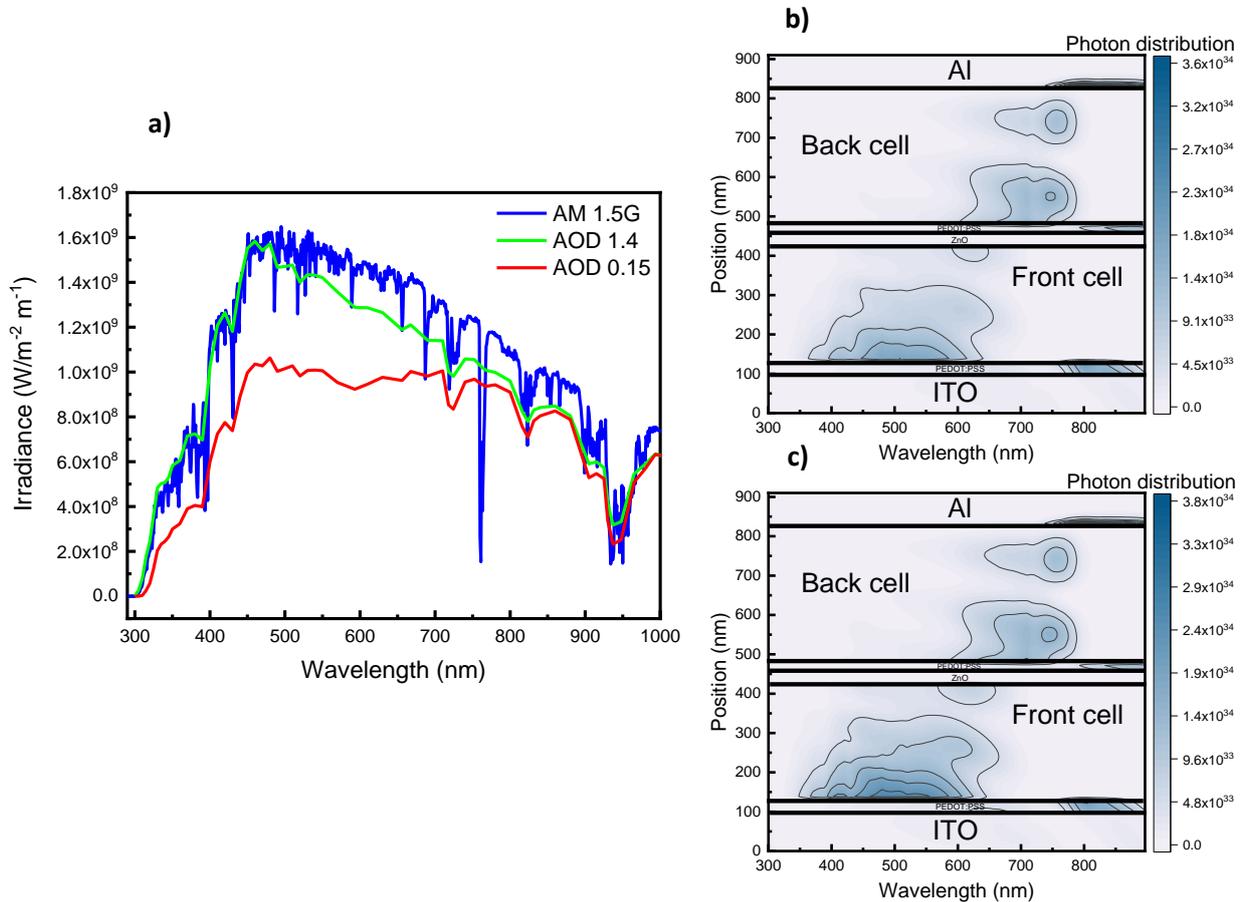
Figure 7.8. a) Solar irradiance spectrum of AM 1.5G and spectrums corresponding to the effects of diffuse irradiance due to varied AOD. Distribution of photon absorption in tandem devices (photons/m^3) with thicknesses of $x_F = 300$ nm and $x_B = 350$ nm. b) Shows photon map of a device considering an irradiance corresponding to Freiburg with AOD (0.15 cm^{-1}) and A_1/A_2 ratio of 1.2. c) Shows photon map of a device considering an irradiance corresponding to Beijing with AOD (1.4 cm^{-1}) and A_1/A_2 ratio of 1.5.

Spectra generated using this model from AOD values of ~0.15 to 5 were used to calculate the ratio A_1/A_2 for the device shown in Figure 7.4, considering: latitude, longitude, AOD, water vapor, air pressure and pollution like nitrogen dioxide (NO_2). Details are included in Appendix 7.11. Thus, Figure 7.8b, c shows in greater detail the photon absorption maps for the two cases of AOD relating to Freiburg (0.15 cm^{-1}) and Beijing (1.4 cm^{-1}) respectively. For the parameters considered here, it can be seen from Figure 7.8a, c that the tandem device related to Beijing has a higher absorption in the front cell which is attributed to the latitude, longitude and time of the year.

Thus, as varying illumination conditions can lead to differing relative absorption in the front and back cells thus they can influence the current matching in the tandem cell. Figure 7.5 has useful input here as it shows that the slope of PCE with A_1/A_2 differs depending on whether the device is balanced, electron-enhanced, or hole-enhanced. Like so, if a tandem device with $A_1/A_2 \sim 1$ under AM1.5 condition operates under conditions which push A_1/A_2 higher, it is favourable to have an electron-enhanced tandem, whereas if conditions are expected to reduce A_1/A_2, it is favourable to have a hole-enhanced tandem.

7.8 Conclusions

In this Chapter, a tandem approach was utilised with drift diffusion simulations to expand our horizons beyond current matched devices, to see how they operate, and demonstrate ways to mitigate challenges associated. First, three main situations were examined: The base model with balanced mobilities in both cells followed by electron enhanced mobility in the back cell and hole enhanced mobility in the front cell. It was demonstrated that imbalanced absorption leads to enhanced recombination in the cell that performs most of the absorption. This enhanced recombination was shown to be alleviated by improving the transport properties of the cell performing least of the absorption so that photo generated charges from the most absorbing cell can transit more efficiently into the contact. Thereby, this approach results in an effective strategy to fabrication, by showing that high performing tandems can be realised despite imbalanced absorption, lessening the constraints for device engineers to be able to use a variety of materials and layer structures.

Further, the absorption of the front cell was shifted towards higher and lower wavelengths compared to the standard absorption, as it may be the case when choosing different absorber materials. It is shown that peak performance of the tandem OPVs for equal mobilities does not occur when the absorption is balanced. Instead, modelling presented here predicts a peak in performance for balanced mobilities when there is a slight excess of absorption in the back cell, attributed to the position of photogeneration in the tandem device, thus revealing the importance of optical modelling such as the one utilised here to assist with device design. The implications of a tandem operating under real world conditions were also shown. Our modelling results demonstrate the impact on the spectrum characteristics depending on whether there is more or less illumination due to dust, pollution and region (e.g. Germany or China). It is shown that any drop-off in illumination performance could be alleviated by choosing different materials.

Lastly, it is apparent from this Chapter that modelling and simulations are helpful as predictive instruments and not only to reproduce experimental data, which can aid to effectively engineer new devices and cell architectures, as the tandems examined here.

7.9 References

1. Zhang, K., et al., *Toward Efficient Tandem Organic Solar Cells: From Materials to Device Engineering.* ACS Appl. Mater. Interfaces, 2020. **12**(36): p. 39937-39947.

2. Ameri, T., et al., *Organic Tandem Solar Cells: A Review.* Energy Environ. Sci., 2009. **2**(4): p. 347-363.

3. Di Carlo Rasi, D. and R.A.J. Janssen, *Advances in Solution-Processed Multijunction Organic Solar Cells.* Adv. Mater., 2019. **31**(10): p. 1806499.

4. Biswas, S., et al., *Organic Tandem Solar Cells Under Indoor Light Illumination.* Prog. Photovolt.: Res. Appl., 2020. **28**(9): p. 946-955.

5. Phelan, M., et al., *Outdoor Performance of a Tandem InGaP/Si Photovoltaic Luminescent Solar Concentrator.* Sol. Energy Mater. Sol. Cells, 2021. **223**.

6. Ameri, T., N. Li, and C.J. Brabec, *Highly Efficient Organic Tandem Solar Cells: A Follow up Review.* Energy Environ. Sci., 2013. **6**(8): p. 2390-2413.

7. Yongfang, L., *Molecular Design of Photovoltaic Materials for Polymer Solar Cells: Toward Suitable Electronic Energy Levels and Broad Absorption.* Acc. Chem. Res., 2012. **45**(5): p. 723-733.

8. Scharber, M.C., et al., *Design Rules for Donors in Bulk-Heterojunction Solar Cells— Towards 10 % Energy-Conversion Efficiency.* Adv. Mater., 2006. **18**(6): p. 789-794.

9. Shockley, W. and H.J. Queisser, *Detailed Balance Limit of Efficiency of p-n Junction Solar Cells.* J. Appl. Phys., 1961. **32**(3): p. 510-519.

10. Li, G., W.-H. Chang, and Y. Yang, *Low-Bandgap Conjugated Polymers Enabling Solution-Processable Tandem Solar Cells.* Nat. Rev. Mater., 2017. **2**(8): p. 17043.

11. Dou, L., et al., *Tandem Polymer Solar Cells Featuring a Spectrally Matched Low-Bandgap Polymer.* Nat. Photon., 2012. **6**(3): p. 180-185.

12. Jia, Z., et al., *High Performance Tandem Organic Solar Cells via a Strongly Infrared-Absorbing Narrow Bandgap Acceptor.* Nat. Commun., 2021. **12**(1): p. 178.

13. Salim, M.B., R. Nekovei, and R. Jeyakumar, *Organic Tandem Solar Cells With 18.6% Efficiency.* Sol. Energy, 2020. **198**: p. 160-166.

14. Gevaerts, V.S., et al., *Solution processed polymer tandem solar cell using efficient small and wide bandgap polymer:fullerene blends.* Adv Mater, 2012. **24**(16): p. 2130-4.

15. Li, W., et al., *Efficient tandem and triple-junction polymer solar cells.* J Am Chem Soc, 2013. **135**(15): p. 5529-32.

16. Min Nam, Y., J. Huh, and W.H. Jo, *A Computational Study on Optimal Design for Organic Tandem Solar Cells.* Sol. Energy Mater. Sol. Cells, 2011. **95**(4): p. 1095-1101.

17. Jin Young Kim, K.L., Nelson E. Coates, Daniel Moses, Thuc-Quyen Nguyen, Mark Dante, Alan J. Heeger, *Efficient Tandem Polymer Solar Cells Fabricated by All-Solution Processing.* Science, 2007. **317**(5835): p. 222-225.

18. Altazin, S., et al., *Refined drift-diffusion model for the simulation of charge transport across layer interfaces in organic semiconductor devices.* Journal of Applied Physics, 2018. **124**(13).

19. Sievers, D.W., V. Shrotriya, and Y. Yang, *Modeling Optical Effects and Thickness Dependent Current in Polymer Bulk-Heterojunction Solar Cells.* J. Appl. Phys., 2006. **100**(11).

20. Häusermann, R., et al., *Coupled optoelectronic simulation of organic bulk-heterojunction solar cells: Parameter extraction and sensitivity analysis.* Journal of Applied Physics, 2009. **106**(10).

21. da Silva, W.J., et al., *High performance polymer tandem solar cell.* Sci Rep, 2015. **5**: p. 18090.

22. Zuo, L., et al., *High-Efficiency Nonfullerene Organic Solar Cells with a Parallel Tandem Configuration.* Adv Mater, 2017. **29**(34).

23. Firdaus, Y., et al., *Novel Wide-Bandgap Non-Fullerene Acceptors for Efficient Tandem Organic Solar Cells.* J. Mater. Chem. A., 2020. **8**(3): p. 1164-1175.

24. Cheng, P., et al., *Efficient Tandem Organic Photovoltaics with Tunable Rear Sub-cells.* Joule, 2019. **3**(2): p. 432-442.

25. Firdaus, Y., et al., *Key Parameters Requirements for Non-Fullerene-Based Organic Solar Cells with Power Conversion Efficiency >20.* Adv. Sci., 2019. **6**(9): p. 1802028.

26. Firdaus, Y., et al., *Efficient Double- and Triple-Junction Nonfullerene Organic Photovoltaics and Design Guidelines for Optimal Cell Performance.* ACS Energy Letters, 2020. **5**(12): p. 3692-3701.

27. Huang, J., et al., *Highly Efficient Organic Solar Cells Consisting of Double Bulk Heterojunction Layers.* Adv. Mater., 2017. **29**(19).

28. Armin, A., et al., *Electro-Optics of Conventional and Inverted Thick Junction Organic Solar Cells.* ACS Photonics, 2015. **2**(12): p. 1745-1754.

29. Wang, C., et al., *Ternary Organic Solar Cells with Minimum Voltage Losses.* Advanced Energy Materials, 2017. **7**(21).

30. You, J., et al., *A Polymer Tandem Solar Cell With 10.6% Power Conversion Efficiency.* Nat. Commun., 2013. **4**: p. 1446.

31. Gilot, J., M.M. Wienk, and R.A.J. Janssen, *Double and Triple Junction Polymer Solar Cells Processed from Solution.* Appl. Phys. Lett., 2007. **90**(14).

32. Fallahpour, A.H., et al., *Modeling and Simulation of Energetically Disordered Organic Solar Cells.* J. Appl. Phys., 2014. **116**(18).

33. Groves, C., R.A. Marsh, and N.C. Greenham, *Monte Carlo Modeling of Geminate Recombination in Polymer-Polymer Photovoltaic Devices.* J. Chem. Phys., 2008. **129**(11): p. 114903.

34. Tress, W., K. Leo, and M. Riede, *Optimum Mobility, Contact Properties, and Open-Circuit Voltage of Organic Solar Cells: A Drift-Diffusion Simulation Study.* Phys. Rev. B., 2012. **85**(15): p. 155201.

35. Shieh, J.-T., et al., *The Effect of Carrier Mobility in Organic Solar Cells.* J. Appl. Phys., 2010. **107**(8).

36. Groves, C., *Simulating Charge Transport in Organic Semiconductors and Devices: A Review.* Rep. Prog. Phys., 2017. **80**(2): p. 026502.

37. Fukuhara, T., Y. Tamai, and H. Ohkita, *Nongeminate Charge Recombination in Organic Photovoltaics.* Sustain. Energy Fuels, 2020. **4**(9): p. 4321-4351.

38. Li, M., et al., *Solution-processed organic tandem solar cells with power conversion efficiencies >12%.* Nature Photonics, 2016. **11**(2): p. 85-90.

39. Ghasemi, M., et al., *Panchromatic Sequentially Cast Ternary Polymer Solar Cells.* Adv Mater, 2017. **29**(4).

40. Wang, Y., et al., *Achieving Balanced Crystallization Kinetics of Donor and Acceptor by Sequential-Blade Coated Double Bulk Heterojunction Organic Solar Cells.* Advanced Energy Materials, 2020. **10**(28).

41. Fernandez, E.F., et al., *Effect of Spectral Irradiance Variations on the Performance of Highly Efficient Environment-Friendly Solar Cells.* IEEE J. Photovolt., 2015. **5**(4): p. 1150-1157.

42. Laboratory, N.R.E. *Bird Simple Spectra Model*. 2021 [Accesed: 06-sep-2021]; Available from: https://www.nrel.gov/grid/solar-resource/spectral.html.

CHAPTER 8

CONCLUSIONS AND SUGGESTED FUTURE WORK

8.1 Conclusions

Since the development of the first practical solar cells in the 1950's, the search for cost effective PV technologies has been substantial. Amidst the different PV alternatives to inorganic solar cells, OPVs represent a serious competition because they are flexible, can be integrated into existing buildings, as well as potentially being cheap. For instance, it is believed that solution-processing and roll-to-roll printing of flexible substrates will allow for a cost effective OPV manufacturing, that can result on electrical energy production for the grid or the development of products for niche markets. However, a main restriction to realise commercialisation at present are the low efficiencies when compared to inorganic counterparts. Particularly, morphology control and loss mechanisms need to be fully understood in order to enhance the efficiency. In this thesis, we investigate direct interventions that will improve PV values and efficiency, so that one may develop methods and criterions on how to best optimise OPVs. To achieve the objective, three main approaches to enhance the efficiency were considered: formulation, novel materials and device engineering. Below, a summary is provided of the key results achieved in this work.

Herein, in this thesis we began with a preparatory work based on P3HT:PCBM to determine the optimal conditions of binary BHJs fabricated in the Durham Engineering cleanroom, so that OPVs could be further investigated utilising the main approaches proposed to enhance efficiency. Thus, P3HT:PCBM blends were optimised by TA and SVA since these methods have been demonstrated in the past to influence the morphology and yield higher efficiencies. Results presented in Chapter 4 showed that both methods are promising in that the crystallinity is enhanced. However, TA treatment for 10 min at 120 °C resulted in a more profound impact in the performance. Suitable crystalline structures were observed throughout the film's surface resulting in a morphology that was more appropriate for exciton dissociation as seen with larger EQE obtained. Further, optical absorption for the 10 min sample was red-shifted as a consequence of enhanced

crystallinity, which is also consistent with an increment in the hole mobility in this type of blends. Hence, this optimised recipe was considered as a base going forward.

Following, having achieved an optimal binary blend, the formulation approach to enhance efficiency was investigated in Chapter 5 which consisted in adding a third component to a binary BHJ resulting in a ternary blend. In this study, ICBA was selected as the third constituent to discern the impact on the efficiency. Two ternary blend systems were examined: P3HT:ICBA:PC$_{71}$BM and PTB7:ICBA:PC$_{71}$BM and as the reference binary systems fabricated of P3HT:PC$_{71}$BM and PTB7:PC$_{71}$BM. This is the first time that the same approach has systematically been applied to two blend systems. It was concluded that the impact of ICBA on the molecular morphology on either blend was different, despite both blend systems being fabricated with the same concentrations of fullerenes (PC$_{71}$BM:ICBA). First, P3HT-blends gained large increase in V$_{OC}$ of 200 mV and 100 mV considering a 25 wt% of ICBA without and with additive respectively. This increase was attributed to an effective alloy, that was attributed to a greater molecular mixing of fullerenes that were not able to interpose between P3HT side-chains. Secondly, the evidence provided suggested that fullerenes can readily interpose between polymer side-chains of PTB7-blends, resulting in a greater reduction in recombination losses due to a cascade effect. This led to high improvements of IQE in the order of 25% for PTB7 ternary blends with additive when compared to the control reference. Valuable insights derived from this Chapter demonstrate that ternary blends can certainly enhance efficiency and that the observed behaviour depends upon the polymer donor, and whether acceptor materials can or cannot interpose between polymer side-chains, thus dictating the benefit that a ternary blend can offer.

Next, we focused the attention on charge carrier mobility which is an important factor in semiconductors that plays a key role on PV characteristics. Specifically, in Chapter 6 we examined the transport properties of electron-only diodes fabricated from a family of novel materials comprised of NFA, hybrid fullerenes and fullerenes which were probed for the first time. These materials were synthesised by Dr. Avestro and fellow PhD Phil Hope in a collaborative work, and our role was to fabricate the electron-only diodes. First, SEM analysis on NFA components revealed semi-crystalline and large crystalline morphologies for NDI$_2$ and *bis*-NDI respectively. Then, electron-only diodes based on NDI$_2$ and thick *bis*-NDI achieved mobilities 0.80×10^{-6} m^2 V^{-1} s^{-1} and 0.73×10^{-8} m^2 V^{-1} s^{-1} respectively, which were close to reference PCBM with 2.90×10^{-6} m^2 V^{-1} s^{-1}.

On the other hand, hybrid fullerenes based on $NDI_{12}C_{60}$ and $Alk_{12}C_{60}$, depicted no noticeable morphology for the resolutions examined and yielded insulating mobilities in the order of 10^{-11} m^2 V^{-1} s^{-1}, thus showing that the synthetic strategy to fabricate these hybrid fullerenes did not work to enhance electron mobility. In this way, the results from this Chapter highlight a necessary step before commercialisation of novel materials, which is that they need to ensure sufficient carrier mobility if they are to be incorporated into a working OPV device.

Finally, further analysis on how one can increase the efficiency through the device engineering was carried out by stacking two photoactive layers to a device, termed as tandem OPVs. It is known that in this type of devices to attain a higher performance the photo generated current between the front and back cells needs to be matched. However, this is a difficult aspect in practice considering all the different combination of materials and their controlling parameters. Thus, with advanced modelling we investigated how can one increase the efficiency by device engineering tandem OPVs, utilising blends of $PCDTBT:PC_{71}BM$ (front cell) and $PTB7-Th:PC_{71}BM$ (back cell) as the main base. By changing the carrier mobilities and absorption properties, we demonstrated that the performance on tandem devices with unbalanced current is dominated by the cell performing most of the absorption. Also, it is shown that the recombination could be lessened by changing the transport properties of the cell performing least of the absorption, so that photo generated charges from the more absorbing cell can transit to the contacts efficiently. Thus, the results from this Chapter showed that high performing tandems can be achieved even with current mismatching, offering a methodology that can reduce the constraints to design tandems under real-world illumination conditions that may deviate from AM 1.5 because of pollution or dust.

To conclude, although OPVs have already surpassed the 17% efficiency mark under standardised conditions, more is needed to finally realise commercialisation and compete with well-established mature PV technologies. The approaches offered in this study demonstrate that efficiency can be increased, and underline the importance to continue to investigate this pressing subject. To date, various scenarios are being developed that have the potential to further increase the performance in OPVs. Two approaches are discussed in the next section.

8.2 Suggested future work

In this section we focus on two alternative approaches that can potentially increase efficiency in OPVs. Such suggestions are discussed below:

8.2.1 Ternary blends based on novel NFAs

As observed in Chapter 5, ternary blends have attracted large amounts of attention as a way to increase efficiency in OPVs for instance, by optimising morphology and reducing the recombination [1]. Up until now, most high performing OPVs are based on polymer:fullerene BHJ blend systems. However, an important drawback with fullerenes is that the absorption in the visible spectrum is weak (compared to donor materials) and have poor molecular tuneability [2]. This in turn has paved the way for researchers to look at alternative materials, such as novel acceptors. In recent times, NFAs have attracted tremendous attention due their advantages such as synthetic flexibility and molecular tuneability of the electronic and optical properties that can potentially lead to higher performances [2]. As stated before, ternary blends have focused mostly on polymer:fullerene systems based on a combination of two donor materials and a fullerene acceptor, or more seldom reported, two fullerene acceptors and one donor [3]. In this regard, ternary blends fabricated with emerging NFA have been scarcely investigated. Thus, it is important to further expand the material choice if one wants to continue to advance in OPV's efficiency.

This leads us to the first suggestion of a NFA ternary blend which can be fabricated of a polymer:NFA:fullerene system to study the cascade mechanisms to ameliorate recombination losses. Such system could be fabricated based on PTB7-Th:$PC_{71}BM$:COi8DFIC. A blend like this presents suitable energy alignment between components in addition to a good miscibility between the main polymer and fullerene. In addition, by utilising a fullerene (good electron mobility) and a NFA (strong absorption) higher efficiencies can potentially be reached. Relevant experiments suggested are first UV-vis to reveal the absorption differences between the control and ternary composites. Following, J-Vs and EQE may further reveal enhancement in the absorption by increases in J_{SC} and FF which may indicate improved generation and transport of charges. To validate this, charge carrier mobilities can be examined with the SCLC formulism by fabricating single-carrier devices. Also, modelling can be used to fit experimental J-Vs

by changing transport parameters and reveal more detail about transport and recombination mechanisms. Lastly, morphological analysis based on AFM and TEM can also provide interesting and complementary information regarding nanostructures and phase separation.

Another suggestion would be ternary blends based on a polymer:NFA:NFA system, such as PTB7-Th:TPE-4PDI:ITIC. In here, an interesting approach would be to see the experimental impact of the two novel acceptors on the V_{OC}. Relevant experiments suggested (besides J-Vs and EQE) include UV-vis, to elucidate the absorption profile that the NFA offer compared to the known properties of fullerenes. To reveal insights on the possibility of an alloy between the acceptor constituents, different weight ratios of the third component (i.e. TPE-4PDI) ranging from 0% to 50% can be investigated and PV values characterised. In addition, X-ray measurements (i.e. Grazing Incidence X-ray Diffraction, GIXD) and TEM can be used to shed light on the morphology; for instance, crystallinity features and insight regarding if π-π stacking is perturbed or not with the ternary blends. Moreover, experiments can be repeated considering other donor materials such as PBDB-T or PCDTBT which present larger polymer backbones compared to PTB7-Th and thus potentially more possibility for the acceptors to interpose between polymer side-chains.

8.2.2 Tandem OPVs with indoor illumination or diffuse irradiance

Indeed, as observed in Chapter 7, tandem OPVs certainly have the potential to keep increasing the efficiency beyond current marks [4, 5]. Although there have been some studies showing the potential of PVs for indoor applications, a specific study concerning tandem OPVs is still missing. The results offered in Chapter 7 are promising because it shows that tandem OPVs can be used under different illumination conditions and how is it that by material selection, loss mechanisms can be mitigated.

Thusly, as a first suggestion to fill this gap, it would be interesting to consider tandem OPVs operating with other light sources in addition to fluorescent such as: sodium lamps, LED tubes, incandescent lamps and metal halide lamps that can normally be found in many buildings and households. More specifically, the normalised AM 1.5 spectrum could be compared against these other light sources. Then, optical and electrical modelling could be used to characterise and determine main PV values. These results could offer valuable information, for instance, what is the distribution of photons on each

layer at different thicknesses and how can one best engineer them to yield higher J_{SC} and PCE. Also, efficiencies obtained could be compared to single junction OPVs to emphasise on the benefit of using tandems. Further, energy bandgaps, mobilities and absorption of different layers could be modified in the simulations revealing spectral mismatch and electrical parameters that can assist to design a suitable tandem to operate in these conditions.

A last suggestion would be to come up with a complete methodology on how to simulate and test tandem OPVs under indoor applications or diffused light since they are seldom reported and are still lacking.

8.3 References

1. Jiang, K., et al., *Multiple Cases of Efficient Nonfullerene Ternary Organic Solar Cells Enabled by an Effective Morphology Control Method.* Adv. Energy Mater., 2018. **8**(9).

2. Fu, H., Z. Wang, and Y. Sun, *Advances in Non-Fullerene Acceptor Based Ternary Organic Solar Cells.* Solar RRL, 2018. **2**(1).

3. Xu, W. and F. Gao, *The Progress and Prospects of Non-Fullerene Acceptors in Ternary Blend Organic Solar Cells.* Mater. Horiz., 2018. **5**(2): p. 206-221.

4. Ameri, T., N. Li, and C.J. Brabec, *Highly Efficient Organic Tandem Solar Cells: A Follow up Review.* Energy Environ. Sci., 2013. **6**(8): p. 2390-2413.

5. Li, G., W.-H. Chang, and Y. Yang, *Low-Bandgap Conjugated Polymers Enabling Solution-Processable Tandem Solar Cells.* Nat. Rev. Mater., 2017. **2**(8): p. 17043.

APPENDIXES CHAPTER 4

Appendix 4.1. Example of thermal annealing, TA (left) and solvent vapour annealing, SVA (right).

Binary blend	Thermal annealing	Film thickness (nm)	Solvent vapour annealing	Film thickness (nm)
P3HT:PCBM	Control	110	Control	109
P3HT:PCBM	120° C and 2 min	108	1.5 ml DCB, 3 min	105
P3HT:PCBM	120° C and 5 min	152	1.5 ml DCB, 5 min	106
P3HT:PCBM	120° C and 10 min	168	1.5 ml DCB, 15 min	104
P3HT:PCBM	120° C and 15 min	155	1.5 ml DCB, 30 min	112
P3HT:PCBM	120° C and 20 min	120	1.5 ml DCB, 60 min	106

Appendix 4.2. Thin film thicknesses of P3HT:PCBM blends with TA and SVA processing.

Binary blend	Thermal annealing	Voc (V)	Jsc (mA/cm^2)	FF (%)	PCE (%)
P3HT:PCBM	Control	0.34	2.1	56%	0.4%
P3HT:PCBM	120° C and 2 min	0.34	2.9	49%	0.5%
P3HT:PCBM	120° C and 5 min	0.36	4.3	49%	0.8%
P3HT:PCBM	120° C and 10 min	0.36	6	51%	1.1%
P3HT:PCBM	120° C and 15 min	0.36	5.1	49%	0.9%
P3HT:PCBM	120° C and 20 min	0.32	4.0	47%	0.6%
Binary blend	Solvent vapour annealing	Voc (V)	Jsc (mA/cm^2)	FF (%)	PCE (%)
P3HT:PCBM	Control	0.38	3.2	46%	0.6%
P3HT:PCBM	1.5 ml DCB, 3 min	0.44	4.3	43%	0.8%
P3HT:PCBM	1.5 ml DCB, 5 min	0.4	4.0	47%	0.8%
P3HT:PCBM	1.5 ml DCB, 15 min	0.4	5	47%	0.9%
P3HT:PCBM	1.5 ml DCB, 30 min	0.38	3.1	49%	0.6%
P3HT:PCBM	1.5 ml DCB, 60 min	0.38	2.6	35%	0.3%

Appendix 4.3. PV statistical data of P3HT:PCBM with TA and SVA treatment.

APPENDIXES CHAPTER 5
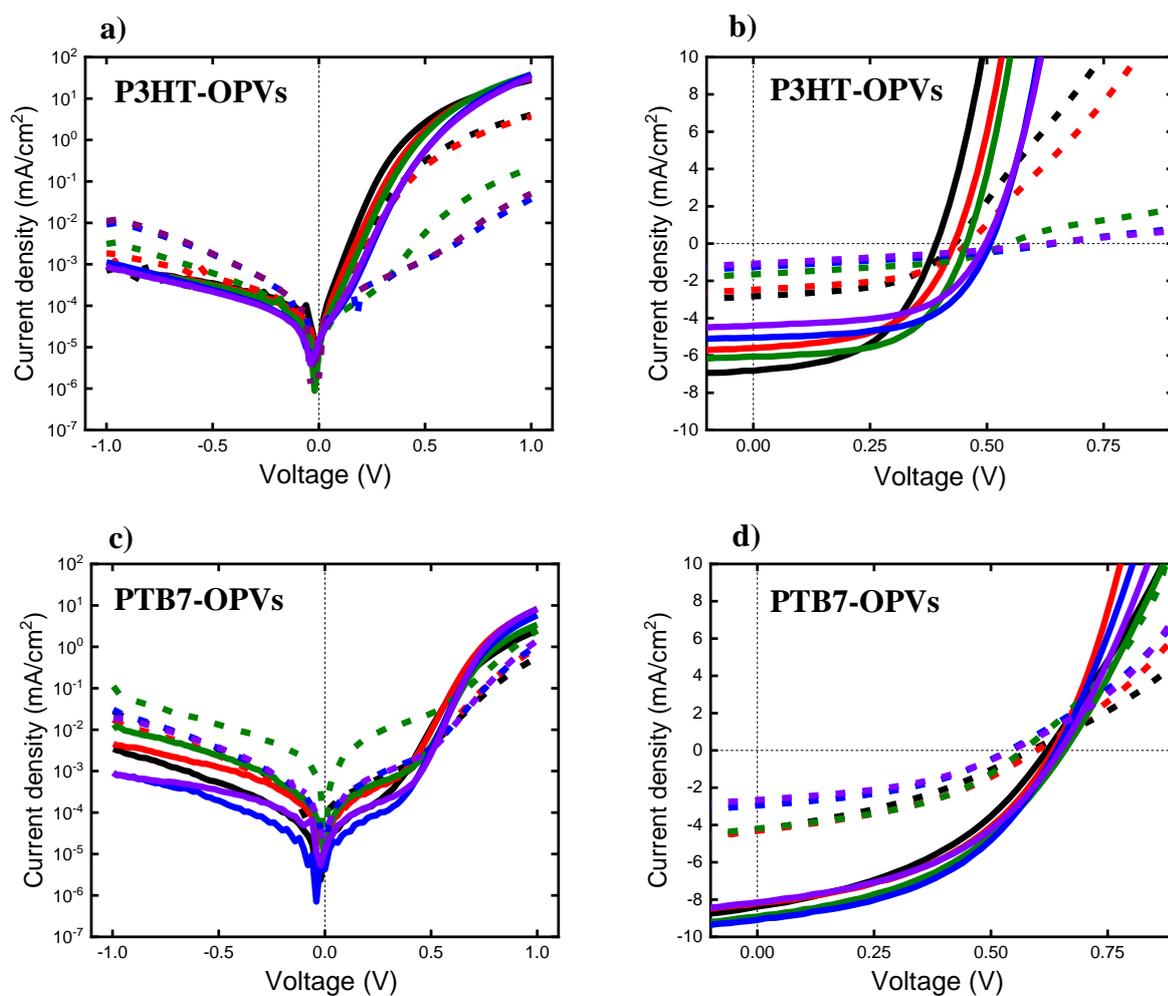
Appendix 5.1. Dark (a, c) and Light (b, d) J-V characteristics for control and ternary a, b) P3HT:$PC_{71}BM$ and c, d) PTB7:$PC_{71}BM$ blends with 0% (black), 10% (red), 20% (green), 25% (blue) and 30% (purple) ICBA loading, with and without 3% of DIO. Solid lines denote OPVs with DIO and short-dash lines denote OPVs without DIO.

PTB7:PC$_{71}$BM ICBA [wt%]	Processing conditions	Voc (V)	Jsc (mA/cm^2)	FF (%)	PCE (%)
0	Without DIO	0.58 ± 0.01	4.3 ± 0.1	35% ± 2.5	0.9% ± 0.2
0	**DIO 3%**	0.62 ± 0.01	8.4 ± 1	41% ± 0.4	2.1% ± 0.4
10	Without DIO	0.60 ± 0.00	4.3 ± 0.1	39% ± 1	1% ± 0.0
10	**DIO 3%**	0.64 ± 0.03	8.2 ± 1	44% ± 1.3	2.3% ± 0.3
20	Without DIO	0.56 ± 0.03	4.2 ± 0.1	43% ± 0.6	1% ± 0.1
20	**DIO 3%**	0.66 ± 0.03	8.9 ± 1	43% ± 3	2.5% ± 0.3
25	Without DIO	0.54 ± 0.02	3.0 ± 0.1	41% ± 1.5	0.7% ± 0.2
25	**DIO 3%**	0.64 ± 0.00	9.1 ± 1	46% ± 0.7	2.7% ± 0.2
30	Without DIO	0.54 ± 0.03	2.7 ± 0.1	41% ± 1.3	0.6% ± 0.1
30	**DIO 3%**	0.64 ± 0.02	8.1 ± 1	45% ± 1.4	2.3% ± 0.3

| P3HT:PC$_{71}$BM ICBA [wt%]	Processing conditions	Voc (V)	Jsc (mA/cm^2)	FF (%)	PCE (%)
0	Without DIO	0.44 ± 0.02	2.8 ± 0.3	50% ± 1.3	0.6% ± 0.1
0	**DIO 3%**	0.40 ± 0.01	6.8 ± 0.6	50% ± 1.5	1.4% ± 0.1
10	Without DIO	0.46 ± 0.01	2.5 ± 0.2	50% ± 0.2	0.6% ± 0.1
10	**DIO 3%**	0.42 ± 0.00	5.6 ± 0.4	54% ± 1.4	1.3% ± 0.2
20	Without DIO	0.54 ± 0.01	1.7 ± 0.1	46% ± 0.3	0.4% ± 0.0
20	**DIO 3%**	0.47 ± 0.01	6.1 ± 0.4	57% ± 1.2	1.6% ± 0.1
25	Without DIO	0.64 ± 0.02	1.3 ± 0.1	34% ± 0.2	0.3% ± 0.0
25	**DIO 3%**	0.5 ± 0.00	5.1 ± 0.1	56% ± 0.6	1.5% ± 0.0
30	Without DIO	0.62 ± 0.01	1.1 ± 0.1	32% ± 0.1	0.2% ± 0.1
30	**DIO 3%**	0.5 ± 0.01	4.4 ± 0.4	56% ± .1	1.2% ± 0.1

Appendix 5.2. Statistical PV data for binary and ternary OPVs with different ICBA content, with and without 3% of DIO tested at room temperature.

| Binary blend [Donor:Fullerene]	Ternary blend [Donor:Fullerene alloy]	Additive	ICBA in alloy (%)	Type of morphology	V_{OC} (V)	J_{SC} (mA/cm^2)	FF (%)	PCE (%)	V_{OC} increment (mV)	Ref. from Chapter
P3HT:PCBM		-	0%	No intercalation	0.61	9.9	60	3.6	60 mV	26
	P3HT:ICBA:PCBM	-	40%		0.67	8.3	58	3.1		
P3HT:PCBM		0.3% CN	0%	No intercalation	0.54	7.2	57	2.2	40 mV	30
	P3HT:ICBA:PCBM		33%		0.58	6.5	59	2.2		
P3HT:PC$_{71}$BM		-	0%	No intercalation	0.44	2.8	50	0.6	100 mV	This work
	P3HT:ICBA:PC$_{71}$BM	-	40%		0.54	1.7	46	0.4		
P3HT:PC$_{71}$BM		3% DIO	0%		0.4	6.8	50	1.4	70 mV	
	P3HT:ICBA:PC$_{71}$BM		40%		0.47	6.1	57	1.6		
PTB7:PC$_{71}$BM		-	0%	Molecular intermixing	0.58	4.3	35	0.9	-20 mV	This work
	PTB7:ICBA:PC$_{71}$BM	-	33%		0.56	4.2	43	1		
PTB7:PC$_{71}$BM		3% DIO	0%		0.62	8.4	41	2.1	40 mV	
	PTB7:ICBA:PC$_{71}$BM		33%		0.66	8.9	43	2.5		
PTB7:PC$_{71}$BM		3% DIO	0%	Molecular intermixing	0.70	15	69	7.2	30 mV	33
	PTB7:ICBA:PC$_{71}$BM		30%		0.73	14	67	6.8		
PTB7:PC$_{71}$BM		3% DIO	0%	Molecular intermixing	0.76	14	70	7.5	0 mV	34
	PTB7:ICBA:PC$_{71}$BM		30%		0.76	13	55	5.5		
PBTTT-C14:PCBM		-	0%	Molecular intermixing	0.48	6.4	53	1.6	30 mV	28
	PBTTT-C14:PCBM:ICBA	-	40%		0.51	3.9	50	1		

Appendix 5.3. Survey on ternary blends specifically with ICBA:PCBM and ICBA:PC$_{71}$BM fullerene alloys comparing the increment of V_{OC} in the alloy versus binary controls. The table describes a range of ICBA in different alloy content between 30-40% due to the differences in fabrication procedures. As such, similar OPV fabrication conditions were considered. The clear area denotes blend systems with no intercalation and the shaded area blend systems with molecular intermixing. Two significant digits on all PV parameters.
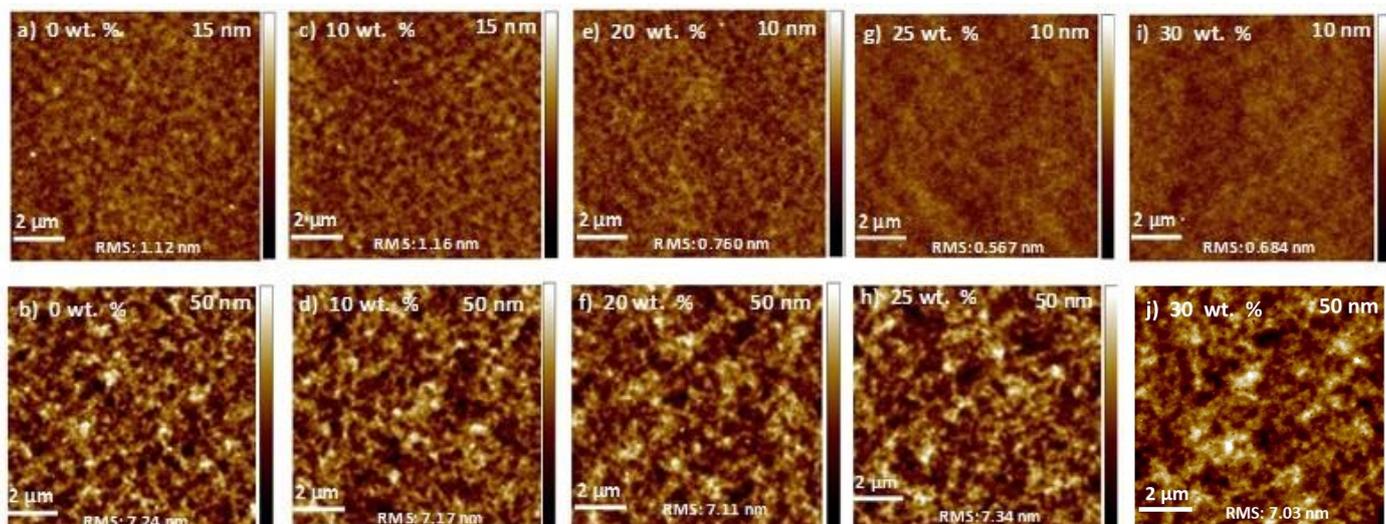
Appendix 5.4. Tapping mode AFM images of reference and ternary P3HT:PC$_{71}$BM blends with different weight loadings of ICBA without and with 3% DIO (top and bottom respectively). Scan area of 10 x 10 μm.
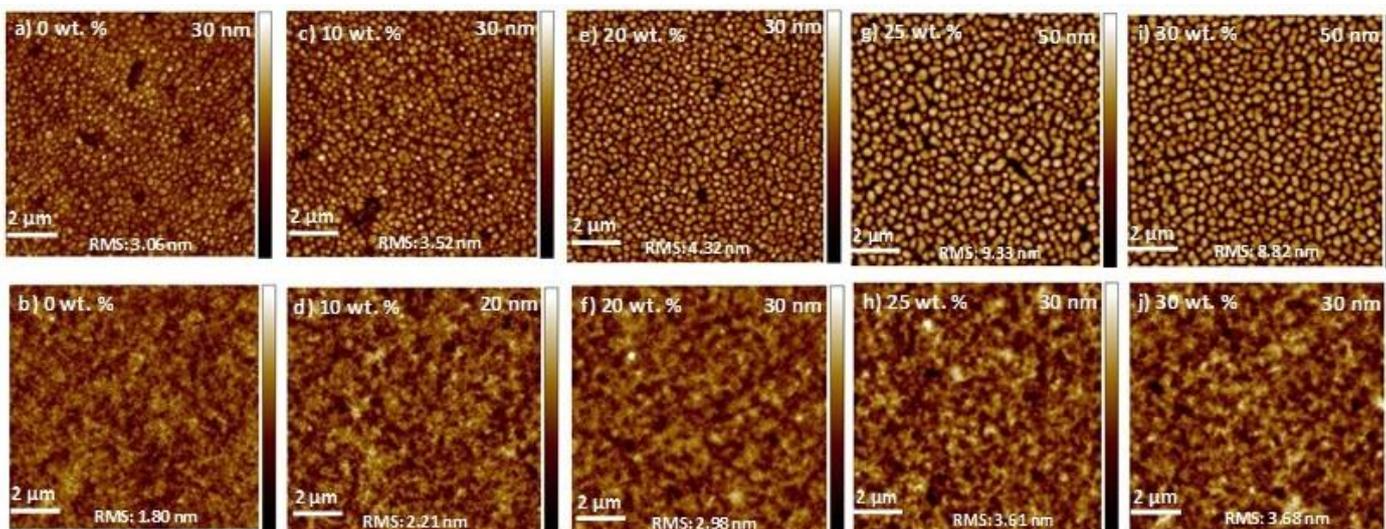
Appendix 5.5. Tapping mode AFM images of reference and ternary PTB7:PC$_{71}$BM blends with different weight loadings of ICBA without and with 3% DIO (top and bottom respectively). Scan area of 10 x 10 μm.
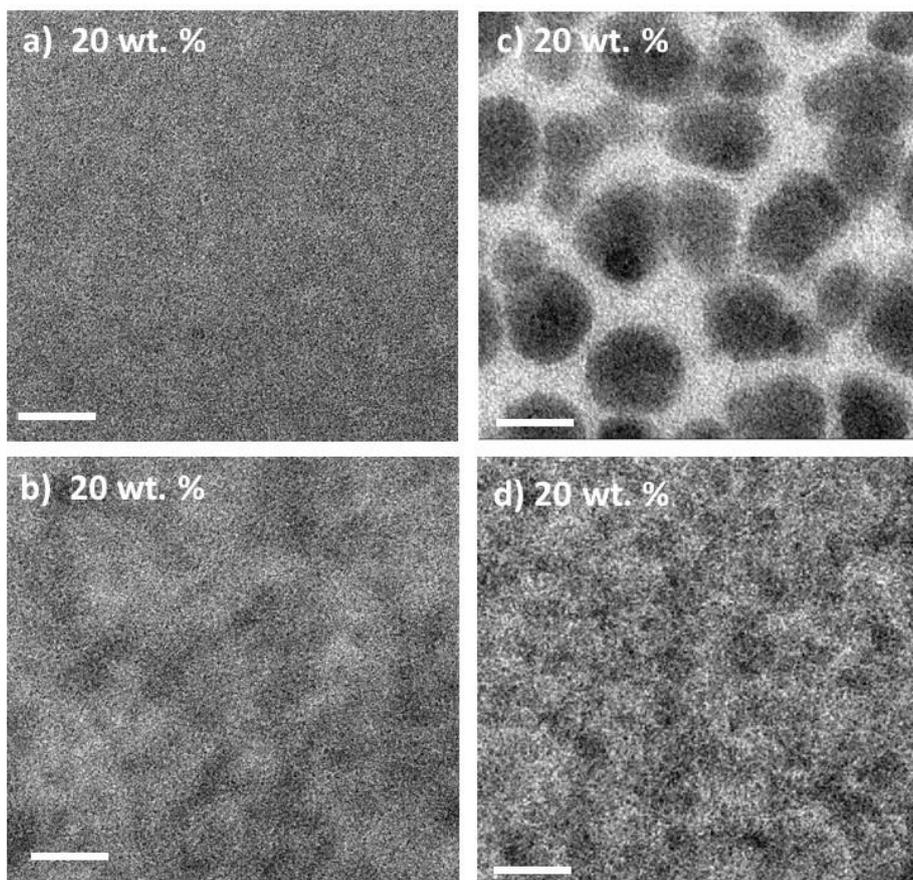
Appendix 5.6. TEM image for a, b) P3HT:PC$_{71}$BM and c, d) PTB7:PC$_{71}$BM ternary film with a 20% content of ICBA. Figures a) and c) represent films with no DIO, b) and d) with 3% of DIO. Scale bar denotes 200 nm.

| P3HT:PC$_{71}$BM ICBA [wt%]	Processing conditions	Film thickness (nm)	RMS (nm)
0	Without DIO	170	1.1
0	**DIO 3%**	155	7.2
10	Without DIO	160	1.2
10	**DIO 3%**	150	7.2
20	Without DIO	132	0.8
20	**DIO 3%**	135	7.1
25	Without DIO	117	0.6
25	**DIO 3%**	137	7.3
30	Without DIO	124	0.7
30	**DIO 3%**	123	7

| PTB7:PC$_{71}$BM ICBA [wt%]	Processing conditions	Film thickness (nm)	RMS (nm)
0	Without DIO	123	3.1
0	**DIO 3%**	118	1.8
10	Without DIO	122	3.5
10	**DIO 3%**	109	2.2
20	Without DIO	114	4.3
20	**DIO 3%**	102	2.3
25	Without DIO	128	9.3
25	**DIO 3%**	108	3.6
30	Without DIO	120	8.8
30	**DIO 3%**	114	3.7

Appendix 5.7. Summary of AFM parameters for binary and ternary P3HT:PC$_{71}$BM (top) and PTB7:PC$_{71}$BM (bottom) with different ICBA loadings, with and without 3% DIO.
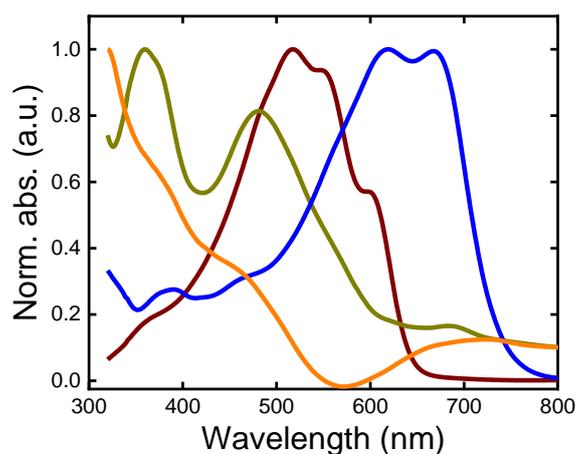
Appendix 5.8. Normalised absorption spectra of PTB7 (blue), P3HT (brown), PC$_{71}$BM (yellow) and ICBA (orange) neat films.
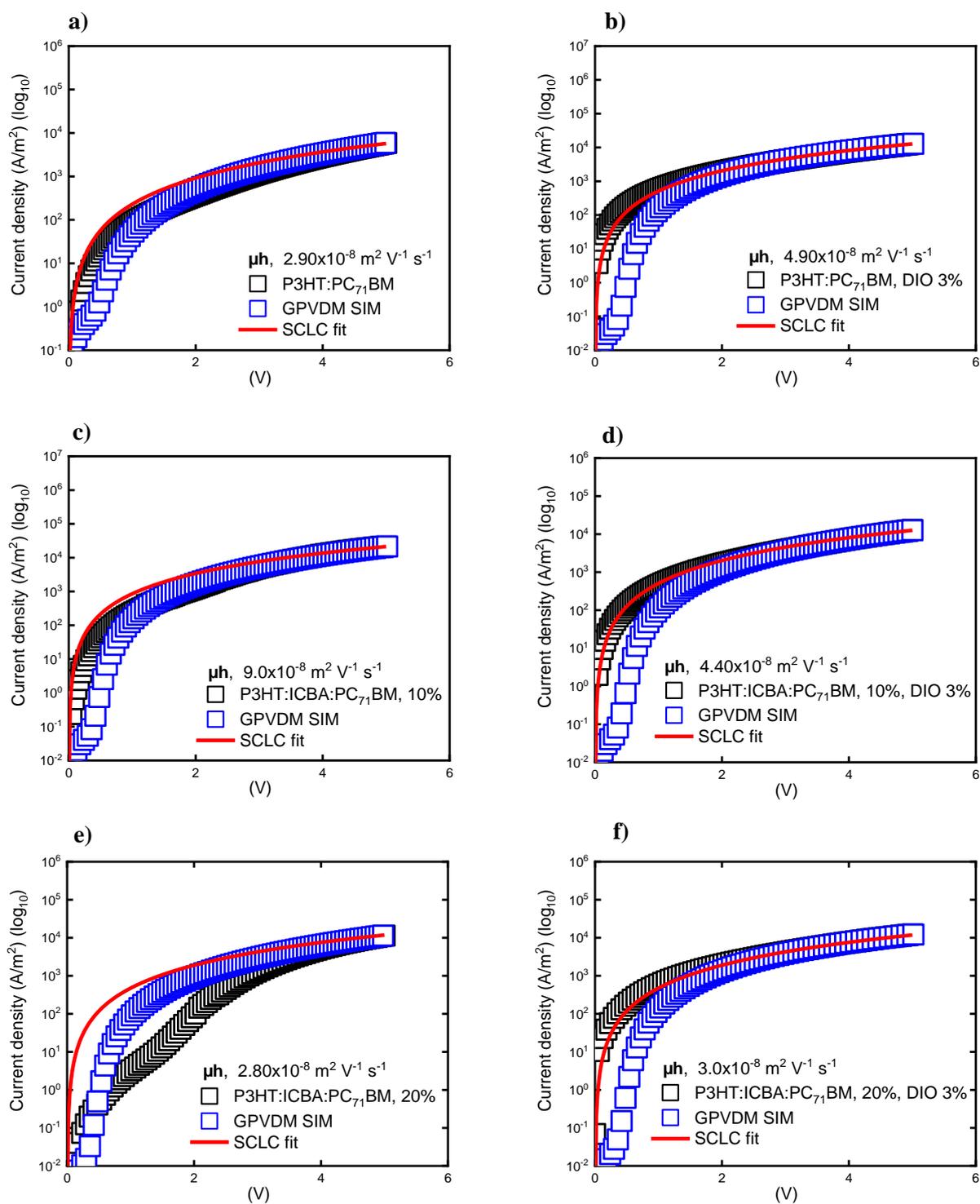
Appendix 5.9. Dark current densities and SCLC model fitting hole-only devices for P3HT-based OPVs. a) Hole mobility (μ_h) of binary blend, b) binary blend with 3% DIO, c) P3HT:PC$_{71}$BM with 10% ICBA d) P3HT:PC$_{71}$BM with 10% ICBA and 3% DIO e) P3HT:PC$_{71}$BM with 20% ICBA f) P3HT:PC$_{71}$BM with 20% of ICBA and DIO 3%. Open black squares represent the experimental data and the blue open squares denote the simulation fitting. The red solid line represents the SCLC fit.
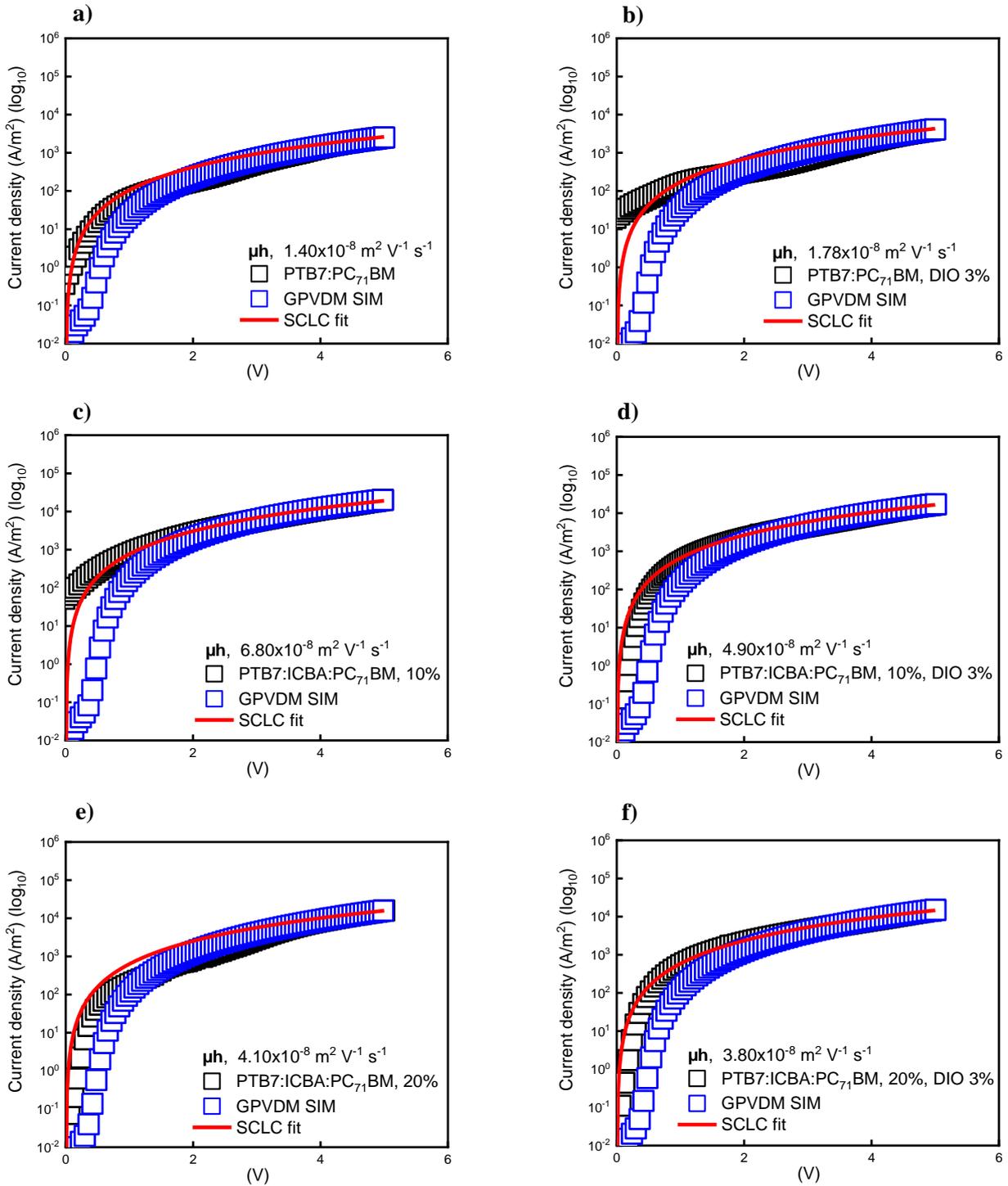
Appendix 5.10. Dark current densities and SCLC model fitting hole-only devices for PTB7-based OPVs. a) Hole mobility (μ_h) of binary blend, b) binary blend with 3% DIO, c) PTB7:PC$_{71}$BM with 10% ICBA d) PTB7:PC$_{71}$BM with 10% ICBA and 3% DIO e) PTB7:PC$_{71}$BM with 20% ICBA f) PTB7:PC$_{71}$BM with 20% of ICBA and DIO 3%. Open black squares represent the experimental data and the blue open squares denote the simulation fitting. The red solid line represents the SCLC fit.

APPENDIXES CHAPTER 6

Modelling of electron transport in novel acceptors

Fitting simulations to experimental curves can be an effective tool to study carrier transport and recombination mechanisms. In here, drift diffusion simulations with GPVDM were used alongside SCLC analysis. As a reference a glassITO/PEDOT:PSS/PCBM/LiF/Al structure was utilised for the device simulations. A realistic absorption profile and refractive index were used for all models, considering a standard PCBM. Modelling was utilised to recreate the experimental J-V characteristics by changing the carrier mobilities, parasitic resistances and trap parameters. This approach enables to determine to what extent the mobility of single carrier devices and recombination parameters should be varied, in order to recreate the experimental values. The electrical parameters chosen to compare experimental and simulated J-V curves are shown below followed by the fitting results.

| Description	Parameter	PCBM	$Alk_{12}C_{60}$	$Alk_{12}C_{60}$	$NDI_{12}C_{60}$	$NDI_{12}C_{60}$	bis-NDI	bis-NDI	NDI_2	$NDI_{12}C_{60}$:NDI_2 (1:1)	$NDI_{12}C_{60}$:NDI_2 (1:2)
Electrical parameters:											
Electron trap density	$m^{-3}eV^{-1}$	3.80×10^{26}	3.80×10^{27}	3.80×10^{27}	3.80×10^{27}	3.80×10^{27}	3.80×10^{28}	3.80×10^{28}	3.80×10^{26}	3.80×10^{27}	3.80×10^{27}
Hole trap density	$m^{-3}eV^{-1}$	1.45×10^{25}	1.45×10^{26}	1.45×10^{26}	1.45×10^{26}	1.45×10^{26}	1.45×10^{25}	1.45×10^{25}	1.45×10^{25}	1.45×10^{25}	1.45×10^{25}
Electron mobility	$m^2V^{-1}s^{-1}$	4.00×10^{-8}	5.73×10^{-11}	7.05×10^{-11}	1.50×10^{-10}	3.85×10^{-11}	1.52×10^{-8}	1.75×10^{-8}	2.44×10^{-8}	2.70×10^{-9}	9.05×10^{-9}
Hole mobility	$m^2V^{-1}s^{-1}$	4.00×10^{-8}	5.73×10^{-11}	7.05×10^{-11}	1.50×10^{-10}	3.85×10^{-11}	1.52×10^{-8}	1.75×10^{-8}	2.44×10^{-8}	2.70×10^{-9}	9.05×10^{-9}
Number of traps	Bands	20	20	20	20	20	20	20	20	20	20
Series resistance	Ohms	0.7	0.15	19	0.15	0.15	0.1	17	1	0.15	0.15
Shunt resistance	Ohms	1.90×10^5	5.00×10^6	5.00×10^6	5.00×10^6	5.00×10^6	1.90×10^5	1.90×10^5	1.90×10^5	4.00×10^6	4.00×10^6
Start voltage	V	0	0	0	0	0	0	0	0	0	0
End voltage	V	5	5	5	5	5	5	5	5	5	5
Light intensity (number of suns)	W/m^2	1	1	1	1	1	1	1	1	1	1
Active layer thickness	nm	240	200	145	189	139	248	100	220	191	167

Appendix 6.1. Summary with modelling inputs for each type of component.
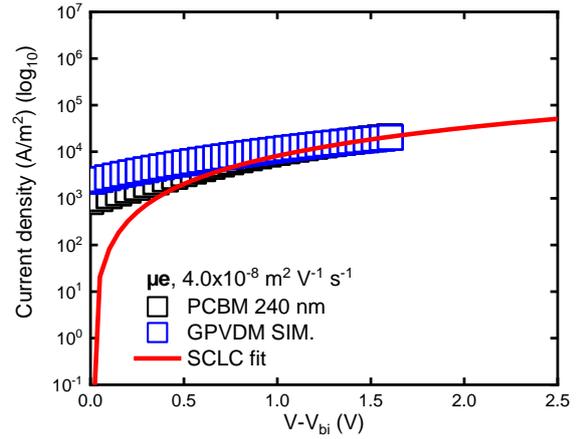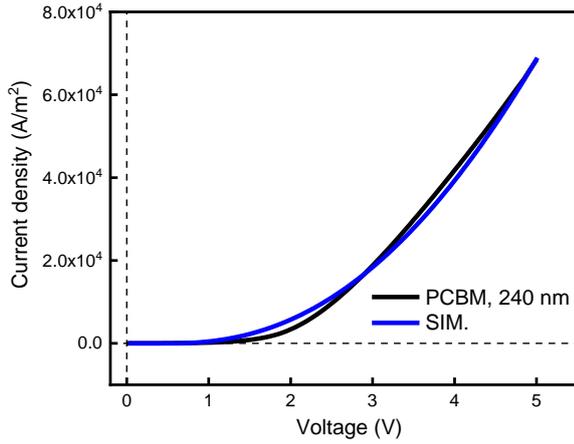
Appendix 6.2. Dark J-V characteristics of PCBM (left) and SCLC fitting represented by a red solid line (right) with electron-only (μ_e) experimental data (hollow black square) used in the model. In plots, GPVDM SIM (hollow blue square) represents the simulation fit.
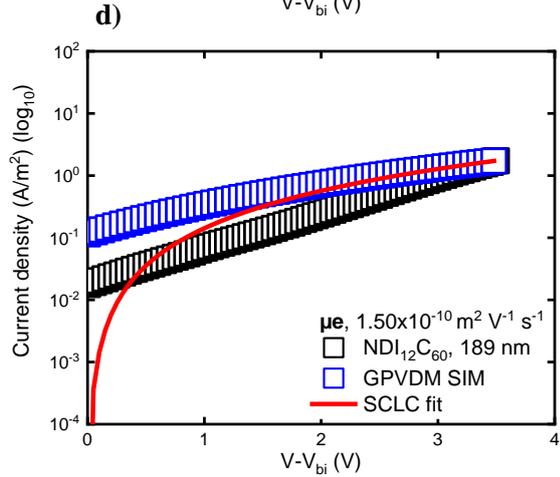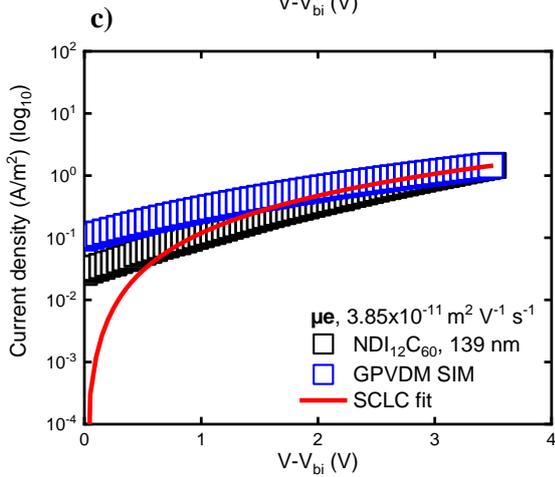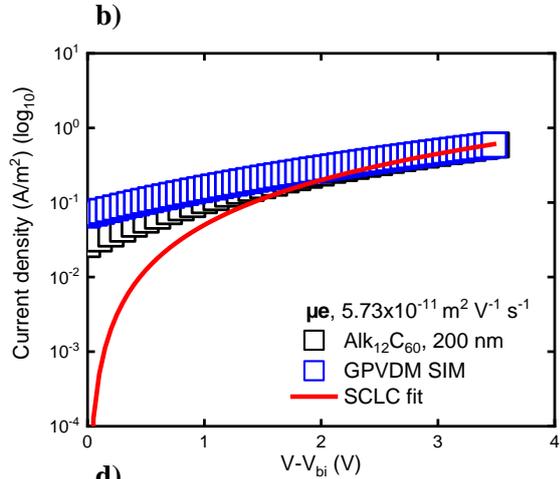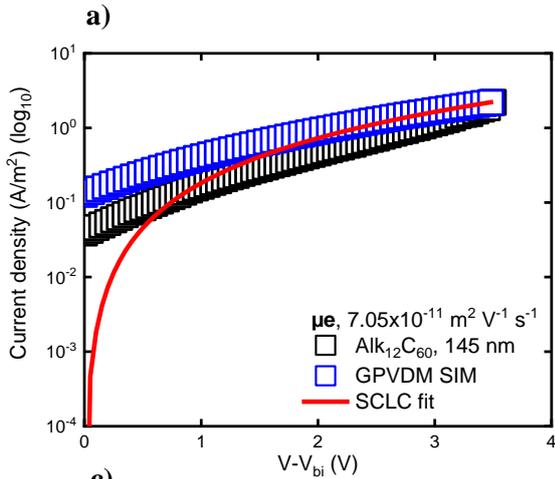
Appendix 6.3. Thin and thick electron-only (μ_e) experimental data (hollow black square) showing SCLC fittings (red solid line) of a, b) $Alk_{12}C_{60}$ and c, d) $NDI_{12}C_{60}$. In plots, GPVDM SIM (hollow blue square) represents the simulation fit.

204
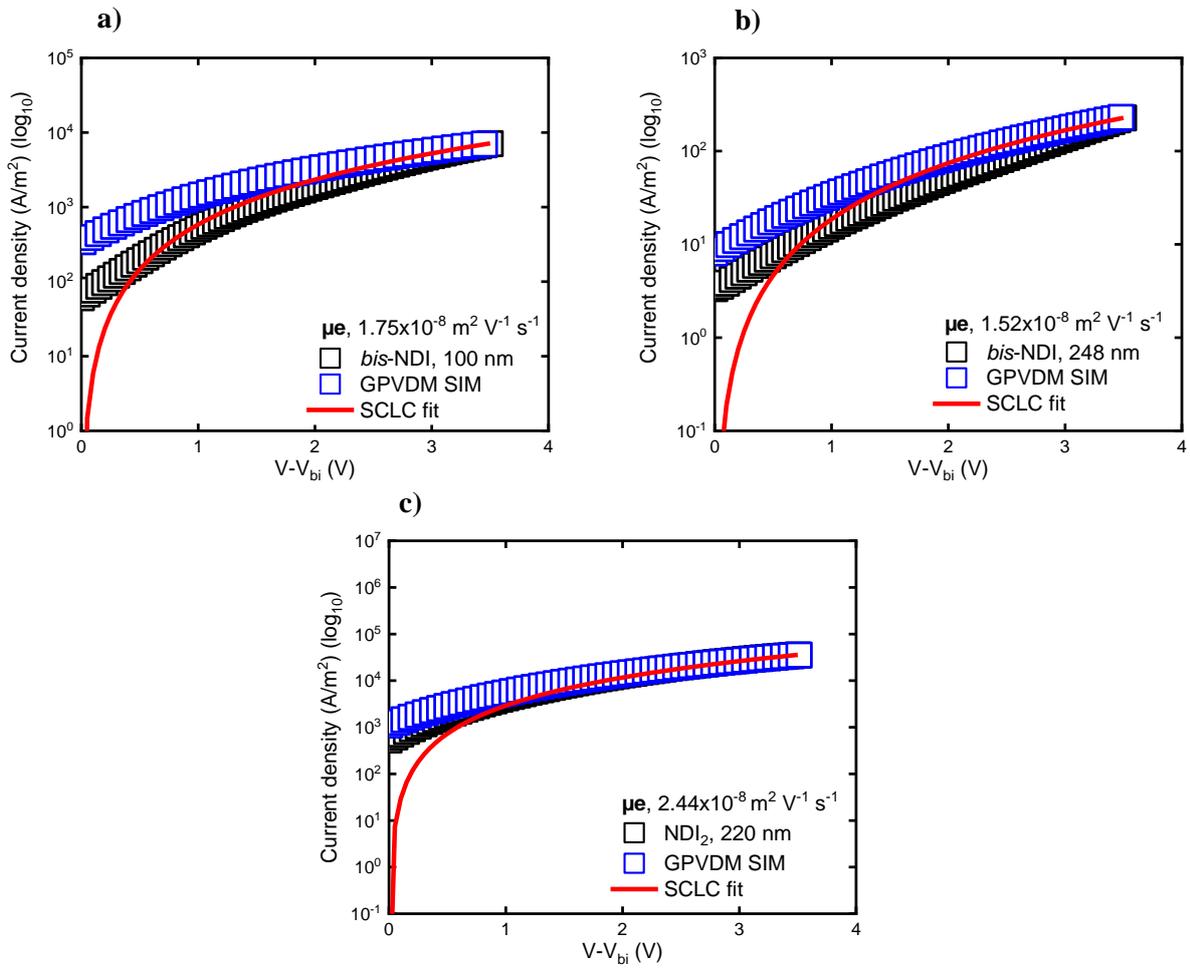
Appendix 6.4. Thin and thick electron-only (μ_e) experimental data (hollow black square) showing SCLC fittings (red solid line) of a, b) *bis*-NDI and c) NDI$_2$. In plots, GPVDM SIM (hollow blue square) represents the simulation fit.
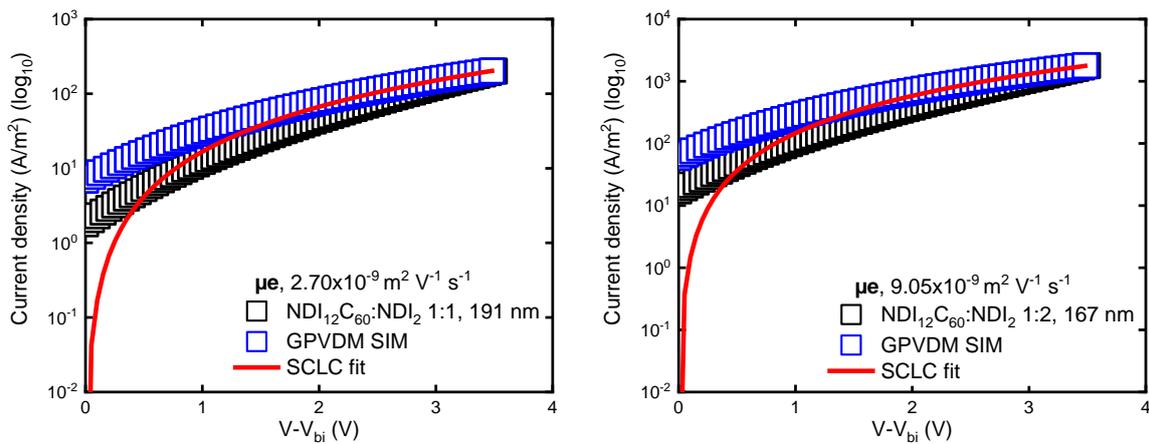

Appendix 6.5. SCLC fittings represented by a red solid line with electron-only (μ_e) experimental data (hollow black square) of NDI$_{12}$C$_{60}$:NDI$_2$ with a 1:1 ratio (left) and 1:2 (right). In plots, GPVDM SIM (hollow blue square) represents the simulation fit.

APPENDIXES CHAPTER 7

| Description	Units	Balanced mobilities		Electron enhanced		Hole enhanced	
		Front cell	Back cell	Front cell	Back cell	Front cell	Back cell
Electron mobility	$m^2\ V^{-1}\ s^{-1}$	1.00×10^{-7}	1.00×10^{-7}	1.00×10^{-7}	1.00×10^{-5}	1.00×10^{-7}	1.00×10^{-7}
Hole mobility	$m^2\ V^{-1}\ s^{-1}$	1.00×10^{-7}	1.00×10^{-7}	1.00×10^{-7}	1.00×10^{-7}	1.00×10^{-5}	1.00×10^{-7}
Relative permittivity	Au	3.8	3.8	3.8	3.8	3.8	3.8
Effective density of free electron states (@300K)	m^{-3}	5.00×10^{-25}	5.00×10^{-25}	5.00×10^{-25}	5.00×10^{-25}	5.00×10^{-25}	5.00×10^{-25}
Effective density of free hole states (@300K)	m^{-3}	5.00×10^{-25}	5.00×10^{-25}	5.00×10^{-25}	5.00×10^{-25}	5.00×10^{-25}	5.00×10^{-25}
ZnO (recombination layer)	$m^2\ V^{-1}\ s^{-1}$	1.00×10^{-8}	1.00×10^{-8}	1.00×10^{-8}	1.00×10^{-8}	1.00×10^{-8}	1.00×10^{-8}
PEDOT:PSS (recombination layer)	$m^2\ V^{-1}\ s^{-1}$	1.00×10^{-8}	1.00×10^{-8}	1.00×10^{-8}	1.00×10^{-8}	1.00×10^{-8}	1.00×10^{-8}
X_i	eV	3.8	3.8	3.8	3.8	3.8	3.8
E_g	eV	1.1	1.1	1.1	1.1	1.1	1.1
Recombination constant	$m^{-3}\ s^{-1}$	1.00×10^{-18}	1.00×10^{-18}	1.00×10^{-18}	1.00×10^{-18}	1.00×10^{-18}	1.00×10^{-18}

Appendix 7.1. List of electrical parameters used in the three different models.
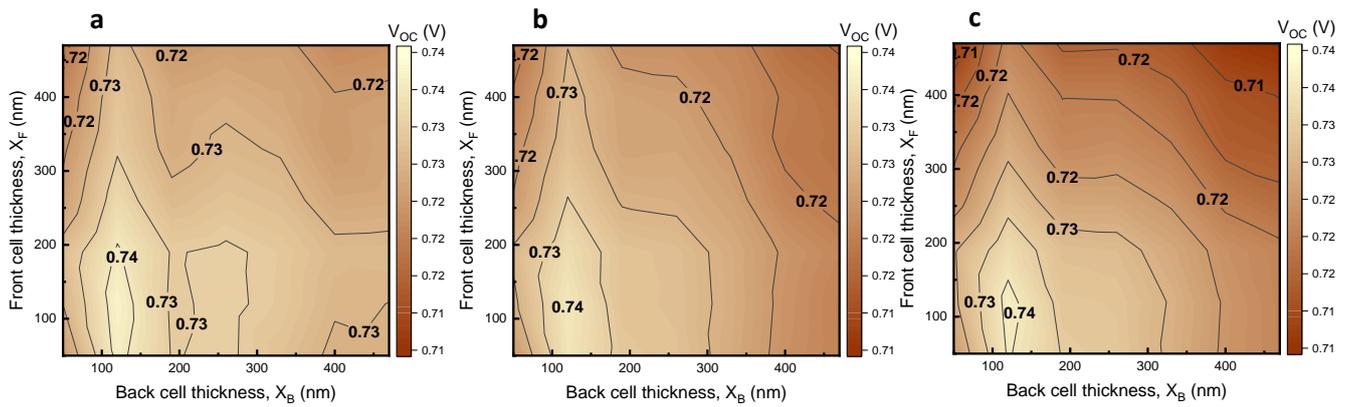
Appendix 7.2. Predictions of V_{OC} for a tandem cell as a function of front (x_F) and back (x_B) cell thickness. a) corresponds to the electron-enhanced model, b) base model, and c) hole-enhanced model.
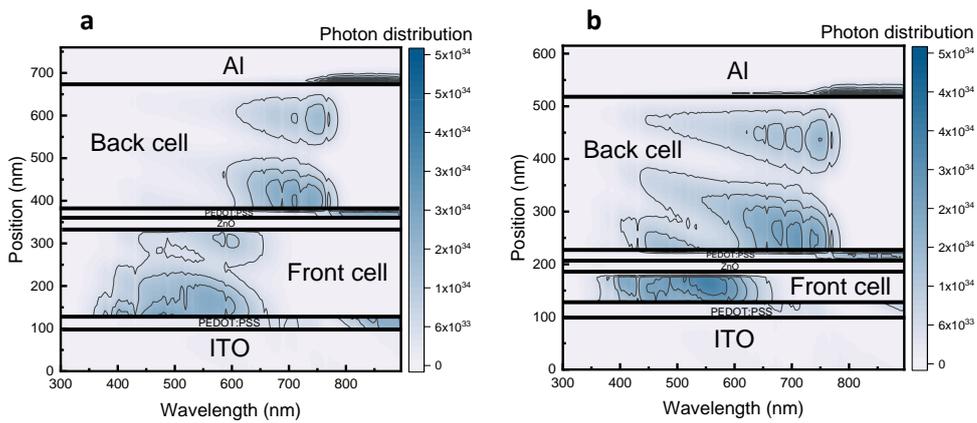

Appendix 7.3. Distribution of photon absorption in tandem devices (photons/m^3). a) shows 200 nm and 300 nm b) shows 50 nm and 300 nm as a function of front (x_F) and back (x_B) cell thickness.
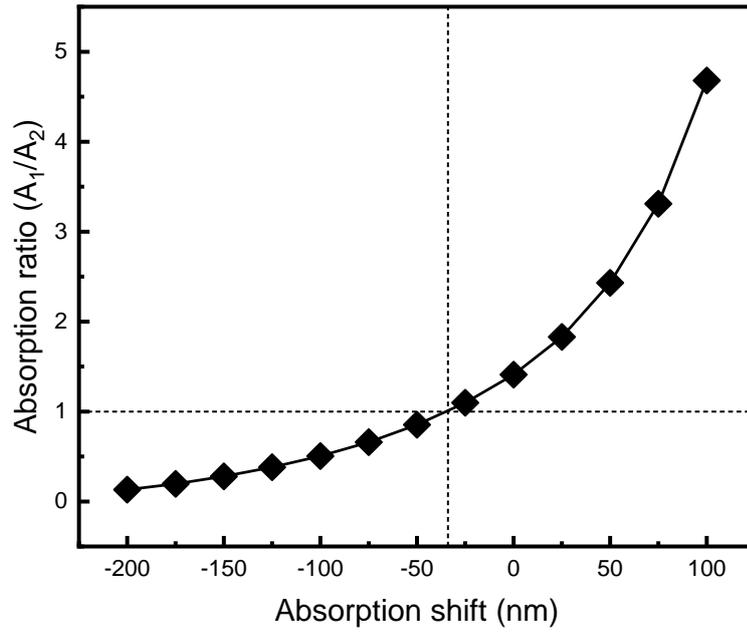
Appendix 7.4. Photon absorption ratio between the front cell and back cell for a tandem cell with $x_F = 300$ nm and $x_B = 350$ nm showing that balanced absorption occurs at a shift of $\sim$ -34 nm.
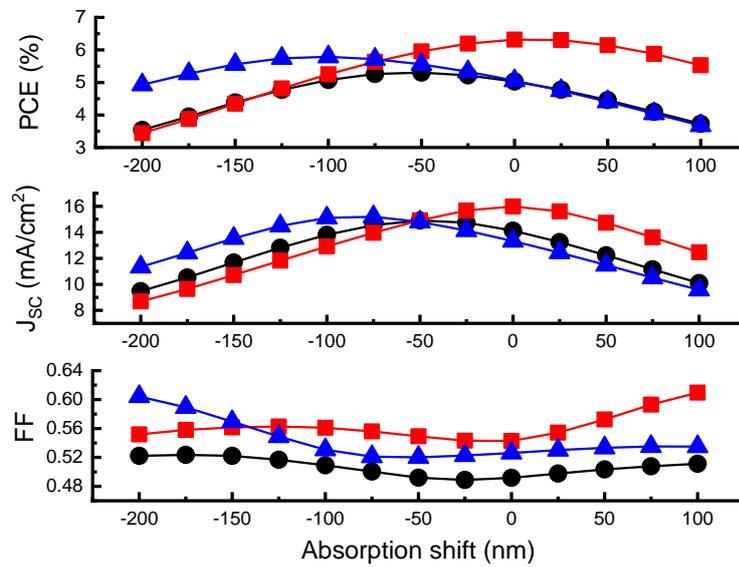

Appendix 7.5. Effect of shifted absorption on PCE, J_{SC} and FF for a tandem cell with $x_F = 300$ nm and $x_B = 350$ nm. Black circles denote the base model, red squares the electron-enhanced and blue triangles the hole-enhanced.
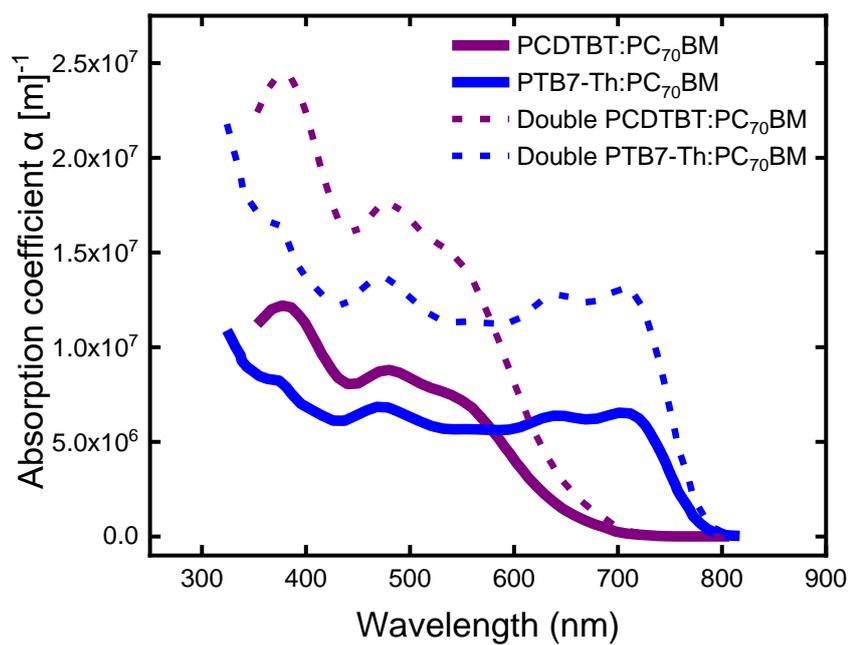
Appendix 7.6. Normal absorption spectrum of the front (PCDTBT:PC$_{70}$BM) and back cell (PTB7-Th:PC$_{70}$BM) in solid lines and doubled absorption profiles in short dots.
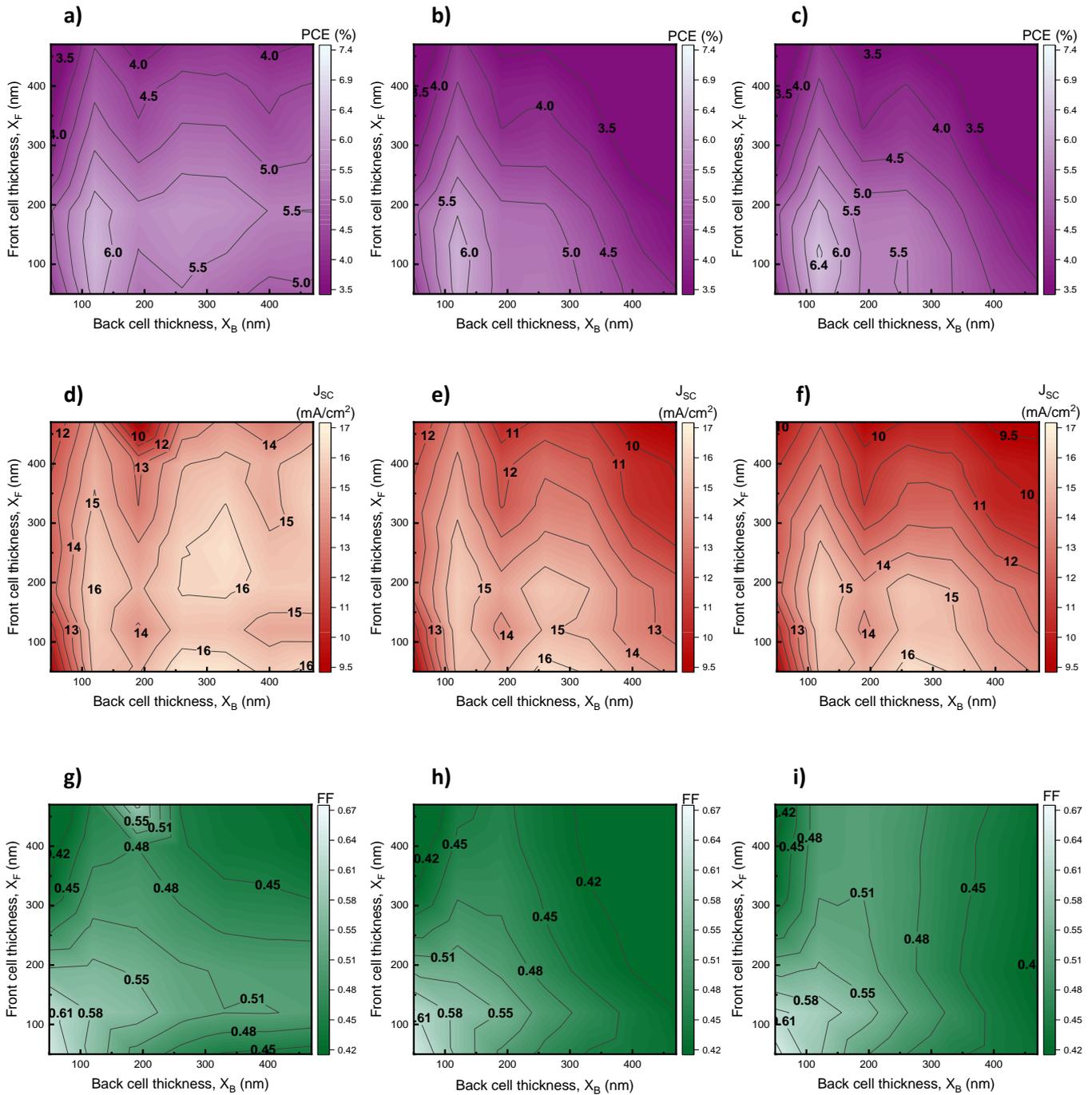
Appendix 7.7. Contour maps with PCE, J_{SC} and FF for tandem OPV devices considering regular absorption and increased recombination rate (by factor of 3) on both cells. a) - g) correspond to the electron-enhanced model, b) - h) to the balanced mobility model and c) - i) to the hole-enhanced model.
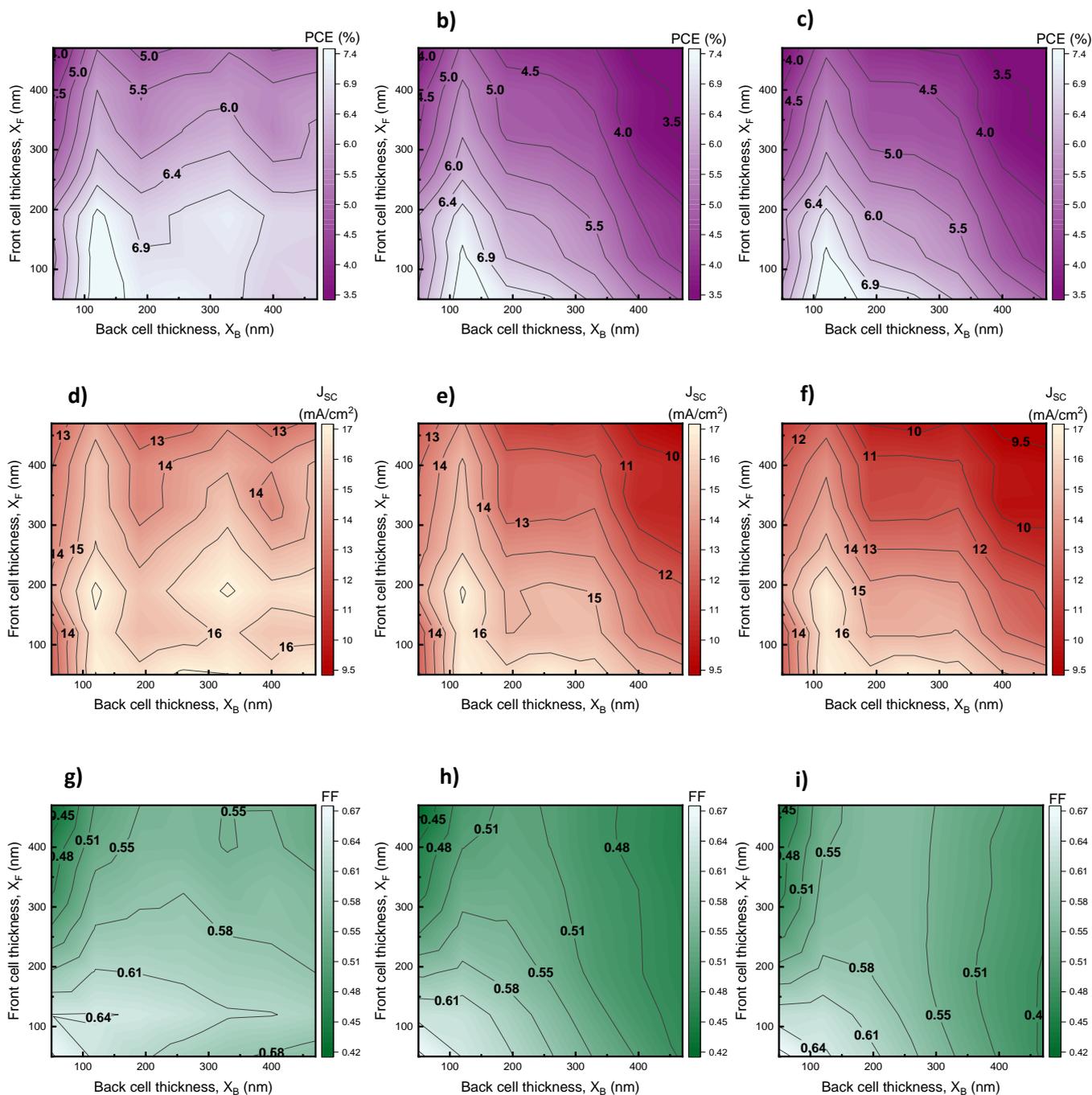
Appendix 7.8. Contour maps with PCE, J_{SC} and FF for tandem OPV devices considering doubled absorption on both cells. a) - g) correspond to the electron-enhanced model, b) - h) to the balanced mobility model and c) - i) to the hole-enhanced model.
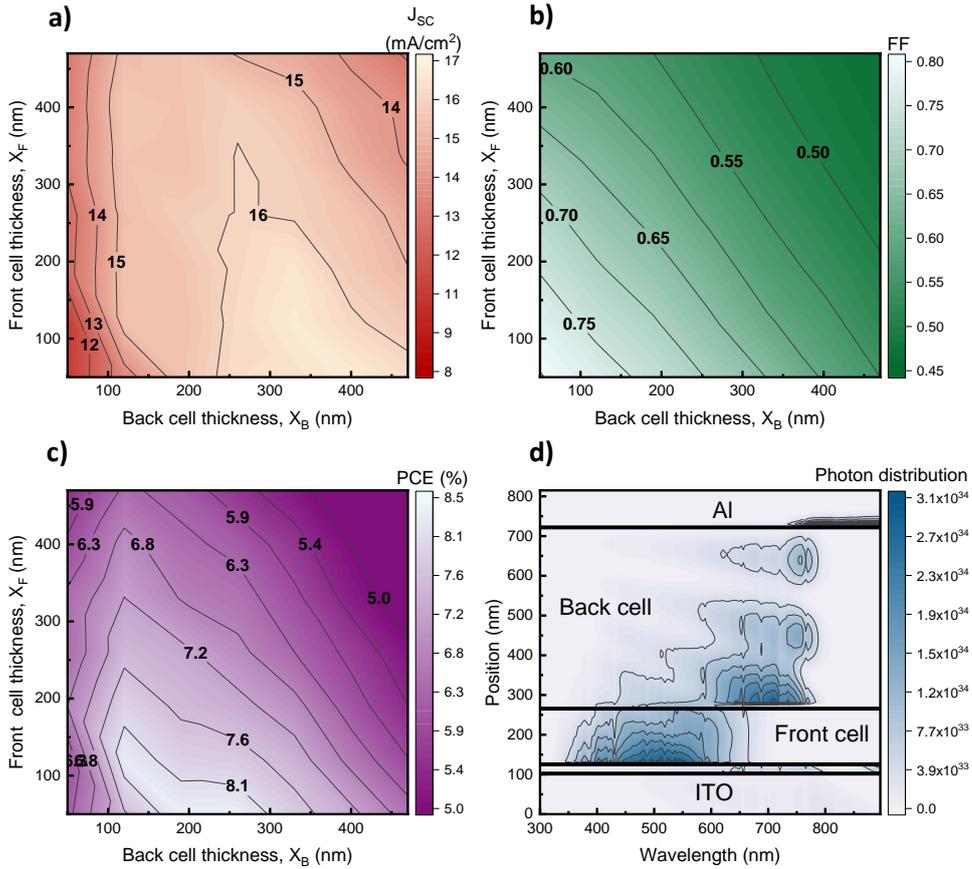
Appendix 7.9. Predictions of a) J_{SC}, b) FF and c) PCE for a double BHJ cell as a function of front (x_F) and back (x_B) cell thickness. d) Shows distribution of photon absorption in the cell (photons/m^3) within a region of optimal J_{SC} $x_F = 150$ nm and $x_B = 300$ nm.
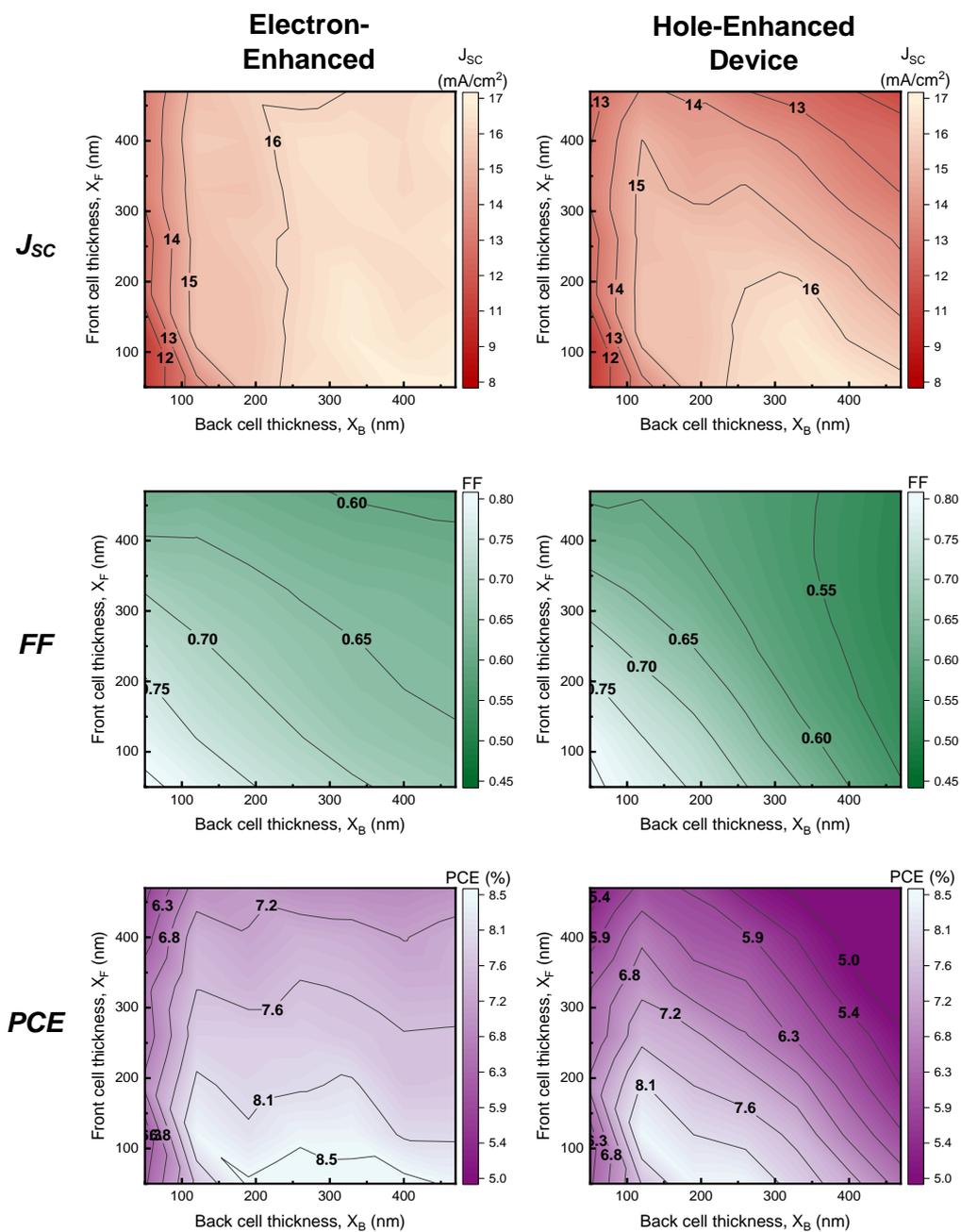
Appendix 7.10. Predictions of J_{SC}, FF and PCE (top, middle and bottom respectively) for both the electron- and hole-enhanced devices (left and right respectively) as a function of cell geometry in a double BHJ device.

Description	Units	Freiburg	Beijing
AOD	cm^{-1}	0.15	1.4
Water vapour	cm	1.6	1.8
NO_2	$\mu g/m^3$	23	54
Latitude	Degree °	48.01	39.54
Longitude	Degree °	7.84	116.38
Pressure	Bar	1.013	1.013

Appendix 7.11. Parameters used to generate spectra for Freiburg and Beijing. Data from 8 months considered and these were the chosen to build the spectra to emphasise on the difference between AOD.